

**ELECTRONIC AND TRANSPORT PROPERTIES
OF LOCALLY DELAMINATED BILAYER
GRAPHENE**

BY

HASAN MOHAMMED HASAN ABDULLAH

A Thesis Presented to the
DEANSHIP OF GRADUATE STUDIES

KING FAHD UNIVERSITY OF PETROLEUM & MINERALS

DHAHRAN, SAUDI ARABIA

In Partial Fulfillment of the
Requirements for the degree of

DOCTOR OF PHILOSOPHY

In

PHYSICS

NOVEMBER 2018

KING FAHD UNIVERSITY OF PETROLEUM & MINERALS
DHAHRAN 31261, SAUDI ARABIA

DEANSHIP OF GRADUATE STUDIES

This thesis, written by **HASAN MOHAMMED HASAN ABDULLAH** under the direction of his thesis adviser and approved by his thesis committee, has been presented to and accepted by the Dean of Graduate Studies, in partial fulfillment of the requirements for the degree of **DOCTOR OF PHILOSOPHY IN PHYSICS**.

Dissertation Committee

Prof. Hocine Bahlouli (Adviser)

Prof. Dr. François Peeters (Co-adviser)

Prof. Ibraheem Nasser (Member)

Prof. Khalil Ali Ziq (Member)

Dr. Saeed Al-Marzoug (Member)

Dr. Abdulaziz Husain M. Al-Aswad
Department Chairman

Dr. Salam A. Zummo
Dean of Graduate Studies

Date

©Hasan M. Abdullah
2018

Dedication

To my beloved wife and son who are the source of my happiness

ACKNOWLEDGMENTS

Foremost, I kneel humbly to Almighty Allah (S.W.T) thanking him for giving me the patience and strength to finish this work.

During my Ph.D. journey, there are many people who made it possible and wonderful. I would like to start with those who directly contributed to the portion of this thesis and without whom this work never could have been done. Firstly, I am heartily thankful to my supervisor Prof. Hocine Bahlouli for his guidance and continuous encouragement during my MSc and Ph.D. studies. His guidance helped me in all the time of studying graduate courses, research, and writing of this thesis.

I would like also to express my sincere gratitude to my co-supervisor Prof. Dr. Prof. Dr. François Peeters for helping and supporting me to handle the challenging issues during my Ph.D. research and I am really honored to be one of his students. I want also to thank him for giving me the opportunity to join his CMT group for three months where I met great scientists and nice people.

In 2013, it was the first time I met Dr. Ben Van Duppen during a workshop in Morocco. We had very enjoyable discussions on graphene that made me more eager to continue my Ph.D. research in the field of graphene. I was so lucky to work with him during the last four years where we did the all work in this thesis together. I want to thank him for

the plenty blackboard discussions we had at Antwerp and long Skype chats during my Ph.D. study. I am so grateful for his guidance, interesting physics discussions that enabled me to develop an understanding of the subject.

I would like to thank all m committee members Prof. Ibrahim Nasser, Prof. Khalil Ziq, and Dr. Saeed Al-Marzoug for their support since I first joined KFUPM as a graduate student in 2010. My deep appreciation goes also to the Physics Department at KFUPM, for the assistance and support. I also would like to acknowledge the material and scientific support of the Saudi Centre for Theoretical Physics (SCPT) for supporting my summer visits to CMT group at Antwerp University, Belgium.

I would like also to thank my collaborators Dr. M. Zarenia, Dr. D. R. da Costa, and Dr. M. Van der Donck for their help and fruitful discussions.

Secondly, I want to thank those who aided and guided my education since I joined College in 2007. I would especially like to express my gratitude to Prof. Mahioub Al-Buhairii who has been supporting, encouraging, and guiding me since I was a sophomore student at Taiz University, Yemen.

Thirdly, I would like to thank those who supported me as friends and family. Special thanks in this regard go to Prof. Mehdi Neek-Amal for his kindness and the generous hospitality during my stay at Antwerp. I would like also to thanks my friend there Hossein Ghorbanfekr Kalashami for the food tours we had together.

I spent the last eight years in KFUPM with an extraordinary friend who always supported me and made life wonderful outside homeland. I am indebted to my closest friends Rashad and Talal for the generous support.

Last and most importantly, I give my heartfelt thanks to all family members for their

continuous support.

TABLE OF CONTENTS

CHAPTER 1 INTRODUCTION	2
1.1 From graphite to graphene	3
1.2 Properties of graphene	4
1.3 Motivation and organization of the thesis	6
CHAPTER 2 THEORETICAL ASPECTS OF GRAPHENE AND ITS BILAYER SYSTEMS	8
2.1 Electronic properties of graphene	9
2.1.1 Crystallographic structure	9
2.1.2 Tight-binding model for π electrons	11
2.1.3 Continuum limit and Dirac-Weyl Hamiltonian	20
2.1.4 Helicity and chirality	23
2.2 Bilayer graphene	25
2.2.1 AB-stacking	25
2.2.2 Effective two-band Hamiltonian	32
2.2.3 AA-stacking	35
2.3 Klein tunneling	37
CHAPTER 3 QUANTUM TUNNELING ACROSS SINGLE AND DOU- BLE DOMAIN WALLS	39
3.1 The electronic model	41
3.1.1 Domain walls in bilayer graphene	43
3.1.2 Scattering definitions	44
3.2 Transmission across a single domain wall	49

3.3	Transport across two domain walls	55
3.3.1	AA-Stacking	55
3.3.2	AB-Stacking	65
3.3.3	AA-2SL-AB junction	81
CHAPTER 4 GATE TUNABLE LAYER SELECTIVITY OF ELECTRONIC TRANSPORT		84
4.1	Layer switch formalism	85
4.2	Smoothness effect on scattering probabilities	89
4.3	Layer selectivity	93
CHAPTER 5 CONFINEMENT IN GRAPHENE QUANTUM BLISTERS		96
5.1	Graphene quantum blisters	99
5.2	Theoretical aspects of GQB	101
5.2.1	Electrons in GQB	101
5.2.2	Inter-layer coupling in a GQB	102
5.2.3	Electronic confinement	103
5.2.4	Wavefunctions outside the GQB	104
5.2.5	Wavefunctions inside the GQB	106
5.3	Confined states in a GQB	110
5.3.1	Homogeneous inter-layer bias	110
5.3.2	Non-homogeneous inter-layer bias	117
5.3.3	Effect of the inter-layer coupling	126
5.3.4	Morphological effects	127
5.4	Controlling layer occupation	129
CHAPTER 6 ELECTRON COLLIMATION AT VAN DER WAALS DOMAIN WALLS		134
6.1	Semi-classical dynamics	136
6.1.1	Transmission probabilities and classical trajectories	139
6.2	Wave packet dynamics	143

6.3	Charge carriers collimation	148
6.4	Effect of a magnetic field	153
CHAPTER 7 CONCLUSIONS		157
APPENDICES		161
REFERENCES		163
VITAE		190

LIST OF FIGURES

1.1	Graphene as the building block of the other carbon allotropes, image adapted from Ref [1].	3
1.2	Few properties of graphene compared with different elements, figure is adopted from Ref [2].	5
2.1	(a) crystalline structure of single layer graphene with red and black balls representing carbon atoms at inequivalent sites that cannot be connected through the lattice vectors a_1 and a_2 . The lattice vectors can span the lattice and locate all the red atoms where the vectors δ_i connect the three nearest neighbor black atoms. Dashed gray region defines the unit cell which contains two atoms whose intralayer coupling is $\gamma_0 = 3$ eV with an intra-atomic distance $a = 0.142$ nm. (b) First BZ with reciprocal lattice vectors b_1 and b_2 , the colored dots indicate the high symmetry points in graphene.	9
2.2	Electronic configuration of (a) isolated (in ground state) carbon atom and being with same or different atoms (excited state).	11
2.3	(a) Schematic explains the sp^2 hybridisation in graphene and (b) shows the formation of the in-plane σ and out-of-plane π bonds which are responsible for the unique mechanical and transport properties in graphene, respectively. Figure taken from Ref. [3, p. 20]	12

2.4	(a) Shows the 3D energy spectrum of single layer graphene obtained from the TB approach, yellow and black colors correspond to conduction and valence bands, respectively, while the colored balls at $E = 0$ are the high symmetry points and the black lines represent the first BZ as illustrated in Fig. 2.1(b). For a better illustration, in panel (b) we show contour plot of the conduction band by superimposing the first BZ and the high symmetry points. (c) shows the valence and conduction bands along the high symmetry points Γ , M and K connected by the dashed-red lines in panel (b).	18
2.5	(a) shows angle-resolved photoemission spectroscopy (ARPES) measurements of energy spectrum in the first BZ along the high symmetry points with the results from the TB model superimposed as black curve. (b) shows the isotropic nature of the spectrum at low energy E_D indicated in panel (a). (c, d) same as (b) but at lower energies E_F and $E_D - 1\text{eV}$. Figure adapted from Ref. [4].	19
2.6	Low energy spectrum of single layer graphene around the Dirac points obtained from (a) tight binding (b) continuum approximation and (c) along q_x , i.e. with $q_y = 0$, red-dashed and blue curves correspond to tight binding and continuum limit, respectively.	22
2.7	Sublattice pseudospin representation in graphene, illustration taken from Ref. [5, p. 22].	24
2.8	Chirality in K - and K' -valleys and its relation with pseudospin and momentum. Yellow and black bands correspond to electrons and holes, respectively, and have opposite chirality in both valleys.	25
2.9	Side and top views of the crystalline structure of AB-BLG and AA-BLG crystalline structure with four atoms in the unit cell labeled by colored circle. In panel (a) the direct interlayer coupling is indicated by black-dashed lines while the coupling established by the skew hopping parameters is represented by green and red-dashed lines which are shown as green and red bonds in panel (c). Dashed gray region defines the unit cell in AB-BLG.	27

2.10	(a, b) show the energy spectrum along the high symmetry points of AB-BLG and AA-BLG obtained from the TB approximation, respectively. (c, d) show the corresponding energy spectrum around the Dirac point obtained using the continuum approximation which is valid in the orange-dashed region in panels (a, b). For AB-BLG, in the TB approximation (solid black bands) all interlayer coupling parameters are included (i.e. $\gamma_{1,3,4}$) while in the continuum approximation only the direct interlayer coupling γ_1 is considered whereas in AA-BLG only the direct interlayer coupling is considered in both approximations.	29
2.11	(a, b) show the four energy bands of AB-BLG and AA-BLG around the K -valley. Solid and dashed curves correspond to pristine and biased ($\delta = 100$ meV) BLG, respectively, while the red and blue color label the two modes in AB-BLG and the two Dirac cones in AA-BLG.	32
2.12	Low energy spectrum of AB-BLG obtained from the four-(dashed-orange) and two-band (solid black) Hamiltonians described by Eqs. (2.41, 2.48), respectively. (a, b) Correspond to pristine and biased ($\delta = 15$ meV) AB-BLG.	34
2.13	Schematic representation explains Klein tunneling in (a) single layer and (b) bilayer graphene. Solid and dashed bands coincide with negative and positive group velocity, respectively. Black, green, and yellow dots represent incident, transmitted, and reflected particles, respectively. v_0 indicates the strength of the electrostatic barrier and E_F is the Fermi energy.	37

3.1	(Colour online) Different geometries for bilayer and two decoupled graphene layer interfaces with schematic representation of the transmission probabilities. (c) two single graphene layers connected to AB-BL(2SL-AB). (b) AA-BL leads with 2SL as intermediate region (AA-2SL-AA). (c) AA or AB stacking bilayer graphene sandwiched between two SL graphene layers (2SL-AA(AB)-2SL) and (d) similar to (b) but now with AB-BL as the leads with two upper (red)-lower (blue) shifted Dirac cones (AB-2SL-AB). (e) left and right leads are bilayer graphene with different stacking connected to the two decoupled graphene sheets (AA-2SL-AB). The possible transmission processes between the different conduction channel are indicated above the respective junctions.	42
3.2	(Colour online) Schematic diagrams, for one domain wall separating 2SL and AB-BL, showing the regions where the modes (k^+ , k^-) in AB-BL are either real (propagating) or imaginary (evanescent). (a) shows the bands of pristine 2SL and gated AB-BL and vice versa in (b). In the yellow region both modes are real (R, R), while one of them is real and the other is imaginary as in the green (I, R) and pink (R, I) regions. In the gray region both modes are imaginary (I, I). Blue, red and dashed black bands correspond to k^+ , k^- and 2SL modes, respectively.	50
3.3	(Colour online) The angle-dependent transmission and reflection probabilities through (a, b) 2SL-AA and (c, d) AA-2SL systems. The systems in (b, d) are the same as in (a, c), respectively, but where now the right side of the junction is subjected to an electrostatic potential of strength $v_0 = 1.5\gamma_1$. In the system 2SL-AA $R_b^{b(t)} = R_t^{t(b)}$ and $T_b^\pm = T_t^\pm$ while $R_+^- = R_-^+ = 0$ and $T_\pm^b = T_\pm^t$ in AA-2SL system. In all panels $E = 1.2 \gamma_1$	51
3.4	(Colour online) Density plot of the transmission and reflection probabilities through 2SL-AA-2SL as a function of Fermi energy and transverse wave vector k_y with $v_0 = \delta = 0$ and width of the AA-BL $d = 25$ nm.	57

3.5	(Colour online) The same as in Fig. 3.4, but now with $v_0 = 1.5\gamma_1$. Red and white dashed curves correspond to the lower and upper Dirac cones in AA-BL, respectively, while the black dashed curves are the bands of 2SL.	58
3.6	(Colour online) The same as in Fig. 3.4, but now with $v_0 = 1.5\gamma_1$ and $\delta = 0.6\gamma_1$.	59
3.7	(Colour online) Density plot of the transmission and reflection probabilities through AA-2SL-AA as a function of Fermi energy and transverse wave vector k_y with $v_0 = \delta = 0$ and width of the 2SL $d = 25$ nm.	60
3.8	(Colour online) The same as in Fig. 3.7, but now with $v_0 = 1.5\gamma_1$.	61
3.9	(Colour online) The same as in Fig. 3.7, but now with $v_0 = 1.5\gamma_1$ and $\delta = 0.3\gamma_1$. Red and white dashed curves correspond to the bands of bottom and top layers of 2SL, respectively, while the black dashed curves are the AA-BL bands.	62
3.10	(Colour online) Conductance of two-block system for different magnitudes of the applied gate: (a, b) $v_0 = \delta = 0$, (c, d) $v_0 = 3\gamma_1/2$, $\delta = 0$. G_T is the total conductance obtained by summation of all possible channels, (e, f) the total conductance for 2SL-2SL and AA-AA junctions, respectively, with $v_0 = 0$ (blue curves) and $v_0 = 1.5\gamma_1$ (black curves).	65
3.11	(Colour online) Conductance of three-block system with different magnitudes of the applied gate: (a, b) $v_0 = \delta = 0$, (c, d) $v_0 = 3\gamma_1/2$, $\delta = 0$ and (e, f) $v_0 = 3\gamma_1/2$, $\delta = 0.6\gamma_1$. G_T is the total conductance obtained by summation of all possible channels.	66
3.12	(Colour online) The angle-dependent transmission and reflection probabilities through (a, b) 2SL-AB and (c, d) AB-2SL junctions. The systems in (b, d) are the same as in (a, c), respectively, but where the right side of the junction is subjected to an electrostatic potential of strength $v_0 = 1.5\gamma_1$. In (a) $E = 1.2\gamma_1$ for all channels while in (b) $E = 1.7\gamma_1$ for $T_{b(t)}^+$ and $E = 0.6\gamma_1$ for the rest of the channels and in (c, d) $E = (0.6, 1.7)\gamma_1$ for $R_+^+/T_+^{b(t)}$ and $R_-^-/T_-^{b(t)}$, respectively. We choose energy values in (b, d) such that they correspond to only one propagating mode in the AB-BL region.	67

3.13 (Colour online) Density plot of the transmission and reflection probabilities through 2SL-AB-2SL as a function of Fermi energy and transverse wave vector k_y with $v_0 = \delta = 0$	68
3.14 (Colour online) The same as in Fig. 3.13, but now with $v_0 = 3\gamma_1/2$	70
3.15 (Colour online) The same as in Fig. 3.13, but now with $v_0 = 3\gamma_1/2$, $\delta = 0.8\gamma_1$. New localized states appear inside the “ <i>Mexican hat</i> ” shape of the low energy bands of AB-BL due to the strong gate potential.	71
3.16 (Colour online) Transmission probabilities as function of Fermi energy and bias for normal incidence.	72
3.17 (Colour online) Density plot of the transmission and reflection probabilities through AB-2SL-AB as a function of Fermi energy and transverse wave vector k_y with $v_0 = \delta = 0$ and $d = 25\text{nm}$	73
3.18 (Colour online) The same as in Fig. 3.17, but here with $v_0 = 3\gamma_1/2$	74
3.19 (Colour online) The same as in Fig. 3.17, but here with $v_0 = 3\gamma_1/2$, $\delta = 0.8\gamma_1$. Red and white dashed curves correspond to the bands of bottom and top layers of 2SL while the black dashed curves are the AB-BL bands.	76
3.20 (Colour online) Conductance of different junctions for different magnitudes of the applied gate: (a, b) $v_0 = \delta = 0$, (c, d) $v_0 = 3\gamma_1/2$, $\delta = 0$, (e, f) the total conductance for 2SL-2SL and AB-AB junctions, respectively, with $v_0 = 0$ (blue curves) and $v_0 = 1.5\gamma_1$ (black curves).	77
3.21 (Colour online) Conductance across the 2SL-AB system as a function of the bias on the AB-BL with $v_0 = 0$. (a) and (b) correspond to the single and double modes regime with $E = 0.3\gamma_1$ and $E = 1.15\gamma_1$, respectively, with $G_T^\pm = G_t^\pm + G_b^\pm$	77
3.22 (Colour online) Conductance of different junctions for different magnitudes of the applied gate: (a, b) $v_0 = \delta = 0$, (c, d) $v_0 = 3\gamma_1/2$, $\delta = 0$ and (e, f) $v_0 = 3\gamma_1/2$, $\delta = 0.8\gamma_1$	78

3.23	(Colour online) Density plot of the transmission and reflection probabilities through AA-2SL-AB junction as a function of Fermi energy and transverse wave vector k_y with $v_0 = 1.5\gamma_1$, $\delta = 0$ and $d = 25\text{nm}$. The superimposed dashed curves represent the bands of AB-BL(black), AA-BL(green) and 2SL (white), with γ_1 being the inter-layer coupling of AB-BL.	79
3.24	(Colour online) (a) Transmission and reflection probabilities for normal incidence for $v_0 = 3\gamma_1/2$, $\delta = 0$. (b) Transmission probabilities with normal incidence for AA-BL (AB-BL) n-p-n junction, green (black) curves. Blue (red) curves are the non-zero channels T_+^+ (T_-^-) in AA-2SL-AB. All energies are considered to be less than the electrostatic potential strength. Conductance of AA-2SL-AB junction for different magnitudes of the applied gate: (c) $v_0 = \delta = 0$, (d) $v_0 = 3\gamma_1/2$, $\delta = 0$, (e) $v_0 = 3\gamma_1/2$, $\delta = 0.6\gamma_1$, with γ_1 being the inter-layer coupling of AB-BL.	80
4.1	(Colour on-line) (a) Schematic presentation of the proposed structure with the indication of the top and back gate, the coupled region (BLG) and the decoupled graphene sheets (2SLG). (b) and (c): cross section of the device with abrupt and smooth transitions from the coupled to the decoupled region respectively. The arrows in (b) indicate the different transmission channels as discussed in the text.	85
4.2	(Colour on-line) Band dispersion relations around the Dirac point for single layer graphene (left), AA-stacked (middle) and AB-stacked (right) bilayer graphene. The dashed curves correspond to the spectrum of the system in case of a finite bias, i.e. $\delta \neq 0$	86
4.3	(Colour on-line) Transmission and reflection probabilities at normal incidence as a function of the Fermi energy, through 2SLG-AB-2SLG structure. (a, b) and (c, d) for the non scattered and scattered channels with $\delta = v_0 = 0$, respectively, solid (dashed) lines for abrupt(smoothed) structure with $L = 25\text{ nm}$, $L_L = L_R = 5\text{ nm}$ and $L_M = 20\text{ nm}$, (see Fig. 4.1 (c)). For only abrupt structure with $v_0 = 3\gamma_1/2$, (e, f) and (g, h) for $\delta = 0, 0.3\gamma_1$, respectively.	90

- 4.4 (Colour on-line) Transmission and reflection probabilities at normal incidence as a function of the bilayer width L for $\delta = v_0 = 0$. (a) for AB-stacking with $E = 3\gamma_1/2$ and (b) for AA-stacking with $E = 3\gamma_1/2$ 91
- 4.5 (Colour on-line) Conductance and reflectance along with their associated layer filtering as a function of the bias through a 2SLG-AB-2SLG structure for $E = 0.3\gamma_1$ and $v_0 = 1.8\gamma_1$ and $L = 25.8$ nm. (a) and (b) conductance and reflectance; (c) and (d) the corresponding layer filtering, respectively. 92
- 4.6 (Colour on-line) Conductance and reflectance along with their associated layer filtering as a function of the bias through 2SLG-AA-2SLG structure for $E = 0.3\gamma_1$ and $v_0 = 1.8\gamma_1$ and $L = 26.4$ nm. (a) and (b) conductance and reflectance, (c) and (d) the corresponding layer filtering, respectively. 93
- 5.1 (Color online) (a) Schematic representation of the structure of a circular GQB with radius R . The graph shows the inter-layer distance (red) and the local band gap (black) when a global bias $\delta = 0.12$ eV is applied. The dashed blue curve corresponds to the approximate band gap profile with an abrupt change at the interface R of the GQB. (b) Top view of the two layer outside the blister placed in AB-stacking. (c) Schematic representation of a cross section of the GQB depicting the position of the different atoms in the unit cell. The black lines denote the π orbitals while the vertical green lines represent the inter-layer coupling. Notice that for illustrative reasons only a small number of atoms are shown. The discussed GQBs in this study typically have radii of several hundreds of atoms or tens of nanometers. (d) Energy spectrum inside (left) and outside (right) the GQB. Red and blue bands in left panel correspond to top and bottom layers while the horizontal black lines in the left figure represent the discrete energy levels that occur due to confinement. These states are only allowed in the range $E < |\delta_G|$ as delimited by the yellow region. The solid black curves in the right figure denote the edge of the continuum spectrum outside the GQB. . . . 98

5.2	Energy levels of the GQB as a function of its radius with the same bias inside and outside the GQB $\delta_{<} = \delta_{>} = 0.25\gamma_1$. The dashed green vertical lines in panel (a) represent the radii where the states residence is the same in both layers. Gray dashed curves correspond to the first energy levels of a biased bilayer nano-disk.	109
5.3	(a-h) Radial probability density of $m = 0$ stats in Fig. 5.2(a) labelled by (1-8), respectively. The green dashed vertical line represents the radius of the GQB. Note that the states close to the continuum spectrum are mainly localized outside the GQB and preferably on the disconnected sublattices A2 and B1 as indicated in panels (g) and (h), respectively.	111
5.4	Real part of the different components of the wavefunction for states with energy $E = 0.2\gamma_1^0$ meV and $E = 0.05\gamma_1^0$ for top and bottom rows, respectively. We assume a blister with radius $R = 10.5l$ and bias $\delta = 0.25\gamma_1^0$. The radius of the blister is indicated by white dashed circle.	112
5.5	Radial probability density outside the blister of the states $\epsilon_{0,1}$ in Fig. 5.2(a) labelled by yellow points (4,9,10). The green vertical line represents the radius of the GQB.	112
5.6	The radial probability density of $m = \pm 1$ states in Fig. 5.2(b) labelled by red and green dots. Top and bottom panels are for the $K-$ and $K'-$ valley, respectively. The green vertical line represents the radius of the GQB. Note that $[\mathcal{P}_{m,n}^\tau(\epsilon, \rho)]_{\text{Layer1}} = [\mathcal{P}_{-m,-n}^\tau(-\epsilon, \rho)]_{\text{Layer2}}$ and $[\mathcal{P}_{m,n}^\tau(\epsilon, \rho)]_{\text{Layer1}} = [\mathcal{P}_{m,n}^{-\tau}(\epsilon, \rho)]_{\text{Layer2}}$ while the total radial probability density is the same in both valleys.	113
5.7	LDOS of the GQB for layer 1 (left) and layer 2 (right), with $R = 10l$ and $\delta_{<} = \delta_{>} = 0.25\gamma_1^0$. The spectral width of the Gaussian profile is $\Gamma = 0.02\delta_{>}$. The dashed green vertical lines represent the radius of the GQB.	117
5.8	Energy levels of the GQB as a function of its radius with different bias inside and outside the GQB $\delta_{<} = 0$ and $\delta_{>} = 0.25\gamma_1^0$. Solid (dashed) curves are for $m > 0$ ($m < 0$) where yellow horizontal lines delimit the gap outside the GQB.	119

5.9	(a-d) Radial probability density of the $m = 0$ states in Fig. 5.8(a) labelled by (1-4), respectively. The green vertical line represents the radius $R = 30l$ of the GQB.	120
5.10	(a-f) Radial probability density of $m = \pm(1, 2, 3)$ states in Fig. 5.8(b,c,d) labelled by green and red dots, respectively. The green vertical line represents the radius of the GQB $R = 30l$	121
5.11	Energy levels of a GQB as a function of angular momentum label m for $R = 20l$ and $\delta_{>} = 0.25\gamma_1^0$ and for different values of $\delta_{<}$	122
5.12	Energy levels of the GQB as a function of its radius for different strength of the bias inside the GQB with $\delta_{>} = 2\delta_{<} = 0.25\gamma_1$. Solid (dashed) curves are for $m > 0$ ($m < 0$) where yellow horizontal lines delimit the gap outside the GQB.	122
5.13	Energy levels of the GQB as a function of its radius opposite bias inside and outside the GQB with $\delta_{>} = -\delta_{<} = 0.25\gamma_1^0$. Solid (dashed) curves are for $m > 0$ ($m < 0$) where yellow horizontal lines delimit the gap outside the GQB.	123
5.14	Energy levels of the GQB as a function of the bias inside the GQB $\delta_{<}$ with $\delta_{>} = 0.25\gamma_1^0$ and $R = 10l$. Solid (dashed) curves are for $m > 0$ ($m < 0$) where yellow horizontal lines delimit the gap outside the GQB. The vertical dashed brown lines represent the points $\delta_{<} = \pm\delta_{>}$	123
5.15	(a-f) Radial probability density of states $\epsilon_{\pm 1, \pm 1}$ in Fig. 5.13(b) labelled by points (1-5). The green vertical line represents the radius of the GQB.	124
5.16	Energy levels of GQB with different strength of the inter-layer coupling inside it, where yellow horizontal dashed and solid lines delimit the gap inside and outside the GQB, respectively, with $\delta_{<} = \delta_{>} = 0.25\gamma_1^0$	125
5.17	Energy levels of GQB with different strength of the inter-layer coupling inside it. Solid (dashed) curves are for $m > 0$ ($m < 0$) where yellow horizontal lines delimit the gap in bilayer graphene with $\delta_{>} = 0.25\gamma_1^0$	126

5.18	Energy levels of a GQB, same as in Fig. 5.2(a), but with a gaussian interface. (a) Dashed-blue, black, and dashed-red curves correspond to a gaussian dome of height $(1.5, 3, 10)c_0$, respectively. (b) The height of the gaussian dome is fixed at $3c_0$ while the inter-layer bias inside the blister is considered constant (black curves) and varies with the inter-layer distance (dashed-orange curves).	128
5.19	(a, b) Show the energy levels where inside the GQB is purely hole- and electron-doped, respectively. Outside the blister the bias is kept $0.25\gamma_1^0$.	130
5.20	Energy levels of a GQB and corresponding layer occupation indicated by the color as shown in the right color bar for angular quantum number $m = 0$. The solid curves in (a) and (b) correspond to the case of a blister with homogenous bias δ or an opposite bias inside the GQB, respectively. Yellow horizontal lines delimit the energy range for confinement, i.e. $E = \pm\delta_G$. In both graphs we have chosen $\delta = 0.25\gamma_1^0$. Dashed and dotted-dashed curves represent the first energy levels of pure holes and electrons confined states inside the blister (the levels labeled by black dots in Fig. 5.19).	132
5.21	Energy levels of GQB as a function of the global homogeneous bias $\delta_{<} = \delta_{>} = \delta$ for $m = 0$ and $R = 21l$. Red dashed and yellow solid curves correspond to $E = \pm\delta$ and $E = \pm\delta_G$, respectively.	133
6.1	Schematic illustration of (a) delaminated bilayer graphene connected to AA-BLG, and (b) single layer graphene attached to AA-BL whose terminated edge of the top layer either zigzag or armchair type. The energy spectrum of (c) single-layer graphene, (d) AA-stacked bilayer graphene. Yellow and Black bands correspond to electrons and holes carriers in SL while in AA-BL they represent electron- and hole-like states. Red and blue bands represents the upper and lower Dirac cones in AA-BL.	137

6.2	(a) Top panel illustrates the 2SLG-BLG junction with an incident and transmitted electron beams in the $x-y$ plane, while the bottom panel shows the transmitted angle θ as a function of the Fermi energy and the incident angle ϕ for SLG-AA junctions with $v_0 = 0.1$ eV. (b) Classical trajectories of an electronic beam impinging on media with different refraction indices. (c) Refraction index with the corresponding band diagram for SLG-AA as a function of the electrostatic potential strength v_0 where the Fermi energy of the incident particles $E = 12$ meV. Blue and red curves correspond to the perspective mode in AA-BLG region.	138
6.3	Cyclotron radius in pristine single-layer graphene, AA-stacked bilayer graphene for different Fermi energy. The red and blue curves correspond to the upper and lower cones in AA-BLG, respectively.	141
6.4	Scattering from 2SLG into lower k^+ (solid lines) and upper k^- (dashed lines) cones in AA-BLG with different incident energies . Both 2SLG and AA-BLG are pristine where left and right columns show trajectories obtained from semi-classical and wave-packet dynamics approaches, respectively. Color bar represents the transmission probability.	148
6.5	The same as in Fig. 6.4 but scattering here from SLG to AA-BLG whose top layer possesses armchair edge at the interface.	149
6.6	Comparison between the transmission probabilities obtained from SC approach for 2SLG-AA and SLG-AA with zigzag- and armchair-edges with $v_0 = 0$. T_+ and T_- are the intra-cone transmission probabilities where carriers scatter into the lower and upper cones, respectively.	150
6.7	Comparison between the transmission probabilities obtained from the wave packet dynamics (WD) and semi-classical approach (SC). Note that for SLG-AA the WD results are only for AC-Edge. The incident energies are (4, 16 meV for top and bottom rows, respectively, while the electrostatic potential $v_0 = 0$	151

6.8	Trajectories of the charge carriers scattering from 2SLG into AA-BLG in the presence of a perpendicular magnetic field $B = 1\text{T}$ (only in the yellow region $y > 40\text{ nm}$) in the $x - y$ plane for 2SLG-AA junction with $v_0 = 0$. Red and blue trajectories correspond to the upper k^- and lower k^+ cones as indicated in the top of Fig. 6.1(b).	154
6.9	Contour plots of the time average for the squared modulus of the Gaussian wave function scattering from 2SLG into AA-stacked BLG with an initial energy (a-b) $E = 4\text{ meV}$ and (e-h) $E = 16\text{ meV}$, for an incident angle $\phi = \pi/6$. The amplitude of the magnetic field was assumed to be (a, c, e, g) $B = 0$ and (b, d, f, h) $B = 1\text{ T}$. The Solid-dashed black line indicates the interface of the junction . Top (bottom) panels correspond to the lower k^+ (upper k^-) cones in the AA-BLG spectrum.	155

THESIS ABSTRACT

NAME: Hasan Mohammed Hasan Abdullah

TITLE OF STUDY: Electronic and transport properties of locally delaminated bilayer graphene

MAJOR FIELD: Physics

DATE OF DEGREE: November 2018

The contemporary isolation of single layer graphite, the so-called graphene, has engendered an avalanche of interest due to its astonishing optical, electronic and mechanical properties. Through this thesis, we will explore the electronic and transport properties of locally delaminated bilayer graphene and give insights to the quest for the deployment of graphene in the electronic industry. Using the continuum model, we show that domain walls separating different inter-layer coupling domains have a considerable effect on the chiral tunnelling properties of the charge carriers. In particular, a strong layer selectivity exists when current flows from delaminated bilayer graphene through a coupled region and this selectivity can be tuned by means of electrostatic gating. In addition, locally delaminated bilayer graphene can provide a perfect electrostatic confinement which is precluded by Klein tunneling in single layer graphene. We scrutinize the electronic properties of these confined states under the variation of interlayer bias, coupling, and size of the confine-

ment area. Interestingly, we find that the discrete energy levels in the system correspond to localized electron and hole states in the top and bottom layers. Finally, show how locally delaminated AA-stacked bilayer graphene can be used to generate highly collimated electron beams which can be steered by a magnetic field. We investigate the electron scattering using semi-classical dynamics and verify the results independently with wave-packet dynamics simulations. This thesis provides new insights into the field of electronics of graphene and could help to achieve the main goal of deployment of graphene-based electronics.

List of abbreviations

1D	One-dimensional
2D	Two-dimensional
TBM	Tight Binding Model
BZ	Brillouin zone
LCAO	Linear combination of atomic orbitals
SL	Single layer graphene
2SL	Two decoupled single layers graphene
AA-BL	AA-stacked bilayer graphene
AB-BL	AB-stacked bilayer graphene
STM	Scanning tunneling microscope
QD	Quantum dot
GQB	Graphene quantum blister
RPD	Radial probability density
LDOS	Local density of states
SC	Semi-classical
WD	Wave-packet dynamics
BCs	Boundary conditions

CHAPTER 1

INTRODUCTION

Materials and their unique properties are always crucial to the science developments and technological advances in all branches. For example, exploiting the sun light to produce clean energy requires materials that are very efficient in converting the radiation into another form of energy such as heat or electricity. In the electronic industry, one of the biggest obstacle that it is facing is the overheat associated with the electronic devices causing a problem in their durability and functionality. In medicine, for instance, scientists are looking for materials that target and kill cancer cells without side effects on the immune system.

Early in the twentieth century a two dimensional material of a one atom thick carbon layer was synthesized for the first time. This material is called graphene and is essentially one layer of the graphite; the well known material used in the pencils. A sheet of graphene is 1000 times thinner than a usual paper and 100 times stronger than steel. A graphene hammock can cradle a 4kg cat while it weighs no more than one of its whiskers. Graphene is a good conductor of heat and electricity, stretchable and yet is almost transparent. It acts as a mesh where it captures the smallest atoms of gas-Helium- and yet allows water

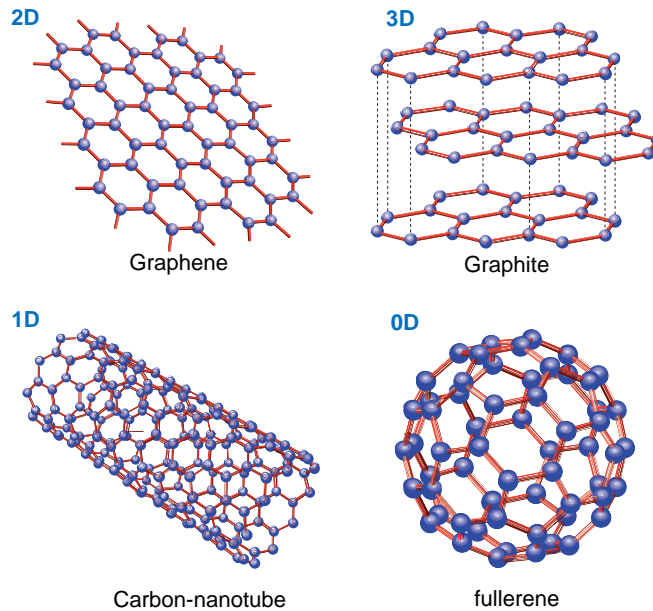


Figure 1.1: Graphene as the building block of the other carbon allotropes, image adapted from Ref [1].

vapour to pass through.

As a physicist, the scope of this thesis is to investigate the electronic and transport properties of graphene flakes composed of different stackings to provide a better understanding of the charge carriers behavior in this unique material.

1.1 From graphite to graphene

Graphite is a well known naturally-occurring material form of crystalline carbon atoms and one layer of graphite is called Graphene. The terminology "graphene" was introduced by Boehm in 1986 [6, 7] and its first part refers to graphite while the suffix is an indication of polycyclic aromatic hydrocarbons. The story of graphene can be tracked back then to 1859 [8] when a British Benjamin Brodie exposed graphite to strong acids and claimed that he discovered "graphon" a new form of graphite. In fact, what he observed

was a graphene sheet covered with dense hydroxyl and epoxide groups [9]. Theoretically graphene was studied in 1947 when P. Wallace [10] investigated the band structure of graphite. Then, in 1962 Boehm performed the first experiment looking for the thinnest flake of reduced graphite oxide which was identified as monolayer [11]. It was believed that single layer of graphite, "graphene", cannot be isolated due to the strong 2D thermal fluctuations which inhibits experimentalists looking for this material. The first ever success to fabricate a single layer of graphene was achieved in 2004 at University of Manchester by Sir Konstantin Novoselov and Sir Andre Geim [12]. They used a very simple technique called Scotch tape technique. After they awarded the Nobel Prize in Physics in 2010 *for their discovery of Graphene*, Novoselov commented on the simple idea behind synthesis of graphene and said, "a playful idea is perfect to start things but then you need a really good scientific intuition that your playful experiment will lead to something, or it will stay as a joke for ever". He continued, "joking for a week or two is the right way to go, but you don't want to make your whole research into a joke".

After the discovery of graphene, scientists now have accessed to all allotropes of carbon-based materials such as carbon-nanotubes and fullerene as illustrated in Fig. 1.1

1.2 Properties of graphene

Since its experimental realization in 2004, graphene, a two-dimensional (2D) layer of carbon atoms with honeycomb crystal structure and its multilayer systems, as shown in Fig. 1.1, have triggered an avalanche of scientific interest. Such enormous interest in graphene resulted from its remarkable electronic, optical, mechanical properties as well

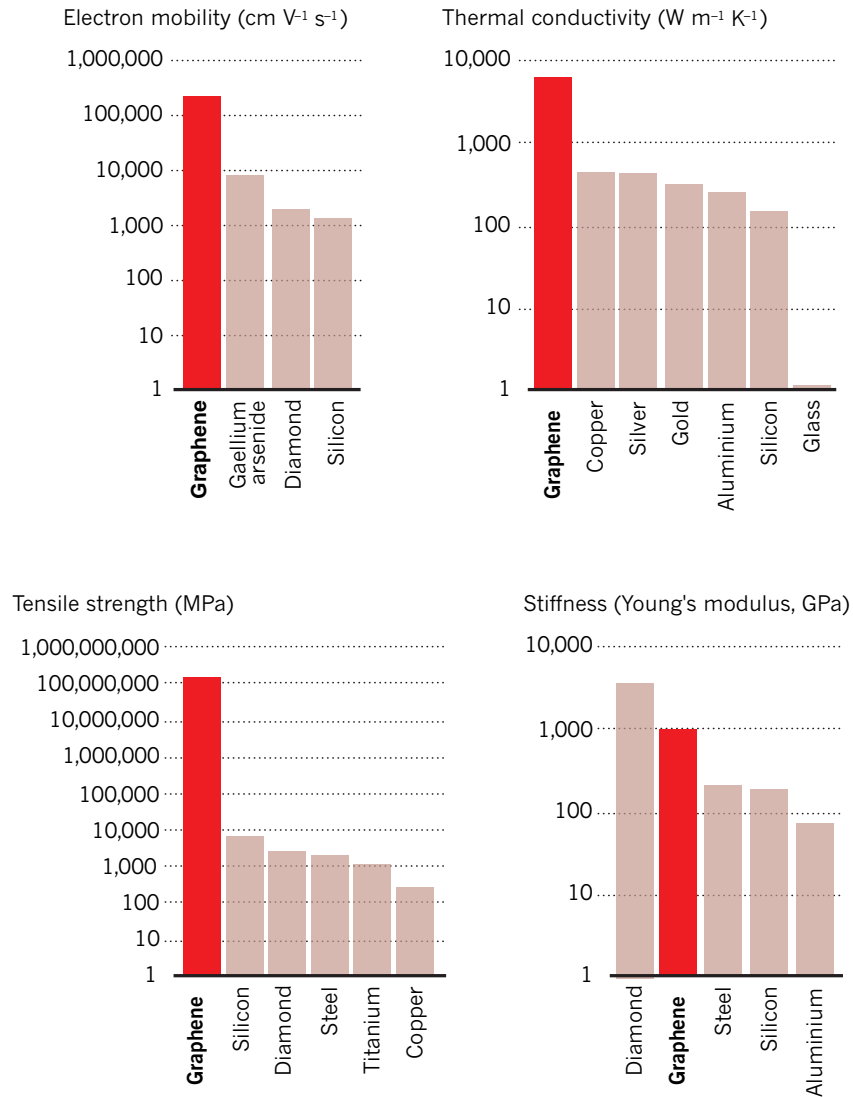


Figure 1.2: Few properties of graphene compared with different elements, figure is adopted from Ref [2].

as its potential use in sensors, detectors, electronics, ..etc. Some of these properties are presented in Fig. 1.2 and compared with other traditional materials such as Silicon, copper, steel, and diamond.

Among others, the relativistic nature of carriers in graphene is the most striking feature where with move with speed of 300 times smaller than of light [13] and with no rest mass (Dirac fermions). This enables researcher to use graphene as a test bed for ultra-

relativistic phenomena such as Klein tunneling [14]. Moreover, it allows the observation of integer quantum Hall effect in single layer [15, 16] graphene and bilayer [17]. Such phenomenon can be even observed even at room temperature in graphene [18] in contrast to the non-relativistic systems where it demands a low temperature.

1.3 Motivation and organization of the thesis

The goal of this thesis is to investigate the electronic and transport properties in locally delaminated bilayer graphene. In particular, it is aiming to examine the charge carriers motion and investigate the possibility of confining them on pristine single layer graphene as well as shading the light on the electron collimation in these systems.

This thesis is organized as follows:

- In chapter 2, we review some of the most important and relevant properties of graphene and its bilayer. We start with the crystalline structures and by implementing the tight binding model we obtain the band structure of single layer graphene. Then we derive the continuum model that is valid at low energy which collapses to the well-known Dirac equation. Afterward, we discuss the chirality and Klein tunneling in graphene and bilayer graphene. In all chapters we solved the Dirac equation in the vicinity K-point to investigate the transport and electronic properties of various systems.
- In chapter 3 the quantum transport across single and double domain walls of delaminated bilayer graphene is scrutinized in the presence of a finite bias.

- In chapter 4 structures whose source and drain is formed of delaminated bilayer graphene is considered where a layer selectivity can exist. The interaction region can be either AA- or AB-stacked bilayer graphene connected smoothly into the leads.
- In chapter 5 the focus is shifted to the confinement in locally delaminated bilayer graphene which we called graphene blister. The confinement is studied under the variation of the inter-layer coupling and bias as well as the blister's size.
- In chapter 6 a locally delaminated bilayer graphene is, again, considered but now to study the electron collimation in such structure....The charge carriers behavior is investigated within two approaches, namely, semi-classical model and wave-packet dynamics simulation.
- In chapter 7 the main results and findings in this thesis are highlighted.

All the results presented in the current thesis are inspired by tremendous discussions with Dr. Ben Van Duppen (University of antwerp, Belgium). Some of the results in this thesis are the fruit of collaborations:

Chapter 5: for the part related to smoothed blister, the numerical calculations were performed by Matthias Van der Donck (University of antwerp, Belgium).

Chapter 6: the wave-packet dynamics simulations were performed by Diego R. da Costa (Universidade Federal do Ceará, Brazil).

CHAPTER 2

THEORETICAL ASPECTS OF GRAPHENE AND ITS BILAYER SYSTEMS

In this chapter we review the electronic properties of graphene and its bi-layered systems. First we discussed the electronic configurations of carbon atoms and their hybridizations in graphene. Understanding the electronic orbital hybridization allows us to introduce the crystallography of graphene and derive its energy spectrum. The linear spectrum of graphene is at the origin of peculiar phenomena such as Klein tunneling, chirality, and negative refraction index. The so called Klein tunneling prevents confinement in graphene. However, there are few methods which enable confinement and hence the realization of quantum dots which are described in this chapter.

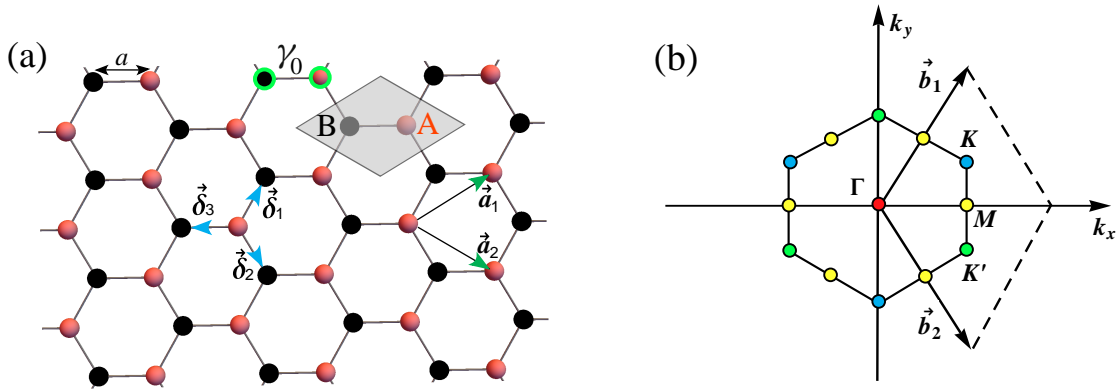


Figure 2.1: (a) crystalline structure of single layer graphene with red and black balls representing carbon atoms at inequivalent sites that cannot be connected through the lattice vectors a_1 and a_2 . The lattice vectors can span the lattice and locate all the red atoms where the vectors δ_i connect the three nearest neighbor black atoms. Dashed gray region defines the unit cell which contains two atoms whose intralayer coupling is $\gamma_0 = 3$ eV with an intra-atomic distance $a = 0.142$ nm. (b) First BZ with reciprocal lattice vectors b_1 and b_2 , the colored dots indicate the high symmetry points in graphene.

2.1 Electronic properties of graphene

2.1.1 Crystallographic structure

Single layer graphene has a hexagonal crystal structure with a unit cell comprises two atoms denoted as A and B whose interatomic distance $a = 0.142$ nm [19], see Fig. 2.1(a). The strength of the coupling between the nearest neighbours is denoted by $\gamma_0 \approx 3$ eV [20]. Note that both atoms A and B are carbon atoms but we need two of them at different sites (A, B) in the unit cell to construct the hexagonal Bravais lattice. This Bravais lattice can be generated using the lattice basis vectors \mathbf{a}_1 and \mathbf{a}_2 superimposed on Fig. 2.1(a)

$$\mathbf{a}_1 = \frac{a}{2} \left(3\mathbf{e}_x + \sqrt{3}\mathbf{e}_y \right), \quad \mathbf{a}_2 = \frac{a}{2} \left(3\mathbf{e}_x - \sqrt{3}\mathbf{e}_y \right), \quad (2.1)$$

where a , as mentioned above, is the carbon-carbon atom distance that is different from the lattice constant given by $\sqrt{3}a$. \mathbf{e}_i are unit vectors pointing in the i direction ($i = x, y, z$). We can generate the sites of sublattice A in the lattice using the lattice translation vector $\mathbf{R}_A = m\mathbf{a}_1 + n\mathbf{a}_2$, where m and n are integers. Each A atom is surrounded by three B atoms, see Fig. 2.1(a), and connected by three vectors $\boldsymbol{\delta}_i$ given by

$$\boldsymbol{\delta}_1 = \frac{a}{2} \left(\mathbf{e}_x + \sqrt{3}\mathbf{e}_y \right), \quad \boldsymbol{\delta}_2 = \frac{a}{2} \left(\mathbf{e}_x - \sqrt{3}\mathbf{e}_y \right), \quad \boldsymbol{\delta}_3 = -a\mathbf{e}_x. \quad (2.2)$$

Thus, within the same unit cell the B sublattice site can be determined by the vector $\mathbf{R}_B = \mathbf{R}_A + \boldsymbol{\delta}_3$ as can seen in Fig. 2.1(a). The corresponding reciprocal lattice in the crystal momentum (\mathbf{k}) space, see Fig. 2.1(b), has the basis vectors

$$\mathbf{b}_1 = \frac{2\pi}{3a} \left(\mathbf{e}_x + \sqrt{3}\mathbf{e}_y \right), \quad \mathbf{b}_2 = \frac{2\pi}{3a} \left(\mathbf{e}_x - \sqrt{3}\mathbf{e}_y \right). \quad (2.3)$$

Like the real space lattice, the first Brillouin zone (BZ) in the \mathbf{k} -space has also a hexagonal form as depicted in Fig. 2.1(b). The BZ has different high symmetry points and one of them is located at the center of the BZ whose energy is the highest energy and is labeled by Γ . The corners of the BZ are also considered high symmetry points around the neutral point and labeled by the K and K' points. We consider these two points to be inequivalent because they cannot be connected to each other by a reciprocal lattice vector. They are situated at

$$\mathbf{K} = \frac{2\pi}{3a} \left(\mathbf{e}_x + \frac{1}{\sqrt{3}}\mathbf{e}_y \right), \quad \mathbf{K}' = \frac{2\pi}{3a} \left(\mathbf{e}_x - \frac{1}{\sqrt{3}}\mathbf{e}_y \right). \quad (2.4)$$

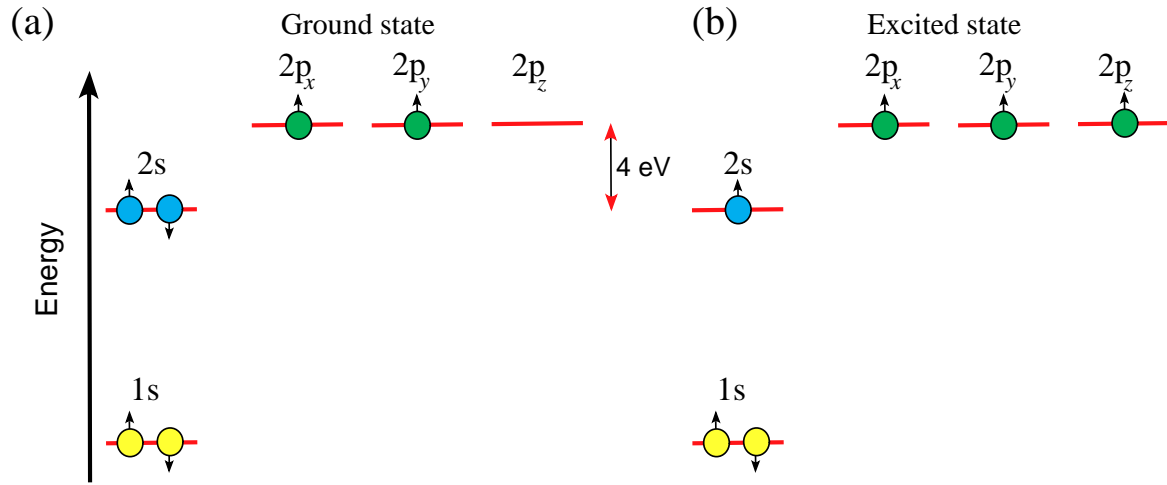


Figure 2.2: Electronic configuration of (a) isolated (in ground state) carbon atom and being with same or different atoms (excited state).

The last high symmetry points are called M and situated in the middle of the edge connecting the corners K and K' . The K and K' points are of particular interest in the physics of graphene because, for pristine graphene, they are located at the Fermi level where all the physical phenomena take place. Later on, the performed calculation of transport properties in the following chapters considered energy ranges only around these two points.

2.1.2 Tight-binding model for π electrons

Before going to the tight binding details let us understand what are the π electrons in graphene. Carbon atoms possess six electrons in the ground states with the configuration $1s^2 2s^2 2p^2$ as shown in Fig. 2.2(a). The inner shell is completely filled and its electrons are not involved in the chemical reaction or in the transport properties. The outer shell is partially filled with four electrons $2s^2 2p^2$. In the presence of other atoms carbon atoms tend to form covalent bonds with its neighbours. This covalent bond requires an extra electron to be excited from the $2s$ orbital to the $2p$, in this case $2p_z$ as shown in Fig.

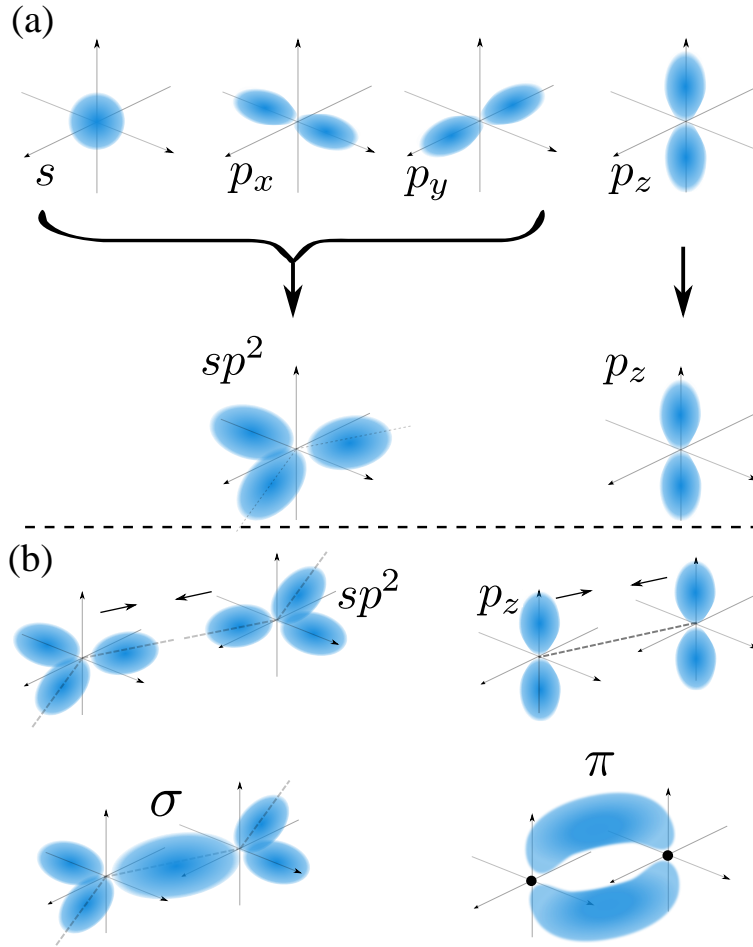


Figure 2.3: (a) Schematic explains the sp^2 hybridisation in graphene and (b) shows the formation of the in-plane σ and out-of-plane π bonds which are responsible for the unique mechanical and transport properties in graphene, respectively. Figure taken from Ref. [3, p. 20]

2.2(b). In the excited state of carbon the four quantum states $|2s\rangle$, $|2p_x\rangle$, $|2p_y\rangle$ and $|2p_z\rangle$ are indistinguishable and thus an electron will occupy a superposition of these states. A superposition of one s -orbital with n p -orbitals is called an sp^n hybridisation. The number of the formed bonds depend on the hybridisation of the s - and p -orbitals of the outer shell. In diamond carbon atoms has sp^3 hybridisation and form four covalent bonds whose length is 0.154 nm [21]. On the other hand, carbon atoms in graphite possess sp^2 hybridisation, see Fig. 2.3(a), and only three covalent bonds are present. The in-plane bond length is 0.142 nm which makes it stronger than diamond. However, the successive

layers in graphite are weakly coupled by van der Waals bond with inter-layer distance about 3.35 nm [19]. In graphene also the sp^2 hybridization allows each carbon atom to form covalent bond (called σ -bond) with the three neighbour atoms as illustrated in Fig. 2.3(b). The last p_z electron in the outer shell form a weak bond with one of the neighbouring atoms, it is called π -bond as shown in Fig. 2.3(b). The σ -electrons are strongly bounded to the atoms and thus cannot contribute to the transport properties of graphene but they are responsible for the unique mechanical properties of graphene. On the contrary, the π -electrons are weakly bounded and can move freely, rendering them controllable by external fields and hence responsible for the transport properties in graphene which are of interest in the study of this thesis.

The electronic band structure of graphene was derived in 1947 by Wallace [10]. He used the tight binding (TB) approximation to describe π -electrons in graphite and along the way he also showed the electronic band structure of single layer of graphite. Here we will review the TB formalism and derive the band structure, following reference [22], as well as setting the notation used in the current thesis.

The idea behind the TB formalism is to write the total wavefunction as a superposition of the atomic orbitals ϕ_i wavefunctions which is called the linear combination of atomic orbitals (LCAO) approximation [23, 24]

$$\Psi(\mathbf{r}) = \sum_i C_i \phi_i, \quad (2.5)$$

where C_i are expansion coefficients and the sum runs over all orbits in the lattice. As mentioned above, π -electrons are our main interest in this study and in graphene there

is one electron associates with each atom and hence two electrons in the unit cell. Thus, one orbital wavefunction must be considered per atom, as a result the total wavefunction reads

$$\Psi_{\mathbf{k}}(\mathbf{r}) = C_A \Phi_{\mathbf{k}}^A(\mathbf{r}) + C_B \Phi_{\mathbf{k}}^B(\mathbf{r}) \quad (2.6)$$

Where

$$\Phi_{\mathbf{k}}^j(\mathbf{r}) = \frac{1}{\sqrt{N}} \sum_{n=1}^N e^{i\mathbf{k} \cdot \mathbf{R}_n^j} \phi(\mathbf{r} - \mathbf{R}_n^j), \quad j = A, B. \quad (2.7)$$

These are the Bloch functions that obey the Bloch theorem:

$$\Phi_{\mathbf{k}}^j(\mathbf{r} + \mathbf{R}) = e^{i\mathbf{k} \cdot \mathbf{R}} \Phi_{\mathbf{k}}^j(\mathbf{r}), \quad (2.8)$$

where N is the total number of unit cells in the lattice. Minimising the energy $\langle E \rangle$ with respect to the expansion coefficients C_i leads to the secular equation

$$\forall i : \sum_j H_{ij} C_j = E \sum_j S_{ij} C_j. \quad (2.9)$$

The expectation value for the energy can be found from

$$\langle E \rangle = \frac{\int \Psi_{\mathbf{k}}^*(\mathbf{r}) \mathbf{H} \Psi_{\mathbf{k}}(\mathbf{r}) d\mathbf{r}}{\int \Psi_{\mathbf{k}}^*(\mathbf{r}) \Psi_{\mathbf{k}}(\mathbf{r}) d\mathbf{r}} = \frac{\sum_{ij} C_i^* C_j H_{ij}}{\sum_{ij} C_i^* C_j S_{ij}} \quad (2.10)$$

and then one can use the variational approach for the minimization using $\frac{\partial E}{\partial C_i^*} = 0$ [25]. Note that the variational approach is equivalent to the Schrodinger equation

$\mathbf{H}|\Psi_{\mathbf{k}}\rangle = E|\Psi_{\mathbf{k}}\rangle$. H_{ij} and S_{ij} are hermitian and called the transfer and overlap ma-

trices, respectively, and defined by:

$$H_{ij} = \int \Phi_k^{i*}(\mathbf{r}) \mathbf{H} \Phi_k^j(\mathbf{r}) d\mathbf{r} = \langle \Phi_k^i | \mathbf{H} | \Phi_k^j \rangle \quad (2.11)$$

$$S_{ij} = \int \Phi_k^{i*}(\mathbf{r}) \Phi_k^j(\mathbf{r}) d\mathbf{r} = \langle \Phi_k^i | \Phi_k^j \rangle. \quad (2.12)$$

Alternatively, Eq. (2.9) can be written in the matrix form as

$$\begin{pmatrix} H_{AA} & H_{AB} \\ H_{BA} & H_{BB} \end{pmatrix} \begin{pmatrix} C_A \\ C_B \end{pmatrix} = E \begin{pmatrix} S_{AA} & S_{AB} \\ S_{BA} & S_{BB} \end{pmatrix} \begin{pmatrix} C_A \\ C_B \end{pmatrix}, \quad (2.13)$$

the components of these matrices are defined as follows:

$$\begin{aligned} H_{AA} &= \int (\Phi_k^A)^* \mathbf{H} \Phi_k^A d\mathbf{r} \\ &= \frac{1}{N} \int \left(\sum_{n'=1}^N e^{-i\mathbf{k} \cdot \mathbf{R}_{n'}^A} \phi(\mathbf{r} - \mathbf{R}_{n'}^A)^* \right) \left(\mathbf{H} \sum_{n=1}^N e^{i\mathbf{k} \cdot \mathbf{R}_n^A} \phi(\mathbf{r} - \mathbf{R}_n^A) \right) d\mathbf{r} \\ &= \frac{1}{N} \sum_{n'=1}^N \sum_{n=1}^N \int e^{-i\mathbf{k} \cdot (\mathbf{R}_n^A - \mathbf{R}_{n'}^A)} (\phi(\mathbf{r} - \mathbf{R}_{n'}^A)^* \mathbf{H} \phi(\mathbf{r} - \mathbf{R}_n^A)) d\mathbf{r} \\ &\approx \begin{cases} 0, n \neq n' \\ \varepsilon_0, n = n' \end{cases} \end{aligned} \quad (2.14)$$

In the results above we used the fact that expected value of the energy is independent of the cell number n i.e. $H\phi(r - R_n^j) = \varepsilon_0\phi(r - R_n^j)$. The above integral only survives when $n = n'$ and is zero otherwise, this means that no hopping between A atoms in different unit cells which is an approximation. ε_0 is called the on-site energy of the A atoms. Similarly, one can show the same results holds for the element H_{BB} . The interesting elements are the off-diagonal element H_{ij} since they represent the major interaction between nearest

neighbors. The first component H_{AB} is defined as

$$\begin{aligned}
H_{AB} &= \int (\Phi_{\mathbf{k}}^A)^* \mathbf{H} \Phi_{\mathbf{k}}^B d\mathbf{r} \\
&= \frac{1}{N} \int \left(\sum_{n'=1}^N e^{-i\mathbf{k}\cdot\mathbf{R}_{n'}^A} \phi(\mathbf{r} - \mathbf{R}_{n'}^A) \right)^* \left(\mathbf{H} \sum_{n=1}^N e^{i\mathbf{k}\cdot\mathbf{R}_n^B} \phi(\mathbf{r} - \mathbf{R}_n^B) \right) d\mathbf{r} \\
&= \frac{1}{N} \sum_{n'=1}^N \sum_{n=1}^N e^{i\mathbf{k}\cdot(\mathbf{R}_n^B - \mathbf{R}_{n'}^A)} \int (\phi(\mathbf{r} - \mathbf{R}_{n'}^A)^* \mathbf{H} \phi(\mathbf{r} - \mathbf{R}_n^B)) d\mathbf{r} \\
&\approx \gamma_0 f(\mathbf{k})
\end{aligned} \tag{2.15}$$

Here the summations indices n and n' run over the all A and B sublattices in the crystal, respectively. Considering only the nearest neighbor interaction we can perform the summation over all the A atoms in the crystal ($n' = 1, 2, \dots, N$) and with each step we sum over the nearest neighbor atoms B which are three ($n = 1, 2, 3$) as illustrated in Fig. 2.1(a). With this approximation the two summations above can be rewritten as $\sum_{n'=1}^N \sum_{n=1}^N \rightarrow \sum_{n'=1}^N \sum_{n=1}^3 = N \sum_{n=1}^3$ and this will lead to the final result $\gamma_0 f(k)$. γ_0 denotes the coupling strength between nearest neighbors and is called the *hopping amplitude* while $f(k)$ called the *geometrical factor* and both are defined as follows

$$\gamma_0 = \int \phi(\mathbf{r} - \mathbf{R}_{n'}^A)^* \mathbf{H} \phi(\mathbf{r} - \mathbf{R}_n^B) d\mathbf{r}, \tag{2.16}$$

$$f(\mathbf{k}) = \sum_{n=1}^3 e^{i\mathbf{k}\cdot\boldsymbol{\delta}_n}, \tag{2.17}$$

where, $\boldsymbol{\delta}_n = (\mathbf{R}_n^B - \mathbf{R}_{n'}^A)$ are the vectors defined in Eq. (2.2). Repeating the same steps we obtain for H_{BA}

$$H_{BA} = H_{AB}^* = \gamma_0 f^*(k) \tag{2.18}$$

Similarly, the overlap matrix has the elements:

$$S_{BA} = S_{AB}^* = s_0 f^*(k), \quad S_{AA} = S_{BB} = 1 \quad (2.19)$$

where $s_0 = \int (\phi(r - R_n^A)\phi(r - R_n^B)) dr$ is the overlap integral. Finally, we can now rewrite the eigenvalue equation (2.13) as

$$\begin{pmatrix} \varepsilon_0 & \gamma_0 f(k) \\ \gamma_0 f^*(k) & \varepsilon_0 \end{pmatrix} \begin{pmatrix} C_A \\ C_B \end{pmatrix} = E \begin{pmatrix} 1 & s_0 f \\ s_0 f^* & 1 \end{pmatrix} \begin{pmatrix} C_A \\ C_B \end{pmatrix}. \quad (2.20)$$

The solutions of the above system must satisfy $\det[H - Es] = 0$ which gives the energy spectrum in the first BZ

$$E_{\pm} = \frac{\varepsilon_0 \pm \gamma_0 |f(k)|}{1 \mp s_0 |f(k)|}, \quad (2.21)$$

where the values of $\gamma_0 = 3.033$ eV and $s_0 = 0.129$ have been extracted experimentally [22].

The geometrical factor can be expanded further as follows

$$\begin{aligned} f(k) &= \sum_{j=1,2,3} e^{ik \cdot \delta_j} \\ &= - [e^{ik \cdot \delta_1} + e^{ik \cdot \delta_2} + e^{ik \cdot \delta_3}] \\ &= - \left[e^{i\frac{a}{2}(k_x + \sqrt{3}k_y)} + e^{i\frac{a}{2}(k_x - \sqrt{3}k_y)} + e^{iak_x} \right] \\ &= -e^{i\frac{a}{2}k_x} \left[2\cos\left(\frac{\sqrt{3}}{2}ak_y\right) + e^{-3i\frac{a}{2}k_x} \right] \end{aligned} \quad (2.22)$$

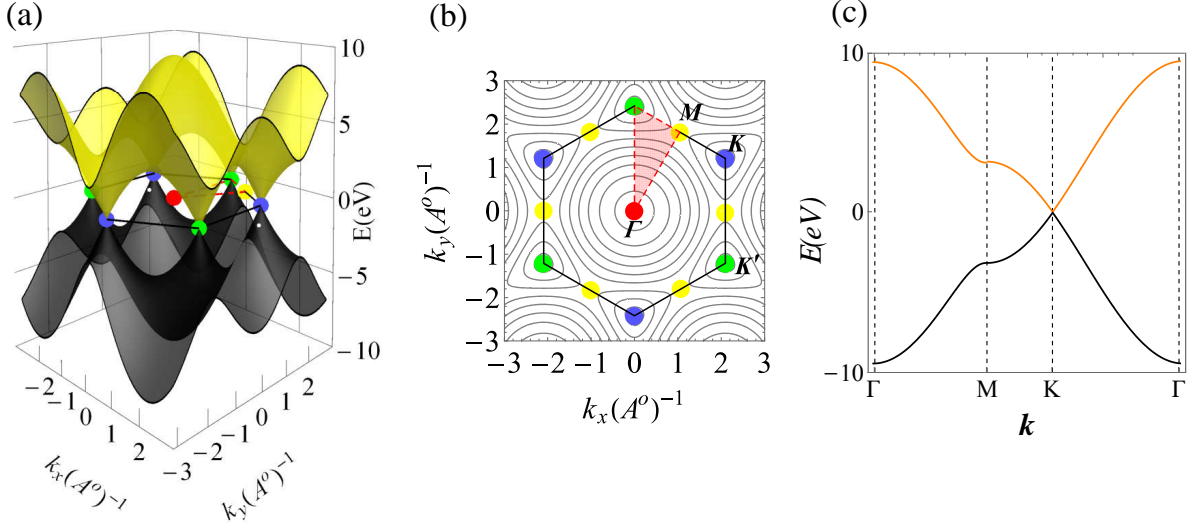


Figure 2.4: (a) Shows the 3D energy spectrum of single layer graphene obtained from the TB approach, yellow and black colors correspond to conduction and valence bands, respectively, while the colored balls at $E = 0$ are the high symmetry points and the black lines represent the first BZ as illustrated in Fig. 2.1(b). For a better illustration, in panel (b) we show contour plot of the conduction band by superimposing the first BZ and the high symmetry points. (c) shows the valence and conduction bands along the high symmetry points Γ , M and K connected by the dashed-red lines in panel (b).

where, $\delta_1 = \frac{a}{2}(1, \sqrt{3})$, $\delta_2 = \frac{a}{2}(1, -\sqrt{3})$ and $\delta_3 = \frac{a}{2}(-2, 0)$ then,

$$|f(k)| = \sqrt{\left[4\cos^2\left(\frac{\sqrt{3}}{2}ak_y\right) + 1 + 4\cos\left(\frac{\sqrt{3}}{2}ak_y\right)\cos\left(\frac{3}{2}ak_y\right) \right]}. \quad (2.23)$$

In Eq. (2.21) we can set the parameter ε_0 to be zero since it only causes a shift in the spectrum. The overlap integral also can be neglected since it is small compared to the hopping amplitude γ_0 . With these approximations the energy spectrum becomes

$$E_\alpha = \alpha\gamma_0|f(k)|, \quad (2.24)$$

where $\alpha = 1(-1)$ is the band index and corresponds to electrons (holes). This spectrum is shown in Fig. 2.4(a) which exhibit four distinct high symmetry points as shown in Fig.

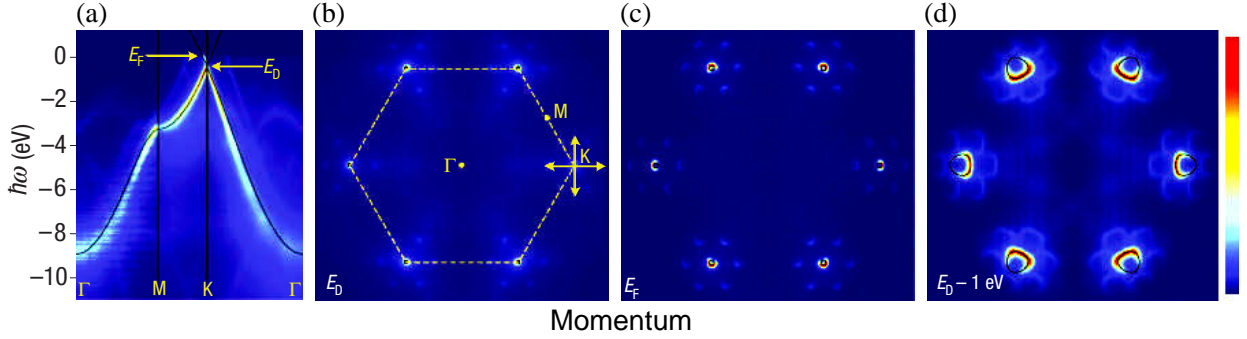


Figure 2.5: (a) shows angle-resolved photoemission spectroscopy (ARPES) measurements of energy spectrum in the first BZ along the high symmetry points with the results from the TB model superimposed as black curve. (b) shows the isotropic nature of the spectrum at low energy E_D indicated in panel (a). (c, d) same as (b) but at lower energies E_F and $E_D - 1\text{eV}$. Figure adapted from Ref. [4].

2.4(b). The energy spectrum along these high symmetry points is depicted in Fig. 2.4(c). Notice that the spectrum exhibit the electron-hole symmetry. However, taking into account the overlap integral s_0 will break such symmetry. Furthermore, we remind the reader that we consider only the nearest neighbour interactions in the above formalism. Including the next nearest neighbour interaction has a small impact on the energy spectrum but will break the electron-hole symmetry [26]. The energy spectrum of graphene was verified using angle-resolved photoemission spectroscopy (ARPES) measurements. The observed energy spectrum in the first BZ is shown in Fig. 2.5. The tunnelling spectra of quasifree-standing graphene monolayer usually measured using scanning tunneling microscope where some researcher showed that it has “V–shape” around the Dirac point [27–31] while others observed an unexpected gap of 60 meV pinned to the Fermi level [32–37]. Recent experiment showed that it is possible to switch the tunnelling spectra between the two distinct features through voltage pulses applied to the STM tip [38].

2.1.3 Continuum limit and Dirac-Weyl Hamiltonian

When studying the transport properties we are only interested in the energy regime near the Fermi level, where the low excitations take place. In pristine graphene the Fermi level is zero $E_F = 0$ which coincides with the Dirac points K and K' , see Figs. 2.4(a, b). Thus, it is convenient to expand the Hamiltonian in Eq. (2.20) near the Fermi energy according to $\mathbf{k} = \mathbf{K} + \mathbf{q}$. Assuming that $|\mathbf{q}| \ll |\mathbf{K}| \sim 1/a$ the Hamiltonian can be expanded up to the first order in \mathbf{q} . This approximation is known as the *continuum limit* and hence using the Taylor expansion we can obtain the first order terms of the geometrical factor as

$$f(k_x, k_y) \simeq f(\mathbf{K}) + (k_x - \frac{2\pi}{3a}) \left. \frac{df(\mathbf{k})}{dk_x} \right|_{\mathbf{K}} + (k_y - \frac{2\pi}{3a}) \left. \frac{df(\mathbf{k})}{dk_y} \right|_{\mathbf{K}}, \quad (2.25)$$

and we can show that

$$\left. \begin{aligned} f\left(\frac{2\pi}{3a}, \frac{2\pi}{3\sqrt{3}a}\right) &= 0 \\ \frac{d}{dk_x} f\left(\frac{2\pi}{3a}, \frac{2\pi}{3\sqrt{3}a}\right) &= \frac{3}{4}\gamma_0 a(\sqrt{3} - i) \\ \frac{d}{dk_y} f\left(\frac{2\pi}{3a}, \frac{2\pi}{3\sqrt{3}a}\right) &= \frac{3}{4}\gamma_0 a(1 + i\sqrt{3}) \end{aligned} \right\}. \quad (2.26)$$

Then, according to $k_x = \frac{2\pi}{3a} + q_x$ and $k_y = \frac{2\pi}{3\sqrt{3}a} + q_y$ Eq. (2.25) becomes

$$f(q_x, q_y) = \frac{3}{4}\gamma_0 a \left[(\sqrt{3} - i)q_x + (1 + i\sqrt{3})q_y \right] \quad (2.27)$$

this equation can be simplified further to take the form

$$f(q_x, q_y) = \frac{3}{2}\gamma_0 a (q_x + iq_y) e^{-i\frac{\pi}{6}} \quad (2.28)$$

the extra phase $\frac{\pi}{6}$ can be absorbed in the wave function and the Hamiltonian around the K Dirac point becomes

$$H = \begin{pmatrix} 0 & v_F(p_x - ip_y) \\ v_F(p_x + ip_y) & 0 \end{pmatrix} \quad (2.29)$$

where, $v_F = \frac{3}{2\hbar}\gamma_0 a \simeq 10^6$ m/s [19,26,39] is the Fermi velocity of charge carriers in graphene with $p_{x,y} = \hbar q_{x,y}$ being the particle momentum. Finally, we can write Eq. (2.29) as

$$\mathbf{H}_K = v_F \boldsymbol{\sigma} \cdot \mathbf{p}. \quad (2.30)$$

Here, $\boldsymbol{\sigma} = (\sigma_x, \sigma_y)$ are Pauli Matrices. The Hamiltonian in Eq. (2.30) is the Dirac-Weyl Hamiltonian [40] that describes massless relativistic particles moving in two dimensions. The only difference here is that the speed of light is replaced by the Fermi speed v_F . The eigenvalues of the Hamiltonian in Eq. (2.30) are given by $E = \alpha v_F |p|$. In Fig. 2.6(a) we show the low energy bands obtained from the tight binding approach, in the first BZ, given by Eq. (2.21), while in Fig. 2.6(b) we show the spectrum obtained using the continuum limit described by Eq. (2.30) and in Fig. 2.6(c) we plot the energy spectrum along the k_x direction. In a similar way we can expand the Hamiltonian around the K'

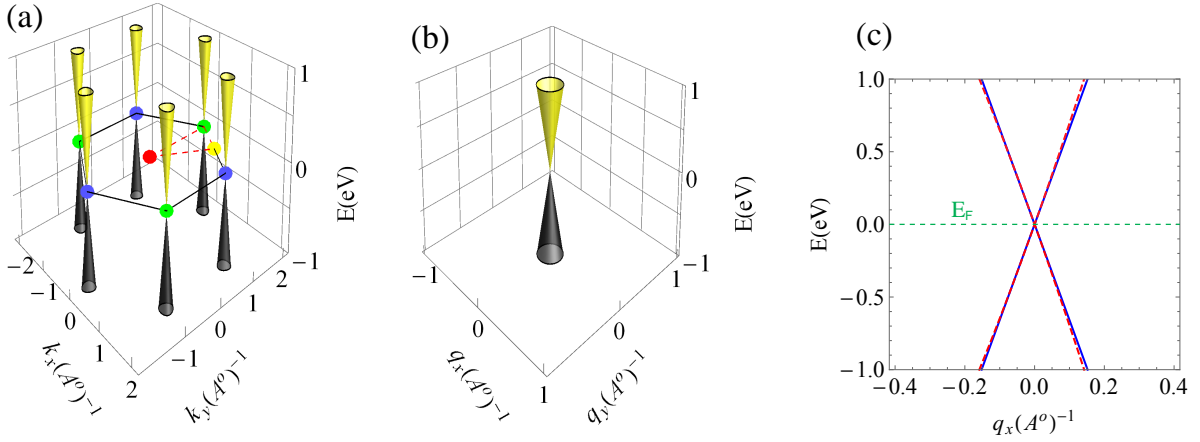


Figure 2.6: Low energy spectrum of single layer graphene around the Dirac points obtained from (a) tight binding (b) continuum approximation and (c) along q_x , i.e. with $q_y = 0$, red-dashed and blue curves correspond to tight binding and continuum limit, respectively.

point and obtain the following result:

$$H_{K'} = v_F \boldsymbol{\sigma}' \cdot \mathbf{p} \quad (2.31)$$

where $\boldsymbol{\sigma}' = (-\sigma_x, \sigma_y)$. Note that this is not exactly the same as Eq. (2.30) where its eigenvalues are given by $E = -\alpha v_F |p|$. Hence the Hamiltonian around either point can be written as

$$H_\tau = \tau \begin{pmatrix} 0 & v_F(p_x - i\tau p_y) \\ v_F(p_x + i\tau p_y) & 0 \end{pmatrix}, \quad (2.32)$$

where $\tau = 1(-1)$ indicates that the expansion is performed around the K (K') point.

Thus, the corresponding eigenvalues are

$$E_\alpha^\tau = \tau \alpha v_F |p| = \tau \alpha v_F \hbar \sqrt{q_x^2 + q_y^2}. \quad (2.33)$$

As we mentioned earlier, this Hamiltonian is valid only in the continuum limit, i.e. $|\mathbf{q}| = \xi/a$ with $\xi \ll 1$. Implementing this condition to the energy spectrum from Eq.

(2.33) yields $E_\alpha^\tau = \tau\alpha\xi(3\gamma_0/2) \ll \gamma_0$. This explains the energy range where the continuum limit is valid and thus the Hamiltonian defined by Eq. (2.32).

As we mentioned earlier that the two valleys K and K' are inequivalent hence a scattering process may occur between the two valleys over the barrier at the M point. This scattering can take place at high energy (of the order of γ_0) and with short range interaction i.e. $\Delta k \sim |K - K'| \sim 1/a$. However, at low energy and for long range interaction, i.e. $\Delta k \ll |K - K'| \sim 1/a$, we can consider the charge carriers living around either valley as independent from each other and this is the so called single valley approximation or *valley degeneracy*. This extra degeneracy of the charge carriers motivated researchers to use graphene in logic operations or the so-called *valleytronics* [41–43]. Note the condition for the single valley approximation is the is equivalent to the continuum limit.

2.1.4 Helicity and chirality

In the field of high energy physics, particles have real spin and its projection onto the direction of motion is defined by a relevant quantity called helicity. In graphene particles have sublattice pseudospin, instead of real spin, as illustrated in Fig. 2.7. Hence, we call the quantity that defines the sublattice pseudospin projection into the direction of propagation as *chirality*

$$\eta_\tau = \tau \frac{\mathbf{p} \cdot \boldsymbol{\sigma}}{|\mathbf{p}|}, \quad (2.34)$$

where $\boldsymbol{\sigma} = (\sigma_x, \sigma_y)$ are the Pauli matrices and represent the sublattice pseudospin and \mathbf{p} denotes the particle momentum, and $\tau = +1(-1)$ is the valley index associate with the $K(K')$ valley . In nature, there are many objects that exhibit chiral symmetry such as

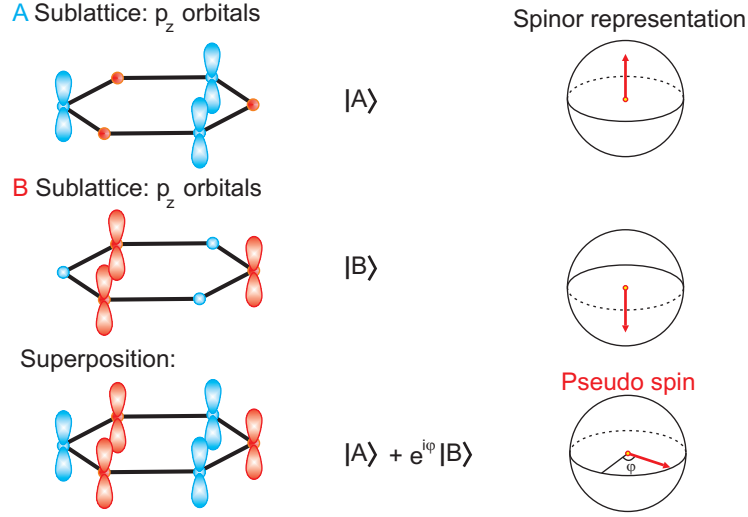


Figure 2.7: Sublattice pseudospin representation in graphene, illustration taken from Ref. [5, p. 22].

gloves, shoes, and the well known Möbius strip. Mathematically, we can say that an object is chiral if it cannot be mapped to its mirror image by only rotations and translations.

Chirality operator in Eq. (2.34) is unitary and hermitian and can be expressed in terms of the Hamiltonian defined in Eq. (2.30) as $\eta_\tau = H_\tau/v_F |\mathbf{p}|$. In the single valley approximation (i.e. absence of inter-valley scattering) chirality is a conserved quantity, only in the absence of electrostatic potential, and hence commutes with H_τ and share the same eigenstates. Since the eigenvalue of H_τ are $\alpha\tau v_F |\mathbf{p}|$, then the eigenvalues of chirality are $\alpha\tau$ as can be deduced from the equations above. Here $\alpha = +1(-1)$ the band index and correspond to electron (holes). In a specific valley, the chirality eigenvalues are $\eta = \alpha = \pm 1$ which indicates that electrons and holes have opposite chirality as shown in Fig. 2.8. Note that this argument is valid only in the absence of the electrostatic potential as will be elucidated when we discuss Klein tunneling later on.

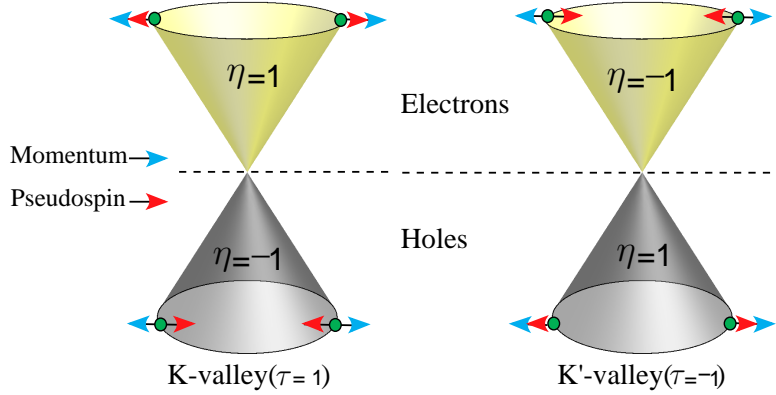


Figure 2.8: Chirality in K - and K' -valleys and its relation with pseudospin and momentum. Yellow and black bands correspond to electrons and holes, respectively, and have opposite chirality in both valleys.

2.2 Bilayer graphene

Bilayer graphene consists of two single layers of graphene which can be stacked in two stable configurations: AB-stacked bilayer graphene (AB-BLG) [44] or AA-stacked bilayer graphene (AA-BLG). In this section we review the crystallographic and band structure of AB- and AA- stacked bilayer graphene. These two types have distinct band structures and thus their transport properties.

2.2.1 AB-stacking

The crystallographic structure of the AB-BLG is shown Fig. 2.9(a). It consists of two single layer graphene where atom $B1$ in the top layer is placed directly above atom $A2$ in the bottom layer with van der Waals inter-layer coupling parameter γ_1 . The other skew hopping parameters γ_3 and γ_4 describe the nearest interlayer coupling between the atoms $B2 \leftrightarrow A1$ and $(B1 \leftrightarrow B2 \text{ or } A1 \leftrightarrow A2)$, respectively. γ_0 represents the intra-layer coupling between the atoms $(B1 \leftrightarrow A1 \text{ or } B2 \leftrightarrow A2)$.

To describe the tight binding model for AB-BLG, let us consider an infinite sheet as

schematically shown in Fig. 2.9(c). The unit cell, delimited by yellow region Fig. 2.9(c), consists of four atoms instead of two as in SLG. We choose the origin of the system to be at the center of the unit cell along the $B1 \leftrightarrow A2$ dimer and half way the inter-layer distance $c_0 \approx 0.3$ nm [28]. We denote the origin by \mathbf{r} and define a vector \mathbf{G}_n pointing to the center of any unite cell and n runs from one to the total number N of unit cells in the system. Each atoms in a unit cell can be located from the center of the unit cell by the vector \mathbf{R}_j where j stands for the atomic sites $A1, B1, A2,$ and $B2$. Since π electrons are the only important one as mentioned above, thus only one orbital wave function $\phi_k^j(\mathbf{r})$ must be considered per atomic site j . Assuming periodic boundary conditions and considering that those orbital basis satisfy Bloch theorem, they reads:

$$\Phi_k^{A1}(\mathbf{r}) = \frac{1}{\sqrt{N}} \sum_{n=1}^N e^{i\mathbf{k} \cdot (\mathbf{G}_n - \delta_3 - \frac{\mathbf{c}_0}{2})} \phi(\mathbf{r} - \mathbf{G}_n + \delta_3 + \frac{\mathbf{c}_0}{2}) \quad (2.35a)$$

$$\Phi_k^{B1}(\mathbf{r}) = \frac{1}{\sqrt{N}} \sum_{n=1}^N e^{i\mathbf{k} \cdot (\mathbf{G}_n - \frac{\mathbf{c}_0}{2})} \phi(\mathbf{r} - \mathbf{G}_n + \frac{\mathbf{c}_0}{2}) \quad (2.35b)$$

$$\Phi_k^{A2}(\mathbf{r}) = \frac{1}{\sqrt{N}} \sum_{n=1}^N e^{i\mathbf{k} \cdot (\mathbf{G}_n + \frac{\mathbf{c}_0}{2})} \phi(\mathbf{r} - \mathbf{G}_n - \frac{\mathbf{c}_0}{2}) \quad (2.35c)$$

$$\Phi_k^{B2}(\mathbf{r}) = \frac{1}{\sqrt{N}} \sum_{n=1}^N e^{i\mathbf{k} \cdot (\mathbf{G}_n + \delta_3 + \frac{\mathbf{c}_0}{2})} \phi(\mathbf{r} - \mathbf{G}_n - \delta_3 - \frac{\mathbf{c}_0}{2}). \quad (2.35d)$$

It is clear now that $\mathbf{R}_{B1(A2)} = -(+)c_0/2\mathbf{e}_z$ while $\mathbf{R}_{A1(B2)} = -(+) [\delta_3\mathbf{e}_x + c_0/2\mathbf{e}_z]$.

The total wavefunction can be written then as a linear combination of the above orbital wave functions as defined in Eq. (2.5). We choose the total wavefunction to be in the basis $(\phi_k^{A1}, \phi_k^{B1}, \phi_k^{A2}, \phi_k^{B2})^T$. Hence the transfer matrix, defined in Eq. (2.11) can be

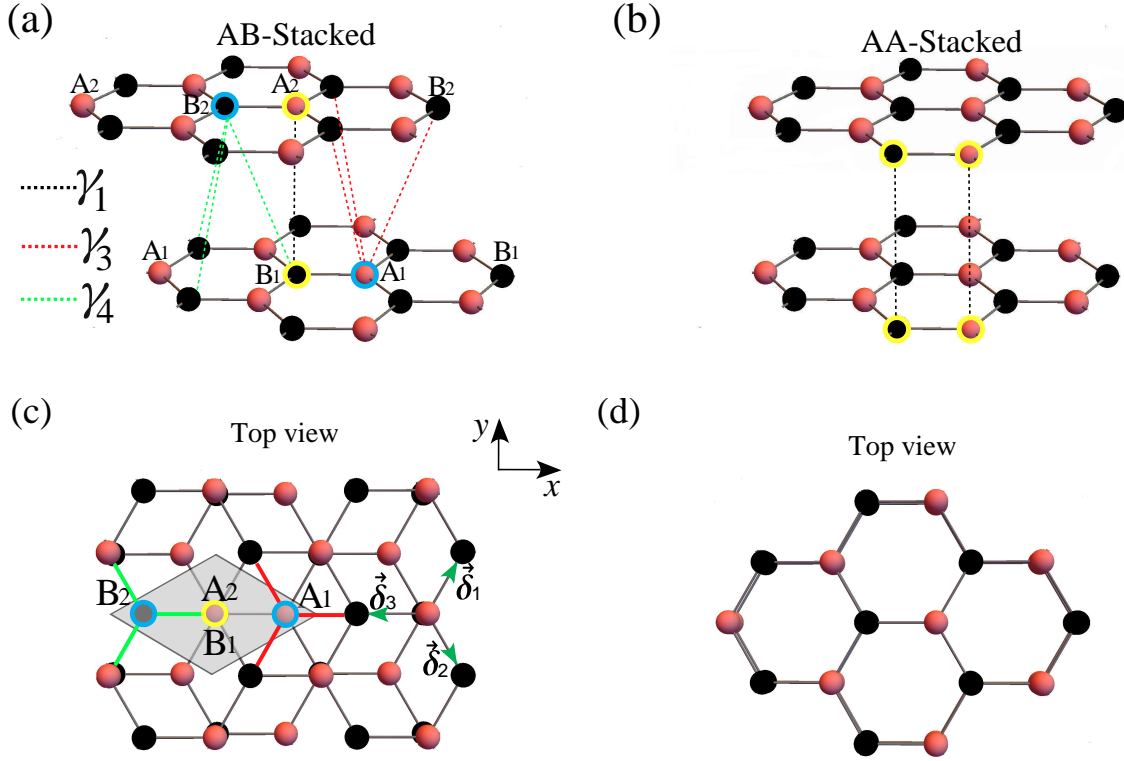


Figure 2.9: Side and top views of the crystalline structure of AB-BLG and AA-BLG crystalline structure with four atoms in the unit cell labeled by colored circle. In panel (a) the direct interlayer coupling is indicated by black-dashed lines while the coupling established by the skew hopping parameters is represented by green and red-dashed lines which are shown as green and red bonds in panel (c). Dashed gray region defines the unit cell in AB-BLG.

written as

$$H_{AB} = \begin{pmatrix} \varepsilon_{A_1} & \gamma_0 f(k) & \gamma_4 f(k) & \gamma_3 f^*(k) \\ \gamma_0 f^*(k) & \varepsilon_{B_1} & \gamma_1 & \gamma_4 f(k) \\ \gamma_4 f^*(k) & \gamma_1 & \varepsilon_{A_2} & \gamma_0 f(k) \\ \gamma_3 f(k) & \gamma_4 f^*(k) & \gamma_0 f^*(k) & \varepsilon_{B_2} \end{pmatrix} \quad (2.36)$$

where the new **TB** parameters are defined as:

$$\begin{aligned}
\gamma_1 &= \langle \phi(\mathbf{r} - \mathbf{G}_n - \mathbf{R}_{B1}) | \mathbf{H} | \phi(\mathbf{r} - \mathbf{G}_n - \mathbf{R}_{A2}) \rangle \\
\gamma_3 &= \langle \phi(\mathbf{r} - \mathbf{G}_n - \mathbf{R}_{A1}) | \mathbf{H} | \phi(\mathbf{r} - \mathbf{G}_n - \mathbf{R}_{A1} - \mathbf{c}_0 - \boldsymbol{\delta}_i) \rangle \\
\gamma_4 &= \langle \phi(\mathbf{r} - \mathbf{G}_n - \mathbf{R}_{B2}) | \mathbf{H} | \phi(\mathbf{r} - \mathbf{G}_n - \mathbf{R}_{B2} + \mathbf{c}_0 + \boldsymbol{\delta}_i) \rangle \\
&= \langle \phi(\mathbf{r} - \mathbf{G}_n - \mathbf{R}_{A2}) | \mathbf{H} | \phi(\mathbf{r} - \mathbf{G}_n - \mathbf{R}_{A2} + \mathbf{c}_0 + \boldsymbol{\delta}_i) \rangle \quad (2.37) \\
\varepsilon_{A_i} &= \langle \phi(\mathbf{r} - \mathbf{G}_n - \mathbf{R}_{A_i}) | \mathbf{H} | \phi(\mathbf{r} - \mathbf{G}_n - \mathbf{R}_{A_i}) \rangle \\
\varepsilon_{B_i} &= \langle \phi(\mathbf{r} - \mathbf{G}_n - \mathbf{R}_{B_i}) | \mathbf{H} | \phi(\mathbf{r} - \mathbf{G}_n - \mathbf{R}_{B_i}) \rangle
\end{aligned}$$

the hopping parameters are illustrated in Fig. 2.9(a), where γ_1 represents the direct inter-layer coupling between the atoms ($A_2 \leftrightarrow B_1$), γ_3 denotes the interlayer coupling between the atoms ($A_1 \leftrightarrow B_2$) and γ_4 describes the interlayer coupling between ($A_1 \leftrightarrow A_2$) as well as ($B_1 \leftrightarrow B_2$). The typical values of these hopping parameters in bilayer graphene are $\gamma_1 = 0.40$ eV, $\gamma_3 = 0.30$ eV, $\gamma_4 = 0.15$ eV [22]. $\varepsilon_{A(B)_i}$ characterizes the identical on site energies and cause a shift in the whole spectrum thus we can consider them zero without affecting the physical observation.

In the continuum limit the Hamiltonian defined in Eq. (2.36) can be written as

$$H_{AB}^\tau = \tau \begin{pmatrix} 0 & v_F \hat{\pi}_+ & v_4 \hat{\pi}_+ & v_3 \hat{\pi}_- \\ v_F \hat{\pi}_- & 0 & \gamma_1 & v_4 \hat{\pi}_+ \\ v_4 \hat{\pi}_- & \gamma_1 & 0 & v_F \hat{\pi}_+ \\ v_3 \hat{\pi}_+ & v_4 \hat{\pi}_- & v_F \hat{\pi}_- & 0 \end{pmatrix} \quad (2.38)$$

where $v_{3,4} = \frac{3}{2\hbar} \gamma_{3,4} a$ are related to the skew hopping parameters, $\hat{\pi}_\pm = \hat{p}_x \pm i\tau \hat{p}_y$ represents

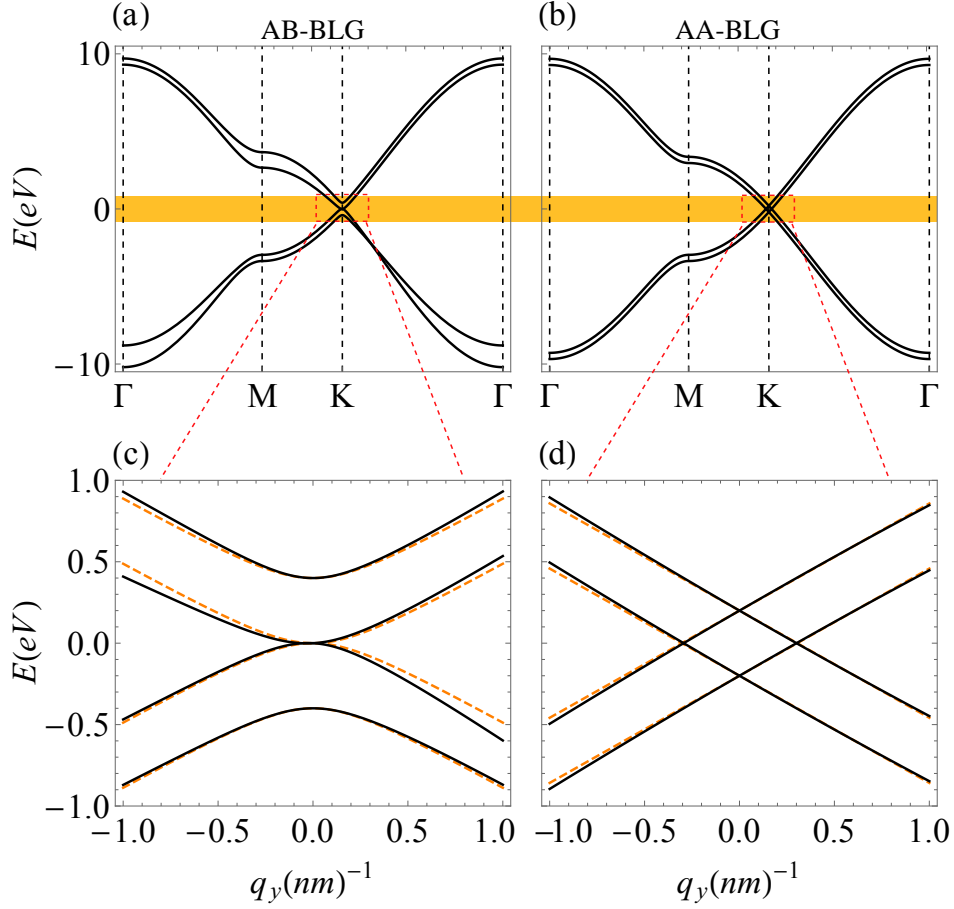


Figure 2.10: (a, b) show the energy spectrum along the high symmetry points of AB-BLG and AA-BLG obtained from the TB approximation, respectively. (c, d) show the corresponding energy spectrum around the Dirac point obtained using the continuum approximation which is valid in the orange-dashed region in panels (a, b). For AB-BLG, in the TB approximation (solid black bands) all interlayer coupling parameters are included (i.e. $\gamma_{1,3,4}$) while in the continuum approximation only the direct interlayer coupling γ_1 is considered whereas in AA-BLG only the direct interlayer coupling is considered in both approximations.

the canonical momentum with $\hat{p}_{x,y} = -i\hbar\partial_{x,y}$ and $\tau = (+, -)$ for the valleys K and K' , respectively. In Fig. 2.10(a) we show the energy spectrum of the AB-BLG obtained from the TB approach, see Eq. (2.36), along the high symmetry points in the first BZ including the three hopping parameters. To compare it with the one from the continuum approximation we show both spectra around the K -valley in Fig. 2.10(c) as solid black and dashed orange curves, respectively. Note that the skew hopping parameters have a

very small impact on the energy spectrum at high energy and the dominant parameter is only γ_1 in the high energy regime. The importance of the skew hopping parameters becomes relevant only at low energy $E < 1$ meV [45]. Even though these parameters have peculiar effects on the transport properties at low energy [46], their impact becomes negligible at high energy [47]. In the current study we only consider high energy regimes and thus the skew hopping parameters γ_3 and γ_4 will be neglected henceforth. The absence of a band gap in graphene leads to different proposals for gap generation [48–50]. For example, by changing the size of the graphene flakes into nanoribbons or quantum dots, one can control the energy gap through size quantization [51–53]. In AB-BLG spectrum, a tunable band gap can be opened and controlled by applying an interlayer bias [48, 54, 55]. Introducing an interlayer bias δ and considering only the direct interlayer coupling γ_1 , the AB-BLG Hamiltonian in the K -valley reads

$$H_{AB} = \begin{pmatrix} \delta & v_F \hat{\pi}_+ & 0 & 0 \\ v_F \hat{\pi}_- & \delta & \gamma_1 & 0 \\ 0 & \gamma_1 & -\delta & v_F \hat{\pi}_+ \\ 0 & 0 & v_F \hat{\pi}_- & -\delta \end{pmatrix} \quad (2.39)$$

whose eigenvalues are

$$E_s^\alpha = \alpha \left[\hbar^2 v_F^2 (k_x^2 + k_y^2) + \delta^2 + \frac{\gamma_1^2}{2} - \alpha s \sqrt{\hbar^2 v_F^2 (k_x^2 + k_y^2) (4\delta^2 + \gamma_1^2) + \frac{\gamma_1^4}{4}} \right]^{1/2}, \quad (2.40)$$

where $\alpha = 1(-1)$ is the band index and corresponds to electrons (holes) and $s = 1(-1)$ is the mode index (or chirality index). In Fig. 2.11(a) we show the energy spectrum

of pristine AB-BLG and biased AB-BLG as solid and dashed curves, respectively, while the blue and red colors stand for the modes $s = +1$ and $s = -1$, respectively. This notation of the modes will become handy when we discuss the transport properties of bilayer graphene in the coming sections. Note that in the literature a different basis may be used and as a result we can see a different form for the Hamiltonian in Eq. (2.41). For example, in the basis $(\phi_{A1}, \phi_{B1}, \phi_{B2}, \phi_{A2})^T$ it becomes

$$H'_{AB} = \begin{pmatrix} \delta & v_F \hat{\pi}_+ & 0 & 0 \\ v_F \hat{\pi}_- & \delta & 0 & \gamma_1 \\ 0 & 0 & -\delta & v_F \hat{\pi}_- \\ 0 & \gamma_1 & v_F \hat{\pi}_+ & -\delta \end{pmatrix}. \quad (2.41)$$

Note that both Hamiltonians are connected by a unitary transformation U such that $H'_{AB} = U^\dagger H_{AB} U$ with $U = u_1 I + u_2 \sigma_x$ where

$$U = \begin{pmatrix} I & 0 \\ 0 & \sigma_x \end{pmatrix}, \quad (2.42)$$

where I is 2×2 identity matrix and σ_x is Pauli matrix. In our notation above we assumed that the direct interlayer coupling γ_1 is between the dimer $B1 \leftrightarrow A2$. However, sometimes the direct coupling is considered to be between $B2 \leftrightarrow A1$, in this case we will see the AB-BLG Hamiltonian in the two different bases mentioned above takes the forms

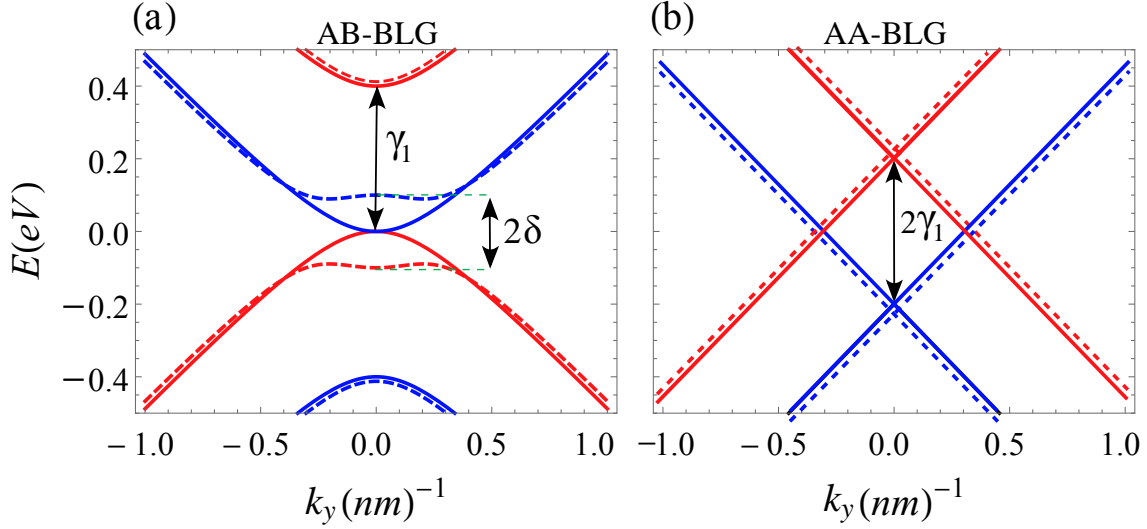


Figure 2.11: (a, b) show the four energy bands of AB-BLG and AA-BLG around the K -valley. Solid and dashed curves correspond to pristine and biased ($\delta = 100$ meV) BLG, respectively, while the red and blue color label the two modes in AB-BLG and the two Dirac cones in AA-BLG.

$$H_1 = \begin{pmatrix} \phi_{A1} & \phi_{B1} & \phi_{B2} & \phi_{A2} \\ \delta & v_F \hat{\pi}_+ & \gamma_1 & 0 \\ v_F \hat{\pi}_- & \delta & 0 & 0 \\ \gamma_1 & 0 & -\delta & v_F \hat{\pi}_- \\ 0 & 0 & v_F \hat{\pi}_+ & -\delta \end{pmatrix}, \quad H_2 = \begin{pmatrix} \phi_{A1} & \phi_{B1} & \phi_{A2} & \phi_{B2} \\ \delta & v_F \hat{\pi}_+ & 0 & \gamma_1 \\ v_F \hat{\pi}_- & \delta & 0 & 0 \\ 0 & 0 & -\delta & v_F \hat{\pi}_+ \\ \gamma_1 & 0 & v_F \hat{\pi}_- & -\delta \end{pmatrix}, \quad (2.43)$$

and again we can switch between both bases using the unitary transformation U mentioned above such that $H_1 = U^\dagger H_2 U$. So, it is arbitrary and a matter of convenience to choose the suitable basis for specific problem.

2.2.2 Effective two-band Hamiltonian

The energy spectrum of the AB-BLG is parabolic with four bands, as shown in Fig. 2.10(c), two of them touch at zero energy, whereas the other two bands are split away by

an energy γ_1 . It is useful when studying the low energy electronic excitations of a AB-BLG to describe the system with an effective Hamiltonian (or two-band Hamiltonian). Such Hamiltonian can be obtained by considering only the direct interlayer coupling γ_1 and an interlayer potential difference δ , the Hamiltonian then reads

$$H_{AB} = \begin{pmatrix} \delta & v_F\pi^\dagger & 0 & 0 \\ v_F\pi & \delta & \gamma_1 & 0 \\ 0 & \gamma_1 & -\delta & v_F\pi^\dagger \\ 0 & 0 & v_F\pi & -\delta \end{pmatrix}, U = \begin{pmatrix} 0 & 0 & 1 & 0 \\ 0 & 1 & 0 & 0 \\ 1 & 0 & 0 & 0 \\ 0 & 0 & 0 & 1 \end{pmatrix} \quad (2.44)$$

Performing the unitary transformation $U \cdot H \cdot U^\dagger$, the above Hamiltonian can be written

as

$$H = \begin{pmatrix} -\delta & \gamma_1 & 0 & v_F\pi^\dagger \\ \gamma_1 & \delta & v_F\pi & 0 \\ 0 & v_F\pi^\dagger & \delta & 0 \\ v_F\pi & 0 & 0 & -\delta \end{pmatrix} = \begin{pmatrix} H_{11} & H_{12} \\ H_{21} & H_{22} \end{pmatrix} \quad (2.45)$$

where H_{ij} is a 2×2 block. Using Schur determinant identity

$$\text{Det}[H - E] = \text{Det}[H_{11} - E] \cdot \text{Det} [H_{22} - E - H_{12}(H_{11} - E)^{-1}H_{21}] = 0 \quad (2.46)$$

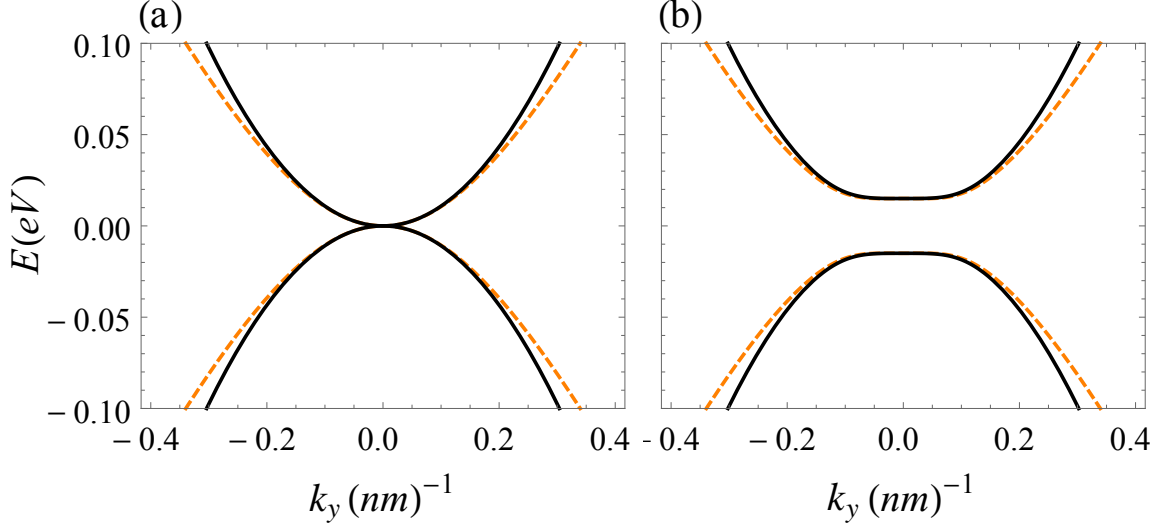


Figure 2.12: Low energy spectrum of AB-BLG obtained from the four-(dashed-orange) and two-band (solid black) Hamiltonians described by Eqs. (2.41, 2.48), respectively. (a, b) Correspond to pristine and biased ($\delta = 15$ meV) AB-BLG.

and with $H_{11} - E \rightarrow H_{11}$ for $E \ll \gamma_1$ [56], one obtain

$$\begin{aligned}
 H &= \text{Det} [H_{22} - H_{12}(H_{11})^{-1}H_{21}] \\
 &= \begin{pmatrix} \delta + [\delta v_F^2 \pi^\dagger \pi / (-\gamma_1^2 - \delta^2)] & \gamma_1 v_F^2 \pi^{\dagger 2} / (-\gamma_1^2 - \delta^2) \\ \gamma_1 v_F^2 \pi^2 / (-\gamma_1^2 - \delta^2) & -\delta - [\delta v_F^2 \pi \pi^\dagger / (-\gamma_1^2 - \delta^2)] \end{pmatrix} \quad (2.47)
 \end{aligned}$$

For $\delta \ll \gamma_1$, $(-\gamma_1^2 - \delta^2) \rightarrow -\gamma_1^2$, the effective Hamiltonian becomes

$$H_{eff} = \frac{1}{2m} \begin{pmatrix} 0 & \pi^{\dagger 2} \\ \pi^2 & 0 \end{pmatrix} + \delta \left[\sigma_z - \frac{v_F^2}{\gamma_1^2} \begin{pmatrix} \pi^\dagger \pi & 0 \\ 0 & -\pi \pi^\dagger \end{pmatrix} \right] \quad (2.48)$$

where, $m = \gamma_1 / (2v_F^2)$ is the effective mass of electrons in bilayer graphene. An effective Hamiltonian that also takes trigonal warping (v_3) into account can be obtained in the same manner. The same result can be obtained using Green function to derive the effective

Hamiltonian [57].

$$H_{eff} = \frac{1}{2m} \begin{pmatrix} 0 & \pi^{\dagger 2} \\ \pi^2 & 0 \end{pmatrix} + v_3 \begin{pmatrix} 0 & \pi^{\dagger} \\ \pi & 0 \end{pmatrix} + \delta \left[\sigma_z - \frac{v_F^2}{\gamma_1^2} \begin{pmatrix} \pi^{\dagger} \pi & 0 \\ 0 & -\pi \pi^{\dagger} \end{pmatrix} \right] \quad (2.49)$$

This effective Hamiltonian is applicable for energy range $|E| < \frac{\gamma_1}{4}$ [57]. In Fig. 2.12(a) we show the low energy spectrum from the two- and four-band Hamiltonians considering only the interlayer coupling γ_1 while the effect of bias is shown in Fig. 2.12(b).

2.2.3 AA-stacking

The crystallographic structure of the AB-BLG is shown Fig. 2.9(b, d). In the AA-stacked graphene bilayer the two single layer graphene are placed exactly on top of each other such that atoms A_2 and B_2 in the top layer are located directly above the A_1 and B_1 atoms in the bottom layer with a direct inter-layer coupling $\gamma_1 = 0.2 \text{ eV}$ [58], see Fig. 2.9(b). Its unit cell also comprises of four atoms as in the AB-BLG and thus the same steps can be followed to find the transfer matrix in the AA-BLG to obtain

$$H_{AA} = \begin{pmatrix} \varepsilon_{A_1} & \gamma_0 f(k) & \gamma_1 & 0 \\ \gamma_0 f^*(k) & \varepsilon_{B_1} & 0 & \gamma_1 \\ \gamma_1 & 0 & \varepsilon_{A_2} & \gamma_0 f^*(k) \\ 0 & \gamma_1 & \gamma_0 f(k) & \varepsilon_{B_2} \end{pmatrix}. \quad (2.50)$$

In the continuum approximation and in the presence of an interlayer bias the AA-BLG hamiltonian in the $K-$ valley becomes

$$H_{AA} = \begin{pmatrix} \delta & v_F \hat{\pi}_+ & \gamma_1 & 0 \\ v_F \hat{\pi}_- & \delta & 0 & \gamma_1 \\ \gamma_1 & 0 & -\delta & v_F \hat{\pi}_+ \\ 0 & \gamma_1 & v_F \hat{\pi}_- & -\delta \end{pmatrix}. \quad (2.51)$$

The eigenvalues of this Hamiltonian can be written in the form

$$E_s^\alpha = \alpha \left[\hbar v_F \sqrt{k_x^2 + k_y^2} - \alpha s \sqrt{\delta^2 + \gamma_1} \right]^{1/2}, \quad (2.52)$$

while $s = (+1, -1)$ associates with upper and lower Dirac cones shown by red and blue bands in Fig. 2.11(b), while $\alpha = (+1, -1)$ stands for electron- and hole-like states [59] coincided with each Dirac cone, respectively. In contrast to AB-BLG where the interlayer bias opens a gap in the energy spectrum, in AA-BLG the bias just slightly shifts the two Dirac cones without affecting the linearity of the spectrum, see dashed curves in Fig. 2.11(b). However, it significantly affects the transport properties of AA-BLG as we will discover soon.

In AA-BLG all atoms take part in the interlayer coupling contrary to the AB-BLG where only half of the atoms participate and as a consequence we see that the interlayer coupling $\gamma_1^{AB} = 2\gamma_1^{AA} \approx 0.4$ eV [60–62]. Another difference is that the latter one has asymmetric interlayer coupling, in other words, atom A_1 coupled to atom B_2 while the coupling is symmetric in the AA-BLG. Such differences give rise to the distinct band

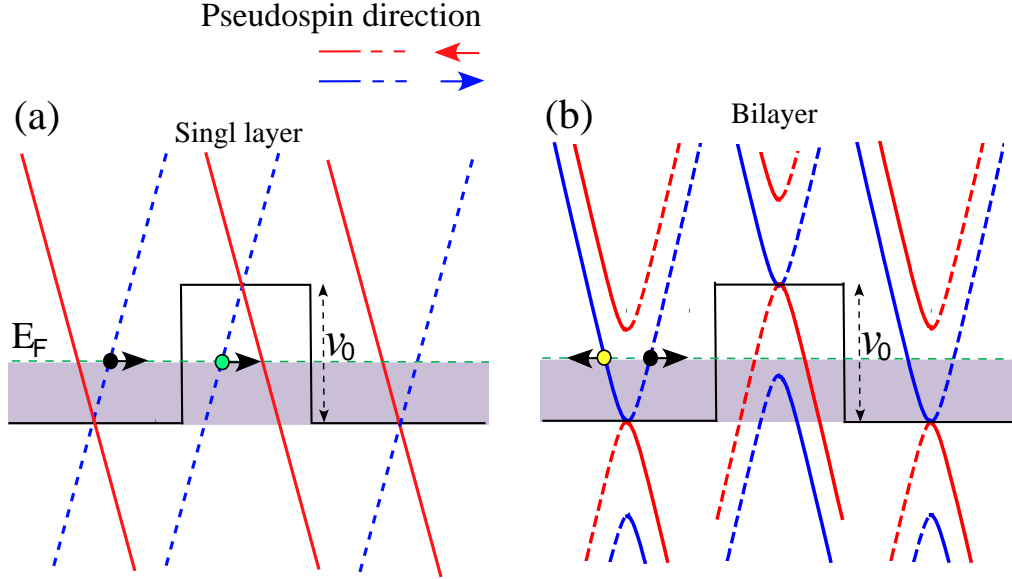


Figure 2.13: Schematic representation explains Klein tunneling in (a) single layer and (b) bilayer graphene. Solid and dashed bands coincide with negative and positive group velocity, respectively. Black, green, and yellow dots represent incident, transmitted, and reflected particles, respectively. v_0 indicates the strength of the electrostatic barrier and E_F is the Fermi energy.

structure and chirality transport in both types of stackings.

2.3 Klein tunneling

One of the peculiar properties as discussed earlier is the chirality of charge carriers in graphene. Another peculiar phenomenon in graphene is *Klein tunneling* and was first predicted by *Oskar Klein* in 1929 when he applied Dirac equation to the problem of electron scattering from 1D potential barrier. He showed that for normal incidence electrons unimpededly tunnel (full transmission) through an electrostatic barrier $V(\mathbf{r})$ even when the barrier width or strength approaches infinity. In graphene, Klein tunneling also holds for normal incidence, but here it is a consequence of the pseudospin conservation [26, 39, 63, 64]. Note that in the presence of a 1D electrostatic barrier $V(x)$, the

Hamiltonian becomes $\mathbf{H} = v_F \boldsymbol{\sigma} \cdot \mathbf{p} + V(x)\mathbf{I}$ where \mathbf{I} stands for 2×2 identity matrix. We can now see that the new Hamiltonian does not commute with chirality as it was the case in Sec. 2.1.4 when $V(x) = 0$. Therefore, chirality is not a conserved quantity in the presence of an electrostatic potential. However, we can show that for normal incidence pseudospin is a conserved quantity. So, The Hamiltonian can be written as $H = v_F(p_x\sigma_x + p_y\sigma_y) + V(x)\mathbf{I}$ and it can be shown that $[\sigma_x, H] = 2ip_y\sigma_z$ where p_y here is a conserved quantity since H is translational invariant along the y -direction. It is clear now that the pseudospin along the x -direction σ_x is a conserved quantity only for normal incidence, i.e. $p_y = 0$. Note that chirality in multilayer systems is different, in SLG the pseudospin direction rotates as fast as the momentum while in AB-BLG it is twice faster than momentum [65]. Hence, in AB-BLG a complete reflection coincides with normal incidence as observed [63, 65]. In Figs. 2.13(a, b) we show the process of tunneling for a particle impinging on an electrostatic barrier along the normal incidence direction in single and AB-BLG, respectively. Note that, since AA-BLG has a linear energy spectrum Klein tunneling also holds through the intra-cone tunneling [59]. Experimentally, Klein tunneling can be observed by measuring the angle-dependent transmission through quasi-ballistic graphene heterojunction [66–68].

CHAPTER 3

QUANTUM TUNNELING ACROSS SINGLE AND DOUBLE DOMAIN WALLS

¹The increasing control over the structure of graphene flakes allowed for new devices that could constitute the building blocks for a fully integrated carbon based electronics. An example of this is deformed bilayer graphene, where the two layers are not aligned due to a mismatch in orientation or stacking order resulting in e.g. twisted bilayer graphene. Its electronic structure is strongly different from normal bilayer graphene and exhibits very peculiar properties such as the appearance of additional Dirac cones [69–74]. Quantum transport of single layer graphene and its multilayer have been intensely investigated in the last decade. However, graphene composite made of two layers that are only locally

¹*The results of this chapter were published as:*

Hasan M. Abdullah, B. Van Duppen, M. Zarenia, H. Bahlouli, and F. M. Peeters, *J. Phys.: Condens. Matter* **29**, 425303 (2017). This paper was selected for the *annual journal highlights* (2017) among 5 top articles in the field of *Nanostructures and nanoelectronics*.

coupled by van der Waals interaction to single layer remains open. Recent experiments have shown that epitaxial graphene can form step-like bilayer/single layer (SL/BL) interfaces or that it is possible to create bilayer graphene flakes that are connected to single layer graphene regions [75–77]. The appearance of these structures fueled theoretical and experimental investigations on the behavior of massless and massive particles in such junctions. For example, few works have investigated different domain walls that separate, for instance, different type of stacking [78, 79] or even different number of layers [80–82]. Most of these recent theoretical works considered domain walls separating patches of bilayer graphene with different stacking type or where only a single layer was connected to a bilayer graphene sheet. Very recently, however, a number of new bilayer graphene platforms have been synthesized. These consist of regions where the coupling between the two graphene layers is changed. For example in the case of folded graphene [83, 84] part of the fold forms a coupled bilayer structure, while other parts remained uncoupled [76, 85, 86]. One has also observed systems with domain walls separating regions with different Bernal stacking [87, 88]. In general, these systems can be modelled as being composed of two single layers of graphene (2SLG) which are locally bound by van der Waals interaction into an AA- or AB-stacked bilayer structure.

From a theoretical point of view, one can wonder how charge carriers will respond to transitions between systems that have completely different transport properties. For example, single layer graphene and AA-stacked bilayer graphene are known to feature Klein tunnelling at normal incidence while AB-stacked bilayer graphene shows anti-Klein tunnelling [63, 66]. It is, therefore, interesting to investigate under which conditions these peculiar chirally-assisted tunnelling properties pertain in combined systems, as well as

to investigate how the presence of multiple transport channels changes the transport properties.

In this chapter we present a systematic study of electrical transport across domain walls separating regions of different inter-layer coupling. We discuss the dependence on the coupling between the graphene layers, on the distance between subsequent domain walls and on local electrostatic gating. For completeness, we also present all possible combinations of locally detached bilayer systems. Analytical expressions for the transport across a single domain wall are also obtained.

3.1 The electronic model

From a theoretical point of view, one can wonder how charge carriers will respond to transitions between systems that have completely different transport properties. For example, single layer graphene and AA-stacked bilayer graphene are known to feature Klein tunnelling at normal incidence while AB-stacked bilayer graphene shows anti-Klein tunnelling [63,66]. It is, therefore, interesting to investigate under which conditions these peculiar chirally-assisted tunnelling properties remain in combined systems, as well as to investigate how the presence of multiple transport channels changes the transport properties. So, in the next section we will start by describing the geometry of our system.

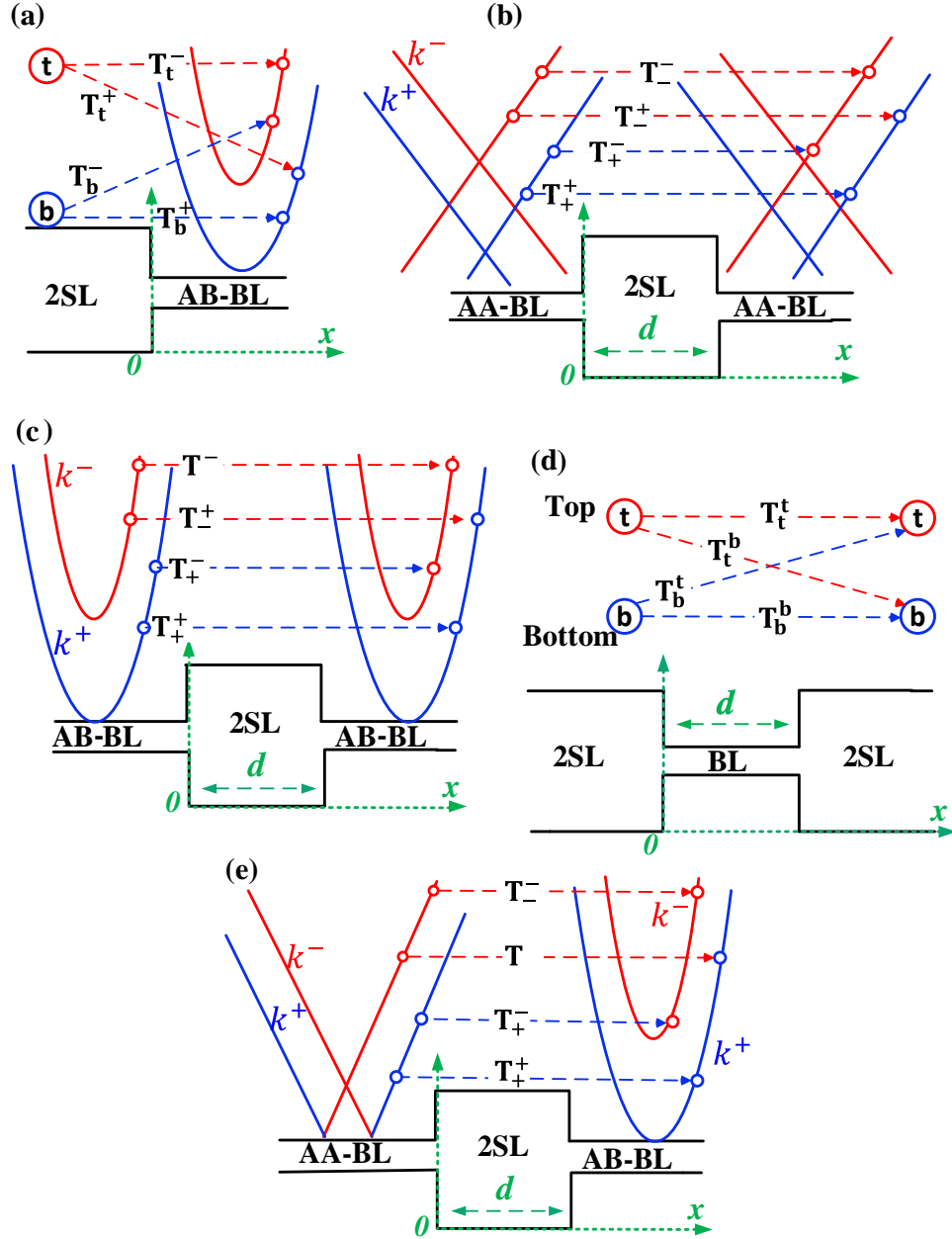


Figure 3.1: (Colour online) Different geometries for bilayer and two decoupled graphene layer interfaces with schematic representation of the transmission probabilities. (c) two single graphene layers connected to AB-BL (2SL-AB). (b) AA-BL leads with 2SL as intermediate region (AA-2SL-AA). (c) AA or AB stacking bilayer graphene sandwiched between two SL graphene layers (2SL-AA(AB)-2SL) and (d) similar to (b) but now with AB-BL as the leads with two upper (red)-lower (blue) shifted Dirac cones (AB-2SL-AB). (e) left and right leads are bilayer graphene with different stacking connected to the two decoupled graphene sheets (AA-2SL-AB). The possible transmission processes between the different conduction channels are indicated above the respective junctions.

3.1.1 Domain walls in bilayer graphene

As we mentioned earlier, different domain walls have been introduced before and showed distinctive transport properties and even supported topological states. In this work we consider different junctions that comprise single or double domain walls and can be made from different building blocks as depicted in Figs. 2.1(a) and 2.9(a, b): monolayer, AA-stacked and AB-stacked bilayer graphene. Without loss of generality, we assume that the charge carriers are always propagating from the left to the right hand side. Then we consider four different configurations: (i) A structure where a single domain wall separates an AB (AA) stacked structure from two decoupled single layers. We will assign the abbreviation 2SL-AB (2SL-AA) to this structure if the charge carriers are incident on one of the two decoupled layers or AB-2SL (AA-2SL) if the coupled bilayer structure is connected to the source. This is depicted in Fig. 3.1(a). Then we consider structures with two domain walls (ii) where the middle region is made up of two decoupled monolayers and whose leads are AB (AA) stacked bilayer graphene. This is depicted in Figs. 3.1(b, c). Such a configuration henceforth will be referred to as AB-2SL-AB (AA-2SL-AA). (iii) a structure where the leads on the left ($x < 0$) and on the right hand side ($x > d$) consist of two decoupled single layers while in between they are connected into an AB-BL (AA-BL) configuration. This is depicted in Fig. 3.1(d). We will refer to such a structure as 2SL-AB-2SL (2SL-AA-2SL). (iv) left and right leads are bilayer graphene with AA- and AB stacking, respectively, separated by a domain where the two layers are completely decoupled (AA-2SL-AB), see Fig. 3.1(e).

To describe transport in the above mentioned structures, we allow for scattering between the layers as well as between the different propagating modes in an AB-BL or

between the two Dirac cones in AA-BL. In the next section, we describe the transport modes in 2SL and BL and how charge carriers can be scattered between them.

3.1.2 Scattering definitions

In this section we define the model Hamiltonian that describes the different structures. For this purpose we use a suitable basis defined by $\Psi = (\Psi_{A1}, \Psi_{B1}, \Psi_{A2}, \Psi_{B2})^T$, whose elements refer to the sublattices in each layer. The general form of the Hamiltonian near the K -point reads

$$H = \begin{pmatrix} V_1 & v_F\pi^\dagger & \tau\gamma_1 & 0 \\ v_F\pi & V_1 & \zeta\gamma_1 & \tau\gamma_1 \\ \tau\gamma_1 & \zeta\gamma_1 & V_2 & v_F\pi^\dagger \\ 0 & \tau\gamma_1 & v_F\pi & V_2 \end{pmatrix}. \quad (3.1)$$

The coupling between the two graphene layers is controlled by the parameters τ and ζ through which we can “*switch on*” or “*switch off*” the inter-layer hopping between specific sublattices. This allows to model different stackings by assigning different values to these parameters. For $\tau = \zeta = 0$, the two layers are decoupled and the Hamiltonian reduces to two independent SL sheets. To achieve AA-stacking we select $\tau = 1$ and $\zeta = 0$ while for AB-stacking we need $\tau = 0$ and $\zeta = 1$. In Eq. (3.1) V_1 and V_2 are the potentials on layers 1 and 2 [89]. In the present study, we only apply these potentials in the intermediate region. We assume that the domain wall is oriented in the y -direction and of infinite length. Therefore, the system is translational invariant and the momentum p_y is conserved. This enables us to write the wave function as $\Psi(x, y) = e^{ik_y y} \Phi(x)$.

Delaminated bilayer graphene

The eigenfunctions of the 2SL Hamiltonian are those of the isolated graphene sheet [19],

$$\Phi = \begin{pmatrix} \phi_1 \\ \phi_2 \end{pmatrix}, \phi_j = \begin{pmatrix} \mu_j^- & -\mu_j^+ \\ 1 & 1 \end{pmatrix} \begin{pmatrix} e^{ik_j x} \\ e^{-ik_j x} \end{pmatrix}, \quad (3.2)$$

where $j = 1, 2$ is the layer index, $k_j = \sqrt{(\epsilon + s_j \delta)^2 - k_y^2}$ with $s_j = \text{sgn}(j - 1.5)$, $\mu_j^\pm = (k_j \pm ik_y)/(\epsilon + s_j \delta)$, $\epsilon = E - v_0$, $\delta = (V_1 - V_2)/2$, $v_0 = (V_1 + V_2)/2$. Introducing the length scale $l = \hbar v_F/\gamma_1$, which represents the inter-layer coupling length, allows us to define the following dimensionless quantities:

$$\epsilon \rightarrow \frac{\epsilon}{\gamma_1}, \quad v_0 \rightarrow \frac{v_0}{\gamma_1}, \quad \delta \rightarrow \frac{\delta}{\gamma_1}, \quad k_y \rightarrow lk_y, \quad \text{and} \quad \vec{r} \rightarrow \frac{\vec{r}}{l}. \quad (3.3)$$

Notice that for the two stacking, AB-BLG and AA-BLG, γ_1 was found to be different. For the AB-BL the value is $\gamma_1 \approx 0.4$ eV while for AA-BL it is $\gamma_1 \approx 0.2$ eV as discussed in Sec. 2.2.

In order to discuss the different scattering modes, we introduce the notation $A_{\text{incoming}}^{\text{outgoing}}$, where A can stand for transmission (T) or reflection (R) probabilities and the indexes denote the mode by which the particles are incoming or outgoing. Fig. 3.1 depicts all possible transitions that are considered in the present work. For example, Fig. 3.1(d) shows all possible transmission processes in a 2SL-BL-2SL system where t denotes the top layer on either side and b the bottom layer. For example, T_t^b denotes a particle coming through the top layer and exiting on the bottom layer.

AB-stacking

For AB-BLG there are two branches corresponding to propagating modes. These branches correspond to the wave vector k^s that can be obtained from Eq. (2.40) and reads

$$k^s = \left[-k_y^2 + \epsilon^2 + \delta^2 + s\sqrt{\epsilon^2(1 + 4\delta^2) - \delta^2} \right]^{1/2}, \quad (3.4)$$

again, $s = \pm 1$ here represents the mode index, see discussion of Fig. 2.11(a). The modes presented in Eq. (3.4) labeled by “ k^+ ” correspond to eigenstates that are odd under layer inversion, while the “ k^- ” modes are even [47]. These modes are shown, respectively, in blue and red in Fig. 3.1(c). This means that there are two available channels for transmission at a given energy, and an additional two for the reflection probabilities. Note that for energies $0 < E < \gamma_1$, there is only one propagating mode and one transmission and reflection channel. Similarly, the wave function of AB-BL can be written as

$$\Psi(x, y) = GM(x)Ce^{ik_y y}, \quad (3.5)$$

where $M(x)$ corresponds to a 4×4 diagonal matrix consisting of exponential terms, while the components of the constant vector C depend on the propagating region, and G is given by

$$G = \begin{pmatrix} \xi_-^+ & -\xi_+^+ & \xi_-^- & -\xi_+^- \\ 1 & 1 & 1 & 1 \\ \rho^+ & \rho^+ & \rho^- & \rho^- \\ \zeta_+^+ & -\zeta_-^+ & \zeta_+^- & -\zeta_-^- \end{pmatrix}, \quad (3.6)$$

where $\xi_{\pm}^{\pm} = (k^{\pm} \pm ik_y)/(E - \delta)$, $\rho^{\pm} = (\epsilon - \delta) [1 - ((k^{\pm})^2 + k_y^2)/(\epsilon - \delta)^2]$ and $\zeta_{\pm}^{\pm} = (\epsilon - \delta)\rho^{\pm}\xi_{\pm}^{\pm}/(\epsilon + \delta)$. The use of the matrix notation will prove to be very useful to construct the transfer matrix as outlined below.

AA-stacking

In the case of an AA-BL, the corresponding wave function can be written similar to Eq. (3.5) but now with the matrix G given by

$$G = \begin{pmatrix} \xi_+^- & \xi_+^+ & \xi_-^- & \xi_-^+ \\ 1 & 1 & 1 & 1 \\ \zeta_+^- & \zeta_+^+ & \zeta_-^- & \zeta_-^+ \\ \rho^+ & \rho^+ & \rho^- & \rho^- \end{pmatrix}, \quad (3.7)$$

where $\rho^{\pm} = \frac{1}{2\epsilon} [-k_y^2 + (k^{\pm})^2 + (\epsilon - \delta)^2 + 1]$, $\xi_{\pm}^{\pm} = (\rho^{\pm} + \delta + \epsilon)(ik_y \pm k^{\pm})/(\delta^2 - \epsilon^2 + 1)$ and $\zeta_s^{\pm} = (\xi_{\pm}^{\pm} - \rho^{\pm}(ik_y \pm k^{\pm})/(\epsilon + \delta))$. To investigate when scattering between the Dirac cones of AA-BL is allowed or forbidden, one can apply a unitary transformation that forms symmetric and anti-symmetric combinations of the top and bottom layer. This yields a Hamiltonian in the basis $\Psi = 2^{-1/2}(\Psi_{A1} + \Psi_{A1}, \Psi_{B2} + \Psi_{B1}, \Psi_{A2} - \Psi_{A1}, \Psi_{B2} - \Psi_{B1})^T$ of the form:

$$H_{AA} = \begin{pmatrix} \gamma_1 + v_0 & v_F\pi^\dagger & -\delta & 0 \\ v_F\pi & \gamma_1 + v_0 & 0 & -\delta \\ -\delta & 0 & -\gamma_1 + v_0 & v_F\pi^\dagger \\ 0 & -\delta & v_F\pi & -\gamma_1 + v_0 \end{pmatrix}. \quad (3.8)$$

For $\delta = 0$, this Hamiltonian is block-diagonal and represents two Dirac cones as shown in Fig. 2.11(b). The two cones correspond to modes with wave vector k^\pm given by

$$k^s = \left[-k_y^2 + \left(\epsilon + s\sqrt{1 + \delta^2} \right)^2 \right]^{1/2}. \quad (3.9)$$

where $s = \pm$ is the cone index. In Fig. 3.1(b) the blue bands correspond to the odd k^+ modes (lower cone) and red bands denoting the even modes k^- (upper cone). In Eq. (3.8), v_0 denotes the energy shift of the whole spectrum. This shift can be chosen zero by assigning the same magnitude but different signs to the electrostatic potentials on both layers $V_1 = -V_2$. Eq. (3.8) shows that for zero electric field ($\delta = 0$) both cones are decoupled and the scattering between them is strictly forbidden. This was used before in Ref. [59] to propose AA-BL as a potential candidate for “*cone-tronics*” based devices. However, this protected cone transport is broken for finite bias ($\delta \neq 0$) and hence scattering between the cones is allowed. Furthermore, one might wonder if the charge carriers stay within their cone transport through a domain consisting of two decoupled layers.

Scattering probability and conductance

In order to calculate the scattering probability in the reflection and transmission channel, we use the transfer matrix method together with boundary conditions that require the eigenfunctions in each domain to be continuous for each sublattice [90,91]. To conserve probability current we normalize transmission probabilities T and reflection probabilities

R such that

$$\sum_{i,j} (T_i^j + R_i^j) = 1, \quad (3.10)$$

where, the index i refers to the incoming mode while the index j denotes the outgoing mode. For a coupled bilayer the different modes are labelled by “−” for the modes that are even under in-plane inversion and by “+” for odd modes. For a decoupled 2SL system, we employ the notation t for the top layer and b for the bottom layer. For example, for the system 2SL-AB-2SL and for an incident particle in the top layer of 2SL gives $T_t^t + T_t^b + R_t^t + R_t^b = 1$. In Fig. 3.1 all possible transition probabilities are shown schematically.

To obtain measurable quantities, we finally calculate the zero temperature conductance that can be obtained from the Landauer-Büttiker formula [92] where we have to sum over all the transmission channels,

$$G_i^j(E) = G_0 \frac{L_y}{2\pi} \int_{-\infty}^{+\infty} dk_y T_i^j(E, k_y), \quad (3.11)$$

with L_y the length of the sample in the y -direction and $G_0 = 4 e^2/h$. The factor 4 comes from the valley and spin degeneracy in graphene. The total conductance of any configuration is the sum of all available channels $G_T = \sum_{i,j} G_i^j$.

3.2 Transmission across a single domain wall

Here we will present analytical expressions for the transmission probabilities of transport across a single domain wall. These analytical expressions will shed light on the

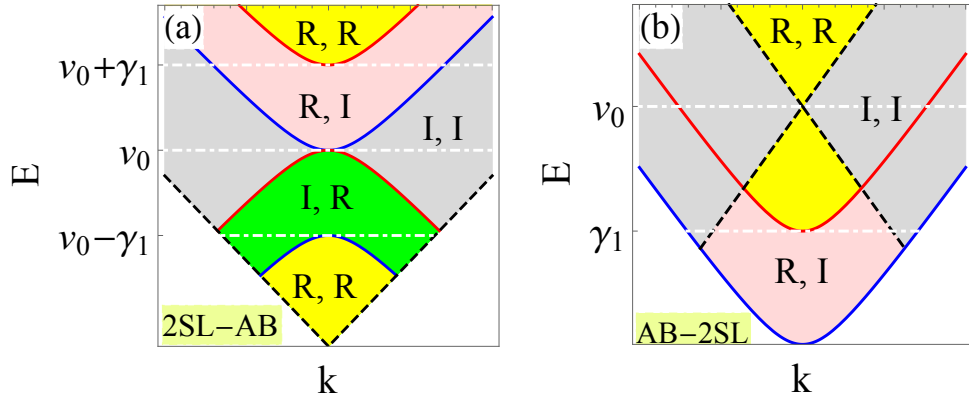


Figure 3.2: (Colour online) Schematic diagrams, for one domain wall separating 2SL and AB-BL, showing the regions where the modes (k^+ , k^-) in AB-BL are either real (propagating) or imaginary (evanescent). (a) shows the bands of pristine 2SL and gated AB-BL and vice versa in (b). In the yellow region both modes are real (R, R), while one of them is real and the other is imaginary as in the green (I, R) and pink (R, I) regions. In the gray region both modes are imaginary (I, I). Blue, red and dashed black bands correspond to k^+ , k^- and 2SL modes, respectively.

requirements for transport across a domain wall and how local electrostatic gating can affect these transport properties. By doing so, we encounter that curiously, electrostatic gates can break the symmetry between the layers in the transmission probability if there are evanescent modes in the system. The breaking of the layer symmetry results in an asymmetric angular distribution of the transmission probability as will be shown further.

We consider a situation where two propagating modes exist in the AB-BL or AA-BL. This requires some caution in defining the incident angle in the calculation of the transmission probabilities. Failing to do so may result in erroneous results such as transmission exceeding unity or unexpected symmetry features [93, 94]. Considering one domain wall, the simplest configuration, separating 2SL and either AA or AB-BL allows to obtain analytic expressions for the transmission probabilities. The incident angle for each propagating mode depends on the type of layer stacking in the incident region. Hence, for

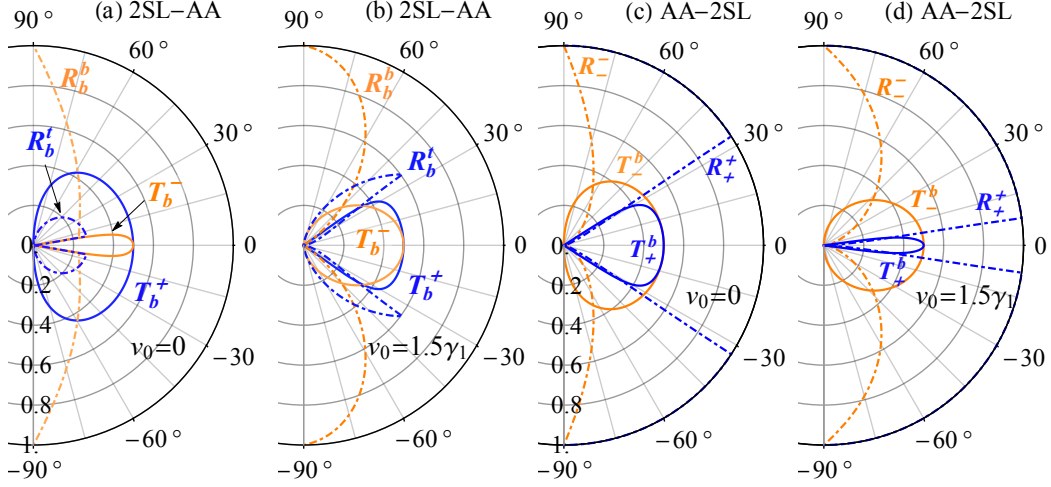


Figure 3.3: (Colour online) The angle-dependent transmission and reflection probabilities through (a, b) 2SL-AA and (c, d) AA-2SL systems. The systems in (b, d) are the same as in (a, c), respectively, but where now the right side of the junction is subjected to an electrostatic potential of strength $v_0 = 1.5\gamma_1$. In the system 2SL-AA $R_b^{b(t)} = R_t^{t(b)}$ and $T_b^\pm = T_t^\pm$ while $R_+^- = R_-^+ = 0$ and $T_\pm^b = T_\pm^t$ in AA-2SL system. In all panels $E = 1.2 \gamma_1$.

charge carriers incident from 2SL we define

$$k_j = E \cos \phi, \quad k_y = E \sin \phi. \quad (3.12)$$

On the other hand, when charge carriers are incident from AB-BL we need to define incident angle for each mode separately such that

$$k^\pm = \sqrt{E^2 \pm E} \cos \phi, \quad k_y = \sqrt{E^2 \pm E} \sin \phi. \quad (3.13)$$

Finally, for charge carriers incident from AA-BL the associated angle is defined by

$$k^\pm = (E \pm 1) \cos \phi, \quad k_y = (E \pm 1) \sin \phi. \quad (3.14)$$

A straightforward calculation results in the transmission probability for charge carriers

incident from 2SL and impinging on AA-BL

$$T_j^\pm = \frac{2(\epsilon + v_0)(\pm 1 + \epsilon)\text{Re}(k^\pm)}{k_j [(\pm 1 + \epsilon + k^\pm \sec \phi)^2 + (\mp 1 + v_0)^2 \tan^2 \phi]}, \quad (3.15)$$

while for the reverse configuration (AA-2SL) it is given by

$$T_\pm^j = \frac{2\epsilon\text{Re}(k_j)}{\cos \phi [(\epsilon + k_j \sec \phi)^2 + (\mp 1 + v_0)^2 \tan^2 \phi]}. \quad (3.16)$$

Similar as performed for the AA-BL Hamiltonian, also the AB-BL Hamiltonian can be expressed in terms of symmetric and anti-symmetric combinations of the two layers. This manipulation allows to determine a closed-form expression for the transmission probability of the 2SL-AB structure. The derivation is outlined in Appendix A and results in

$$T_j^\pm = 4\text{Re}(k^\pm) \left(\frac{\eta \left[\eta^2 + (\text{Im}(k^\mp) + \kappa_j v_0 \sin \phi)^2 \right]}{C_0 + \sum_{m=1}^4 C_m \cos(m\phi)} \right), \quad (3.17)$$

with $\eta = \epsilon \cos \phi$ and $\kappa_j = +1(-1)$ for $j = b(t)$. For the reverse configuration (AB-2SL) the transmission probabilities are

$$T_\pm^j = 4\text{Re}(k_j)k^\pm \frac{\lambda [\mu^\pm + \kappa_j v_0 \sin \phi \text{Im}(k^\mp)]}{|Q^\pm|^2}, \quad (3.18)$$

where λ , C_m , μ^\pm , and Q^\pm are functions defined in Appendix A.

For a domain wall separating 2SL and AA-BL, the transmission probabilities are always symmetric with respect to normal incidence as indicated in Eqs. (3.15,3.16). In other words, for the 2SL-AA $T_b^\pm(\phi) = T_t^\pm(\phi)$ and similarly $T_\pm^b(\phi) = T_\pm^t(\phi)$ for AA-2SL

configuration, and this symmetry still holds when the right side of the junction is gated ($v_0 \neq 0$). We will refer to this symmetry as “*layer symmetry*” since it is a consequence of the equivalence of 2SL layers and the symmetric coupling of the AA-BL.

Notice that Klein tunnelling for normal incidence in SL and AA-BL is also conserved in the combined structure. For example, in 2SL-AA and for normal incidence ($\phi = 0$), the modes become $k_j = \epsilon + v_0$, $k^\pm = \pm 1 + \epsilon$ and hence Eq. (3.15) reads $T_j^\pm = 1/2$. Then, for charge carriers propagating in the bottom (top) layer it may be transmitted into k^+ or k^- states and thus the total probability is $T_{b(t)}^+ + T_{b(t)}^- = 1/2 + 1/2 = 1$. As a result of Klein tunnelling at normal incidence, the corresponding reflection probabilities are zero such that $R_b^{b(t)} = R_t^{t(b)} = 0$. In an analogous manner it can be shown that for normal incidence Eq. (3.16) gives $T_\pm^j = 1/2$.

Turning now to the 2SL-AB/AB-2SL case, one can infer from Eqs. (3.17,3.18) that for $v_0 = 0$ the layer symmetry holds since the only term carrying asymmetric features is proportional to v_0 . However, for $v_0 \neq 0$ it is striking that despite the fact that a homogeneous electrostatic potential does not break any in-plane symmetry in the system, layer symmetry is broken. This leads to an angular asymmetry in the transmission channel, i.e. $T_b^\pm(\phi) = T_t^\pm(-\phi)$ for 2SL-AB and $T_\pm^b(\phi) = T_\pm^t(-\phi)$ for AB-2SL. Upon further analysis of Eqs. (3.17,3.18), one notices that this asymmetric feature is present in regions in the (E, k_y) plane where one of the two modes is propagating while the other is evanescent. In Figs. 3.2(a,b) we show a diagram for these different regions associated with 2SL-AB and AB-2SL, respectively. The layer symmetry is broken in the green and pink regions while in the yellow regions layer symmetry holds.

The mechanism for breaking the layer symmetry in configurations consisting of AB-BL

is attributed only to the evanescent modes. For example, in 2SL-AB (see Fig. 3.2) the transmission probability for charge carriers to be transmitted into k^+ from either bottom or top layers of 2SL is

$$T_j^+ = 4\text{Re}(k^+) \frac{\eta \left[\eta^2 + (\text{Im}(k^-) + \kappa_j v_0 \sin \phi)^2 \right]}{C_0 + \sum_{m=1}^4 C_m \cos(m\phi)}, \quad (3.19)$$

where $\kappa_{b(t)} = 1(-1)$. The above equation shows that layer symmetry is broken, $T_b^+(\phi) = T_t^+(-\phi)$, only when $v_0 \neq 0$ and $\text{Im}(k^-) \neq 0$ which is satisfied in the pink and gray regions in Fig. 3.2(a). However in the gray region there are no k^+ propagating states and consequently the transmission probabilities T_j^+ are zero. The same analysis applies also to T_j^- where the asymmetric feature is preserved only when $\text{Im}(k^+) \neq 0$ as shown by the green region in Fig. 3.2(a). For AB-2SL configuration, the layer asymmetry is only reflected in the T_+^j , see Eq. (3.18), since $\text{Im}(k^-) \neq 0$ corresponds to the pink region in Fig. 3.2(b). While for T_-^j , the k^- propagating states are only available for $E > \gamma_1$ (yellow region in Fig. 3.2(b)) which coincides with $\text{Im}(k^+) = 0$. Thus, the layer symmetry is always conserved in T_-^j as it can be seen in Eq. (3.18). Now it is clear why layer symmetry is not broken in the AA-BL configuration; because there are always two propagating modes associated with any energy value.

The breaking of angular symmetry in this situation is qualitatively similar to that obtained in AB-BL [47] subject to an inter-layer bias. One can connect this layer asymmetry in the vicinity of the two valleys K and K' through time-reversal symmetry. The Hamiltonian $H_{K'}$ can be related to the Hamiltonian H_K through the transformation

$$H_{K'}(\mathbf{k}) = \Theta H_K(-\mathbf{k}) \Theta^{-1}, \quad (3.20)$$

where Θ is the time-reversal symmetry operator. This implies, for example in the $T_{b(t)}^+$ channel, that charge carriers moving from right to left and scattered from the bottom layer to k^+ in K valley are equivalent to those scattered from top layer to k^+ but moving in the opposite direction in the vicinity of K' . If layer symmetry holds in the vicinity of one of the valleys, then the transmission probabilities of charge carriers moving in the opposite directions must be the same. It is worth pointing out here that the layer asymmetry in the K valley is reversed in the K' valley and hence the overall symmetry of the system is restored. Therefore, the macroscopic time reversal symmetry is preserved.

3.3 Transport across two domain walls

We first present the results for transmission, and reflection probabilities and for the conductance in the case of domain walls separating 2SL and AA-BL structures. The different regions as defined in Fig. 3.2 are superimposed as dashed black and white curves. Moreover, in calculating the transport properties we considered different magnitudes for the electrostatic potential v_0 and bias δ applied to the drain structure.

3.3.1 AA-Stacking

2SL-AA/AA-2SL

We consider charge carriers tunnelling through 2SL-AA and AA-2SL systems. In Fig. 3.3(a) we show the transmission and reflection probabilities for charge carriers impinging on pristine AA-BL as a function of incident angle ϕ . As a result of the layer symmetry, charge carriers incident from bottom/top layer of 2SL and transmitted into the lower

Dirac cone (k^+) in the AA-BL will have the same transmission probability $T_b^+ = T_t^+$. Similarly, for those charge carriers transmitted into the upper cone, they will also have the same probability $T_b^- = T_t^-$ regardless which layer they are incident from.

This symmetry stems from the fact that the wavefunction in the 2SL are a superposition of two spinors corresponding to the two sublattices while in AA-BL it is a superposition of four. For this reason, charge carriers incident from top or bottom layer of 2SL have the same dynamics and hence share their transmission probability. A partial reflection into the same layer, $R_b^b = R_t^t$ is shown in Fig. 3.3(a), which corresponds to evanescent modes associated with the upper Dirac cone (k^-). As in transmission, charge carriers can be back scattered between the layers. However, the absence of the electrostatic potential results in a small scattering current as depicted in Fig. 3.3(a). In addition, scattering back from top to bottom layer or vice versa occurs also with the same reflection probabilities $R_b^t = R_t^b$.

Because of chiral decoupling of oppositely propagating waves in AA-BL and in SL, back-scattering is forbidden for normal incidence ($\phi = 0$) and thus the reflection probabilities for each channel are zero, i.e. $R_b^{b(t)}(0) = R_t^{t(b)}(0) = 0$. This is associated with perfect tunnelling $T_b^+(0) + T_b^-(0) = T_t^+(0) + T_t^-(0) = 1$. The effect holds for all forthcoming structures composed of AA-BL and 2SL.

Fig. 3.3(b) shows the numerical results of the same system, 2SL-AA, but now in the AA region, the potential is increased to $v_0 = 1.5\gamma_1$. This shifts the two Dirac cones in energy to $v_0 \pm \gamma_1$. As a result of the presence of the electrostatic potential, a strong scattered reflection R_b^t/R_t^b takes place when there are no propagating modes in the AA section.

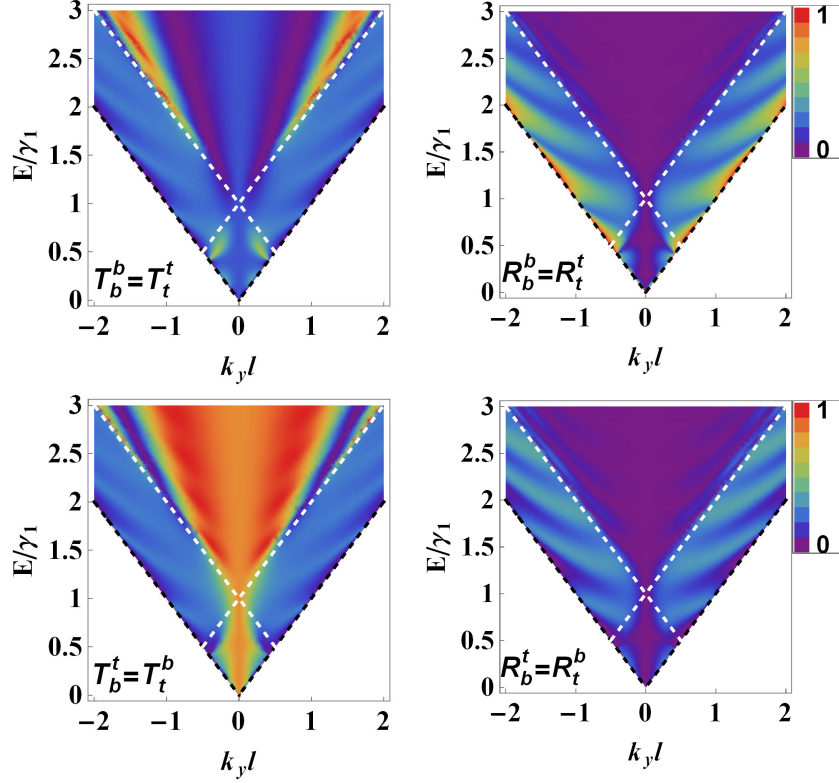


Figure 3.4: (Colour online) Density plot of the transmission and reflection probabilities through 2SL-AA-2SL as a function of Fermi energy and transverse wave vector k_y with $v_0 = \delta = 0$ and width of the AA-BL $d = 25$ nm.

In Figs. 3.3(c,d), we show the reversed configuration, i.e. an AA-2SL system. The transmission and reflection probabilities for zero ($v_0 = 0$) and with nonzero ($v_0 = 1.5\gamma_1$) electrostatic potentials applied to 2SL are reported in panels (c) and (d), respectively. Similar to the 2SL-AA system, we can note that layer symmetry still holds such that $T_+^b = T_+^t$ and $T_-^b = T_-^t$. Furthermore, we find strong non-scattered reflection in the R_+^+ and R_-^- channels that is associated with evanescent modes on both sides of AA-BL and 2SL whereas the scattered reflection channels R_-^+ and R_+^- are always zero due to the protected cone transport discussed earlier.

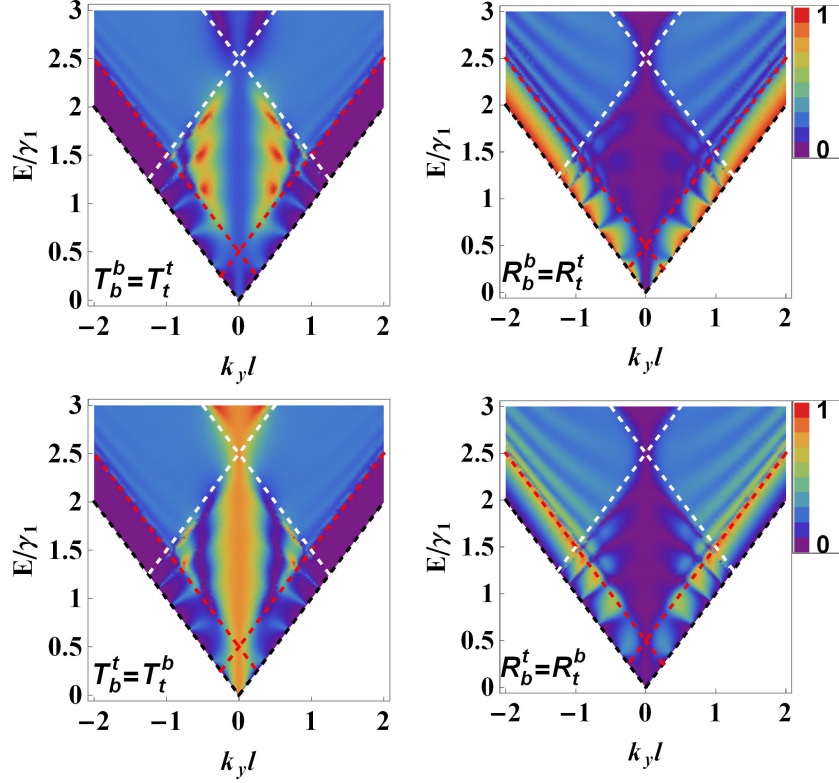


Figure 3.5: (Colour online) The same as in Fig. 3.4, but now with $v_0 = 1.5\gamma_1$. Red and white dashed curves correspond to the lower and upper Dirac cones in AA-BL, respectively, while the black dashed curves are the bands of 2SL.

2SL-AA-2SL

In this Section, we show the results of transport across two domain walls forming a system with three regions; where AA-BL is sandwiched between two regions of 2SL, see Fig. 3.1(b). Such a system can exhibit a strong layer selectivity when current flows through the intermediate region, i.e. AA-BL. This behaviour will be investigated in detail in the next chapter. Here, however, we go in much more detail to show how the different transmission and reflection channels are affected by the electrostatic potential or finite bias applied to the intermediate region.

In Figs. 3.4 and 3.5 we show the scattered and non-scattered channels for transmission and reflection for pristine AA-BL and with electrostatic potential of strength $v_0 = 1.5 \gamma_1$,

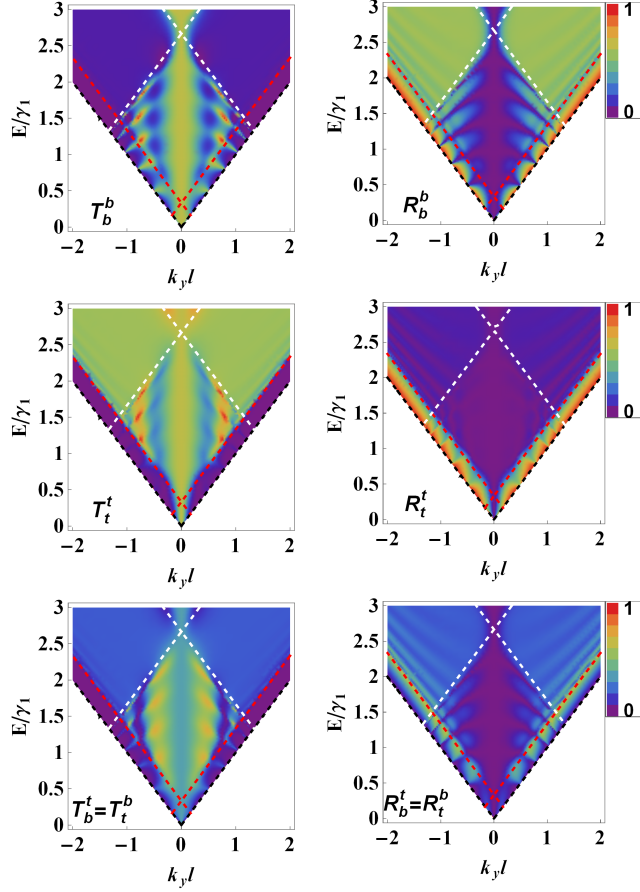


Figure 3.6: (Colour online) The same as in Fig. 3.4, but now with $v_0 = 1.5\gamma_1$ and $\delta = 0.6\gamma_1$.

respectively. Layer symmetry is preserved in both reflection and transmission channels as clarified in Figs. 3.4. and 3.5 which also show strong scattered transmission, especially at normal incidence which can be altered depending on the width of the AA-BL. When an electrostatic potential is applied to the middle domain, resonances appear in the transmission probabilities for $v_0 + \gamma_1 > E > v_0 - \gamma_1$ as shown in Fig. 3.5. This is a consequence of the finite size of the AA-BL and the presence of charge carriers with different chirality in the mentioned range of energies [59]. Introducing a finite bias $\delta = 0.6\gamma_1$ on AA-BL breaks the layer symmetry of the system. As a result, $T_b^b \neq T_t^t$ and $R_b^b \neq R_t^t$. However, it is still preserved in the scattered channels $T_b^t = T_t^b$ and $R_b^t = R_t^b$ (see Fig. 3.6).

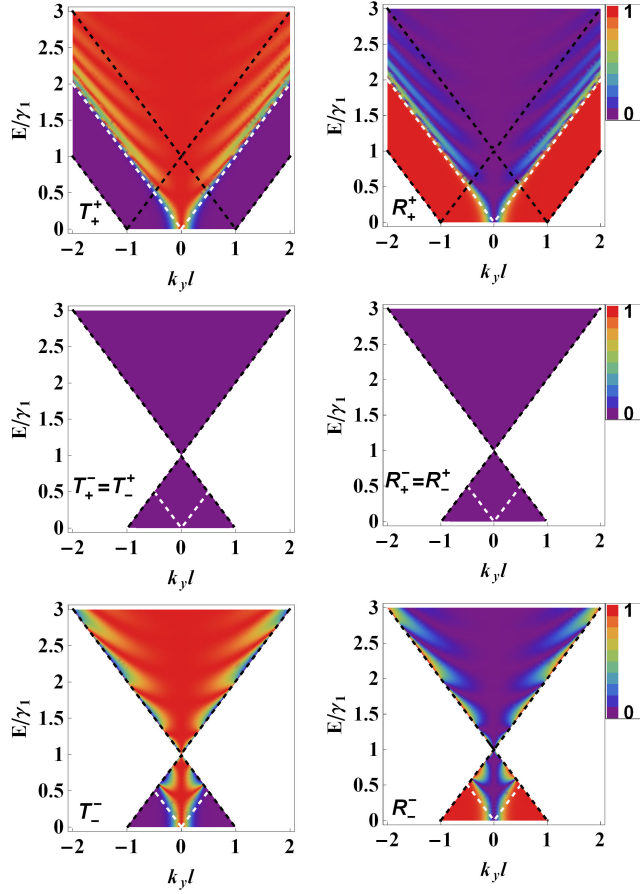


Figure 3.7: (Colour online) Density plot of the transmission and reflection probabilities through AA-2SL-AA as a function of Fermi energy and transverse wave vector k_y with $v_0 = \delta = 0$ and width of the 2SL $d = 25$ nm.

It is worth mentioning here that the finite bias does not break the angular symmetry with respect to normal incidence in the transmission and reflection probabilities as it does for normal AB-BL [47]. This is a manifestation of the symmetric inter-layer coupling in AA-BL.

AA-2SL-AA

In this system we interchange the AA-BL and 2SL as shown in Fig. 3.1(b). In this case, scattering is defined between the two cones in the AA-BL regions. In Figs. 3.7 and 3.8 we show the transmission and reflection probabilities between the two Dirac cones

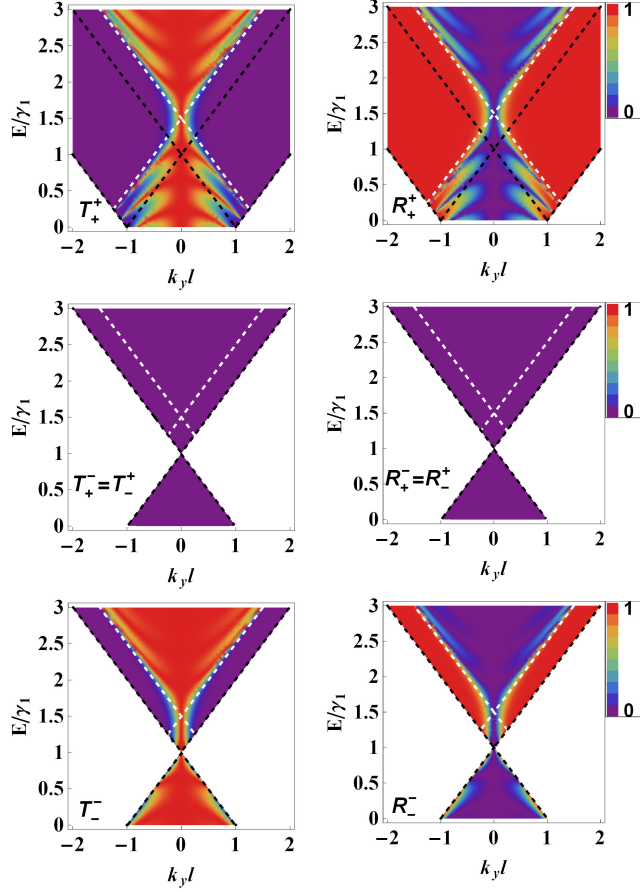


Figure 3.8: (Colour online) The same as in Fig. 3.7, but now with $v_0 = 1.5 \gamma_1$.

through the pristine 2SL and in the presence of an electrostatic potential, respectively. The first and the last rows of Figs. (3.7) and (3.8) show the non-scattered transmission and reflection probabilities corresponding to the lower and upper Dirac cones, respectively. We notice that Klein tunnelling is preserved at normal incidence. This shows that Klein tunnelling in AA-stacked bilayer graphene is a robust feature that is insensitive to local changes in the inter-layer coupling. On the other hand we see that scattering between two different Dirac cones remains strictly forbidden even with a local decoupling of the two layers. Therefore, these devices could be used for conetronics. As a result, in the second row of Figs. 3.7 and 3.8 the scattered transmission and reflection channels are

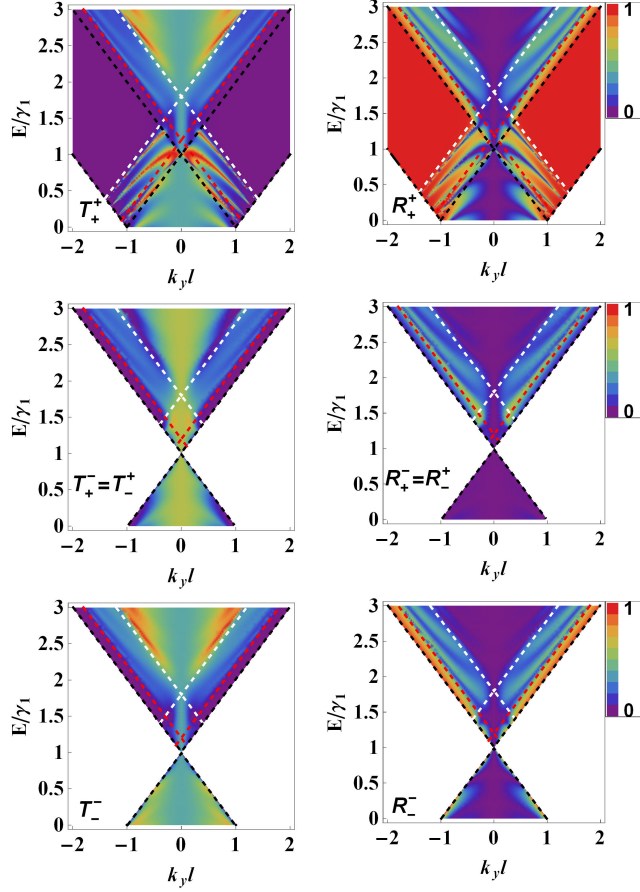


Figure 3.9: (Colour online) The same as in Fig. 3.7, but now with $v_0 = 1.5\gamma_1$ and $\delta = 0.3\gamma_1$. Red and white dashed curves correspond to the bands of bottom and top layers of 2SL, respectively, while the black dashed curves are the AA-BL bands.

zero $T_+^- = T_-^+ = R_+^- = R_-^+ = 0$.

In Fig. 3.9 we plot the transmission and reflection probabilities for a potential strength $v_0 = 1.5 \gamma_1$ and inter-layer bias $\delta = 0.3 \gamma_1$. The shift in the bands of the top (white) and bottom (red) layer of 2SL is due to the inter-layer bias which couples the two Dirac cones as shown in Eq. (3.8). Therefore, the suppression of the scattering transmission and reflection probabilities due to the protected cone transport does not hold anymore. It is, therefore, possible that scattering between different cones takes place as clarified in the second row of Fig. 3.9.

Conductance

The conductance of two and three-block systems is shown in Figs. 3.10 and 3.11, respectively. For the two systems 2SL-AA and AA-2SL with pristine AA-BL and 2SL, the conductance for different channels is shown in Figs. 3.10(a, b). It shows that the conductance of these two systems are identical. Referring to Figs. 3.3(a, c) we notice that the transmission probabilities for pristine 2SL-AA and AA-2SL are quite different. However, the corresponding conductances (see Fig. 3.10) exhibit time reversal symmetry in spite of the fact that the domain wall separates two different systems. This is a strong point which can be verified experimentally even in the case of zero electrostatic potential.

Adding an electrostatic potential to one of the two sides leads to different behavior in the conductance of the above mentioned two systems as depicted in Figs. 3.10(c,d). In Fig. 3.10(c) the charge carriers incident from 2SL and impinging on AA-BL whose bands are shifted by v_0 . Each conductance channel gives zero at $E = 0$ due to the absence of propagating states in the 2SL at this energy, even though there are propagating states available in AA-BL corresponding to two cones. We note also that $G_b^\pm = G_t^\pm$ are almost zero at upper and lower cones $v_0 \pm \gamma_1$ as a result of the absence of states at these points as seen in Fig. 3.10(c). In Fig. 3.10(d) we see that the conductance of different channels is not zero in contrast to the previous case because here at $E = 0$ there are propagating states available in both AA-BL and 2SL. Furthermore, all channels have one minimum, due to the lack of states, at $E = v_0$ which corresponds to the Dirac cone in 2SL shifted by v_0 while $G_-^{t/b}$ has also another minimum at the upper cone $E = \gamma_1$ as shown in Fig. 3.10(d). Finally, for comparison we add in Figs. 3.10(e, f) the conductance that will be measured in the absence of a domain wall for 2SL-2SL and AA-AA junctions with $v_0 = 0$ (blue

curves). Our results indicate that domain walls are experimentally identifiable channels even in the absence of a gate. As a reference we also calculate the total conductance in the presence of an electrostatic potential ($v_0 = 1.5\gamma_1$) as shown with black curves in Figs. 3.10(e, f) which corresponds, in this case, to the usual p-n junctions in single-layer graphene and AA-BL, respectively.

The conductance of three-block systems is shown in Fig. 3.11 where left and right panels correspond to AA-2SL-AA and 2SL-AA-2SL structure, respectively. Protected cone transport leads to zero conductance in the scattered channels $G_-^+ = G_+^- = 0$ as shown in Fig. 3.11(a). A close inspection also reveals that $G_-^- = G_+^+$ at $E = 0$ with finite and non-zero values, regardless of the fact that in the 2SL region there are no available propagating states. This is attributed to the evanescent modes in 2SL at $E = 0$ which are responsible for ballistic transport in graphene [95]. We thus also expect that G_-^- (red curve in Fig. 3.11(a)) should be exactly zero at the Dirac cone $E = \gamma_1$ as a result of the absence of propagating states in the leads at this energy.

By shifting the bands of 2SL using a local potential with strength $v_0 = 1.5\gamma_1$, a local minimum appears in the conductance G_T at $E = v_0$ which corresponds to the position of the charge-neutrality point in 2SL as shown in Fig. 3.11(c). This minimum can be obtained by aligning the upper cone in AA-BL and the Dirac cone in 2SL such that they are located at the same energy, this can be achieved by choosing $v_0 = \gamma_1$. The main difference introduced by applying an inter-layer bias is the broken protected cone transport where now $G_+^- = G_-^+ \neq 0$ as depicted in Fig. 3.11(e). For completeness, we performed similar calculations but now with 2SL as the leads (2SL-AA-2SL) and the results for the conductance with pristine, gated and biased AA-BL are shown in Figs.

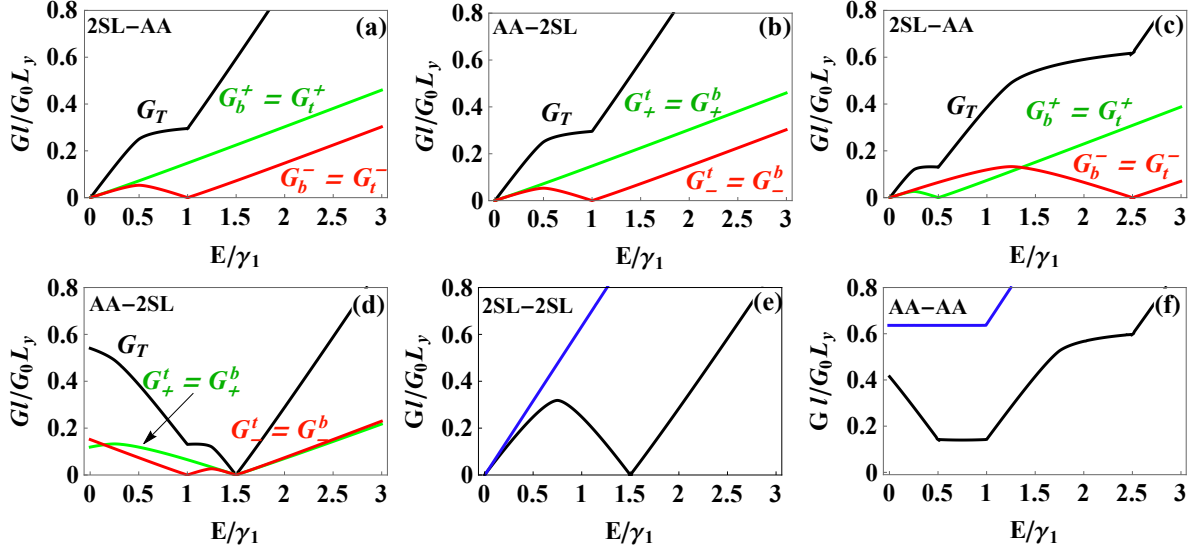


Figure 3.10: (Colour online) Conductance of two-block system for different magnitudes of the applied gate: (a, b) $v_0 = \delta = 0$, (c, d) $v_0 = 3\gamma_1/2$, $\delta = 0$. G_T is the total conductance obtained by summation of all possible channels, (e, f) the total conductance for 2SL-2SL and AA-AA junctions, respectively, with $v_0 = 0$ (blue curves) and $v_0 = 1.5\gamma_1$ (black curves).

3.11(b, d, f), respectively. Here, all conductance channels are zero at $E = 0$ such that $G_t^t = G_b^b$ and $G_b^t = G_t^b$ as shown in Figs. 3.11(b, d). Similarly, the main features in Fig. 3.11(f) are in qualitative agreement with those shown in Figs. 3.11(b, d) but now the tunnelling equivalence through the same channel is broken so that $G_t^t \neq G_b^b$. This is a direct consequence of the perpendicular electric field which leads to the breaking of the inter-layer sublattice equivalence. The peaks appearing in the total conductance are due to the finite size of the AA-BL region.

3.3.2 AB-Stacking

2SL-AB/AB-2SL

In this section, we evaluate how the stacking of the connected region changes the transport properties across a domain wall. The angle-dependent transmission and reflection

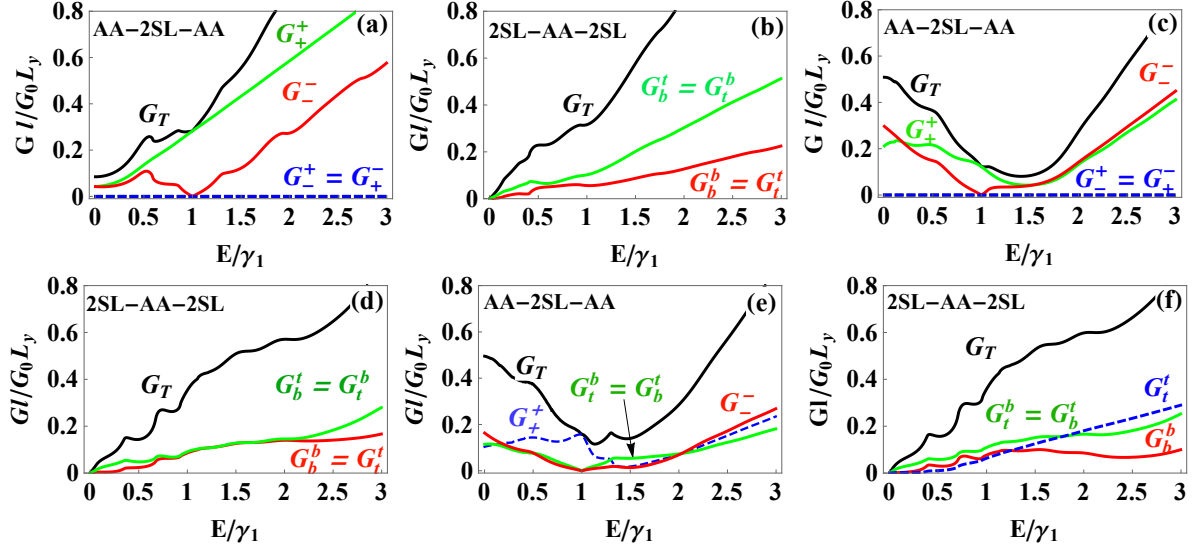


Figure 3.11: (Colour online) Conductance of three-block system with different magnitudes of the applied gate: (a, b) $v_0 = \delta = 0$, (c, d) $v_0 = 3\gamma_1/2$, $\delta = 0$ and (e, f) $v_0 = 3\gamma_1/2$, $\delta = 0.6\gamma_1$. G_T is the total conductance obtained by summation of all possible channels.

probabilities for pristine systems 2SL-AB are plotted in Fig. 3.12(a). The charge carriers can be incident from the two layers in the 2SL structure and impinge on AB-BL where, depending on their energy, they can access only one propagating mode k^+ or two k^\pm if the energy is large enough. Scattering from the top or bottom layer of 2SL into one of these modes is equivalent $T_t^\pm = T_b^\pm$ as well as backscattering $R_t^{t(b)} = R_b^{b(t)}$ and hence, as before, layer symmetry is preserved (see Fig. 3.12(a)). In Fig. 3.12(b) we show results with the AB-BL region subjected to an electrostatic potential of strength $v_0 = 1.5\gamma_1$. Surprisingly, we see that the layer symmetry is broken and an asymmetric feature with respect to normal incidence shows up in the transmission and non-scattered reflection probabilities, see Appendix A, such that $[T/R](\phi) = [T/R](-\phi)$. For example, $T_b^\pm(\phi) = T_t^\pm(-\phi)$ as well as the non-scattered reflection channels $R_b^b(\phi) = R_t^t(-\phi)$ as discussed in Sec. 3.2. This asymmetric feature can be understood by resorting to the bands on both sides of the junction, where due to the electrostatic potential the band alignment of 2SL and AB-BL

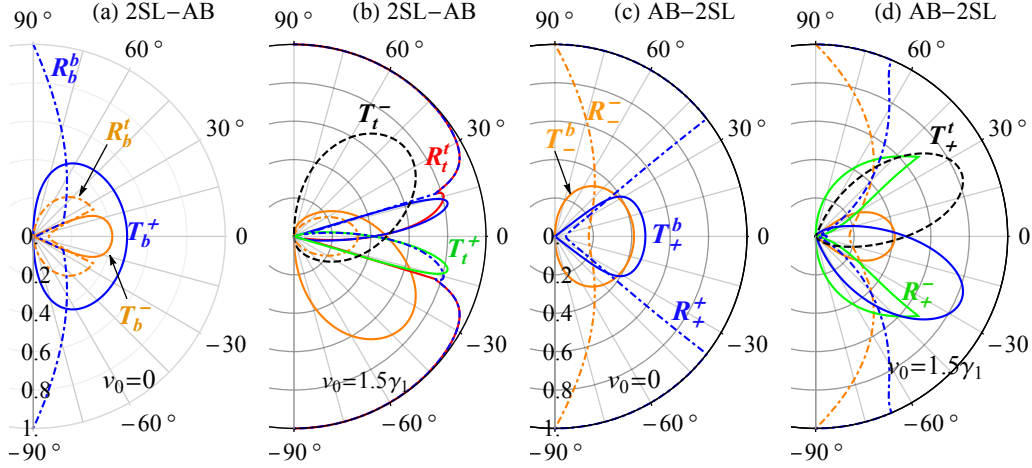


Figure 3.12: (Colour online) The angle-dependent transmission and reflection probabilities through (a, b) 2SL-AB and (c, d) AB-2SL junctions. The systems in (b, d) are the same as in (a, c), respectively, but where the right side of the junction is subjected to an electrostatic potential of strength $v_0 = 1.5\gamma_1$. In (a) $E = 1.2\gamma_1$ for all channels while in (b) $E = 1.7\gamma_1$ for $T_{b(t)}^+$ and $E = 0.6\gamma_1$ for the rest of the channels and in (c, d) $E = (0.6, 1.7)\gamma_1$ for $R_+/T_+^{b(t)}$ and $R_-/T_-^{b(t)}$, respectively. We choose energy values in (b, d) such that they correspond to only one propagating mode in the AB-BL region.

is altered. In this case, the center of the AB-BL band is shifted upwards in energy with respect to the crossing of the 2SL energy bands [96]. The origin of such asymmetry is a direct consequence of the asymmetric coupling in AB-BL which leads to shifting of the bands by γ_1 . Therefore, at low energy $|E - v_0| < \gamma_1$ there is only one propagating mode k^+ (i.e one type of charge carrier) and consequently only $T_{b(t)}^+$ is available. For larger energy, on the other hand, there are two modes available giving rise to four channels $T_{b(t)}^\pm$.

The angular asymmetry feature is present only in the region in the (E, k_y) -plane where there is only one propagating mode. This can be also understood as a manifestation of the asymmetric amplitude of the wave function in the AB-BL side due to the evanescent modes in this region [97]. The theory of tunnelling through an interface of monolayer and bilayer was presented earlier [97] and such asymmetry was noticed as well. Moreover, in our case there are two single layer graphene sheets connected to the bottom and top

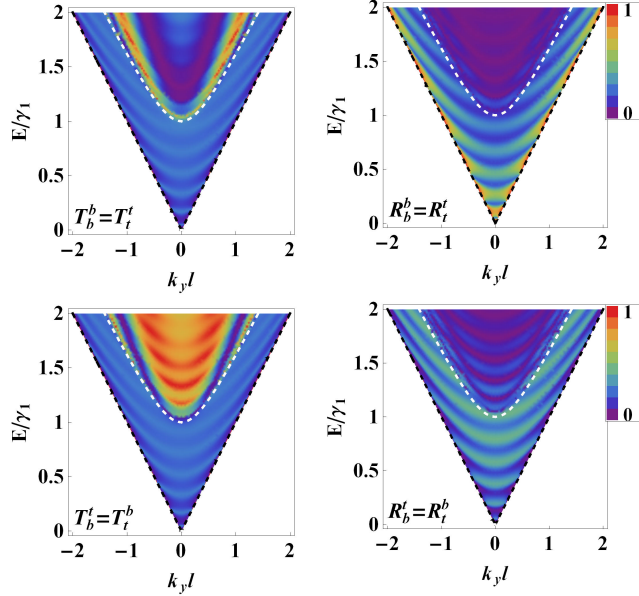


Figure 3.13: (Colour online) Density plot of the transmission and reflection probabilities through 2SL-AB-2SL as a function of Fermi energy and transverse wave vector k_y with $v_0 = \delta = 0$.

layers of the bilayer system but the asymmetric feature in Ref. [97] will be recovered when considering only one propagation channel. For instance, the transmission probabilities T_t^\pm and T_b^\pm presented in Fig. 3.12(b) show the same asymmetric features discussed in Ref. [24]. This asymmetry feature is reversed in the other valley, so that the total transmission or reflection averaged over both layers is symmetric as can be seen from Fig. 3.12(b). However, this valley-dependent angular asymmetry could also be used for the basis of a layer-dependent valley-filtering device as proposed in other works [41, 51].

The above analogy, which is discriminating between the presence of one or two modes, applies also to the non-scattered reflection probabilities R_b^b and R_t^t . These non-scattered currents are carried by the states localized on the disconnected sublattices A_2 and B_1 , as seen in Fig. 2.9(a). In that case, there is one traveling mode [79] and thus, inherently, a layer asymmetric feature will be present. In contrast, for the scattered channels R_b^t and R_t^b the charge carriers must jump between the layers of AB-BL. This occurs through the

localized states on the connected sublattices α_1 and β_2 where there are two travelling modes and, hence, these probabilities exhibit layer symmetry as shown in Fig. 3.12(b). In the AB-2SL configuration, where charge carriers incident from the AB-BL impinge on the 2SL, we show the angle-dependent transmission and reflection probabilities in Fig. 3.12(c) for pristine 2SL and AB-BL.

Similar to the previous configuration 2SL-AB, the results are symmetric in this case because the Dirac cones of both systems (2SL and AB-BL) are aligned. Furthermore, there is an equivalence in the transmission channels such that $T_{\pm}^t = T_{\pm}^b$ with partial reflection associated with the non-scattered channels R_{-}^{-} and R_{+}^{+} . While for the scattered channels R_{+}^{-} and R_{-}^{+} are almost zero. This is due to efficient transmission resulting from the absence of the electrostatic potential in the 2SL. An electrostatic potential of strength $v_0 = 1.5\gamma_1$ induces a scattering between the two modes in the reflection channels so that now $R_{-}^{+} = R_{+}^{-} \neq 0$ as depicted in Fig. 3.12(d). In addition, it breaks the band alignment and gives rise to the layer asymmetry feature in the transmission probabilities $T_{+}^{b(t)}$ where only one travelling mode exists i.e. $E < \gamma_1$. Thus, $T_{-}^{b(t)}$ always preserves layer symmetry in this case, see Fig. 3.12(d), because the mode k^{-} exists for $E > \gamma_1$ where also the mode k^{+} is available as discussed above. This is also the same reason that configurations consisting of AA-BL always preserve layer symmetry. Indeed, AA-BL does not have a region in the (E, k_y) -plane with only one propagating mode, and there are always two travelling modes for all energies.

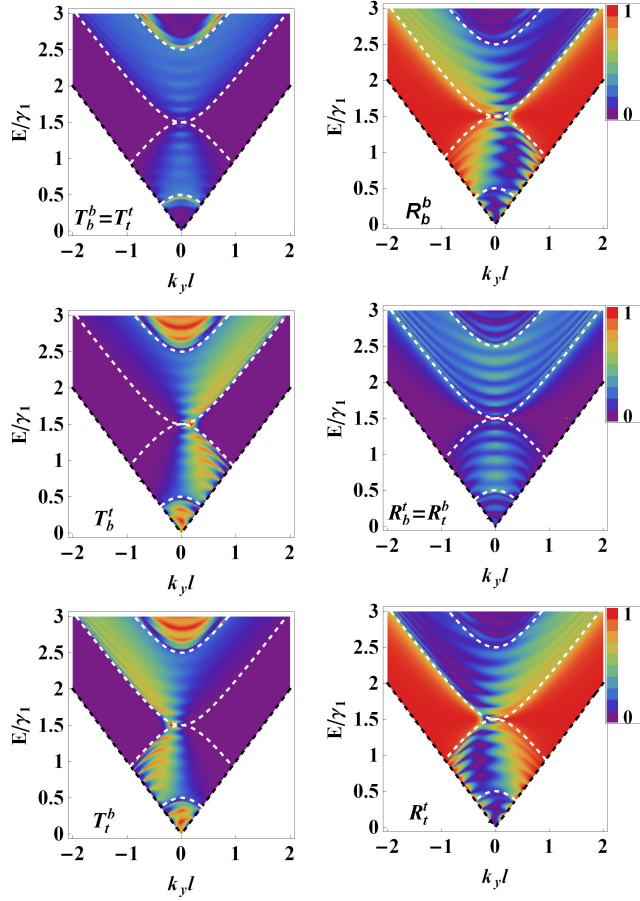


Figure 3.14: (Colour online) The same as in Fig. 3.13, but now with $v_0 = 3\gamma_1/2$.

2SL-AB-2SL

Now, two SL are connected to the AB-stacked bilayer, see Fig. 3.1(d). In Fig. 3.13 we show the dependence of the transmission and reflection probabilities on the transverse wave vector k_y and the Fermi energy. It appears that all channels are symmetric with respect to normal incidence since the Dirac cones of AB and 2SL are aligned. It also implies that scattered and non-scattered channels of the transmission and reflection are equivalent such that $(T/R)_b^t = (T/R)_t^b$ and $(T/R)_t^t = (T/R)_b^b$ (see Fig. 3.13).

Another interesting feature of this configuration is that for $E < \gamma_1$ the scattered and non-scattered transmissions are equal $T_i^j = T_i^i$. In this energy regime such a device can

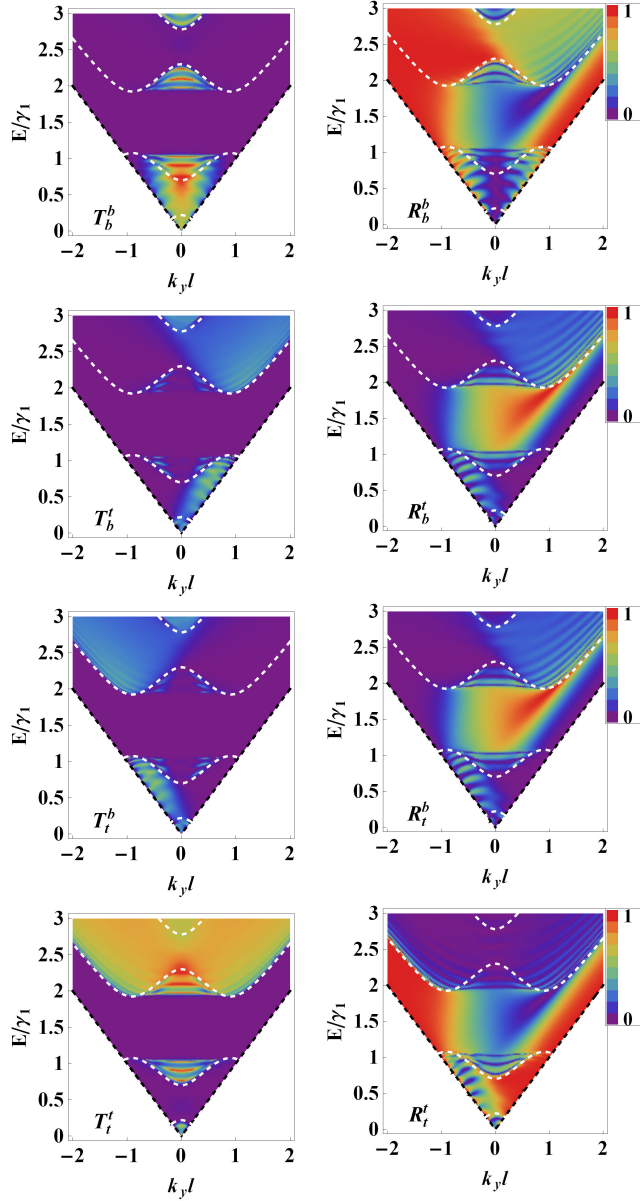


Figure 3.15: (Colour online) The same as in Fig. 3.13, but now with $v_0 = 3\gamma_1/2$, $\delta = 0.8\gamma_1$. New localized states appear inside the “Mexican hat” shape of the low energy bands of AB-BL due to the strong gate potential.

be used as an electronic beam splitter [98,99].

Fig. 3.14 displays the same plot as in Fig. 3.13 but with an electrostatic potential on the AB-BL region. There is an important difference as compared to the pristine AB-BL case, the layer symmetry is broken such that $T_t^b(k_y) = T_b^t(-k_y)$ as clarified in Fig. 3.14.

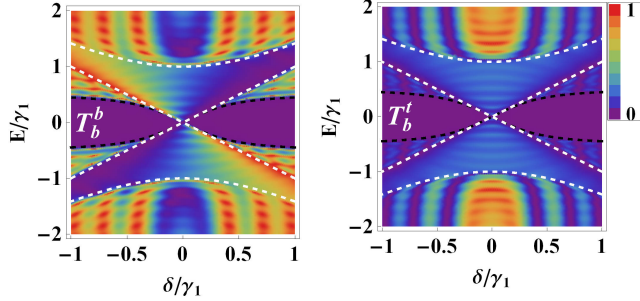


Figure 3.16: (Colour online) Transmission probabilities as function of Fermi energy and bias for normal incidence.

This can be also understood by pointing out that charge carriers scattered from top to bottom when moving from left to right in the K valley are equivalent to charge carriers scattering from bottom to top when moving oppositely in the second valley K' .

Introducing a finite bias ($\delta > 0$) to the AB-BL region along with an electrostatic potential ($v_0 > 0$) will shift the bands and opens a gap in the spectrum. As a result of the presence of a strong electric field, the transmission channels are completely suppressed inside the gap due to the absence of traveling modes as seen in Fig. 3.15. Moreover, non-zero asymmetric reflection appears in the gap as well as a violation of the equivalence of non-scattered transmission channels. This is a result of the breaking of inter-layer sublattice equivalence [47]. In addition, some localized states appear inside the “Mexican hat” of the low energy bands where they are pushed by the strong electric field ($\delta = 0.8\gamma_1$), see Fig. 3.15.

There is a link between the transmission probabilities of our system 2SL-AB-2SL and those investigated by González *et al.* [96]. The channels T_b^b and T_b^t are qualitatively equivalent to those obtained in Ref. [96]. For example, T_b^b shows electron-hole ($e-h$) and $\delta \rightarrow -\delta$ symmetry whereas T_b^t exhibits another symmetry which can be obtained under the exchange $(e, \delta) \leftrightarrow (h, -\delta)$. The results in Fig. 3.16 are in good agreement with those

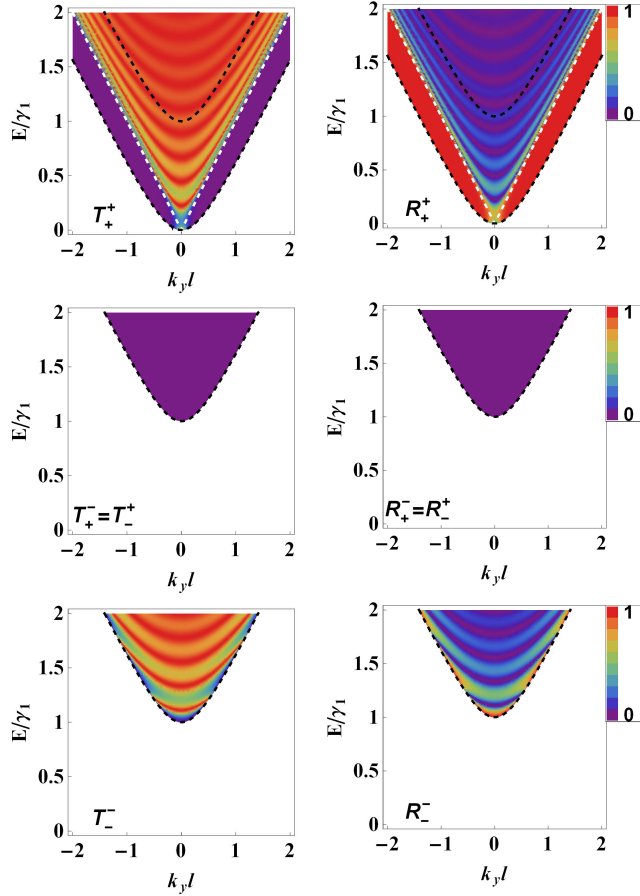


Figure 3.17: (Colour online) Density plot of the transmission and reflection probabilities through AB-2SL-AB as a function of Fermi energy and transverse wave vector k_y with $v_0 = \delta = 0$ and $d = 25\text{nm}$.

of Ref. [34] where we fix $v_0 = 0$ and $d = 25 \text{ nm}$.

AB-2SL-AB

For leads composed of AB-BL where the intermediate region is pristine 2SL, we show the results in Fig. 3.17 for the transmission and reflection probabilities. Now charge carriers will scatter between the different modes of the AB-BL on the left and right leads as shown in Fig. 3.1(c). As expected, all channels are symmetric and as a result of the finite size of the 2SL region, resonances appear in T as shown in Fig. 3.17. These so-called Fabry-Pérot

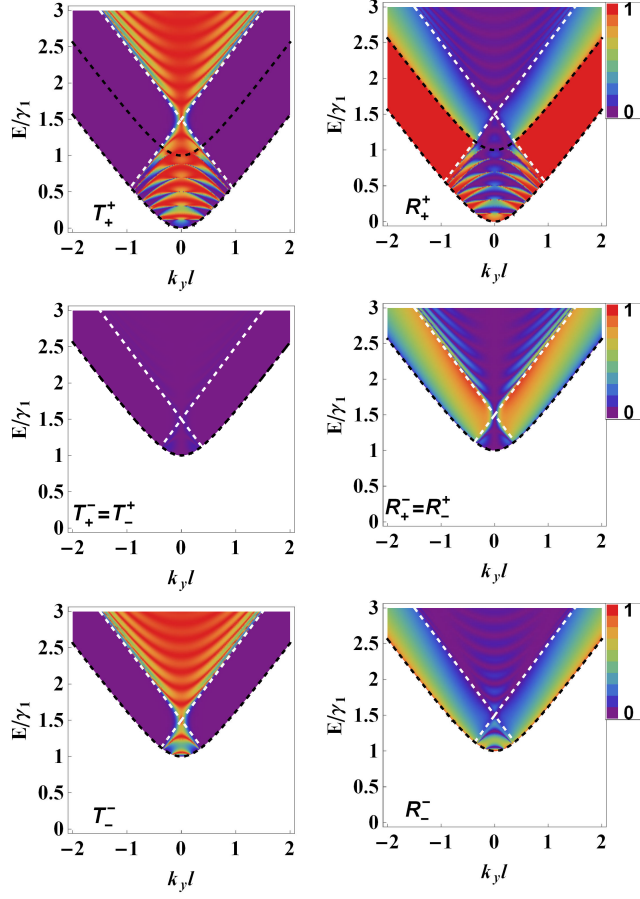


Figure 3.18: (Colour online) The same as in Fig. 3.17, but here with $v_0 = 3\gamma_1/2$

resonances appear at quantized energy levels [100]

$$E_{SL}^n(k_y) = \sqrt{k_y^2 + \left(\frac{n\pi}{d}\right)^2}. \quad (3.21)$$

This is the dispersion relation for modes confined in the 2SL region of width d .

The results presented in Fig. 3.17 reveal no scattering between the two modes k^+ and k^- and charge carriers are only transmitted or reflected through the same channel from which they came from. Unexpectedly, introducing an electrostatic potential induces a strong scattering in the reflection channels ($R_+^- = R_-^+ \neq 0$) and very weak scattering in the transmission channels ($T_+^- = T_-^+ \neq 0$), as seen in Fig. 3.18. When the 2SL are biased,

the Dirac cones at bottom and top layers will be shifted up (white dashed lines) and down (red dashed lines) in energy, respectively (see Fig. 3.19). This bias will strengthen the coupling between the two modes resulting in a strong scattering between them. In addition, the inversion symmetry is broken due to the bias leading to an asymmetry with respect to normal incidence.

Conductance

The conductance of the two-block system consisting of 2SL and BA-BL is shown in Fig. 3.20 for different values of the applied gate voltage. Figs. 3.20(a,b) reveal that the system where charge carriers are incident from the 2SL and impinge on AB-BL and vice versa are equivalent to the case when both 2SL and AB-BL are at the same potential. As seen in Figs. 3.20(a,b), $G_+^{t(b)} = G_{t(b)}^+$ are contributing to the total conductance G_T starting from $E = 0$ where the k^+ mode exists. On the contrary, $G_-^{t(b)} = G_{t(b)}^-$ only contributes when $E > \gamma_1$ where k^- states are available and this appears as a sharp increase in G_T at $E = \gamma_1$. On the other hand, considering an applied electrostatic potential on the right side of the two-block system will break this equivalence as seen in Figs. 3.20(c,d). In addition, as a result of the shift of the Dirac cone in AB-BL (see Fig. 3.20(c)) or 2SL (see Fig. 3.20(d)) due to the electrostatic potential, all conductance channels are zero at $E = v_0$. Similar to the AA-BL case, the conductances of the pristine systems 2SL-AB/AB-2SL (see Figs. 3.20(a, b)) clearly preserve the time reversal symmetry. Even though, both systems have different transmission probabilities as can be seen from Figs. 3.12(a, c). We also show in Figs. 3.20(e, f) the total conductance in the absence of domain wall in 2SL-SL and AB-AB systems, respectively, for $v_0 = 0$ (blue curves) and $v_0 = 1.5\gamma_1$ (black curves).

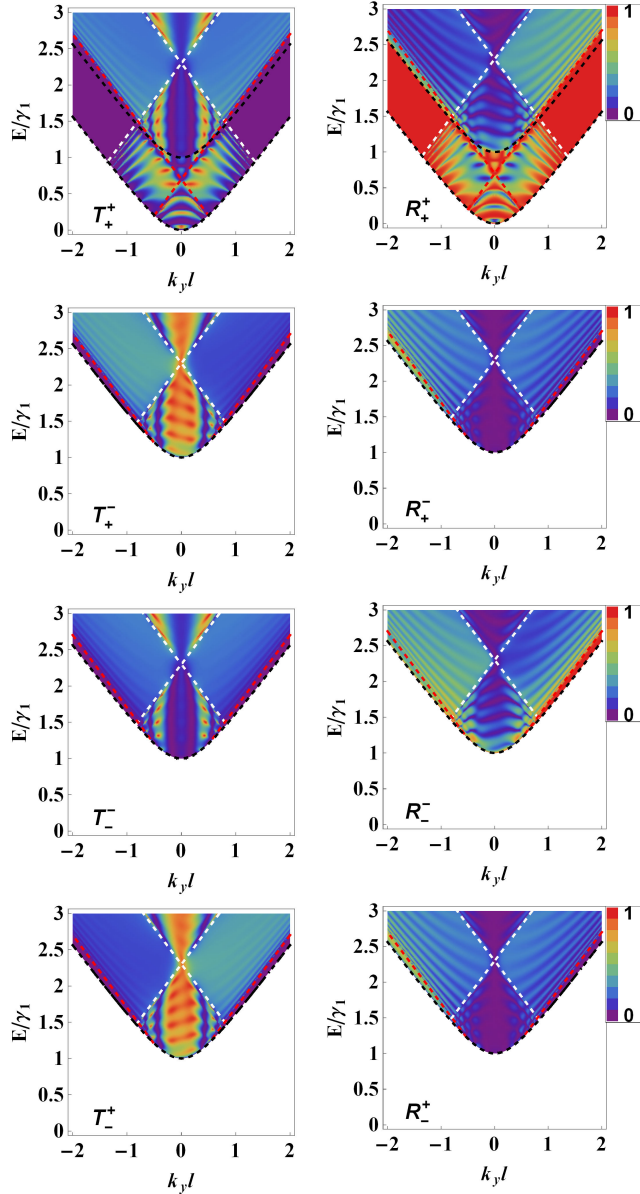


Figure 3.19: (Colour online) The same as in Fig. 3.17, but here with $v_0 = 3\gamma_1/2$, $\delta = 0.8\gamma_1$. Red and white dashed curves correspond to the bands of bottom and top layers of 2SL while the black dashed curves are the AB-BL bands.

This shows that transport channels in the presence of domain walls are experimentally distinguishable.

In Fig. 3.21 we show the conductance in a 2SL-AB system as a function of the bias for transport using a single Fig. 3.21(a) or a double Fig. 3.21(b) mode. The results show that the contribution from the top and bottom layers to the conductances have opposite

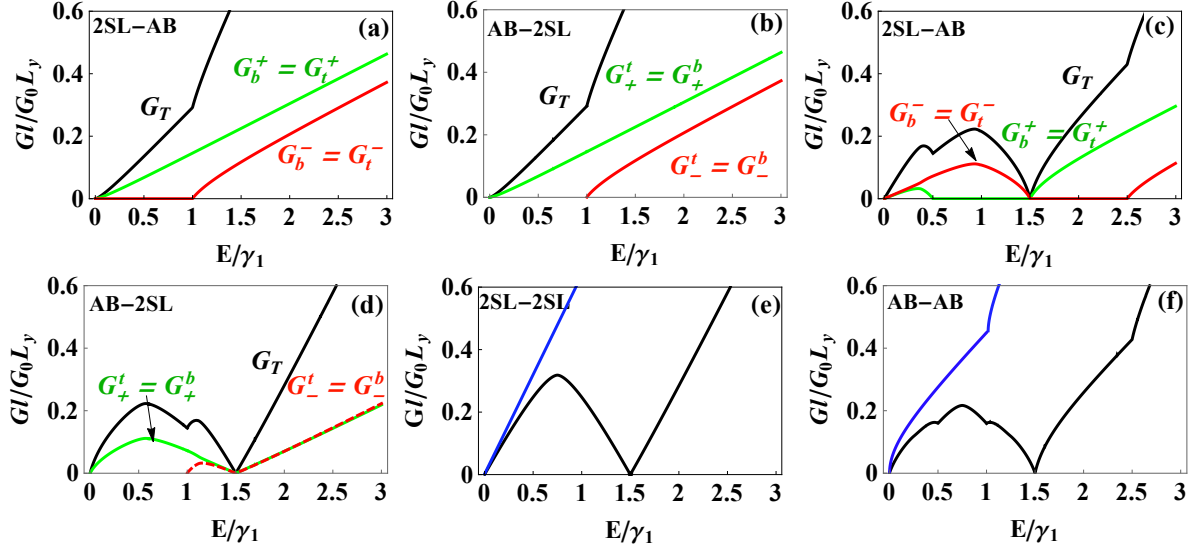


Figure 3.20: (Colour online) Conductance of different junctions for different magnitudes of the applied gate: (a, b) $v_0 = \delta = 0$, (c, d) $v_0 = 3\gamma_1/2$, $\delta = 0$, (e, f) the total conductance for 2SL-2SL and AB-AB junctions, respectively, with $v_0 = 0$ (blue curves) and $v_0 = 1.5\gamma_1$ (black curves).

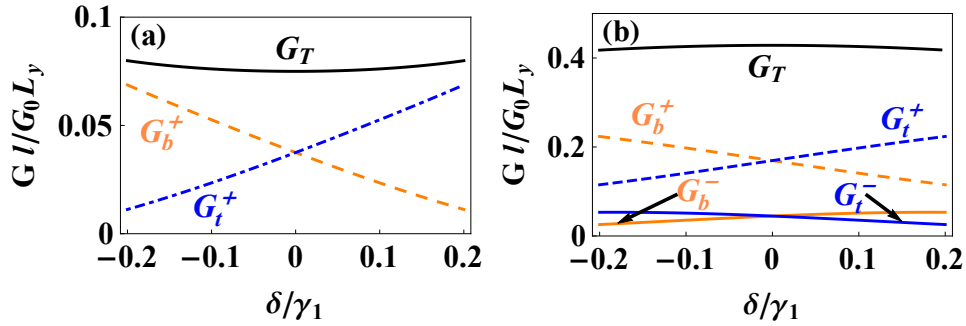


Figure 3.21: (Colour online) Conductance across the 2SL-AB system as a function of the bias on the AB-BL with $v_0 = 0$. (a) and (b) correspond to the single and double modes regime with $E = 0.3\gamma_1$ and $E = 1.15\gamma_1$, respectively, with $G_T^\pm = G_t^\pm + G_b^\pm$.

behaviours as a function of the inter-layer bias. The total conductance G_T , however, has a convex form, increasing with the application of an inter-layer bias. From Fig. 3.21(b), on the other hand, we see that when a second mode is available, four channels contribute to the conductance and the total conductance assumes a concave form, i.e. decreasing with increasing inter-layer bias. This is a characteristic experimental feature that can signal the presence of a second propagation mode.

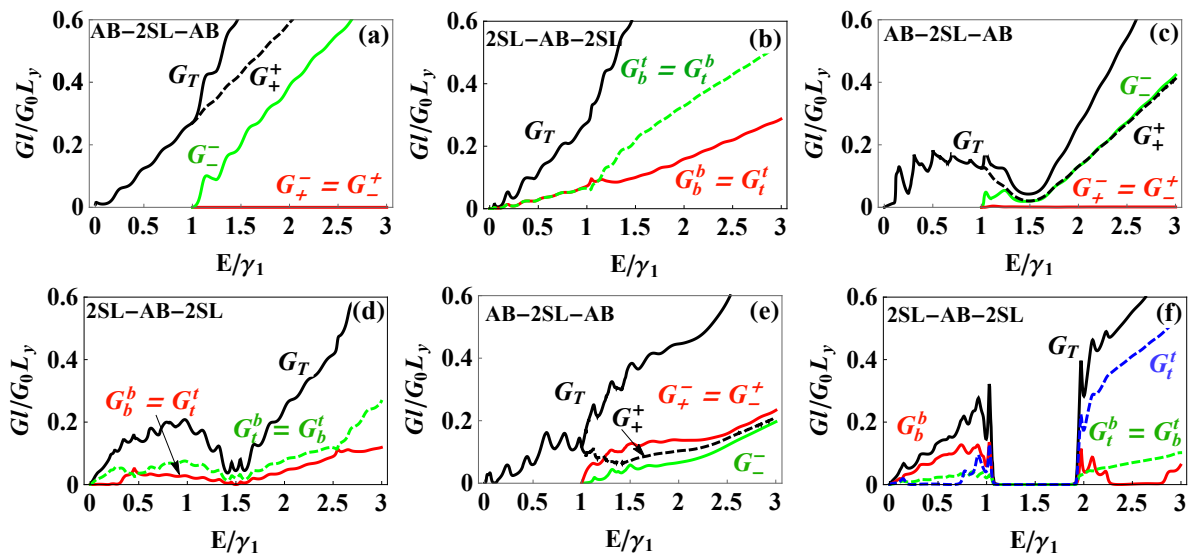


Figure 3.22: (Colour online) Conductance of different junctions for different magnitudes of the applied gate: (a, b) $v_0 = \delta = 0$, (c, d) $v_0 = 3\gamma_1/2$, $\delta = 0$ and (e, f) $v_0 = 3\gamma_1/2$, $\delta = 0.8\gamma_1$.

For the three-block system we show the conductance of the configuration AB-2SL-AB and 2SL-AB-2SL in the left and right columns of Fig. 3.22, respectively. The resulting conductance of the first configuration shows only two non-zero channels G_+^+ and G_-^- , while the scattered ones $G_+^- = G_-^+ = 0$ since $T_+^- = T_-^+ = 0$ (see Fig. 3.22(a)). Furthermore, for low energy $G_T = G_+^+$ since the mode k^- is not available in this regime but it starts conducting when $E > \gamma_1$. The applied electrostatic potential on the 2SL keeps the scattered conductance channels at zero and a minimum in the conductance appears around the shifted Dirac cone $E = v_0$ of the 2SL as depicted in Fig. 3.22(c). As pointed out before, if the Fermi energy approaches the strength of the electrostatic potential, a non-zero minimum is present in the conductance because charge carriers can be transmitted through a width d of 2SL via evanescent modes [95]. In Fig. 3.22(f) this minimum disappears and the conductance dramatically increases at $E = \gamma_1$. This is because the bias will couple the two modes and two additional scattered channels G_+^- and G_-^+ start

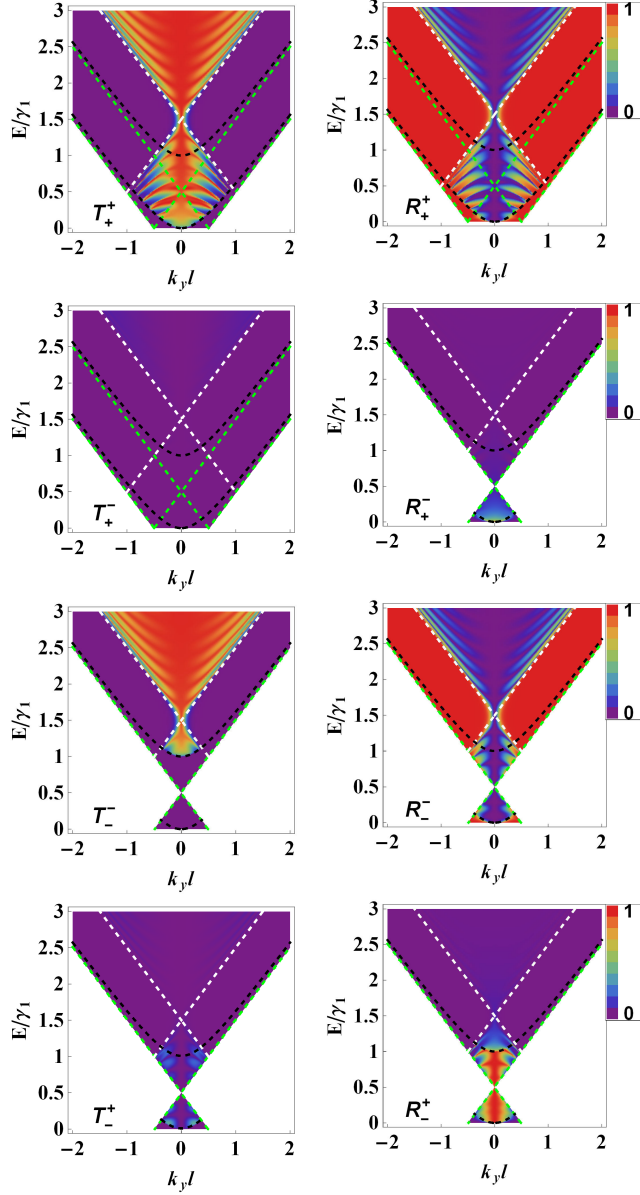


Figure 3.23: (Colour online) Density plot of the transmission and reflection probabilities through AA-2SL-AB junction as a function of Fermi energy and transverse wave vector k_y with $v_0 = 1.5\gamma_1$, $\delta = 0$ and $d = 25\text{nm}$. The superimposed dashed curves represent the bands of AB-BL(black), AA-BL(green) and 2SL (white), with γ_1 being the inter-layer coupling of AB-BL.

conducting. The resonant peaks in the conductance, see Figs. 3.22(a,c,e), are due to the finite size of the intermediate region and hence strictly depend on its width d . On the other hand, the conductance of the configuration 2SL-AB-2SL has different features. In Fig. 3.22(b) the four channels, in contrast to the previous configuration, start conducting

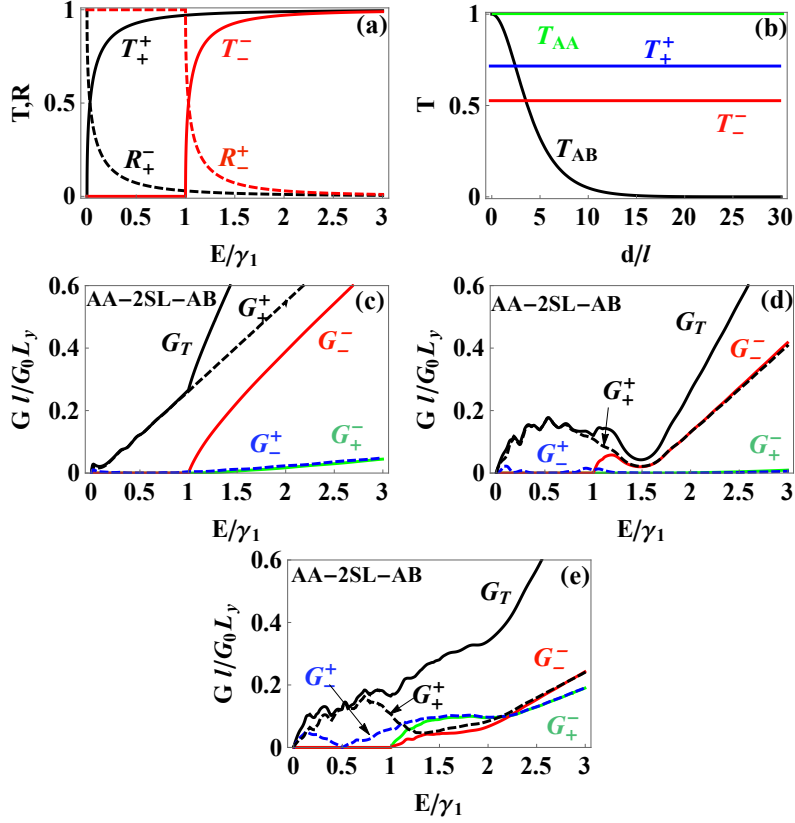


Figure 3.24: (Colour online) (a) Transmission and reflection probabilities for normal incidence for $v_0 = 3\gamma_1/2$, $\delta = 0$. (b) Transmission probabilities with normal incidence for AA-BL (AB-BL) n-p-n junction, green (black) curves. Blue (red) curves are the non-zero channels T_+^+ (T_-^-) in AA-2SL-AB. All energies are considered to be less than the electrostatic potential strength. Conductance of AA-2SL-AB junction for different magnitudes of the applied gate: (c) $v_0 = \delta = 0$, (d) $v_0 = 3\gamma_1/2$, $\delta = 0$, (e) $v_0 = 3\gamma_1/2$, $\delta = 0.6\gamma_1$, with γ_1 being the inter-layer coupling of AB-BL.

from $E = 0$. This possess layer symmetry such that $G_t^t = G_b^b$ and $G_b^t = G_t^b$. Of particular importance is the equivalence of the four channels for $E < \gamma_1$ while for $E > \gamma_1$ charge carriers strongly scatter between the layers (*i.e.* $G_i^j > G_i^i$) as shown in Fig. 3.22(b). This equivalence of the four channels in the regime $E < \gamma_1$ vanishes when an electrostatic potential is applied ($v_0 > 0$) to the intermediate region as seen in Fig. 3.22(d). However, the scattered and non-scattered conducting channels are still equivalent in this case where $G_t^{t(b)} = G_b^{b(t)}$ with $G_i^j > G_i^i$ for all energy ranges, see Fig. 3.22(d).

As discussed before, the most characteristic feature of the inter-layer bias in the AB-BL is the opening of a gap in the energy spectrum between $v_0 \pm \delta$ which is reflected in the conductance as seen in Fig. 3.22(f). The resonant sharp peaks in the conductance near the edges of the gap result from the localized states inside the Mexican hat of the low energy bands. Another consequence of the inter-layer bias is the breaking of the equivalence in the non-scattered conducting channels where now $G_t^t \neq G_b^b$ as seen in Fig. 3.22(f).

3.3.3 AA-2SL-AB junction

Here we consider the case where the leads consist of BL with different stackings separated by two uncoupled graphene sheets. Such a structure can be formed if in the decoupled region one of the graphene sheets has larger lattice constant, e.g. due to strain, leading to an inter-layer shift when the two layers couple.

Notice that the inter-layer coupling strength γ_1 differs for the two bilayer structures. Their ratio is $\gamma_1^{AA}/\gamma_1^{AB} \approx 1/2$ [58, 60, 61]. To account for this difference the energy is normalized to γ_1^{AB} such that the upper Dirac cone of pristine AA-BL is now located at $E = 1/2$ instead of $E = 1$ as in the previous sections. In the junction AA-2SL-AB the charge carriers incident from AA-BL and transmitted through 2SL into AB-BL. The results for the transmission and reflection probabilities of this junction are shown in Fig. 3.23 for $v_0 = 1.5\gamma_1$, $\delta = 0$ and $d = 25$ nm. The carriers incident from lower(k^+)/upper(k^-) Dirac cones in AA-BL can be transmitted into one of the modes (k^+ or k^-) in the AB-BL, see Fig. 3.1(e). On the other hand, the reflection process occurs between the intra- or inter-cone in the AA-BL.

Remarkably, Fig. 3.23 shows that the scattered transmission probabilities are very small and that almost all transmission is carried by the non-scattered channels. This is not immediately expected since a priori the k^+ -mode in AA-BL is not related to the k^+ -mode in AB-BL. However, both modes have the same parity under in-plane inversion, showing that this feature is robust against variations in the inter-layer coupling.

In contrast to the AA-2SL-AA junction where the scattering between lower and upper cones is forbidden in case of zero bias, here the two cones are coupled even without bias. This results in non-zero reflection in the scattered channels R_{\mp}^- and R_{\mp}^+ .

For normal incidence, the scattered transmission (T_{\mp}^- and T_{\mp}^+) and the non-scattered reflection (R_{\mp}^+ and R_{\mp}^-) channels are zero (see Fig. 3.23) because in that case both the AA and AB Hamiltonian are block diagonal in the even and odd modes basis. Now, we can investigate Klein tunnelling when transitioning in-between the two types of stacking. For this, we show the non-zero channels of transmission and reflection for normal incidence in Fig. 3.24(a). We find that in contrast with the AA-2SL-AA case, perfect Klein tunnelling does not occur in the junction AA-2SL-AB. However, as shown in Fig. 3.24(b), we do find that the transmission probability does not depend on the length or even presence of the 2SL region, in contrast to the previous cases with two domain walls.

For $\delta \neq 0$ the coupling between the different modes is strengthened and, hence, strong scattering in the transmission and reflection channels occurs. Furthermore, the symmetry with respect to normal incidence in the reflection and transmission channels is broken.

The conductance for the discussed structure is shown in Figs. 3.24(c, d, e) for $(v_0 = \delta = 0)$, $(v_0 = 1.5\gamma_1, \delta = 0)$ and $(v_0 = 1.5\gamma_1, \delta = 0.6\gamma_1)$, respectively. For pristine 2SL, the dominant channels are G_{\mp}^+ and G_{\mp}^- . Notice that the latter one starts conducting

only when $E > \gamma_1$ and this shows up as a rapid increase in the total conductance G_T at $E = \gamma_1$. The scattered channels G_+^- and G_-^+ are only weakly contributing to the total conductance as a result of weak coupling of the modes. In contrast to the junctions AA(AB)-2SL-AA(AB), in this case the scattered channels of the conductance are not equivalent $G_+^- \neq G_-^+$, see Fig. 3.24(c,d). This is because the scattering occurs between modes in bilayer graphene of different stackings. The electrostatic potential introduces a minimum at $E = v_0$ in the total conductance due to the absence of propagating states at this energy in the 2SL, see Fig. 3.24(d). Biasing the intermediate region (2SL) of the junction AA-2SL-AB provides propagating states at $E = v_0$, and hence removing the minima in G_T as shown in Fig. 3.24(e). In addition, the contribution of the scattered channels G_+^- and G_-^+ becomes more pronounced as a result of the strong coupling between the modes induced by the bias.

Finally, notice that the counterpart junction AB-2SL-AA, represents the time-reversal case of the system discussed above. We have verified that the transmission channels are equivalent in the absence of a bias. In the presence of a bias, the angular symmetry is broken and, consequently, the reversed junction features the opposite angular asymmetry, preserving time-reversal invariance.

In Conclusion, the results presented above reveal that the presence of the local domain wall in bilayer graphene samples change the transport properties significantly. Our results may shed light on the design of electronic devices based on bilayer graphene. Finally, we showed that for a given sample with unknown sizes of local stacking domains, the average inter-layer coupling can be estimated through quantum transport measurements.

CHAPTER 4

GATE TUNABLE LAYER SELECTIVITY OF ELECTRONIC TRANSPORT

¹In the previous chapter we studied the electronic transport of delaminated bilayer graphene structures. For example, we showed that the configuration 2SI-BL-2SL shown in Fig. 3.1(d) has the ability to be used as a beam splitter when the incident energy $E < \gamma_1$. In this chapter we will show the possibility to use such configuration as layer switch and investigate the effect of the domain walls smoothness and the type of stacking on the layer selectivity of the system.

¹*The results of this chapter were published as:*
Hasan M. Abdullah, M. Zarenia, H. Bahlouli, F. M. Peeters and B. Van Duppen, Europhys. Lett. **113**, 17006 (2016).

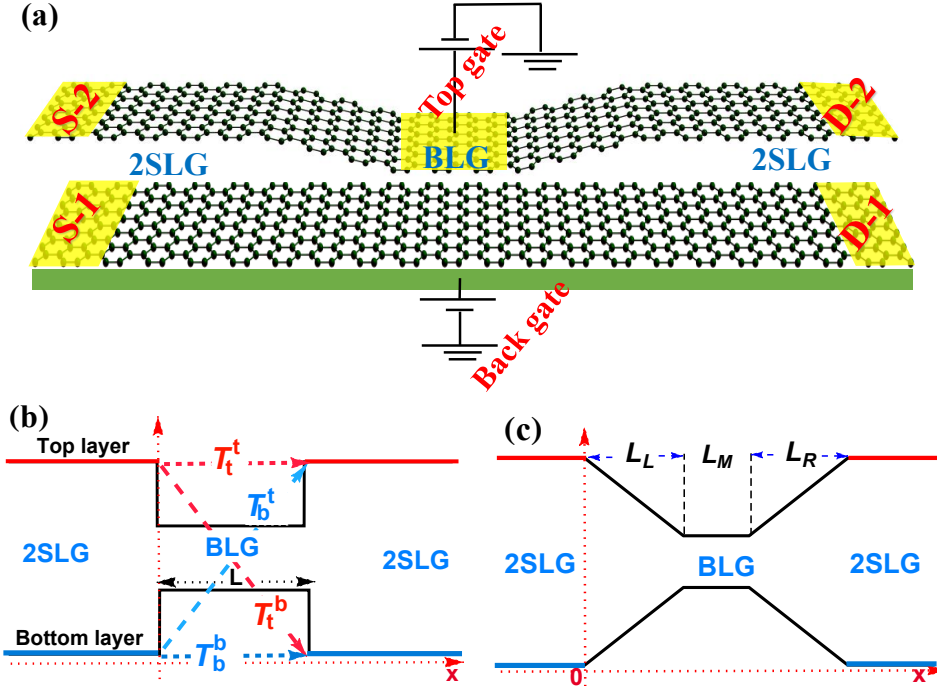


Figure 4.1: (Colour on-line) (a) Schematic presentation of the proposed structure with the indication of the top and back gate, the coupled region (BLG) and the decoupled graphene sheets (2SLG). (b) and (c): cross section of the device with abrupt and smooth transitions from the coupled to the decoupled region respectively. The arrows in (b) indicate the different transmission channels as discussed in the text.

4.1 Layer switch formalism

We model the layer switch as two SLG that are locally joined together by van der Waals forces into an AA- or AB-BLG structure as depicted in Fig. 4.1(a). We consider an abrupt and smooth SLG-BLG interfaces (see Fig. 4.1(b, c)). We describe the dynamics of the carriers in the different regions by the continuum Hamiltonian written in the basis of atomic orbitals $\Psi = (\Psi_1, \Psi_2)^T$ with $\Psi_i = (\Psi_{Ai}, \Psi_{Bi})$ being the SLG spinor. Then the Hamiltonian of the system is the one described in Eq. and can be written as

$$H(\mathbf{r}) = \begin{bmatrix} H_1 & C_{\tau,\zeta}(\mathbf{r}) \\ C_{\tau,\zeta}^\dagger(\mathbf{r}) & H_2 \end{bmatrix}, \quad (4.1)$$

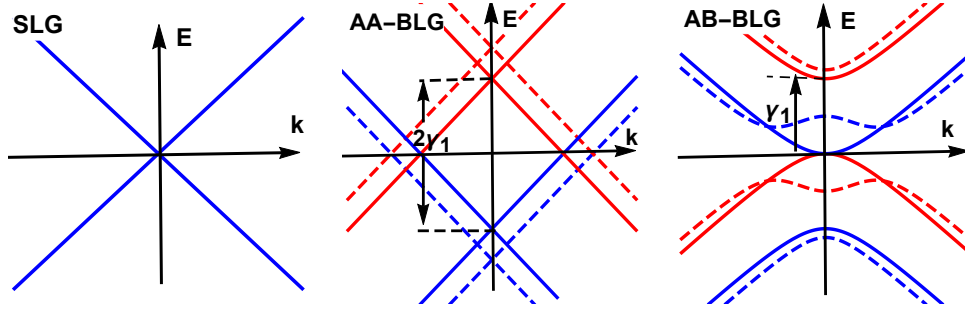


Figure 4.2: (Colour on-line) Band dispersion relations around the Dirac point for single layer graphene (left), AA-stacked (middle) and AB-stacked (right) bilayer graphene. The dashed curves correspond to the spectrum of the system in case of a finite bias, i.e. $\delta \neq 0$.

where $H_i = v_F \vec{\sigma} \cdot \vec{p} + V_i$ is the SLG Hamiltonian with V_i the electrostatic potential on the i -th layer which can be varied by gating the sample with top and back gates as shown in Fig.4.1(a). In Eq. (4.1) $C_{\tau,\zeta}(\mathbf{r})$ is the inter-layer coupling and is defined by

$$C_{\tau,\zeta}(\mathbf{r}) = \begin{bmatrix} \tau\gamma_1(\mathbf{r}) & 0 \\ \zeta\gamma_1(\mathbf{r}) & \tau\gamma_1(\mathbf{r}) \end{bmatrix}, \quad (4.2)$$

where the parameters τ and ζ can model different stacking types by assigning different values to these parameters as discussed in Sec. 3.1.2 . The strength of the interlayer coupling $\gamma_1(\mathbf{r})$ is determined by the distance between both layers. Since the coupling is related to the overlap between the orbital eigenstates of the two carbon atoms right above each other, it decreases exponentially with inter-layer distance. For simplicity, we consider in our model that the interlayer coupling decies linearly through the smooth parts of the system whose widths are L_R, L_L Fig.4.1(c) while in the middle region with width L_M it retains its standard values for stable AB- and AA-BLG as $\gamma_1 = (0.4, 0.2)$ eV, respectively. To remind the reader about differences of these types of stacking we show the energy spectra of SLG and BLG in Fig. 4.2. Note that in Eq. (4.2) we neglected

the skew inter-layer hopping parameters corresponding to the sublattices which are not directly above each other. The final result does not depend strongly on this assumption since these hopping parameters are off diagonal contributions accompanied by a term linear in the momentum [47].

To determine the layer selectivity we first note that translation symmetry in the y -direction implies conservation of k_y . Then we connect the eigenstates of each region defined in Fig. 4.1(b) as “2SLG” for the decoupled single layer and “BLG” for the bilayer regions at the intermediate boundaries by matching each sublattice spinor component with its counterpart in the other region.

The eigenstates in the 2SLG regions consist of a set of oppositely propagating states in each layer separately. This allows us to define a layer resolved current by applying appropriate boundary conditions and identifying the coefficients of each mode with electrons propagating in one of the two SLG layers. In this manner we can calculate the inter- and intra-layer transmission and reflection probabilities as the square of the modulus [90]. The scattering probabilities are denoted by A_t^t or A_b^b for intra-layer transitions and by A_b^t or A_t^b for inter-layer transitions where A stands for transmission T or reflection R . The different transmission channels that are considered in this work are illustrated in Fig. 4.1(b). The number of transmission channels depends on the availability of propagating modes in the BLG part of the device. As can be inferred from the energy spectra depicted in Fig. 4.2, for each energy it is possible to have up to two modes of propagation (indicated in red and blue in Fig. 4.2). Note that for the AA-BLG part there are always two propagating modes, while for AB-BLG it is possible to have none if the energy is in the gap, one if the energy is below the second band (i.e. $E < \gamma_1$) or two if the energy is sufficiently high.

In order to take into account a smooth transition between the 2SLG and BLG regions, we used the transfer matrix approach [90]. This approach subdivides the smooth transition into a series of steps. As we mentioned above, we assume that the inter-layer hopping $\gamma_1(\mathbf{r})$ increases linearly from zero in the SLG region until standard γ_1 in the joined region as shown in Fig. 4.1(c).

We derive the conductance of the sample from the transmission coefficients using the Landauer-Büttiker [92] formula defined by

$$G_{ij}^T = G_0 L_y \sum_{k_y} T_{ij}(k_y), \quad (4.3)$$

where $G_0 = 4e^2/h$ and L_y is the length of the sample in the y -direction. Analogously we can also obtain the reflectance as

$$G_{ij}^R = G_0 L_y \sum_{k_y} R_{ij}(k_y), \quad (4.4)$$

which gives a measure for the amount of current that is reflected at the junction back into the leads where it came from or into the other layer. These quantities can be used to define a measure of layer filtering as follows

$$F_{ij}^A = \frac{G_{ij}^A}{G_{i,\text{tot}}^A}, \quad (4.5)$$

where $G_{i,\text{tot}}^A = G_{it}^A + G_{ib}^A$ such that, for example, F_{bt}^T measures the filtering to the top layer (t) in the transmission channel (T) when the particle was incident in the bottom layer (b).

4.2 Smoothness effect on scattering probabilities

In Fig. 4.3 we show the transmission and reflection probabilities as a function of the Fermi energy at normal incidence for different bias $\delta = (V_1 - V_2)/2$, and potential strength $v_0 = (V_1 + V_2)/2$ for an AB-stacked junction region. In Figs. 4.3 (a - d) the structure is ungated ($v_0 = 0$) and unbiased ($\delta = 0$) with solid (dashed) lines for abrupt (smoothed) interface. T_{bb} and T_{tb} are equal for energies less than the inter-layer hopping γ_1 . In contrast, for $E \gtrsim \gamma_1$, the electrons strongly scatter from the top (bottom) layer on the left lead into the bottom (top) layer on the right. This difference is due to the presence of two possible transmission channels in BLG while only one channel exists for $E < \gamma_1$. On the other hand, the reflection probability shows no layer selectivity except for $E = 0$ where electrons completely reflect into the same layer. This is because at this energy there are no available propagating states in BLG.

Applying an electric field on BLG ($v_0 > 0$) will shift the energy spectrum and affect the transmission probability as shown in Figs. 4.3(e, f). The high selectivity or strong scattering between the layers is preserved in the region where the two channels are available, i.e. in the energy intervals $0 < E < v_0 - \gamma_1$ and $E > v_0 + \gamma_1$. Similarly, the reflection probability here has no significant selectivity and the strong reflection in R_{bb} channel is shifted by v_0 since it occurs now at $E = v_0$.

In the case when BLG is biased ($\delta > 0$) and gated ($v_0 > 0$), the band gap induced by the inter-layer bias suppresses the transmission in the energy region between $v_0 \pm \delta$, as seen in Figs. 4.3(g, h). Moreover, $T_b^b(R_b^b)$ and $T_t^t(R_t^t)$ are almost the same, except in the region where there is only one channel in the BLG region. However, $T_b^t = T_t^b$ for all energies, which is a manifestation of a breaking of the inter-layer sublattice equivalence.

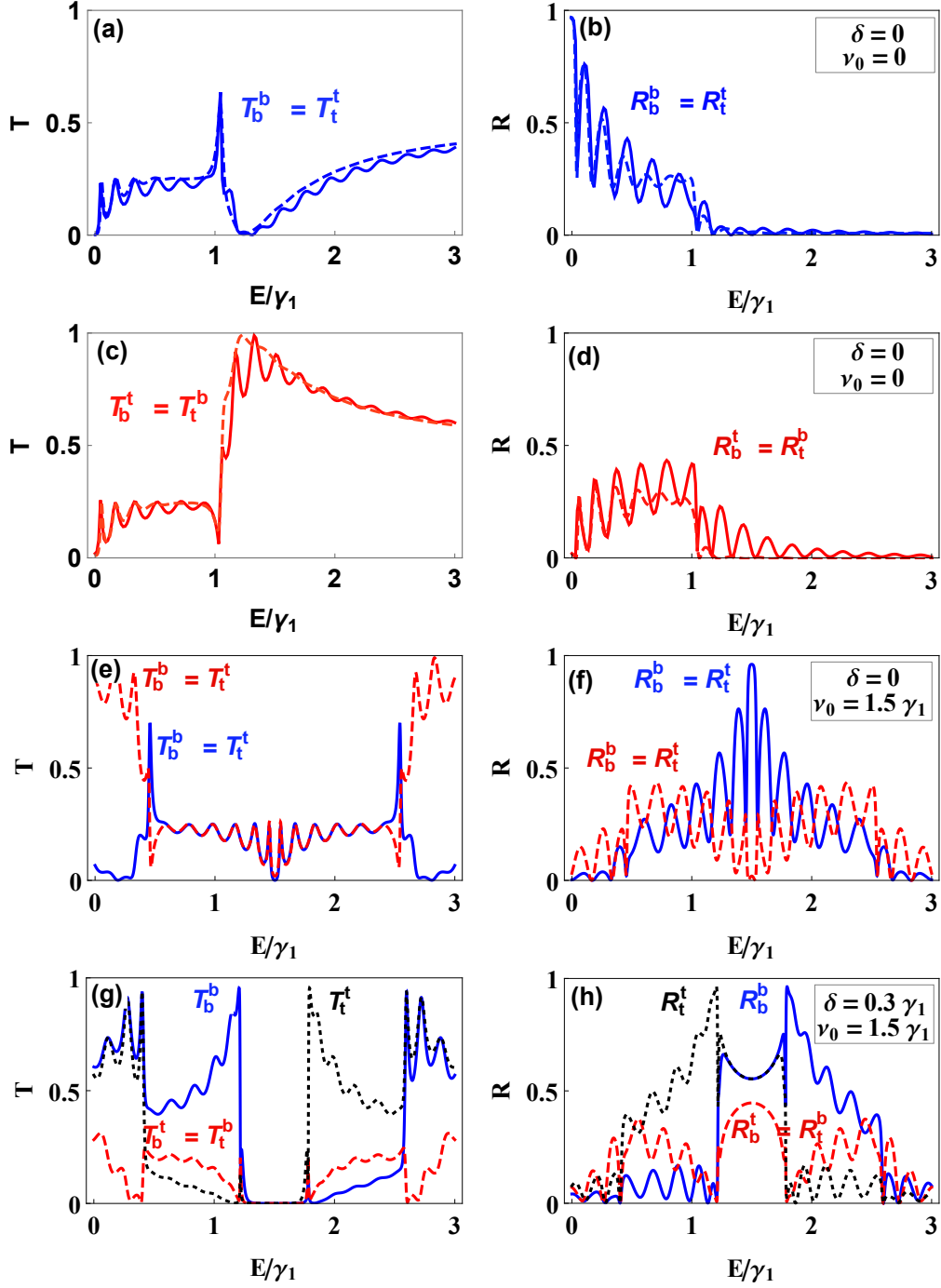


Figure 4.3: (Colour on-line) Transmission and reflection probabilities at normal incidence as a function of the Fermi energy, through 2SLG-AB-2SLG structure. (a, b) and (c, d) for the non scattered and scattered channels with $\delta = v_0 = 0$, respectively, solid (dashed) lines for abrupt(smoothed) structure with $L = 25$ nm, $L_L = L_R = 5$ nm and $L_M = 20$ nm, (see Fig. 4.1 (c)). For only abrupt structure with $v_0 = 3\gamma_1/2$, (e, f) and (g, h) for $\delta = 0, 0.3\gamma_1$, respectively.

Due to the finite size of the interaction region, the propagating mode in the BLG region interferes with itself resulting in oscillations of the transmission probabilities, see Figs. 4.3(a, c). These so-called Fabry-Pérot resonances appear at energies quantized as [?]

$$E_{BLG}^n = \frac{1}{2} \left(-1 \pm \sqrt{1 + 4l^2 \left(\frac{n\pi}{L} \right)^2} \right), \quad (4.6)$$

with $l = \frac{\hbar v_F}{\gamma_1} \approx 1.7\text{nm}$ (AB-stacking) and $l \approx 3.3\text{nm}$ (AA-stacking) is the inter-layer coupling length.

The effect of smoothing the SLG-BLG interface on the transmission and reflection probabilities is shown in Figs. 4.3. In this figure we show the non-scattered and scattered channels in Fig. 4.3(a, b) and (c, d), respectively, for abrupt (solid curves) and smoothed (dashed curves) structures. Our results show that the only effect of the smoothness is to remove the oscillations in the transmission and reflection probabilities. However, the qualitative and quantitative behaviour of the transmission and reflection coefficients is preserved and the selectivity is not significantly influenced by the smoothness.

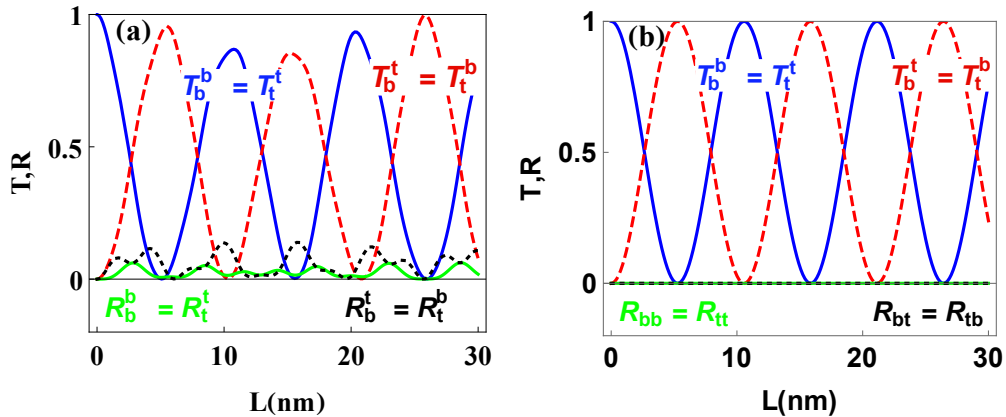


Figure 4.4: (Colour on-line) Transmission and reflection probabilities at normal incidence as a function of the bilayer width L for $\delta = v_0 = 0$. (a) for AB-stacking with $E = 3\gamma_1/2$ and (b) for AA-stacking with $E = 3\gamma_1/2$.

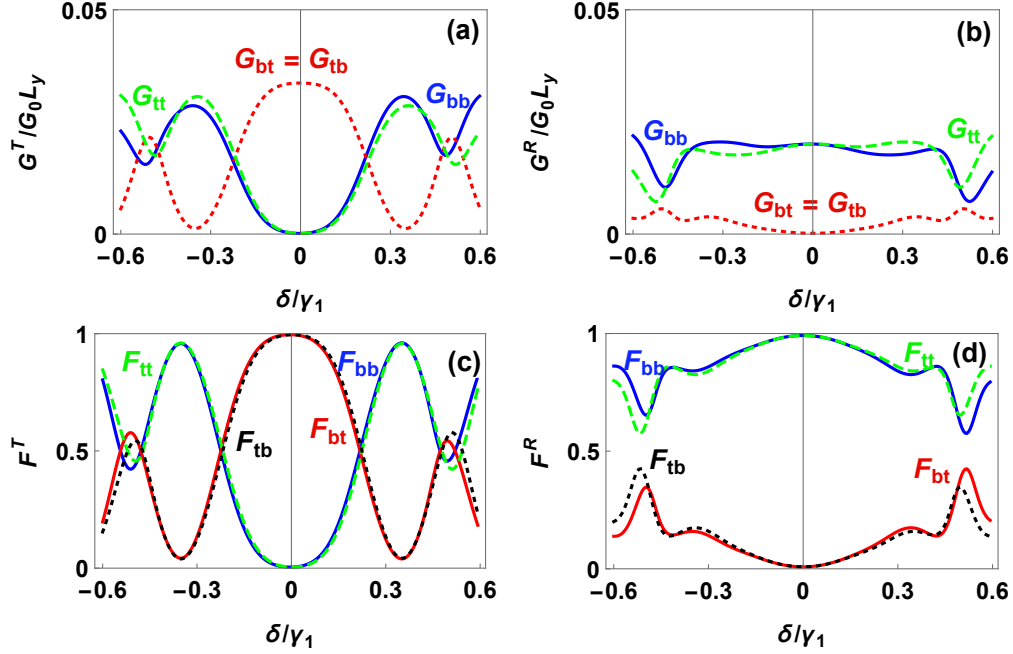


Figure 4.5: (Colour on-line) Conductance and reflectance along with their associated layer filtering as a function of the bias through a 2SLG-AB-2SLG structure for $E = 0.3\gamma_1$ and $v_0 = 1.8\gamma_1$ and $L = 25.8$ nm. (a) and (b) conductance and reflectance; (c) and (d) the corresponding layer filtering, respectively.

Fig. 4.4 shows the AB-BLG (left panel) and AA-BLG (right panel) width dependence of the transmission and reflection probabilities for normal incidence. For both types of stacking, T_t^t and T_b^b are equal and oscillate with the width of the BLG, while the transmission $T_b^t = T_t^b$ oscillates out of phase. This behaviour is due to the interference of the two propagating modes in BLG, but for AB-BLG this will not hold for $E \lesssim \gamma_1$, because there is only one propagating mode in this case. On the other hand, the reflection probabilities for AA-stacking are zero for the whole range of L , which is due to Klein tunnelling, while for AB-stacking we still have partial reflection. The location of the resonances in T_b^b (T_t^t) for AA and AB stacking are given by [52]

$$L_m = \xi\pi l (m + \eta) \quad (4.7)$$

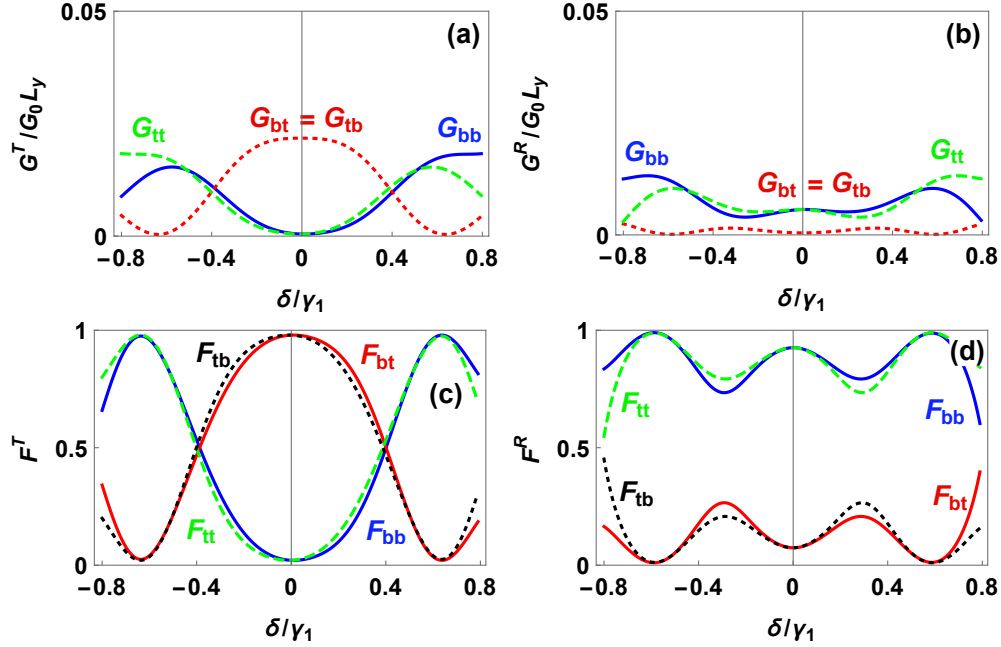


Figure 4.6: (Colour on-line) Conductance and reflectance along with their associated layer filtering as a function of the bias through 2SLG-AA-2SLG structure for $E = 0.3\gamma_1$ and $v_0 = 1.8\gamma_1$ and $L = 26.4$ nm. (a) and (b) conductance and reflectance, (c) and (d) the corresponding layer filtering, respectively.

with m an integer, $\xi = 1$ for AA-stacking and $\xi = 2$ for AB-stacking and $\eta = 0, \frac{1}{2}$ for T_b^b and T_b^t , respectively. The different value for ξ is due to the fact that when the crystal is AB-stacked only half of the atoms contribute in the inter-layer coupling while all atoms participate in AA-stacking.

The layer filtering can be controlled by applying an electric field which shifts the potential of the total structure by an amount $v_0 > 0$ and applies a finite potential difference between the layers $\delta > 0$.

4.3 Layer selectivity

In Fig. 4.5 we present the conductance and reflectance with the corresponding layer filtering as a function of bias for AB-BLG. The conductance shows a certain complementarity:

the maxima in the G_{bb}^T (G_{tt}^T) coincide with the minima in G_{bt}^T (G_{tb}^T) as seen in Fig. 4.5(a). This behaviour clearly shows up in the layer filtering as shown in Fig. 4.5(c), where for $\delta \approx -0.35\gamma_1$ the particle is incident on the bottom layer and then is transmitted into the same layer, resulting in $F_{bb}^T \approx 1$. While for $\delta = 0$ we find that $F_{bt}^T = 1$, which means that the particle is incident on the bottom layer and is then transmitted into the top layer on the other side of the junction. This result demonstrates that the structure under consideration has a gate tunable layer selectivity and that it can act as a layer switch. Indeed, by tuning the voltage across the joined region, one can switch the transmitted current between the two layers.

The reflectance with the corresponding layer filtering is shown in Figs. 4.5(b, d), respectively. We see small oscillations in G_{bb}^R (G_{tt}^R) which are out of phase compared to G_{bt}^R (G_{tb}^R) with weak current flow. The results show that also the reflection can be tuned by changing the bias potential δ , but not with the strong selectivity that is possible in the transmission channel.

Also for the AA-stacked variant the scattered and non scattered conductances are exactly out of phase as shown in Fig. 4.6(a). The layer filtering is nearly perfect for $\delta \approx \pm 0.63 \gamma_1$ with $F_{bb}^T \approx 1$ and $F_{bt}^T \approx 0$, whereas at $\delta \approx 0$ the particles are completely scattered between the layers with $F_{bt}^T \approx 1$ and $F_{bb}^T \approx 0$ as shown in Fig. 4.6 (c). The same analogy here applies to the reflectance and the associated layer filtering as shown in Figs. 4.6(b, d).

Finally, we can say that we perform our calculation for abrupt and smooth SLG-BLG interfaces and showed that these types of interfaces show no quantitative or qualitative differences. This reveals that the switching effect is robust against the smoothing of the

SLG-BLG junction. In addition, we found that the type of stacking configuration strongly influences the layer selectivity of the system.

CHAPTER 5

CONFINEMENT IN GRAPHENE QUANTUM BLISTERS

¹The previous chapters we focused on studying the transport properties and layer filtering across Van der Waals domain walls in bilayer graphene. This chapter is devoted to investigation confinement in delaminated bilayer graphene. Ever since the discovery of graphene, researchers have tried to confine electrons in graphene-based quantum dots (QDs) [101, 102]. Quantum dots are very interesting because of the vast range of new applications in for instance electronic circuitry [103, 104], photovoltaics [105], qubits [106], and gas sensing [107]. The use of graphene as a basis for these quantum dots could enable fast and flexible quantum computing devices. On a more fundamental level, the gapless band structure of graphene has made researchers wonder how the electron and hole states in such zero-dimensional quantum system would interact with each other and how the ultra-relativistic nature of graphene charge carriers would respond to confinement

¹*The results of this chapter were published as:*

H.M. Abdullah, M. Van der Donck, H. Bahlouli, F. M. Peeters and B. Van Duppen, *Appl. Phys. Lett.* **112**, 213101 (2018).
Hasan M. Abdullah, H. Bahlouli, F. M. Peeters and B. Van Duppen, *J. Phys.: Condens. Matter* **30**, 385301 (2018).

[108–110]. It is, however, exactly this peculiar nature of the charge carriers that prohibits the use of traditional QD fabrication techniques such as local electrostatic gating [111,112]. Indeed, because of the Klein tunnelling effect [14,63], electrons will use hole states in the gated region to escape confinement. The graphene quantum blister (GQB), proposed in this Article, overcomes these limitations and acts as a tunable graphene quantum dot that still harnesses the peculiar electric properties of graphene charge carriers.

There have been many different propositions to confine Dirac fermions in graphene quantum dots such as combining electrostatic gates with a magnetic field [108,113–117], cutting a graphene flake into small nanostructures [118–122], and introducing a gap induced by the substrate [111,123]. However, magnetic fields tend to bring along many difficulties in nanostructured systems [124–126], QDs made in nanostructures are highly sensitive to the precise form of the edge which is hard to control [117], and the band gap produced in graphene by a substrate is very difficult to control which makes it far from ideal in applications [127–133]. These difficulties have significantly limited experimental realization of graphene QDs and hence hindering their possible applications.

However, this has not withheld researchers from trying to apply extreme external conditions. Under high magnetic field [134] or supercritical charges [135] confinement was realized but only quasi-bound states with a relatively short life time [136] were observed. Recently, a few experiments [137–142] were conducted to detect quasi-bound states in single layer graphene by using advanced substrate engineering and the incorporation of an electrostatic potential induced by the tip of the scanning tunneling electron microscope (STM). There is only one recent experiment [143] that realized bound states with a longer lifetime in a QD in a graphene sheet through a strong coupling between the graphene sheet

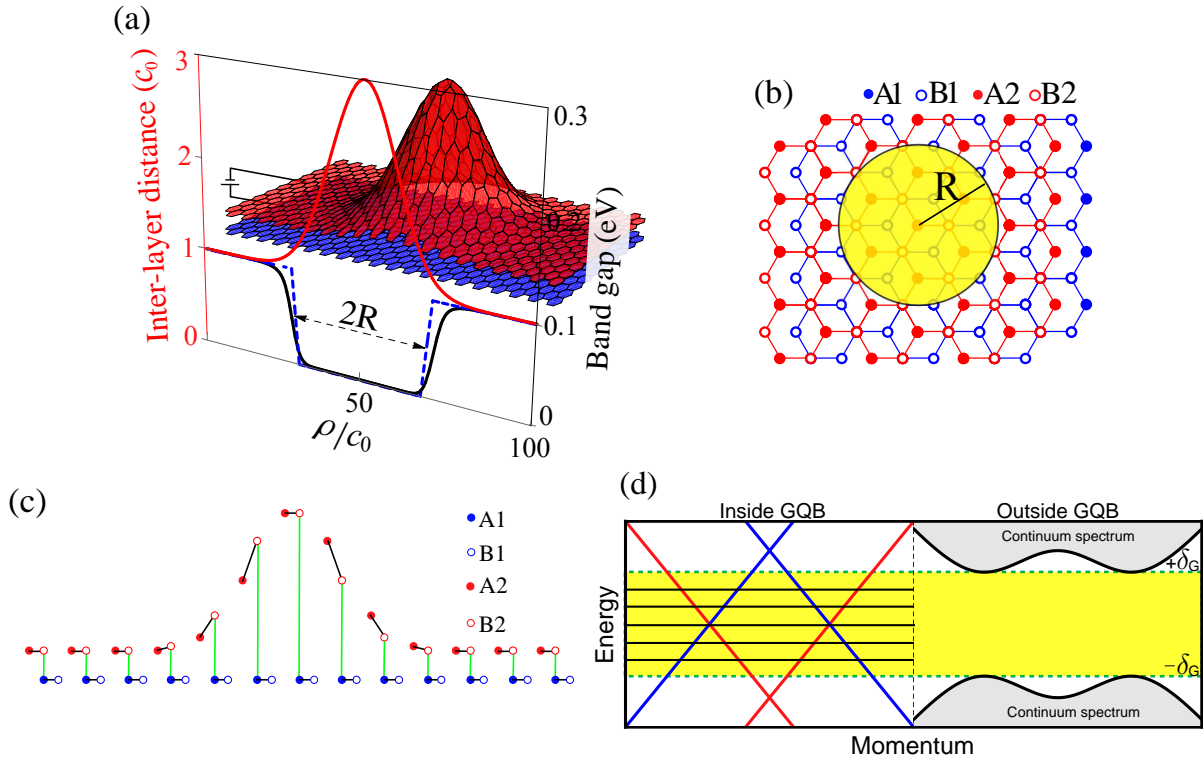


Figure 5.1: (Color online) (a) Schematic representation of the structure of a circular GQB with radius R . The graph shows the inter-layer distance (red) and the local band gap (black) when a global bias $\delta = 0.12$ eV is applied. The dashed blue curve corresponds to the approximate band gap profile with an abrupt change at the interface R of the GQB. (b) Top view of the two layer outside the blister placed in AB-stacking. (c) Schematic representation of a cross section of the GQB depicting the position of the different atoms in the unit cell. The black lines denote the π orbitals while the vertical green lines represent the inter-layer coupling. Notice that for illustrative reasons only a small number of atoms are shown. The discussed GQBs in this study typically have radii of several hundreds of atoms or tens of nanometers. (d) Energy spectrum inside (left) and outside (right) the GQB. Red and blue bands in left panel correspond to top and bottom layers while the horizontal black lines in the left figure represent the discrete energy levels that occur due to confinement. These states are only allowed in the range $E < |\delta_G|$ as delimited by the yellow region. The solid black curves in the right figure denote the edge of the continuum spectrum outside the GQB.

and the substrate. However, the realized bound states in such systems are only externally tunable through careful controlling of the distance between the sample and the STM tip.

An alternative way is to use bilayer graphene as a basis to make a QD [144–146].

For these systems the electronic energy spectrum is parabolic instead of linear as is the

case in single layer graphene, and can be gapped by applying a potential bias to the two layers [57]. By nano-engineering electrostatic gates such that the bilayer graphene spectrum is gapped everywhere except in a locally defined region, charge carriers can indeed be confined [145]. However, in practice it is challenging to engineer the gates such that the bias profile has the desired shape and the resulting confined electron states lose their interesting ultra-relativistic character.

Recently, delaminated bilayer graphene attracted attention because it can provide well-defined one-dimensional channels and exhibit layer selectivity in transport [62, 147–149]. Such structures have been experimentally observed in mechanically exfoliated graphene samples [78, 88]. GQBs are based on delaminated bilayer graphene, but here the delamination is concentrated in a circular region. By application of a global bias gate, states are trapped in this region and retain the interesting graphene-like characteristics.

The proposed GQB supports bound states and overcomes the above mentioned limitations. It is free of magnetic fields, relatively easy to manufacture without losing graphene's quality. Finally GQBs also allow external tunability of the electronic spectrum by application of a simple global gate [48, 150] and one can even control the layer localization of the confined states themselves.

5.1 Graphene quantum blisters

A GQB can be made from Bernal bilayer graphene by locally deforming the upper layer, hence creating a blister in the top layer as shown in Fig. 5.1. Its electronic spectrum can be probed using STM [151], but in contrast to other experiments the electric field

of the STM tip is not necessary to confine electrons [137, 138, 142]. As a result of the deformation, the inter-layer coupling strength γ_1 is strongly reduced and practically zero inside the blister. Therefore, the charge carriers have a degenerate linear energy spectrum inside the blister as they belong to independent layers. Outside the blister, however, the two layers are coupled in a Bernal bilayer structure [57] and have the characteristics of a parabolic energy spectrum. By applying a global gate that induces a potential difference between top and bottom layer, a gap can be opened outside the GQB but inside the blister the linear energy spectrum of the two separate layers is only shifted up and down in energy, allowing states for energies in the bilayer gap. These states are bound in the GQB as shown in Fig. 5.1(c). Since they cannot exist anywhere except in the GQB, the life time of the state diverges and we, therefore, have real bound states.

In order to create the blister structure described in the previous paragraph, one could follow several routes. This first one uses the local separation of two graphene layers that is found in several samples [76, 77, 83, 86, 152]. By applying a global gate to these of nanostructures, states will confine inside the blister. A second route follows a deliberate introduction atoms in-between two graphene layers with, for example, intercalation techniques [153–160]. A final route could consist of using graphene samples that are decorated with nanoclusters as a basis material during growth of bilayer graphene. It was shown that current techniques can precisely control over the size and content of these clusters [161]. It is, therefore, expected that by following this technique, we could also precisely control the radius of the GQBs that are made in this way. Creating GQBs as such remains an open quest, but a major advantage of using nanoclusters is that the material type also influences the electronic properties of the confined modes. For example if the nanoclusters

are metallic, an dipole will be induced in the nanocluster, which in its turn influences the electric potential felt by the states in a specific and material-dependent way.

5.2 Theoretical aspects of GQB

5.2.1 Electrons in GQB

In Figs. 5.1(a, b) we show schematically the atomic structure of a circular GQB with radius R . The continuum limit is valid if the size of the GQB is much larger than the inter-atomic distance, then one can describe charge carriers by a 4×4 tight-binding Hamiltonian written in an arbitrary basis of orbital eigenfunctions of the four atoms making up the crystallographic unit cell of bilayer graphene [57]. The labelling of the different atoms and the direct interlayer coupling are illustrated in Fig. 5.1(b, c). In the basis $\Psi = (\Psi_{A1}, \Psi_{B1}, \Psi_{B2}, \Psi_{A2})^T$, the Hamiltonian in position representation in valley K^τ reads [95, 162–164]

$$\hat{H}(\mathbf{r}) = \begin{pmatrix} \delta(\mathbf{r}) & v_F \hat{\pi}_+ & \xi \gamma_1(\mathbf{r}) & 0 \\ v_F \hat{\pi}_- & \delta(\mathbf{r}) & 0 & 0 \\ \xi \gamma_1(\mathbf{r}) & 0 & -\delta(\mathbf{r}) & v_F \hat{\pi}_- \\ 0 & 0 & v_F \hat{\pi}_+ & -\delta(\mathbf{r}) \end{pmatrix}, \quad (5.1)$$

In Eq. (5.1), $\hat{\pi}_\pm = \hat{p}_x \pm i\hat{p}_y$ is the canonical momentum, which in polar coordinates become [120]

$$\hat{\pi}_\pm^\tau = \frac{\hbar}{i} e^{\pm i\tau\phi} \left[\frac{\partial}{\partial \rho} \pm \frac{i\tau}{\rho} \frac{\partial}{\partial \phi} \right]. \quad (5.2)$$

In Eq. (5.1) the parameter $\xi = (0, 1)$ defines the system inside and outside the GQB, which stands for two decoupled graphene sheets and AB-stacked bilayer graphene, respectively.

5.2.2 Inter-layer coupling in a GQB

In Eq. (5.1) the function $\gamma_1(\mathbf{r})$ describes the coupling between the *A1* and *B2* atoms in each layer and together with $\delta(\mathbf{r})$ determine the band gap throughout the device.. If we consider the GQB as in Fig. 5.1(a) where one of the layers departs from the other one in the form of a Gaussian dome, one can describe the inter-layer distance $c(\mathbf{r})$ is given by

$$c(\mathbf{r}) = c_M \exp\left(-4\frac{\rho^2}{R_{\text{QB}}^2}\right), \quad (5.3)$$

where c_M is the inter-layer distance at the top of the blister, R_{QB} is the radius of the blister and ρ is the radial component. Because the inter-layer coupling strength $\gamma_1(\mathbf{r})$ arises from the overlap of two orbital eigenfunctions in the tight-binding formalism, its value decreases exponentially with increasing inter-layer distance. Following standard practice [69, 71, 73], we can write the inter-layer coupling function as

$$\gamma_1(\mathbf{r}) = \gamma_1^0 \exp\left(-\beta\frac{c(\mathbf{r}) - c_0}{c_0}\right). \quad (5.4)$$

In Eq. (5.4) we have introduced $c_0 \sim 0.33$ nm the equilibrium inter-layer distance and $\gamma_1^0 = 0.38$ eV [58, 60, 61] the equilibrium inter-layer coupling. The quantity β/c_0 is the inverse inter-layer coupling decay length. For the calculations in this paper we choose $\beta \sim 13.3$, as was used before to match with the values for the skew hopping parameters in twisted bilayer graphene [73]. However, this value can be even larger when the blister

is formed by insertion of nanoclusters in-between two graphene layers as these clusters screen the van der Waals interaction between the layers.

By plugging Eq. (5.3) into Eq. (5.4), one can calculate the radial dependence of the inter-layer coupling for a GQB.

In Fig. 5.1(a) we show the band gap in the GQB as a function of the distance to the center of a gaussian GQB. The result shows that the gap vanishes inside the blister and then increases very sharply at the edge of the GQB. This defines a sharp transition in the energy gap inside and outside the blister.

5.2.3 Electronic confinement

In left and right panels of Fig. 5.1(d) we show the energy spectra, respectively, inside and outside the GQB under the application of a finite inter-layer bias $\delta(\mathbf{r})$. Because of the lack of inter-layer coupling the energy spectrum is linear and gapless inside the GQB. The application of a different potential to both layers, therefore, shifts the Dirac point in energy. As a result, for every energy there are electron or hole states available. Outside the GQB, right panel of Fig. 5.1(d) shows that the situation is substantially different. Because here the inter-layer coupling is strong, the inter-layer bias $\delta(\mathbf{r})$ opens up a gap in the energy spectrum. In this region, only evanescent states are allowed and, therefore, the energy spectrum inside the GQB will be discrete and the corresponding modes are confined. The energy range where confinement appears is given by the range $[-\delta_G(\mathbf{r}), \delta_G(\mathbf{r})]$, where $\delta_G(\mathbf{r})$ is related to the inter-layer bias as [165]

$$\delta_G(\mathbf{r}) = \delta(\mathbf{r}) \left(1 + 4 \frac{\delta^2(\mathbf{r})}{\gamma_1^2(\mathbf{r})} \right)^{-1/2}. \quad (5.5)$$

In the following section we calculate the energy spectrum and wavefunctions of the confined states in a GQB assuming that the inter-layer coupling, and thus the band gap, profile has an abrupt transition at position $\rho = R$ as shown in Fig. 5.1(a) by the dashed-blue line. For this, we first need to obtain the wavefunctions inside and outside the GQB and require continuity for each of the spinor components at the interface $\rho = R$ to find the energy eigenstates of the GQB in the presence of an inter-layer bias [111, 166]. In all calculations and results, the energy is scaled with the equilibrium inter-layer hopping parameter, γ_1^0 , while $l = \hbar v_F / \gamma_1^0 \sim 1.65$ nm is the measure for the length scales.

5.2.4 Wavefunctions outside the GQB

In order to obtain the wavefunction outside the GQB, we solve the Schrödinger equation $\hat{H}^\tau(\mathbf{r})\Phi^\tau(\mathbf{r}) = \epsilon\Phi^\tau(\mathbf{r})$ for the Hamiltonian given in Eq. (5.1) with $\gamma_1(\mathbf{r}) = \gamma_1^0$. The equation for the angle $\phi(\mathbf{r})$ directly yields a relation between the phases of each spinor component. This means that the four-component wave function $\Phi^\tau(\mathbf{r})$ in the τ valley can be written as [120]

$$\Phi^\tau(\mathbf{r}) = \begin{pmatrix} \phi_{A1}^\tau(\rho)e^{im\phi} \\ i\phi_{B1}^\tau(\rho)e^{i(m-\tau)\phi} \\ \phi_{B2}^\tau(\rho)e^{im\phi} \\ i\phi_{A2}^\tau(\rho)e^{i(m+\tau)\phi} \end{pmatrix}. \quad (5.6)$$

Solving the Schrödinger equation for the radial functions $\phi_i^\tau(\rho)$, we obtain the following set of coupled equations:

$$\left[\frac{d}{d\rho} - \frac{(\tau m - 1)}{\rho} \right] \phi_{B1}^\tau = (\epsilon - \tau\delta)\phi_{A1}^\tau - \phi_{B2}^\tau, \quad (5.7a)$$

$$\left[\frac{d}{d\rho} + \frac{\tau m}{\rho} \right] \phi_{A1}^\tau = -(\epsilon - \tau\delta)\phi_{B1}^\tau, \quad (5.7b)$$

$$\left[\frac{d}{d\rho} + \frac{(\tau m + 1)}{\rho} \right] \phi_{A2}^\tau = (\epsilon + \tau\delta)\phi_{B2}^\tau - \phi_{A1}^\tau, \quad (5.7c)$$

$$\left[\frac{d}{d\rho} - \frac{\tau m}{\rho} \right] \phi_{B2}^\tau = -(\epsilon + \tau\delta)\phi_{A2}^\tau. \quad (5.7d)$$

We remind the reader that in this set of equations, the energetic quantities are scaled with γ_1^0 and the radial component ρ by l , yielding dimensionless equations. The set of first-order differential equations can be written as a single fourth-order differential equation. As explained previously [166], this fourth-order differential equation has two sets of orthogonal solutions given by the solutions of the following second-order differential equations:

$$\left[\frac{d^2}{d\rho^2} + \frac{1}{\rho} \frac{d}{d\rho} - \left(\frac{m^2}{\rho^2} + \alpha_\pm^2 \right) \right] \phi_{A1}^\tau(\rho) = 0. \quad (5.8)$$

The two equations only differ by the value of

$$\alpha_\pm^2 = -(\epsilon^2 + \delta^2) \pm \sqrt{(\epsilon^2 - \delta^2) + 4\epsilon^2\delta^2}. \quad (5.9)$$

In the energy range where confinement is expected, the square root of Eq. (5.9) is imaginary. As a consequence, the solutions to Eq. (5.8) are Bessel functions with a complex argument [167]. Because we are outside of the GQB, the spinor components need to be finite in the limit $\rho \rightarrow \infty$, so we choose the modified Bessel function of the second kind

$K_m(\alpha_{\pm}\rho)$ as solutions. Finally, notice that $\alpha_+ = \alpha_-^*$, such that the two independent solutions of Eq. (5.8) can be written as a superposition of the real and imaginary part of $K_m(\alpha_{\pm}\rho)$, and we have

$$\phi_{A1}^{\tau}(\rho) = C_1^{\tau} \Re [K_m(\alpha_+\rho)] + C_2^{\tau} \Im [K_m(\alpha_-\rho)], \quad (5.10)$$

Using Eqs.(5.7a-5.7d) we can obtain the other components explicitly as

$$\phi_{B1}^{\tau}(\rho) = \frac{1}{(\epsilon - \tau\delta)} (C_1^{\tau} \Re [\alpha_+ K_{m-\tau}(\alpha_+\rho)] + C_2^{\tau} \Im [\alpha_- K_{m-\tau}(\alpha_-\rho)]) , \quad (5.11a)$$

$$\phi_{B2}^{\tau}(\rho) = \frac{1}{(\epsilon - \tau\delta)} (C_1^{\tau} \Re [\eta^+ K_m(\alpha_+\rho)] + C_2^{\tau} \Im [\eta^- K_m(\alpha_-\rho)]) , \quad (5.11b)$$

$$\phi_{A2}^{\tau}(\rho) = \frac{1}{(\epsilon^2 - \delta^2)} (C_1^{\tau} \Re [\eta^+ \alpha_+ K_{m+\tau}(\alpha_+\rho)] + C_2^{\tau} \Im [\eta^- \alpha_- K_{m+\tau}(\alpha_-\rho)]) . \quad (5.11c)$$

In these equations, we have introduced the compact notation $\eta^{\pm} = \alpha_{\pm}^2 + (\epsilon - \tau\delta)^2$.

5.2.5 Wavefunctions inside the GQB

Inside the GQB the inter-layer coupling vanishes and, therefore, in Eq. (5.1) we have to put $\gamma_1(\mathbf{r}) = 0$. Although the angular solution of the Schrödinger equation stays the same

as in Eq. (5.6), the set of radial equations changes to

$$\left[\frac{d}{d\rho} - \frac{(\tau m - 1)}{\rho} \right] \phi_{B1}^\tau = (\epsilon - \tau\delta)\phi_{A1}^\tau , \quad (5.12a)$$

$$\left[\frac{d}{d\rho} + \frac{\tau m}{\rho} \right] \phi_{A1}^\tau = -(\epsilon - \tau\delta)\phi_{B1}^\tau , \quad (5.12b)$$

$$\left[\frac{d}{d\rho} + \frac{(\tau m + 1)}{\rho} \right] \phi_{A2}^\tau = (\epsilon + \tau\delta)\phi_{B2}^\tau , \quad (5.12c)$$

$$\left[\frac{d}{d\rho} - \frac{\tau m}{\rho} \right] \phi_{B2}^\tau = -(\epsilon + \tau\delta)\phi_{A2}^\tau . \quad (5.12d)$$

In this case, the set of equations is already decoupled for each layer. This allows to find a second-order equation for each layer as

$$\left[\frac{d^2}{d\rho^2} + \frac{1}{\rho} \frac{d}{d\rho} - \left(\frac{m^2}{\rho^2} - \mu_\pm^2 \right) \right] \phi_{B2/A1}^\tau(\rho) = 0. \quad (5.13)$$

In Eq. (5.13), $\mu_\pm = \epsilon \pm \tau\delta$ and the subscript of the function $\phi_i^\tau(\rho)$ refers to $B2$ for μ_+ and to $A1$ for μ_- . The solutions of Eq. (5.13) are Bessel functions. Dropping the ones singular in the origin, we find

$$\phi_{A1}^\tau(\rho) = D_1^\tau J_m(\mu_- \rho) , \quad (5.14a)$$

and

$$\phi_{B2}^\tau(\rho) = D_2^\tau J_m(\mu_+ \rho) . \quad (5.14b)$$

The other two components can then be found from Eqs. (5.12b) and (5.12d) and yield

$$\phi_{B1}^\tau(\rho) = -\tau D_1^\tau J_{m-\tau}(\mu_- \rho) , \quad (5.15a)$$

and

$$\phi_{A2}^\tau(\rho) = \tau D_2^\tau J_{m+\tau}(\mu_+\rho) . \quad (5.15b)$$

We are now in a position to find the eigenstates and energy levels of a GQB. For this, we need to equate the spinor components inside the GQB with those outside at position $\rho = R$. Doing so, one obtains a set of four equations for four unknowns that can be written in a matrix formalism as $\mathbf{M}^\tau \cdot \mathbf{D}^\tau = 0$ and gives

$$\begin{pmatrix} -J_m(R\mu_-) & 0 & \Re[K_m(R\alpha_+)] & \Im[K_m(R\alpha_-)] \\ \tau J_{m-\tau}(R\mu_-) & 0 & \Re[b_+ K_{m-\tau}(R\alpha_+)] & \Im[b_- K_{m-\tau}(R\alpha_-)] \\ 0 & -J_m(R\mu_+) & \Re[c_+ K_m(R\alpha_+)] & \Im[c_- K_m(R\alpha_-)] \\ 0 & -\tau J_{m+\tau}(R\mu_+) & \Re[d_+ K_{m+\tau}(R\alpha_+)] & \Im[d_- K_{m+\tau}(R\alpha_-)] \end{pmatrix} \begin{pmatrix} D_1^\tau \\ D_2^\tau \\ C_1^\tau \\ C_2^\tau \end{pmatrix} = 0, \quad (5.16)$$

where $b_\pm = \alpha_\pm / (\epsilon - \tau\delta)$, $c_\pm = [(\epsilon - \tau\delta)^2 + \alpha_\pm^2] / (\epsilon - \tau\delta)$, and $d_\pm = \alpha_\pm [(\epsilon - \tau\delta)^2 + \alpha_\pm^2] / (\epsilon^2 - \delta^2)$. The energy levels $\epsilon_{m,n}(R)$ of a GQB with radius R can be found through the roots of the determinant of the matrix \mathbf{M}^τ . Here, n is the radial quantum number corresponding to states with $|n|$ nodes in the radial direction. The obtained eigenvalues are real and thus correspond to bound states with infinite lifetime. This is a manifestation of the created gap outside the blister induced by the bias. This contrasts with quasi-bound states in the presence of an electrostatic potential in single layer graphene QDs. For these structures, the eigenvalues are complex and thus the states have a finite lifetime [113, 118, 136]. Subsequently, one can obtain the corresponding wavefunction by solving at the given energy for the coefficients C_i^τ and D_i^τ and obtaining the

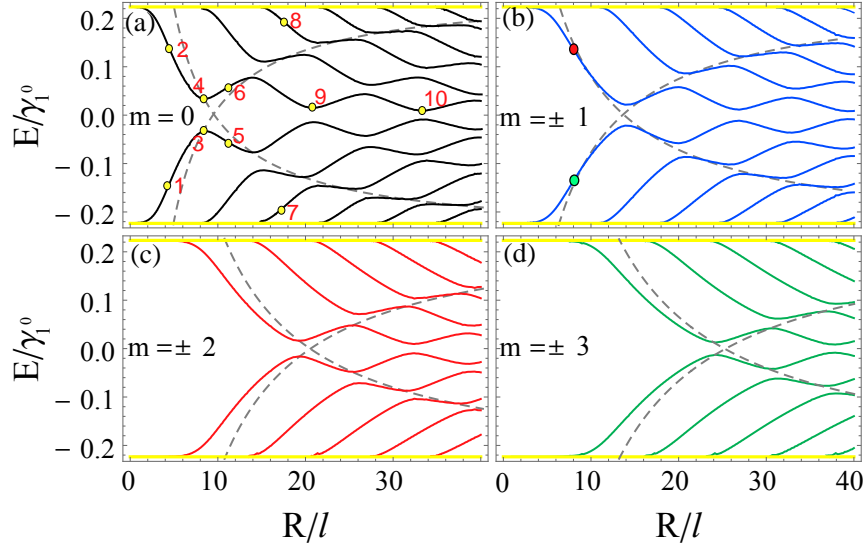


Figure 5.2: Energy levels of the GQB as a function of its radius with the same bias inside and outside the GQB $\delta_{<} = \delta_{>} = 0.25\gamma_1$. The dashed green vertical lines in panel (a) represent the radii where the states residence is the same in both layers. Gray dashed curves correspond to the first energy levels of a biased bilayer nano-disk.

eigenwavefunction $\Phi_{m,n}^\tau(\vec{r})$. From this, the radial probability density (RPD) can be found as [168, 169]

$$\mathcal{P}_{m,n}^\tau(\rho) = \rho |\Phi_{m,n}^\tau(\mathbf{r})|^2 . \quad (5.17)$$

Finally, the local density of states $\mathcal{D}(\mathbf{r}, E)$ for a GQB with radius R can be derived from the eigenstates as

$$\mathcal{D}(\mathbf{r}, \epsilon) = \sum_{m,n} \delta(\epsilon - \epsilon_{m,n}) |\Phi_{m,n}^\tau(\mathbf{r})|^2 . \quad (5.18)$$

In the numerical results displayed in the following section we will replace the Dirac function by a Gaussian profile with a finite spectral width Γ [47].

5.3 Confined states in a GQB

5.3.1 Homogeneous inter-layer bias

Now we turn to the discussion of the numerical results for the energy levels in various configurations of GQBs. The first configuration is the simplest example, i.e. the case where a homogeneous inter-layer bias potential δ is applied to the entire system. In Fig. 5.2 we show the energy levels as a function of the size R of the GQB for $m = 0, \dots, \pm 3$ with $\delta = 0.25 \gamma_1^0$. The results indicate that, indeed, for the energy range as defined in Eq. (5.5) the GQB has confined modes. Panel (a) of Fig. 5.2 shows that in the limit $R \rightarrow 0$, the GQB has two $m = 0$ confined modes at energy $\pm \delta_G$. As the radius of the GQB increases, the modes approach each other, anti-crossing one another around $\epsilon = 0$. As the radius increases further, more $m = 0$ modes are allowed inside the GQB. For a given radius, these modes are denoted by the quantum number n . The number of the confined modes crucially depends on the strength of the applied bias outside the blister $\delta_{>}$ and its size R . The energy spectrum of the different modes form anti-crossings with each other. As a consequence, the energy levels oscillate with the size of the GQB.

In panels (b) - (d) of Fig. 5.2 we show the energy levels for non-zero angular quantum number m . These modes are only supported at larger radii R but their characteristic behavior is similar as the $m = 0$ case shown in panel (a). Notice that the results are the same for positive as for negative m . This is in contrast with previous studies where the symmetry between both signs of the angular quantum number is broken [111, 119, 120]

To investigate the character of the different energy levels and the behaviour at the anti-crossings, in Fig. 5.3 we show the RPD for $m = 0$ and different configurations as indicated

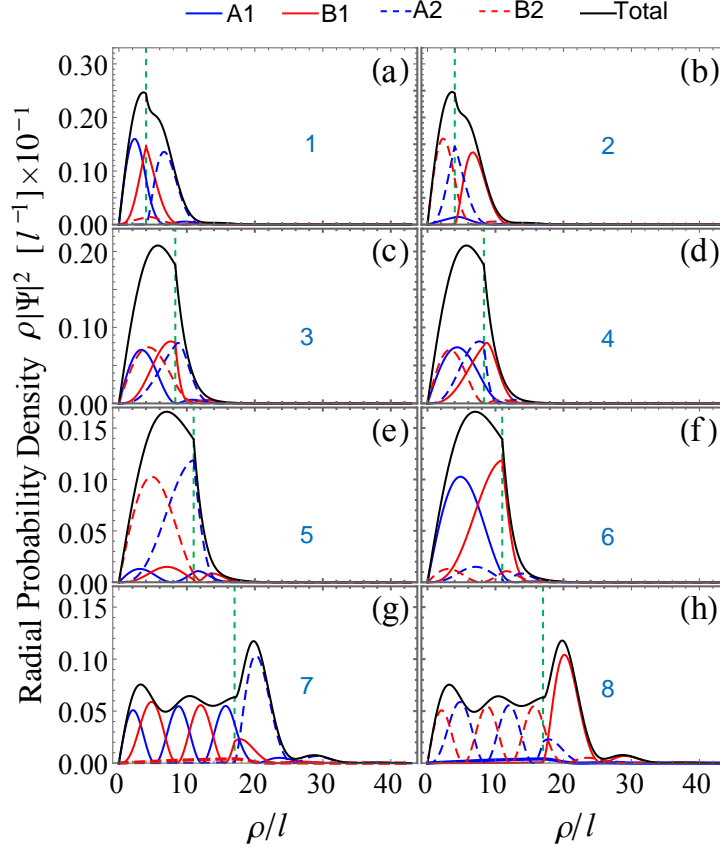


Figure 5.3: (a-h) Radial probability density of $m = 0$ stats in Fig. 5.2(a) labelled by (1-8), respectively. The green dashed vertical line represents the radius of the GQB. Note that the states close to the continuum spectrum are mainly localized outside the GQB and preferably on the disconnected sublattices A2 and B1 as indicated in panels (g) and (h), respectively.

by the points in Fig. 5.2(a). We choose these points to be exactly at an anti-crossing point (points 3 and 4), before (points 1 and 2), and after it (points 5 and 6), and also near the continuum spectrum (points 7 and 8). Furthermore, we show the contribution of each sublattice to the probability density. Comparing for instance Figs. 5.3(a) and (b), we see that inside the GQB, before an anti-crossing point, mainly layer 1 contributes on the negative energy branch, while for the positive energy branch it is layer 2. In addition, we infer from Figs. 5.3(c,d) that at the anti-crossing point both layers contribute exactly the same on the negative and positive energy solutions. A transition in the residence of

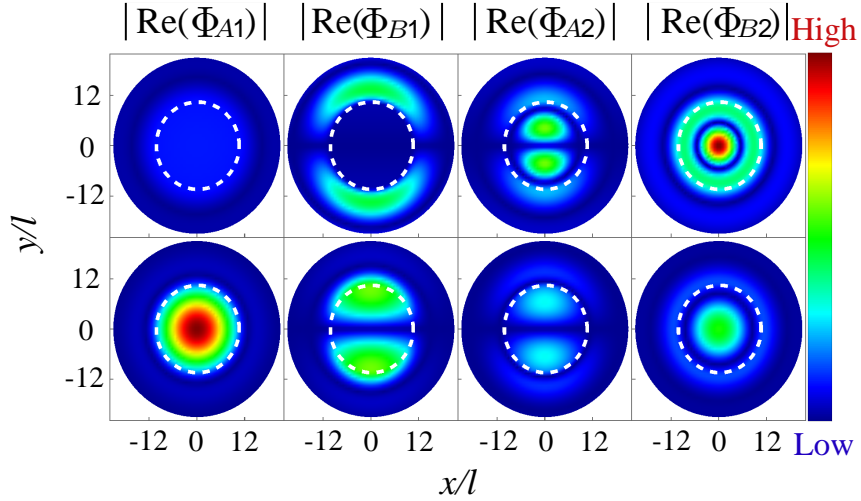


Figure 5.4: Real part of the different components of the wavefunction for states with energy $E = 0.2\gamma_1^0$ meV and $E = 0.05\gamma_1^0$ for top and bottom rows, respectively. We assume a blister with radius $R = 10.5l$ and bias $\delta = 0.25\gamma_1^0$. The radius of the blister is indicated by white dashed circle.

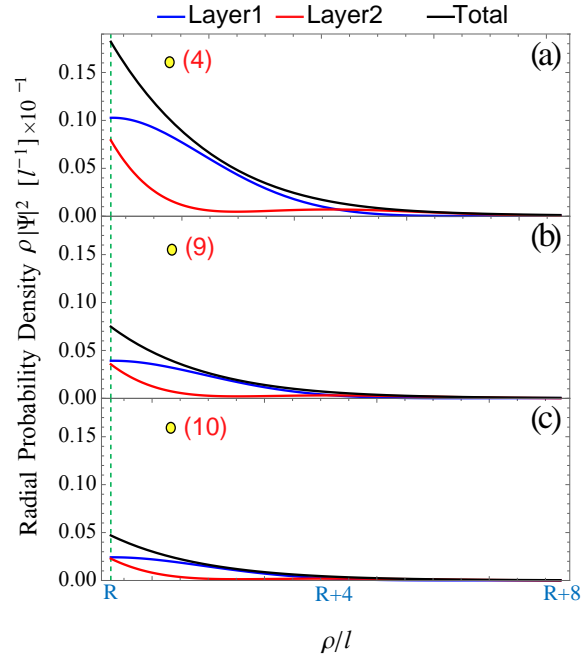


Figure 5.5: Radial probability density outside the blister of the states $\epsilon_{0,1}$ in Fig. 5.2(a) labelled by yellow points (4,9,10). The green vertical line represents the radius of the GQB.

states takes place when passing an anti-crossing point. The states with negative energy mainly reside on layer 2 instead of layer 1 before the anti-crossing point and vice versa for

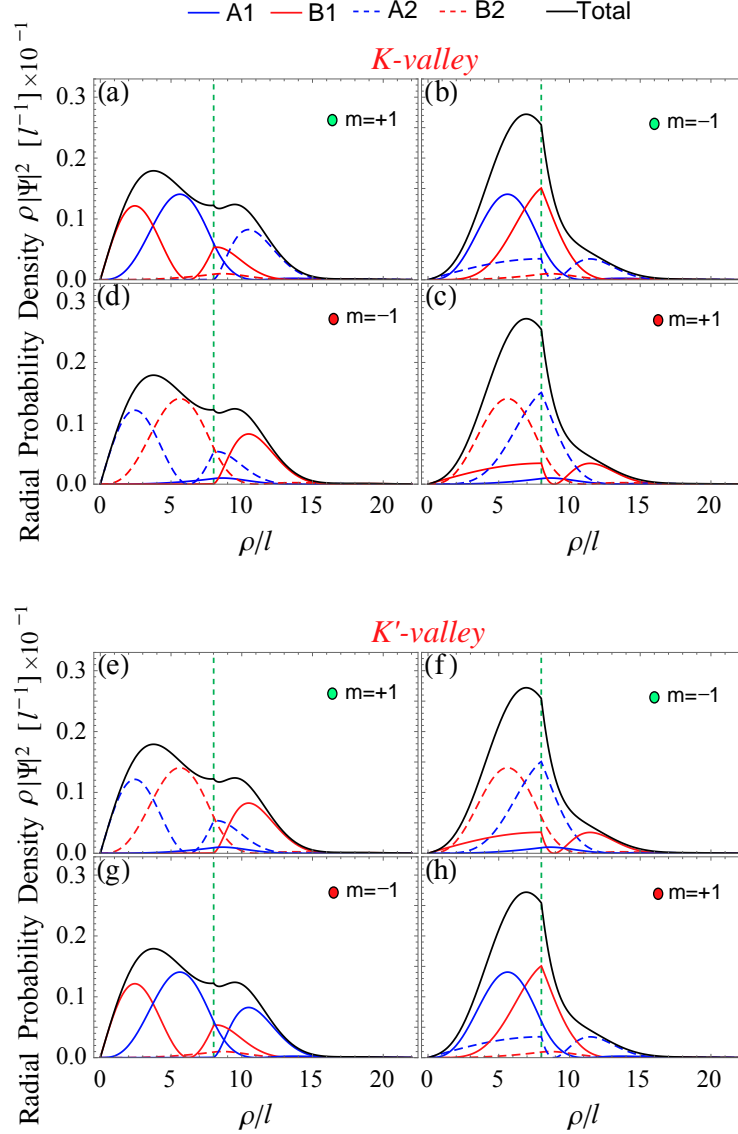


Figure 5.6: The radial probability density of $m = \pm 1$ states in Fig. 5.2(b) labelled by red and green dots. Top and bottom panels are for the K - and K' -valley, respectively. The green vertical line represents the radius of the GQB. Note that $[\mathcal{P}_{m,n}^\tau(\epsilon, \rho)]_{\text{Layer1}} = [\mathcal{P}_{-m,-n}^\tau(-\epsilon, \rho)]_{\text{Layer2}}$ and $[\mathcal{P}_{m,n}^\tau(\epsilon, \rho)]_{\text{Layer1}} = [\mathcal{P}_{m,n}^{-\tau}(\epsilon, \rho)]_{\text{Layer2}}$ while the total radial probability density is the same in both valleys.

the positive one as shown in Figs. 5.3(e,f). This means that the modes $\epsilon_{0,\pm 1}$ anti-cross each other in Fig. 5.2(a) and correspond mainly to states on one of the two layers before or after an anti-crossing points. Since the inter-layer coupling is active only outside the blister, therefore one expects that the eigenstates are mainly localised inside the radius of

the GQB. Peculiarly, however, we find that this is not true for all spinor components of the eigenstate as can be seen in see Figs. 5.3 (g,h). To thoroughly examine this behaviour we show in Fig. 5.4 the real part for each component of the wave function of a blister that supports two energy levels. While for the low-energy state (bottom row) the wave function is almost completely localised inside the blister for all components, we see that the high-energy state (top row) has a significant portion outside the blister's radius on the $B1$ component of the bottom layer.

We can find the radii R_j at which anti-crossing occur through the following partitioning relation:

$$\int_0^{R_j} d\rho [\mathcal{P}_{m,n}^\tau(\rho)]_{\text{Layer1}} = \int_0^{R_j} d\rho [\mathcal{P}_{m,n}^\tau(\rho)]_{\text{Layer2}}, \quad (5.19)$$

with

$$[\mathcal{P}_{m,n}^\tau(\rho)]_{\text{Layer } i} = \rho \left(|\phi_{Ai}^{m,n,\tau}(\rho)|^2 + |\phi_{Bi}^{m,n,\tau}(\rho)|^2 \right) \quad (5.20)$$

where the radial part of the wave functions is normalized according to

$$2\pi \int_0^\infty d\rho \sum_{i=1,2} [\mathcal{P}_{m,n}^\tau(\rho)]_{\text{Layer } i} = 1. \quad (5.21)$$

In other words, two energy levels form an anti-crossing when the radius of the GQB is such that the probability of finding a state inside the GQB is the same for both layers. Note that a point in the middle between two subsequent anti-crossing points associated with modes $\epsilon_{m,n}$ also satisfies Eq. (5.19). This point coincide with the anti-crossing point in the second pair of energy branches, i.e. $\epsilon_{m,|n|+1}$, in the spectrum as can be inferred from Fig. 5.2(a).

Using Eq. (5.19), we can find the radii R_j where the anti-crossing points occur for any pair of energy branches $\epsilon_{m,n}$. For example, the first three anti-crossing points of the first pair of energy branches $\epsilon_{0,\pm 1}$ in Fig. 5.2(a) are located at $R_j = (8.30, 20.74, 33.27)l$. In between these three anti-crossing points, there are two points where both layers also contribute the same to the RPD inside the GQB located at $R_j = (14.46, 26.98)l$. For large GQB we notice that the strength of the anti-crossings becomes weaker. This is a result of leaking interaction between the two layers through the BLG outside the blister. In Fig. 5.5 we show the RPD outside the GQB at the first three anti-crossings labelled by the yellow dots (4, 9, 10) in Fig. 5.2(a). We see that the interaction between states on both layers becomes smaller with increasing the radius of GQB. Hence, in the limit $R \rightarrow \infty$ we expect the RPD to be zero outside the GQB and as result the anti-crossings will vanish and the states will be completely localized inside the blister. In this case, the GQB can be seen as a biased bilayer graphene nano-disk. We superimpose the first energy levels of a biased bilayer nano-disk with the respective angular momentum as gray dashed curves on Fig. 5.2. For a bilayer nano-disk we implement hard wall boundary conditions and the energy levels can be found by solving

$$J_m(\mu_+R) = 0, \quad J_m(\mu_-R) = 0 \quad (5.22)$$

The asymptotic behaviors of Bessel function for small and large argument are

$$J_0(x) = \begin{cases} \sqrt{2/\pi x} \cos(x - \pi/4) & x \rightarrow \infty \\ 1 - x^2/4 & x \rightarrow 0 \end{cases}, \quad (5.23)$$

using Eq.(5.23) one can show that $E \sim 1/R$.

For $m \neq 0$, we investigate the contribution of the two layers to the probability density for only $m = \pm 1$ as shown in Fig. 5.6, and the findings also apply for $|m| > 1$. We choose two points before the first anti-crossing point of the modes $\epsilon_{1,\pm 1}$ marked by red and green dots in Fig. 5.2(b). Because of the symmetry between m and $-m$ in this case, these two points correspond to four modes as indicated in Fig. 5.6. We see that the states $m = \pm 1$ with negative energy (green dot) mainly reside on the lower layer and vice versa for states with positive energy. This corresponds to the case with $m = 0$ and it also holds here for the modes $\epsilon_{\pm 1,|n|>1}$. Similar to the spectrum of $m = 0$, the radii for which the energy forms anti-crossings can be also found using Eq. (5.19). Notice that from the top panel of Fig. 5.6 the RPD acquires the layer symmetry

$$[\mathcal{P}_{m,n}^{\tau}(\epsilon, \rho)]_{\text{Layer1}} = [\mathcal{P}_{-m,-n}^{\tau}(-\epsilon, \rho)]_{\text{Layer2}}. \quad (5.24)$$

In the bottom panel of Fig. 5.6, we show the same results as in the top panel but in the vicinity of the K' -valley. Comparing top and bottom panels of Fig. 5.6, we find that the RPD also attains the following symmetry

$$[\mathcal{P}_{m,n}^{\tau}(\epsilon, \rho)]_{\text{Layer1}} = [\mathcal{P}_{m,n}^{-\tau}(\epsilon, \rho)]_{\text{Layer2}}, \quad (5.25)$$

$$[\mathcal{P}_{m,n}^{\tau}(\epsilon, \rho)]_{\text{Layer } i} = [\mathcal{P}_{-m,-n}^{-\tau}(-\epsilon, \rho)]_{\text{Layer } i}. \quad (5.26)$$

Note that even though the RPD of each layer is different in each valley, the total RPD is the same in both valleys.

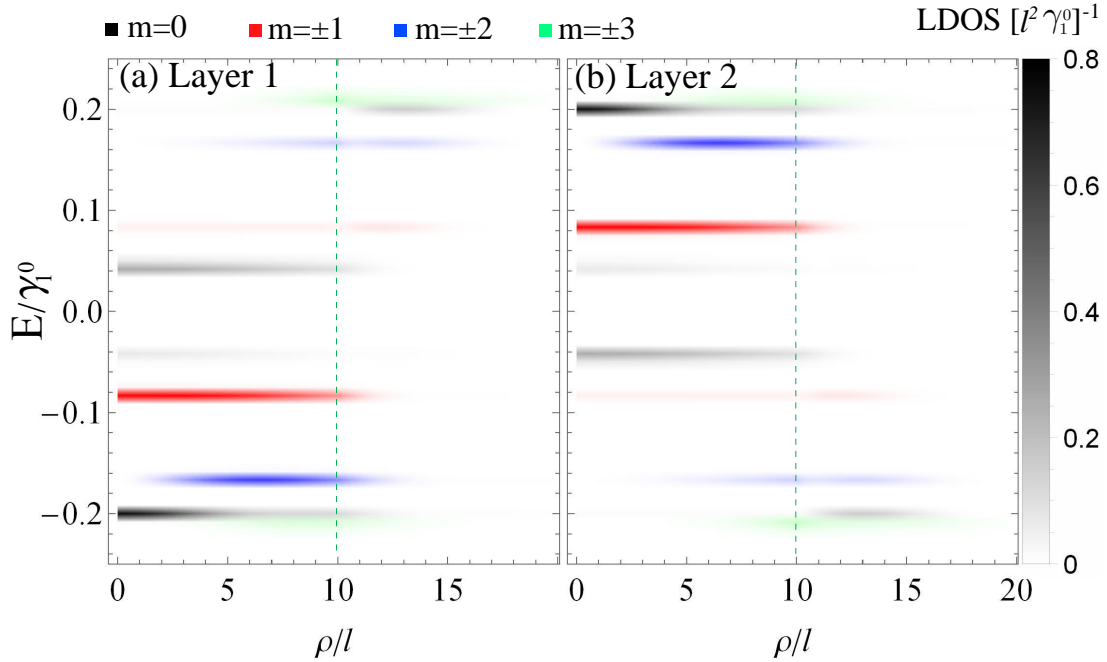


Figure 5.7: LDOS of the GQB for layer 1 (left) and layer 2 (right), with $R = 10l$ and $\delta_{<} = \delta_{>} = 0.25\gamma_1^0$. The spectral width of the Gaussian profile is $\Gamma = 0.02\delta_{>}$. The dashed green vertical lines represent the radius of the GQB.

In Fig. 5.7 we show the local density of states for a GQB of fixed size $R = 10l$ as a function of the energy and distance from the origin for both layers. The results show that the layer selectivity of the modes is not only present for $m = 0$, but also for the other angular quantum numbers. Very pronounced is for example the $m = \pm 1$ mode that is strongly localized on layer 1 for negative energy and on layer 2 for positive energy. Furthermore, the LDOS also shows that states with $|m| > 1$ are not positioned at the center of the GQB, but more towards the edge or even outside the GQB in a classically forbidden region, specially, for those states close to the continuum spectrum.

5.3.2 Non-homogeneous inter-layer bias

In the previous section we have considered the most straightforward case in which the inter-layer bias is the same in all parts of the sample. However, if the blister is formed

by encapsulation of a metal colloid, the applied electric field also induces a dipole in the metallic nanoparticle. This will change the electrostatic potential on each layer. As a result, it can be strongly reduced inside the GQB with respect to outside it. To incorporate this difference, we investigate the case for which the inter-layer bias inside the GQB, $\delta_{<}$, is smaller than the bias $\delta_{>}$ outside.

In Fig. 5.8 we show the energy levels of a GQB with vanishing $\delta_{<}$ inside as a function of the radius of the blister for different values of the angular quantum number m . In this case, the energy levels do not show anti-crossings and approach each other as the size of the GQB increases in a monotonous way. In Fig. 5.8(a) we show the energy spectrum of the state with zero angular momentum. Here, contrary to the homogeneous bias case, each energy branch corresponds to states residing on a specific layer inside the GQB for any R . In Fig. 5.9 we show the RPD for different energy branches, labelled by yellow dots in Fig. 5.8(a). States on the first energy branch $\epsilon_{0,-1}$ reside on the lower layer, see Fig. 5.9(a). While for the second branch $\epsilon_{0,-2}$, the states along it reside on the upper layer as shown in Fig. 5.9(b). Similarly the third $\epsilon_{0,-3}$ and fourth $\epsilon_{0,-4}$ branches, marked by points 3 and 4 in Fig. 5.8(a), the states reside mainly on the lower and upper layer respectively. This is illustrated in Figs. 5.9(c,d). Note that for the counterpart branches in the positive energy regime, the modes residence is opposite compared to the negative energy branches.

For non-zero values of the angular quantum number, however, the symmetry between positive and negative m is broken. This is most clear in the first pair of modes $\epsilon_{m>0,\pm 1}$ in panels (b) - (d) in Fig. 5.8. The lowest of the two is only possible for negative m modes, while the highest is for positive m . These two modes, labelled by green and red dots in

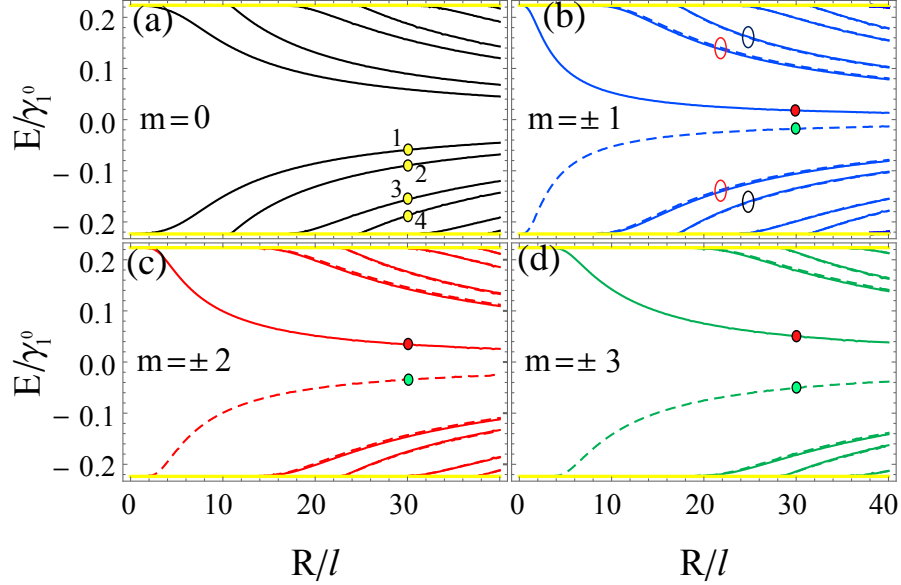


Figure 5.8: Energy levels of the GQB as a function of its radius with different bias inside and outside the GQB $\delta_{<} = 0$ and $\delta_{>} = 0.25\gamma_1^0$. Solid (dashed) curves are for $m > 0$ ($m < 0$) where yellow horizontal lines delimit the gap outside the GQB.

Figs. 5.8(b-d), are mainly localized at the interface of the blister as can be seen in Fig. 5.10. Moreover, inside the blister they mainly reside on the upper and lower layer for $m < 0$ and $m > 0$, respectively, as shown in Fig. 5.10. It turns out that they significantly reside on the disconnected sublattices A2 and B1 for the negative and positive angular momentum, respectively, as shown in Figs. 5.10(a-f). The appearance of these localized modes at the interface of the blister is one of its quintessential traits.

Reminding ourselves that the lowest modes mainly reside on the upper layer while the upper modes reside on the lower layer, it follows that small GQBs only can support modes with a positive angular momentum on the lower layer while the negative angular momentum-modes reside on the upper layer. For large R , we notice that the broken symmetry between the negative and positive angular momentum is almost restored for modes whose radial number $|n| > 1$ such that $\epsilon_{m,n}(R) \approx \epsilon_{-m,n}(R)$ as shown in Figs.

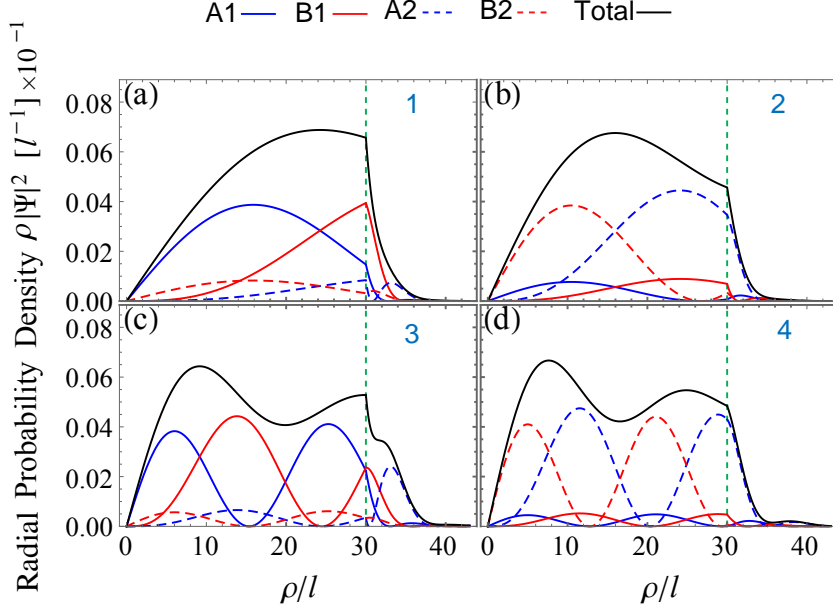


Figure 5.9: (a-d) Radial probability density of the $m = 0$ states in Fig. 5.8(a) labelled by (1-4), respectively. The green vertical line represents the radius $R = 30l$ of the GQB.

5.8(b-d). The contribution of each layer to these modes is exactly the same as in the case of $m = 0$ discussed in Fig. 5.8(a). For example, in the case of $m = \pm 1$, the first pair of modes labelled by the red circles in Fig. 5.8(b), mainly reside on the lower and upper layer for modes whose energy is negative and positive, respectively. The opposite occurs for the second pair of modes, labelled by the black circles, and such trend also holds for $|m| > 1$.

In general, the energy levels still retain the following symmetry [166]

$$\epsilon_{m,n}(R) = -\epsilon_{-m,-n}(R) . \quad (5.27)$$

That this relation holds can be seen in Fig. 5.11 where the energy levels in a GQB with radius $R = 20 l$ are plotted for a homogeneous inter-layer bias (panel (a)) compared with the case for a vanishing inter-layer bias (panel (b)) in the GQB. The results show that

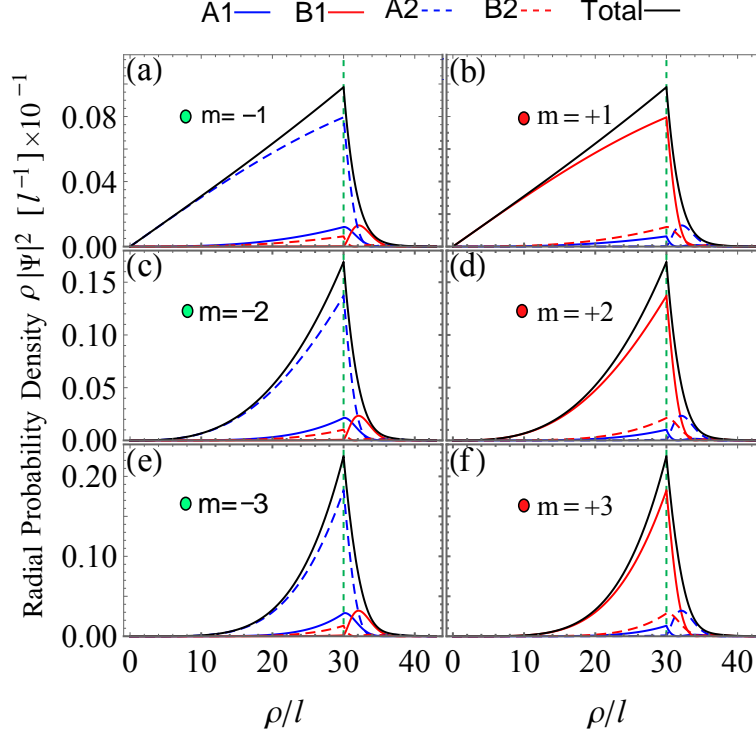


Figure 5.10: (a-f) Radial probability density of $m = \pm(1, 2, 3)$ states in Fig. 5.8(b,c,d) labelled by green and red dots, respectively. The green vertical line represents the radius of the GQB $R = 30l$.

by changing the inter-layer bias inside the GQB, the $m = 0$ modes are pushed away from each other while for the modes with finite angular momentum it even allows the total number of states in the GQB to be reduced.

In Fig. 5.12 we show the energy levels as a function of the radius of the GQB when the inter-layer bias inside the blister is smaller than outside but still non-zero. This result allows to follow the behavior of the modes as the inter-layer bias $\delta_<$ is reduced. We see that in this case the energy levels start showing anti-crossings again, but now at larger radius R . It also shows that for non-zero angular momentum the symmetry with respect to the sign of m remains strongly broken for small R , but that the modes with opposite m make a transition between different radial quantum number n .

Finally, in Fig. 5.13 we show the energy levels in the case when the bias inside the

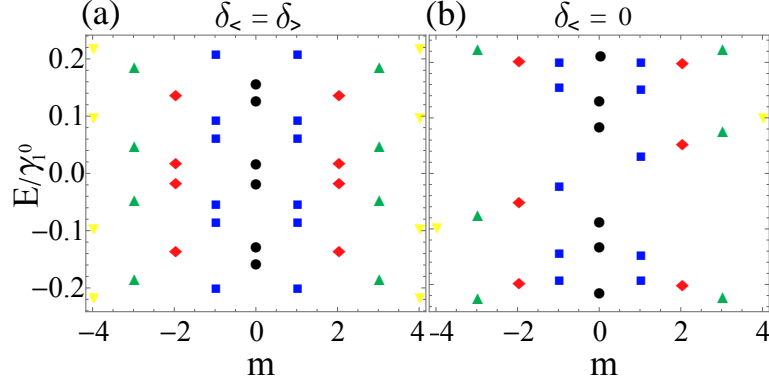


Figure 5.11: Energy levels of a GQB as a function of angular momentum label m for $R = 20l$ and $\delta_{>} = 0.25\gamma_1^0$ and for different values of $\delta_{<}$.

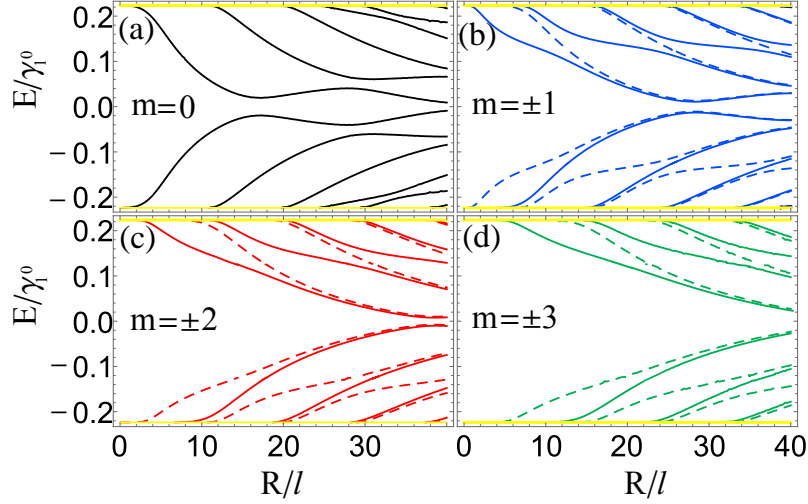


Figure 5.12: Energy levels of the GQB as a function of its radius for different strength of the bias inside the GQB with $\delta_{>} = 2\delta_{<} = 0.25\gamma_1$. Solid (dashed) curves are for $m > 0$ ($m < 0$) where yellow horizontal lines delimit the gap outside the GQB.

GQB is opposite to outside, i.e. $\delta_{<} = -\delta_{>}$. The $m = 0$ result look similar to the case of a homogeneous bias, but they are slightly different, i.e. $\epsilon_{0,n}(R, \delta_{<}) \neq \epsilon_{0,n}(R, -\delta_{<})$, as one would observe from Fig. 5.14(a). For example, the first three anti-crossing points associated with the first pair of energy branches $\epsilon_{0,\pm 1}$ are located at $R_j = (10.93, 23.42, 35.96)l$. The anti-crossings occur for slightly larger GQB in comparison with the homogeneous inter-layer bias case. Of particular importance is also the layer residency of states, where before the anti-crossing the states with negative energy mainly resided on the upper layer

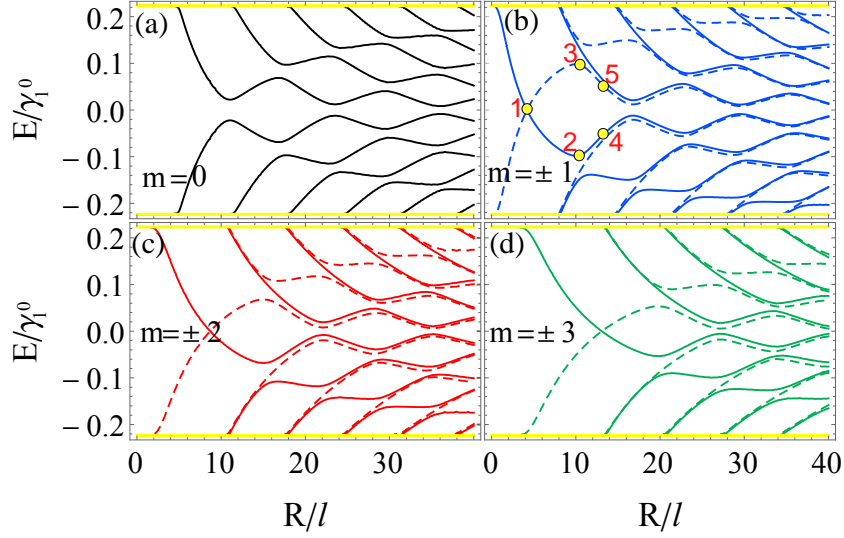


Figure 5.13: Energy levels of the GQB as a function of its radius opposite bias inside and outside the GQB with $\delta_> = -\delta_< = 0.25\gamma_1^0$. Solid (dashed) curves are for $m > 0$ ($m < 0$) where yellow horizontal lines delimit the gap outside the GQB.

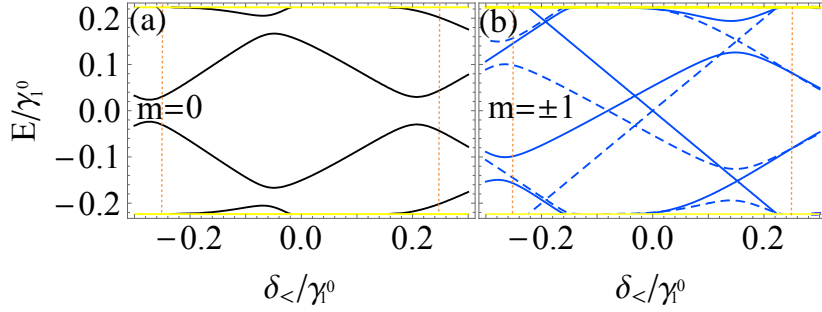


Figure 5.14: Energy levels of the GQB as a function of the bias inside the GQB $\delta_<$ with $\delta_> = 0.25\gamma_1^0$ and $R = 10l$. Solid (dashed) curves are for $m > 0$ ($m < 0$) where yellow horizontal lines delimit the gap outside the GQB. The vertical dashed brown lines represent the points $\delta_< = \pm\delta_>$.

inside the GQB and vice versa for states with positive energy. This is exactly the opposite to what happened in the case with homogeneous bias. The most important result displayed in Fig. 5.14(b) is that the homogeneous case (i. e. $\delta_< = \delta_>$) is distinctive since it preserves the symmetry $\epsilon_{m,n}(R) = \epsilon_{-m,n}(R)$ as shown in panel (b).

For a finite angular momentum, the results in Fig. 5.13 show that the modes get pushed into each other, forming anti-crossings when the angular momentum quantum

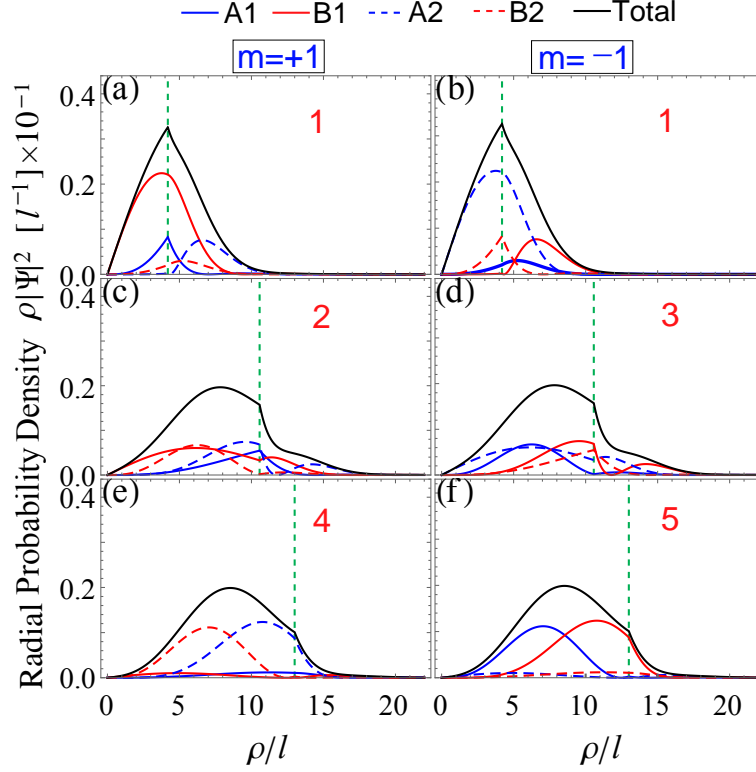


Figure 5.15: (a-f) Radial probability density of states $\epsilon_{\pm 1, \pm 1}$ in Fig. 5.13(b) labelled by points (1-5). The green vertical line represents the radius of the GQB.

number is the same, while it crosses when m is opposite. As a result, for a given inter-layer bias, there is a radius R for which each of the non-zero m modes are degenerate at $\epsilon_{m,1} = \epsilon_{-m,-1} = 0$. We notice that the results of non-homogeneous bias also attains the symmetry $\epsilon_{m,n}(R) = -\epsilon_{-m,-n}(R)$. In Fig. 5.15, we show the RPD of the modes $\epsilon_{1,1}$ and $\epsilon_{-1,-1}$ at different radii indicated by the yellow dots in Fig. 5.13(b). It is evident from Figs. 5.15(a,b), that the degenerated modes $\epsilon_{\pm 1, \pm 1} = 0$, labelled by point 1 in Fig. 5.13(b), are mainly localized at the interface of the blister. These modes are mainly confined on the upper and lower layer inside the GQB for positive and negative angular momentum, respectively, as can be seen from Figs. 5.15(a,b). While at points 2 and 3 the two layers contribute exactly the same to the confinement of the two states $\epsilon_{\pm 1, \pm 1} = \mp 0.1\gamma_1^0$ as shown in Figs. 5.15(c,d). Then, a transition occurs in the layer confinement, where at

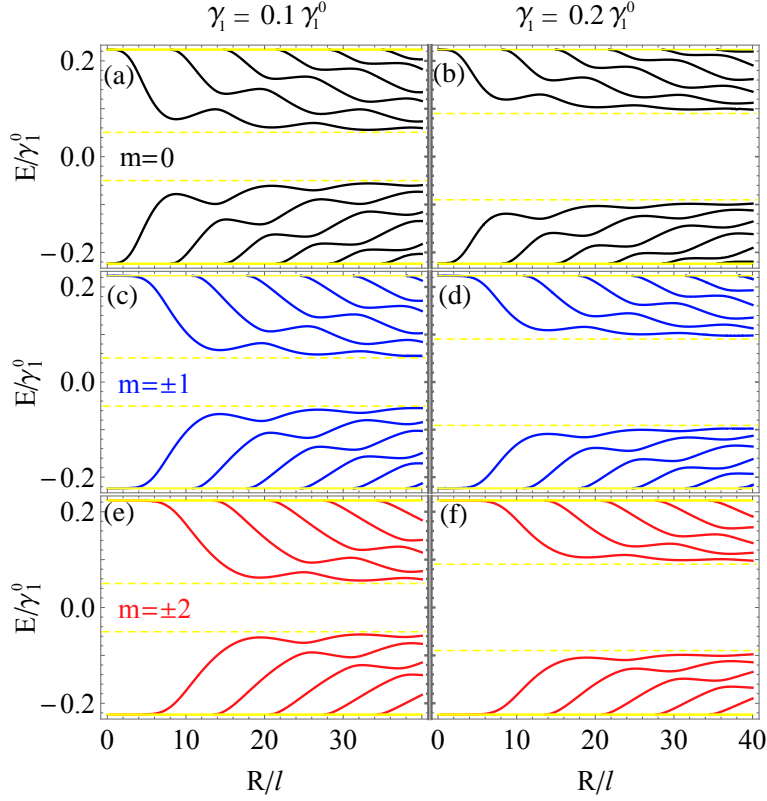


Figure 5.16: Energy levels of GQB with different strength of the inter-layer coupling inside it, where yellow horizontal dashed and solid lines delimit the gap inside and outside the GQB, respectively, with $\delta_{<} = \delta_{>} = 0.25\gamma_1^0$.

the points 4 and 5 the states $\epsilon_{\pm 1, \pm 1} = \mp 0.06\gamma_1^0$ mainly reside on the upper and lower layer for positive and negative angular momentum, respectively. The behaviour of the rest of modes $\epsilon_{\pm 1, |m| > 1}$ resembles that of the case $m = 0$ in Fig. 5.13(a). This means that before and after anti-crossings, the states with negative and positive angular momentum reside on the upper and lower layer, respectively, while at the anti-crossings they are equally distributed. Analogously for $|m| > 1$, we find that modes behave similarly to the case of $m = \pm 1$.

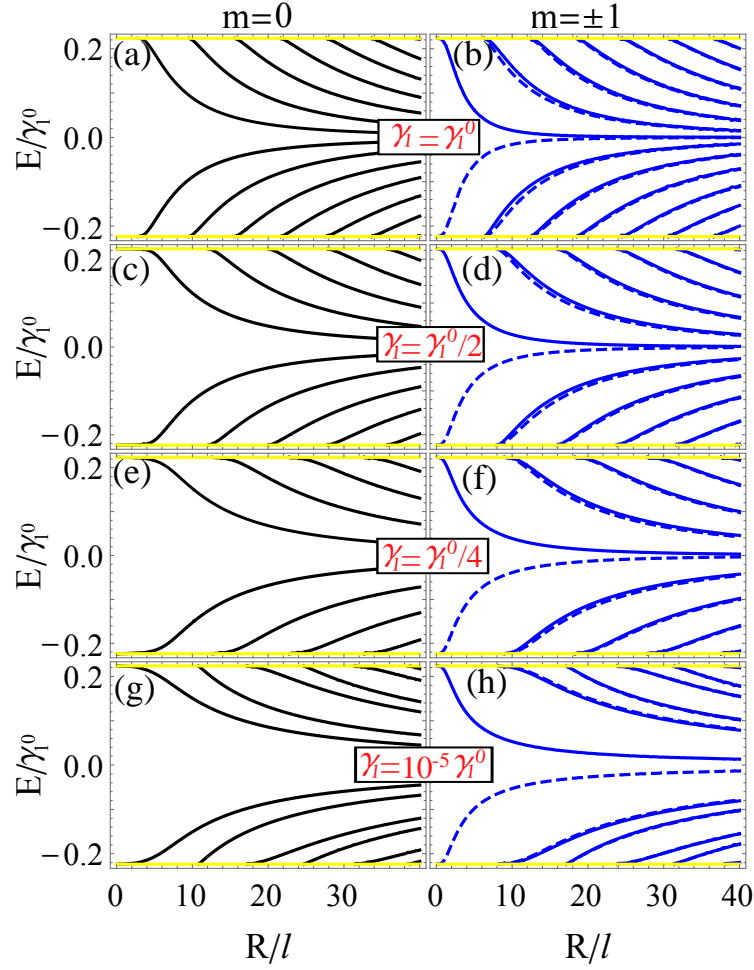


Figure 5.17: Energy levels of GQB with different strength of the inter-layer coupling inside it. Solid (dashed) curves are for $m > 0$ ($m < 0$) where yellow horizontal lines delimit the gap in bilayer graphene with $\delta_{>} = 0.25\gamma_1^0$.

5.3.3 Effect of the inter-layer coupling

The inter-layer coupling γ_1 inside the GQB decreases very fast as the height of the blister increases. However, if the blister is small and the layers in the blister remain loosely coupled, it is expected to show a band gap that is much smaller than outside the blister. Therefore, one also expects to find confined modes in this case. In this section, we investigate the energy levels of a non-zero inter-layer coupling in a GQB. In general, for a fixed gap outside the blister, the number of anti-crossings and their location mainly depend on the bias inside the blister. This allows to control the confinement to be mainly

localized on a specific layer.

In Fig. 5.16 we show the energy levels of a GQB with a homogeneous inter-layer bias but different inter-layer coupling inside the blister as a function of the radius R . We see that for small radii, the energy levels are similar to the case of a completely decoupled blister, but that as the GQB grows, the energy levels do not cross the gap formed inside the GQB. As a consequence, for large R the oscillations of the lowest positive energy level are decreased and this level approaches the value of δ_G , dashed yellow lines, from Eq. (5.5) calculated with the inter-layer coupling inside the blister.

When the screening of the inter-layer bias inside the GQB is important, the inter-layer coupling strongly affects the energy levels. In Fig. 5.17 we show the energy levels as a function of the size of the GQB for different values of the inter-layer coupling and in the absence of an inter-layer bias inside the GQB. The results show that as the inter-layer bias is reduced, the energy levels are pairwise pushed away from each other forming the layer polarized modes as discussed in the previous section.

5.3.4 Morphological effects

Up to now, the analysis was performed by modelling the edge of the blister as an abrupt interface in the band gap parameter describing electronic states. This assumption is justified because of the very sharp transition between gapless to gapped states as shown in Fig. 5.1(a), which is a consequence of the exponential dependence of the inter-layer coupling strength on the inter-layer distance expressed through Eq. (5.4). Because the band gap changes sharply at the edge of the system, the morphological details of the blister are obscured and many different shapes of circular blisters effectively have the

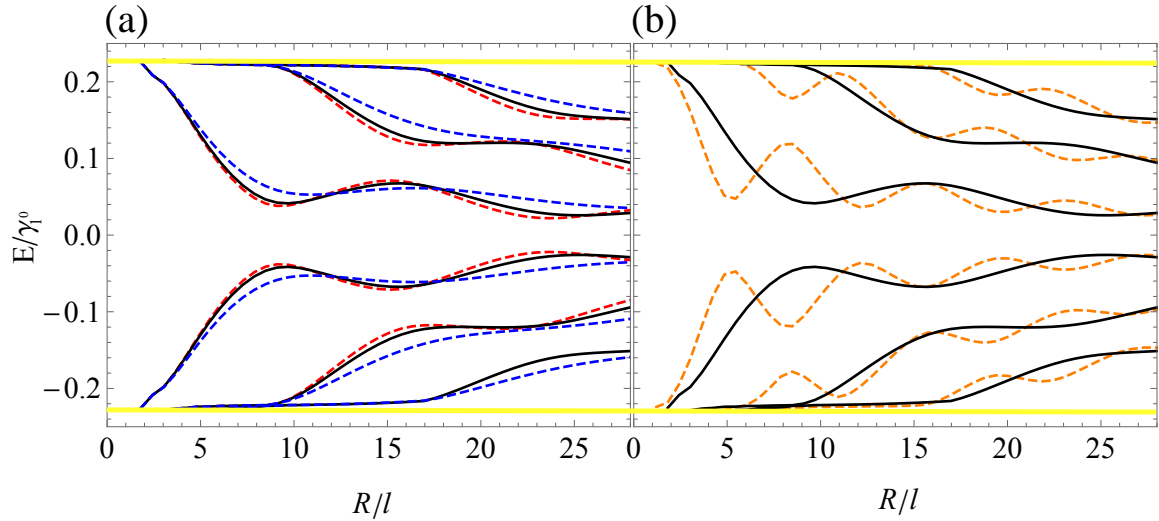


Figure 5.18: Energy levels of a GQB, same as in Fig. 5.2(a), but with a gaussian interface. (a) Dashed-blue, black, and dashed-red curves correspond to a gaussian dome of height $(1.5, 3, 10)c_0$, respectively. (b) The height of the gaussian dome is fixed at $3c_0$ while the inter-layer bias inside the blister is considered constant (black curves) and varies with the inter-layer distance (dashed-orange curves).

same energy spectrum. However, when the height variation of the blister becomes much smaller, this argument might not hold any more. Therefore, in Fig. 5.18(a) we show the energy spectrum for Gaussian GQBs with varying height. In contrast to the previous analysis for these results we have resorted to numerical calculation of the energy levels using a finite element package. The results show that even small blisters support localised eigenstates with a similar energy spectrum. Notice that the morphology of the blister only affects the strength of the anti-crossings but that already for a local doubling of the inter-layer distance the energy levels are very close to the completely decoupled case discussed above.

Finally we also investigate the effect of a change in inter-layer bias due to capacitive effects. Indeed, since the bias arises due to electrostatic gates, the top layer will be influenced differently when closer to the top gate than the bottom layer. In Fig. 5.18(b) we show numerical results (dashed-orange) for a locally changing inter-layer bias. While also

here the confined states result in a robustly discretized energy spectrum, the wavelength of the oscillations due to anti-crossings is strongly reduced. This is because in the latter case the cones inside the GQB are shifted more strongly in energy and, therefore, the confined states have a shorter wavelength.

5.4 Controlling layer occupation

To thoroughly examine the layer localization in GQB and to understand the origin of the confined energy levels and their anti-crossings, we discuss here in details the case of zero angular momentum with homogeneous and non-homogeneous bias. Before going to the desired system, let us first see what will happen if inside the blister is pure hole- or electron-doped while outside the blister we keep the bias constant $\delta_{>} = 0.25\gamma_1^0$. The energy levels of hole- and electron-doped systems are shown in Figs. 5.19(a, b), respectively, with the corresponding energy bands inside and outside the GQB. The red and blue colors of the energy levels indicate that they belong to the top and bottom layer, respectively, i.e. localized on either layer. We note that each branch belongs to a specific layer and that the layer localization of energy levels is opposite in case of electron- and hole-doped systems. In other words, we can say that the electron- and hole-doped systems attain the symmetry $\epsilon_{0,n}^{e-doped} = -\epsilon_{0,n}^{h-doped}$, however, they are localized on opposite layers. Now we turn to our GQB systems with homogeneous and non-homogeneous. For the homogeneous bias the inter-layer bias is applied to the entire sample, also inside the GQB the electronic states are shifted by $-\delta$ or δ for states on the top or bottom layer, respectively, as shown in the left panel of Fig. 5.1(d). Therefore, the bottom layer is effectively hole-doped

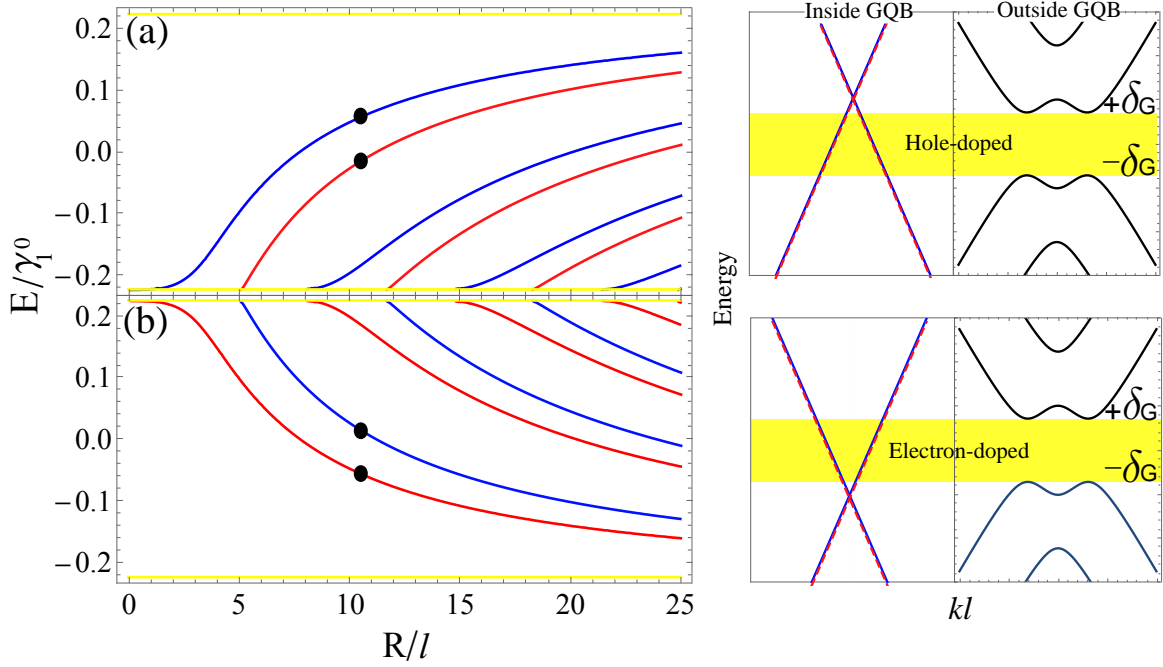


Figure 5.19: (a, b) Show the energy levels where inside the GQB is purely hole- and electron-doped, respectively. Outside the blister the bias is kept $0.25\gamma_1^0$.

while the top layer is electron-doped due to the bias gate. On the other hand, when a non-homogeneous bias is applied the situation is opposite where now the bottom layer is electron-doped and the top layer is electron-doped.

We calculate layer occupation defined by Eq. (5.19) for each state ($m = 0$) with homogeneous and non-homogeneous bias as shown in Figs. 5.20(a, b), respectively. We have color coded the spectrum indicating the layer to which the corresponding eigenstate belongs. From this it is clear that in Fig. 5.20(a) the states with positive energy belong to the top layer, while the negative energy states are positioned at the bottom layer. This is reflected in the behaviour of the confined states; indeed the electron state on the top layer decreases in energy as the GQB increases in size, while the hole state at the top layer increases.

As the two energy levels approach each other, the levels show an anti-crossing at the

radius for which the particles are equally distributed over both layers. This happens every time a hole state from the bottom layer crosses an electron state from the top layer. The level repulsion is consistent with the Wigner-von Neumann theorem and occurs because the wave functions of both states share the same symmetry [170, 171].

As a further proof of the origin of the different energy levels, in Fig. 5.20, we also show the energy levels of a pure hole (dashed) and electron (dot-dashed) doped (the ones labeled by black dots in Fig. 5.19) GQB as a function of the radius of the GQB. In Fig. 5.20(a) the energy levels correspond very closely to the numerically calculated results in the GQB. In this sense, the anti-crossing can be understood as the result of the wave function overlap in the gap of the connected bilayer graphene region as discussed in Fig. 5.5.

In Fig. 5.20(b) we show the energy levels when the bias inside the GQB is opposite to that in the rest of the sample. Since now the top layer is electron doped and the bottom layer is hole doped, the layer occupation is reversed with respect to the previous case with a homogeneous bias. We still observe anti-crossings when electron and hole states become degenerate but they occur at larger radii. From Fig. 5.20(b) we see that the electron states now belong to the bottom layer and the holes belong to the top layer.

Tunability of the GQBs is shown in Fig. 5.21 where the energy levels of a GQB of fixed size are shown as a function of inter-layer bias. The result shows that the number of confined energy levels can be tuned over a wide range by simply changing the applied bias gate. These results can be directly verified by local scanning tunnelling microscopy measurements [140].

Finally, note that the deformation of the top layer to form a GQB is in principle

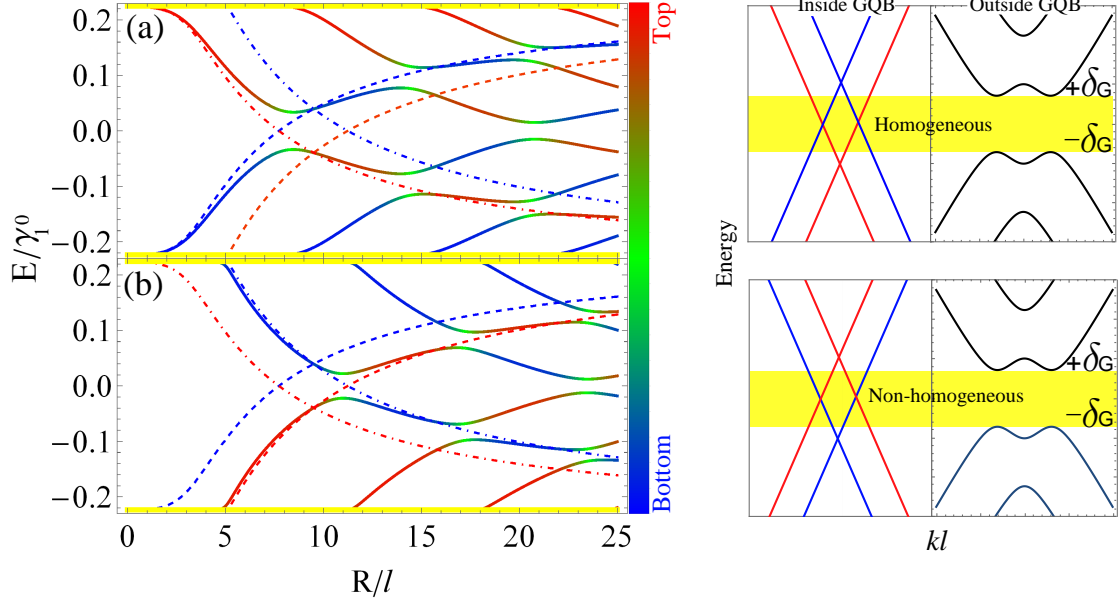


Figure 5.20: Energy levels of a GQB and corresponding layer occupation indicated by the color as shown in the right color bar for angular quantum number $m = 0$. The solid curves in (a) and (b) correspond to the case of a blister with homogenous bias δ or an opposite bias inside the GQB, respectively. Yellow horizontal lines delimit the energy range for confinement, i.e. $E = \pm\delta_G$. In both graphs we have chosen $\delta = 0.25\gamma_1^0$. Dashed and dotted-dashed curves represent the first energy levels of pure holes and electrons confined states inside the blister (the levels labeled by black dots in Fig. 5.19).

associated with a local triaxial strain. Therefore, the inter-atomic distance in the top layer can be slightly larger than the equilibrium distance. This can affect the Fermi velocity v_F of the states in the top layer, however, as discussed by Neek-Amal et al [172], triaxial strain will only introduce pseudo-magnetic fields near the edge of a finite size graphene flake and in the center it is zero. In our case, the size of the GQB is much smaller than the total size of the bilayer graphene sheet and, therefore, strain has a negligible effect on the results obtained in this study.

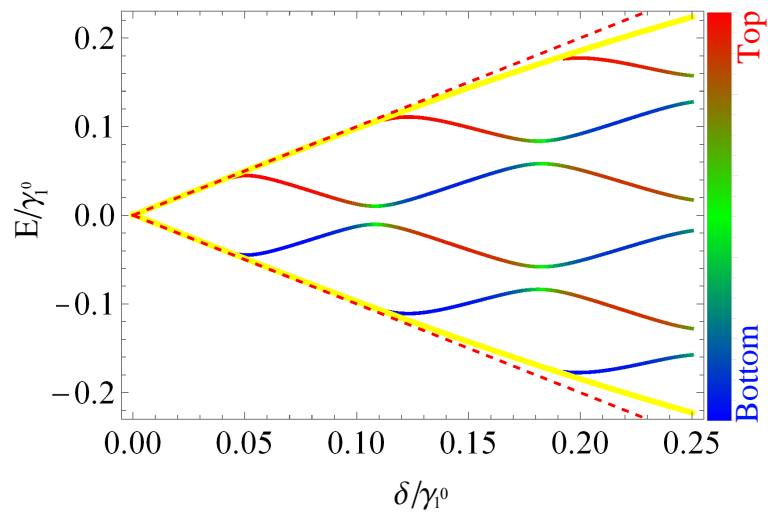


Figure 5.21: Energy levels of GQB as a function of the global homogeneous bias $\delta_{<} = \delta_{>} = \delta$ for $m = 0$ and $R = 21l$. Red dashed and yellow solid curves correspond to $E = \pm\delta$ and $E = \pm\delta_G$, respectively.

CHAPTER 6

ELECTRON COLLIMATION AT VAN DER WAALS DOMAIN WALLS

¹ In this chapter we calculate and compare the collimation of divergent electron beams using two distinct formalisms. In the first formalism, we combine in a semi-classical way quantum mechanical calculation of the transmission and reflection probabilities at a domain wall with a wave propagation described as an optical analog, and in the second formalism we calculate the dynamics of electron wave packets incident on a domain wall to obtain the carriers trajectories.

The wave nature of electrons results in the analogy between optical and electronic transport. For example, it was found that in SLG electrons have a negative refraction index when passing through np junction [173] and, as a result, they converge on the other

¹*The results of this chapter were submitted as:*

Hasan. M. Abdullah, D. R. da Costa M. H. Bahlouli, A. Chaves, F. M. Peeters and B. Van Duppen, "Electron collimation at van der Waals domain walls in bilayer graphene".

side of the junction at the focal point. This behavior is the analog of Veselago lens [174] that was realized earlier in photonic crystals [175,176] and metamaterials [177,178]. These findings led to profound theoretical investigations of electron focusing in SLG [179–181] as well as in AA- [59] and AB-BLG [182] where a valley selective electronic Veselago lens was proposed. Recently, the rigorous control and synthesis of graphene np junctions has reinvigorated the experimental investigations. Two experiments were conducted where a negative refraction was observed for Dirac fermions in graphene [183] and the angle-dependent transmission coefficient was simultaneously measured [184].

Another analogue to light rays across an optical boundary is the collimation of electrons across np junction. This analog becomes perfect in the absence of scattering; however, the disorder-induced scattering has hindered the implementation of such idea. Different proposals have been introduced to maintain collimation of an electron beam such as using graphene superlattices with periodic [185] or disordered [186] potentials. Another route was also established by introducing a mechanical deformation to form a parabolic pn junction [187] or carving pinhole slits in hexagonal Boron Nitride (hBN) encapsulated graphene [188] as well as creating zigzag side contacts [189].

Motivated by the recent experiments where a point source of current in single layer graphene [190,191] and bilayer [192] were achieved, we propose a new system to obtain highly collimated electron beam. We consider a junction composed of a delaminated bilayer graphene on one side and AA-stacked bilayer graphene on the other one as shown in Fig. 6.1(e). Recently, it was shown that such systems exhibit distinct electronic properties [62,120,148,149,193,194]. The energy spectra of SL and AA-BL are shown in Figs. 6.1(c, d), respectively. The AA-BLG spectrum consists of two Dirac cones (lower

and upper cones) shifted by $2\gamma_1$, see blue and red cones in Fig. 6.1(d). These two cones are completely decoupled [59] such that electron- and hole-like carriers are associated with each cone.

We assume that a point source is located in the delaminated bilayer graphene and electrons are emitted and transmitting into AA-BLG. In the low energy regime, the Fermi circle in delaminated region is much smaller than its counterpart in the AA-BLG. This results in a small refraction index forcing the transmitted electrons to nearly move in one-dimension. We used a semiclassical [182, 195–198] approach (SC) to investigate the behavior of electrons in the proposed system and the results were verified by wave-packet dynamics (WD) calculations [185, 186, 199–201]. To control the direction of the collimated beam, we used a magnetic field to steer the electron beam. As a comparison, we also show the collimation in case of only single layer graphene is connected to AA-BL with zigzag or armchair edges as depicted in Fig. 6.1(b).

6.1 Semi-classical dynamics

To describe electron dynamics semi-classically one proceeds in two steps. We first use quantum mechanical formalism to evaluate transmission and reflection probabilities, and second determine the electrons trajectories using the classical approach. This requires to define a general Hamiltonian that describes the delaminated bilayer graphene and AA-BL. Near the K-point and in the basis $\Psi = (\Psi_{A1}, \Psi_{B1}, \Psi_{A2}, \Psi_{B2})^T$, such Hamiltonian can be

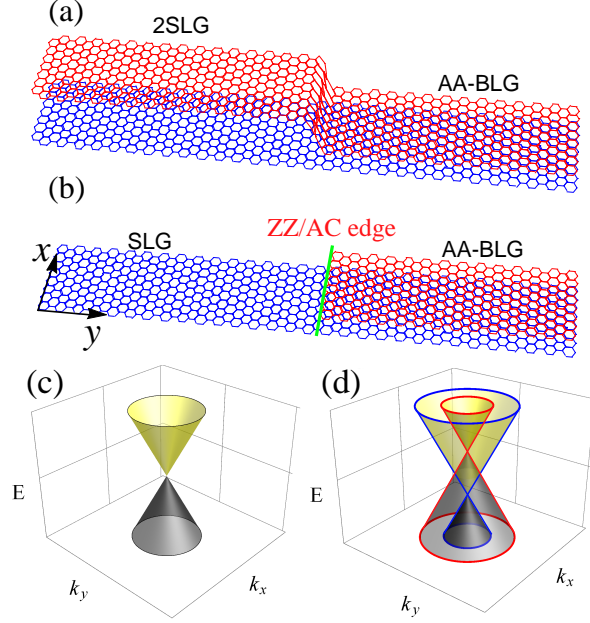


Figure 6.1: Schematic illustration of (a) delaminated bilayer graphene connected to AA-BLG, and (b) single layer graphene attached to AA-BL whose terminated edge of the top layer either zigzag or armchair type. The energy spectrum of (c) single-layer graphene, (d) AA-stacked bilayer graphene. Yellow and Black bands correspond to electrons and holes carriers in SL while in AA-BL they represent electron- and hole-like states. Red and blue bands represents the upper and lower Dirac cones in AA-BL.

written as

$$H = \begin{pmatrix} v_0 & v_F \hat{\pi}_+ & \tau \gamma_1 & 0 \\ v_F \hat{\pi}_- & v_0 & 0 & \tau \gamma_1 \\ \tau \gamma_1 & 0 & v_0 & v_F \hat{\pi}_+ \\ 0 & \tau \gamma_1 & v_F \hat{\pi}_- & v_0 \end{pmatrix}. \quad (6.1)$$

The coupling between the two graphene layers is controlled by the parameter τ through which we can “switch on” or “switch off” the inter-layer hopping between sublattices. For $\tau = 0$, the two layers are decoupled and the Hamiltonian reduces to two independent SL sheets while for AA-stacking we need $\tau = 1$. The domain wall under consideration in this chapter is, therefore, described by a local change in τ from zero to one.

Finally, notice that for the last case of this study, where transport from a single layer

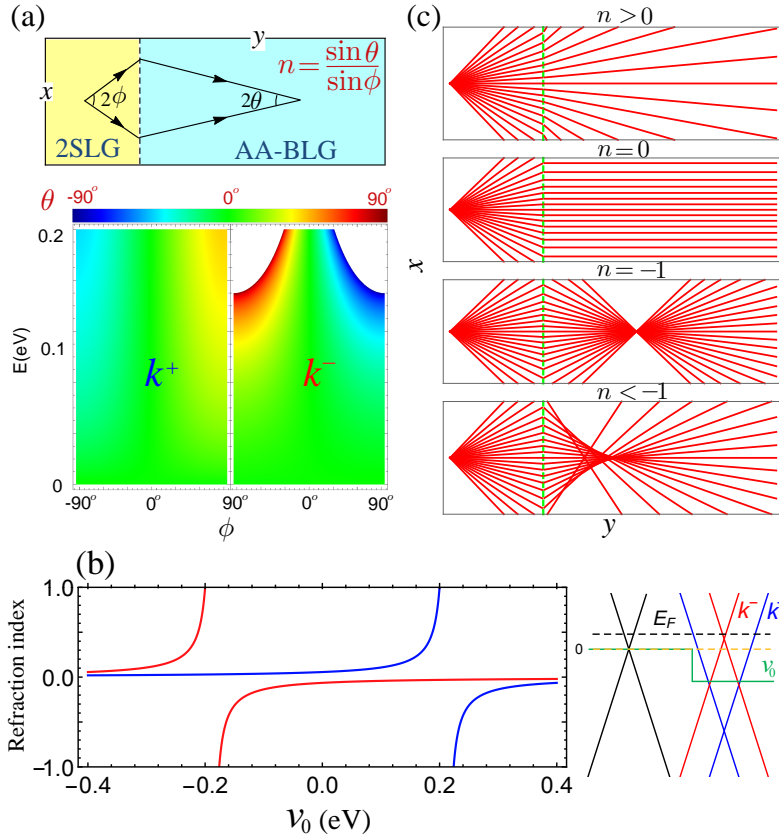


Figure 6.2: (a) Top panel illustrates the 2SLG-BLG junction with an incident and transmitted electron beams in the $x - y$ plane, while the bottom panel shows the transmitted angle θ as a function of the Fermi energy and the incident angle ϕ for SLG-AA junctions with $v_0 = 0.1$ eV. (b) Classical trajectories of an electronic beam impinging on media with different refraction indices. (c) Refraction index with the corresponding band diagram for SLG-AA as a function of the electrostatic potential strength v_0 where the Fermi energy of the incident particles $E = 12\text{meV}$. Blue and red curves correspond to the perspective mode in AA-BLG region.

into an AA-bilayer system is considered, the Hamiltonian in Eq. (6.1) does not suffice. Rather one needs to resort to the 2×2 upper-left block that describes transport in a single layer of graphene. The effect of the atomic structure on the electronic transport is in that case determined through the boundary conditions (B.Cs).

6.1.1 Transmission probabilities and classical trajectories

Before we proceed to show the electron collimation in different systems, we would like to remind the readers of the following: there are three different junctions under the consideration: (I) delaminated bilayer connected to AA-BL (2SL-AA) as depicted in Fig. 6.1(a), (II) single layer graphene connected to AA-BL whose terminated edge can be either zigzag (ZZ-AA) or (III) armchair (AC-AA) as shown in Fig. 6.1(b). So, we need to evaluate the transmission probability across each system. For the system 2Sl-AA, the transmission probability has been calculated earlier in Ch. 3 and given by Eq. (3.15) as follows:

$$T_j^\pm = \frac{2(\epsilon + v_0)(\pm 1 + \epsilon)\text{Re}(k^\pm)}{k_j [(\pm 1 + \epsilon + k^\pm \sec \phi)^2 + (\mp 1 + v_0)^2 \tan^2 \phi]}, \quad (6.2)$$

where k_j is the wave vector in top ($j = 1$) or bottom ($j = 2$) layer in 2SL region, note that both $k_{1,2}$ are the same. While k^\pm are the wave vectors in AA-BL region. For the ZZ-AA and AC-AA systems, the shape of disconnected edge of the bilayer graphene can be either zigzag or armchair. Imposing zigzag boundary can be established through two different ways, namely, ZZ1 and ZZ2 where the sublattices ϕ_{B2} and ϕ_{A2} are set to be zero at the edge, respectively [97]. Note that the two types of the zigzag edges are equivalent in AA-BLG such that $T_{ZZ1}(\phi) = T_{ZZ2}(-\phi)$, where T is the transmission probability, which is not the case for AB-BLG. This can be attributed to the symmetric and asymmetric inter-layer coupling in the AA-BLG and AB-BLG, respectively. For the armchair edge, the single valley approximation is not valid anymore and thus the B.Cs are inter-valley mixed such that [97]

$$\phi_{A2}^K - \phi_{A2}^{K'} = 0, \text{ and } \phi_{B2}^K + \phi_{B2}^{K'} = 0. \quad (6.3)$$

The wavefunction of each sublattice on both side of the junction is presented in Sec. 3.1.2, and by implementing the above BCs we can obtain the transmission probabilities for ZZ-AA and AC-AA. Note that the solutions in both valleys are connected through $\Psi^K(k_y) = \Psi^{K'}(-k_y)$ [202]. To calculate the electron trajectories, we assume a divergent beam starting from a focal point and wave propagation given by the wave vector \vec{k} . Assuming that the propagation is a long the y - direction, the difference in wave vector between the connect and delaminated regions are determined by the relative refractive index as follows [100, 173, 183, 196, 203, 204]

$$n = \frac{\sin \theta}{\sin \phi} = \frac{k_y^j}{k_y^\pm} \quad (6.4)$$

where ϕ and θ are the incident and transmitted angles, respectively, while k_y^j and k_y^\pm are the wave vectors of the incident and transmitted electrons, respectively. For 2SLG-AA junction these wave vectors are given by

$$k_y^j = \frac{E}{v_F \hbar}, \quad k_y^\pm = \frac{1}{v_F \hbar} (\epsilon \pm \gamma_1), \quad (6.5)$$

where $\epsilon = E - v_0$. Using the above equations one can obtain the classical trajectories [182, 197, 198, 205, 206]. In Fig. 6.2(a), we show the system geometry (top panel) and the transmitted angle (bottom panel), according to Eq. (6.4), associated with the lower and upper cones. To achieve perfect collimation, the transmission angle must be zero which corresponds to zero refraction index. The refraction index of electrons incident from SLG and transmitted into gated AA-BLG is shown in Fig. 6.2(b) as a function of the electrostatic gate v_0 . It is clear that the refraction index is almost zero in pristine

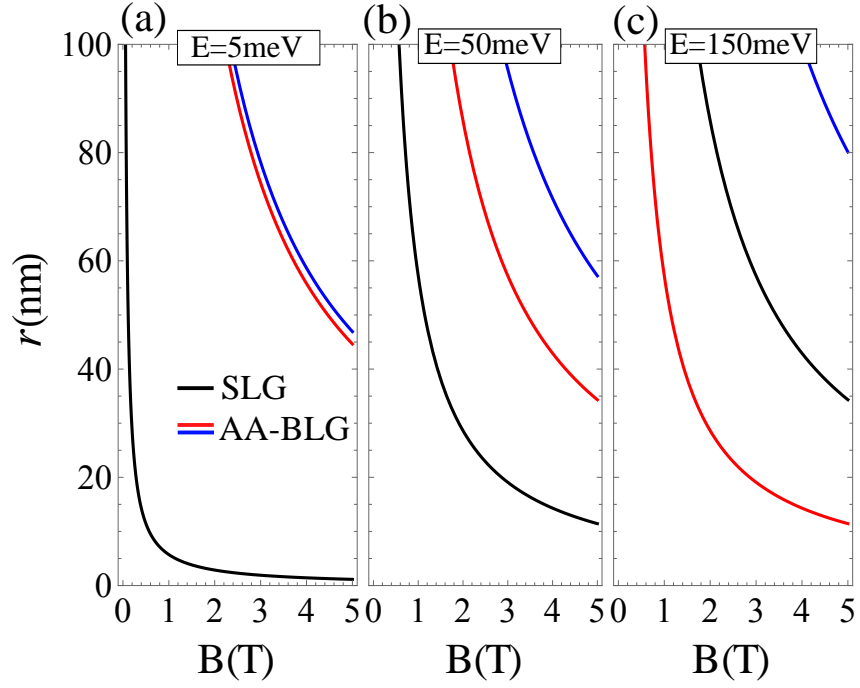


Figure 6.3: Cyclotron radius in pristine single-layer graphene, AA-stacked bilayer graphene for different Fermi energy. The red and blue curves correspond to the upper and lower cones in AA-BLG, respectively.

AA-BLG(i.e. $v_0 = 0$). Henceforth, the gate will be considered zero and the calculations will be based only on pristine AA-BLG. A schematic of the classical trajectories of carriers with different refraction indices is shown in Fig. 6.2(c) and our interest is when $n = 0$ where carriers move in one dimension.

In the presence of a perpendicular magnetic field, the motion of the charge carriers follows a curved trajectory depending on its charge. In the ballistic transport regime where the Fermi wavelength is much smaller than geometric size of the system the charge carriers can be treated as classical point-like particles described by

$$m\vec{a} = -e\vec{v} \times \vec{B}, \quad (6.6)$$

where $|\vec{a}| = |\vec{v}|^2 / r$ and r the cyclotron radius. The effective mass in graphene is [207]

$$m^* = \frac{\hbar^2}{2\pi} \frac{dA(E)}{dE}, \quad (6.7)$$

where $A(E)$ indicates the area in k -space enclosed by a constant energy contour E . This area is circular in single layer graphene and AA-BLG. Hence, from Eqs. (6.6) and (6.7) we obtain the cyclotron radius for AA-BLG and SLG as follows:

$$r_{SL} = \frac{|E|}{ev_F |B|}, \quad (6.8a)$$

$$r_{AA}^{\pm} = \frac{|E \pm \gamma_1|}{ev_F |B|}. \quad (6.8b)$$

Finally, the equations of motion in the $x - y$ plane can be written as

$$x = x_o + r \cos(\theta) - r \cos\left(\frac{v_F}{r} \Delta t + \theta\right), \quad (6.9a)$$

$$y = y_o - r \sin(\theta) + r \sin\left(\frac{v_F}{r} \Delta t + \theta\right), \quad (6.9b)$$

where θ is the transmission angle in the system described in the top panel of Fig. 6.2(a) and Δt is the time interval for the electron calculated once it enters the magnetic field region. Using the above equations we can trace the trajectories of the charge carriers in a magnetic field. In Fig. 6.3, we show the cyclotron radii for SLG and AA-BLG as a function of the magnetic field at different Fermi energies. At low energy, we see that the SLG cyclotron radius is sensitive to the magnetic field while in AA-BLG the cyclotron radii of the lower and upper cones (blue and red curves, respectively) are almost the same,

see Fig. 6.3(a). Note that as a result of the spectrum resemblance of SLG and AA-BLG, we have $r_{AA}^{\pm}(E) = r_{SL}(E \pm \gamma_1)$ which can be inferred from Figs. 6.3(b, c).

6.2 Wave packet dynamics

To calculate the quantum electronic trajectories using a wave packet, we use the nearest-neighbor tight-binding model Hamiltonian for the description of electrons in a bilayer graphene system associated with the split-operator technique [51, 200, 208–216]. We have added to this technique the van der Waals domain walls as a local variation in the inter-layer coupling parameter as described by the parameter τ in Eq. (6.1). Following the numerical procedure developed in details by da Costa et al. in Ref. [51], that is based on the split-operator technique, we calculate the time-evolution of the wave packet for two different setups composed of two disconnected SLG bounded with a AA-stacked BLG and two disconnected SLG.

Among the many different techniques to treat the formal solution of the time-evolution problem, such as Green’s functions techniques [217], here we decided to choose the split-operator technique, since using this approach, one has the possibility of observing the transmitted and reflected trajectories of the total wave packet describing the electron propagating through the system, as well as the separated trajectories in each layer and also the scattered trajectories projected on the different Dirac cones. Moreover, this approach has the advantages of being faster and easier than e.g. Green’s functions techniques and, is pedagogical and physically a transparent approach for the understanding of transport properties in quantum systems, like the ones studied here.

The wave packet propagates in a system obeying the time-dependent Schrödinger equation $i\hbar\partial\Psi(\vec{r},t) = H\Psi(\vec{r},t)$ where the Hamiltonian H is defined in Eq. (6.1). The bilayer graphene flake considered in our tight-binding calculations has 3601×1000 atoms in each layer, thus being a rectangle with dimensions of $\approx 213 \times 443$ nm². Such a large ribbon-like flake is necessary, in order to avoid edge scattering by the wave packet. Therefore, no absorption potential at the boundaries is needed to avoid spurious reflection.

The initial wave packet is assumed as a circularly symmetric Gaussian distribution, multiplied by a four spinor in atomic orbital basis $\Psi = [\psi_{A1}, \psi_{B1}, \psi_{A2}, \psi_{B2}]^T$ and by a plane wave with wave vector $\vec{k} = (k_x, k_y)$, which gives the wave packet a non-zero average momentum, defined as

$$\Psi(\vec{r}, t=0) = N \begin{pmatrix} \psi_{A1} \\ \psi_{B1} \\ \psi_{A2} \\ \psi_{B2} \end{pmatrix} \exp\left[-\frac{(x-x_0)^2 + (y-y_0)^2}{2d^2} + i\vec{k} \cdot \vec{r}\right], \quad (6.10)$$

where N is a normalization factor, (x_0, y_0) are the coordinates of the initial position of center of the Gaussian wave packet, and d_x (d_y) is its width in the x (y)-direction which considered to be the same such that $d_x = d_y = d$. For all studied cases, the width of the Gaussian wave packet was taken as $d = 10$ nm and its initial position as $(x_0, y_0) = (0, -40)$ nm.

The propagation direction is determined by the pseudospin polarization of the wave packet and plays an important role in defining the direction of propagation. It is characterized by the pseudospin polarization angle Θ , such as $(1, e^{i\Theta})^T$ for the components in

each layer. The choice of the angle Θ depends also on which Dirac valley the initial wave packet is situated [51, 200, 209, 212, 215, 216]. Our choice for the propagation direction here is based on the previous knowledge reported in the literature for wave packet time evolution on monolayer [200, 212, 216] and bilayer [51] graphene systems.

For the monolayer case, it was observed that the motion in the y -direction is perfectly vertical, i.e. $\langle x \rangle = 0$ during the whole propagation, whereas the case for propagation along the x -direction is not perfectly horizontal, i.e. $\langle y \rangle$ does not stay the same, as the wave packet slowly drags towards larger y during propagation, this effect is a manifestation of the *Zitterbewegung* [199]. On the other hand, for the motion of an electron in bilayer graphene it was reported that the oscillatory behavior of the average positions and velocities are present along the wave packet dynamics as a consequence of the *Zitterbewegung* effect even for propagations along the y -direction. Although such oscillations can not be avoided, their amplitudes are weaker for wave packet propagation along the y -direction and exhibit a transient behavior that affects mostly at the first time steps at the beginning of the propagation [51]. For these reasons, we assume the y -direction as the preferential propagation direction.

The initial wave vector is taken in the vicinity of the Dirac point $\vec{k} = (k_x, k_y) + \vec{K}$, where $\vec{K} = (0, \pm 4\pi/(3\sqrt{3}a))$ represents the two non-equivalent K and K' points. As we intend to investigate the wave packet trajectories for different propagation angles and their probabilities, we run the simulation for each system configuration, such as e.g. initial propagation angle, initial wave vector and energy, and then as the Gaussian wave packet propagates, we calculate for each time step the transmission (T) and reflection (R) probabilities for finding the electron after ($y > 0$) and before ($y < 0$) the interface at

$y = 0$, respectively, as the integral of the square modulus of the normalized wave packet in that region, given by

$$T = \int_{-\infty}^{\infty} dx \int_0^{\infty} dy |\Psi(x, y)|^2, \quad (6.11a)$$

$$R = \int_{-\infty}^{\infty} dx \int_{-\infty}^0 dy |\Psi(x, y)|^2, \quad (6.11b)$$

and the total average position, i.e. the trajectory of the center of mass $\langle \vec{r} \rangle$ of the wave packet, that is calculated for each time step by computing

$$\langle x \rangle = \int_{-\infty}^{\infty} dx \int_{-\infty}^{\infty} dy |\Psi(x, y)|^2 x, \quad (6.12a)$$

$$\langle y \rangle = \int_{-\infty}^{\infty} dx \int_{-\infty}^{\infty} dy |\Psi(x, y)|^2 y. \quad (6.12b)$$

For larger t , the value of the transmission (reflection) probability integral increases (decreases) with time until it converges to a number. This number is then considered to be the transmission (reflection) probability of such system configuration.

Essentially, a wave packet is actually a combination of plane-waves, where the wave packet width represents a distribution of momenta and, consequently, of energy. In this sense, we are investigating the dynamics of a distribution of plane-waves with different energies around some average value, whose width can be even related e.g. to the temperature of the system. A large wave packet in real space implies a narrow wave packet in k -space, thus it will be composed of a distribution of plane-waves with different velocities and, therefore, exhibits a strong decay in time. We have checked that the wave packet width in real space considered in our calculations is appropriate for the proposed problem,

being large enough to avoid significant changes of the wave packet within the time scale of interest.

As mentioned before, the propagation of charge carriers in AA-BLG can be described as belonging to the upper or lower cone, respectively denoted by red and blue in Fig. 6.1(d). In order to investigate the wave packet scattering to these upper and lower Dirac cones k^+ and k^- one can apply the following unitary transformation to the four-spinor in Eq. (6.10)

$$U = \frac{1}{\sqrt{2}} \begin{pmatrix} 1 & 0 & 1 & 0 \\ 0 & 1 & 0 & 1 \\ 1 & 0 & -1 & 0 \\ 0 & 1 & 0 & -1 \end{pmatrix}, \quad (6.13)$$

that forms symmetric and anti-symmetric combinations of the top and bottom layer wave functions components, i.e.

$$U\Psi = \Psi' = \frac{1}{\sqrt{2}} \begin{pmatrix} \psi_{A2} + \psi_{A1} \\ \psi_{B2} + \psi_{B1} \\ \psi_{A2} - \psi_{A1} \\ \psi_{B2} - \psi_{B1} \end{pmatrix}. \quad (6.14)$$

The symmetric and anti-symmetric components correspond to the k^+ and k^- energy bands (For more details see Refs. [62]). In our results for AA-BLG case, we use the above wave function to calculate the center mass position and the probability amplitudes.

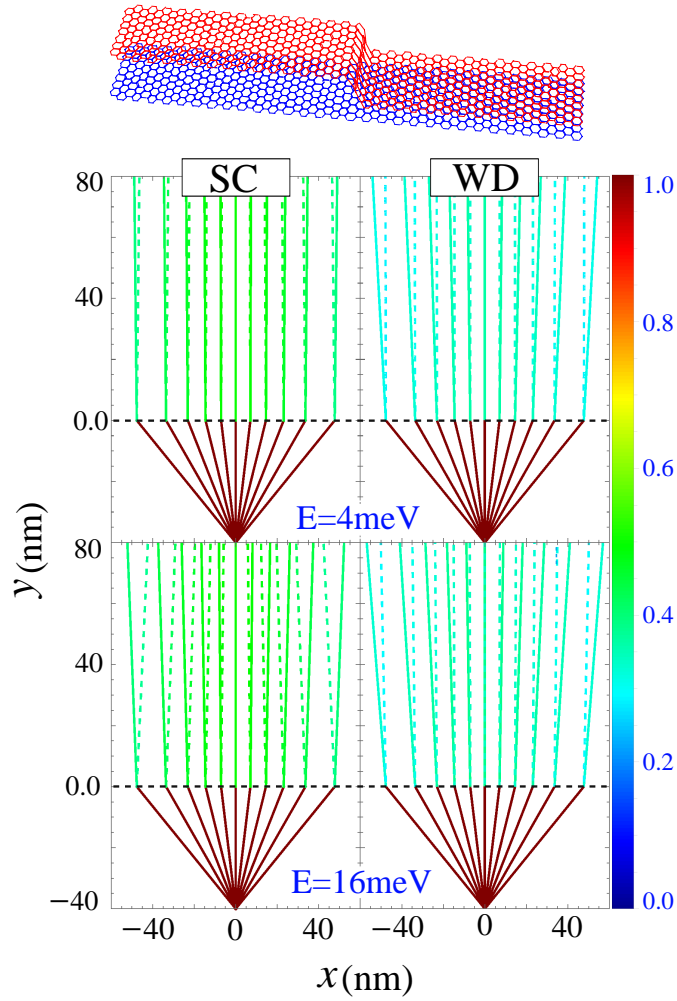


Figure 6.4: Scattering from 2SLG into lower k^+ (solid lines) and upper k^- (dashed lines) cones in AA-BLG with different incident energies. Both 2SLG and AA-BLG are pristine where left and right columns show trajectories obtained from semi-classical and wave-packet dynamics approaches, respectively. Color bar represents the transmission probability.

6.3 Charge carriers collimation

For the SC, the classical trajectories in the three configurations are the same since they depend only on the energy bands on both side of the junction. However, the transmission probability associated with each system is indeed different. On the other hand, for WD the electron trajectories and transmission probability are distinct in 2SLG-AA and AC-AA, while the results for ZZ-AA are not applicable due to the *Zitterbewegung* effect along

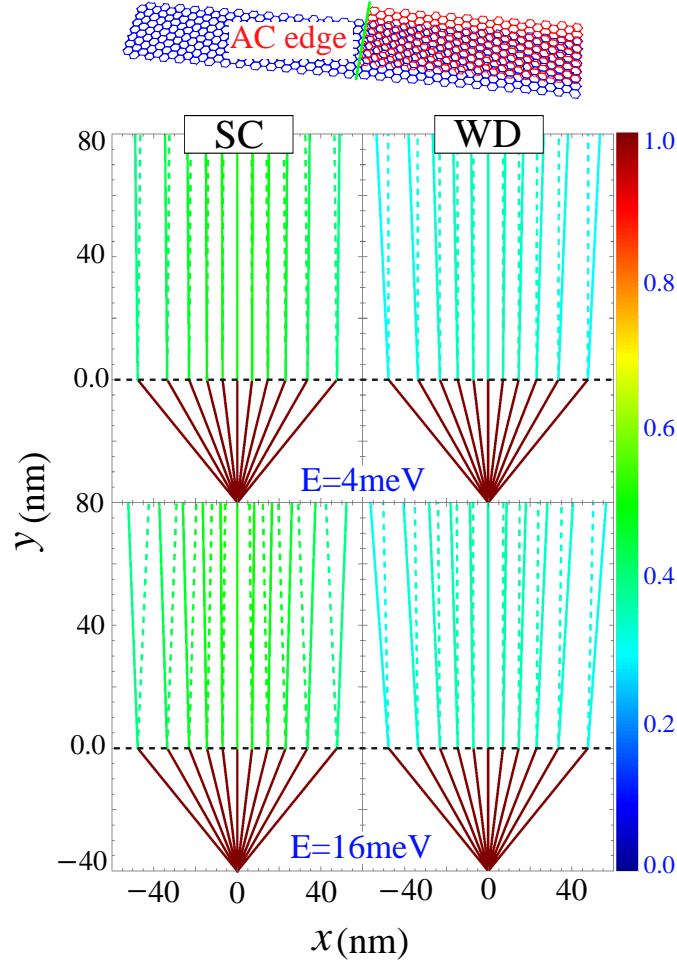


Figure 6.5: The same as in Fig. 6.4 but scattering here from SLG to AA-BLG whose top layer possesses armchair edge at the interface.

the zigzag edge as discussed in Sec. 6.2. Additionally, the fact that the lower and upper cones in AA-BLG are decoupled means that each cone exhibits electron- and hole like carriers. For example, for $\gamma_1 > E > 0$ electron- and hole-like carriers emerge from the lower and upper cones, respectively. Consequently, there will be two different types of collimated beams coming from the two cones as will henceforth be seen.

In Fig. 6.4 we show the carriers collimation through a domain wall that separates 2SLG and AA-BLG obtained from both SC and WD calculations with different Fermi energies. The point source is suited at $y = -40$ nm and then electrons impinging on the

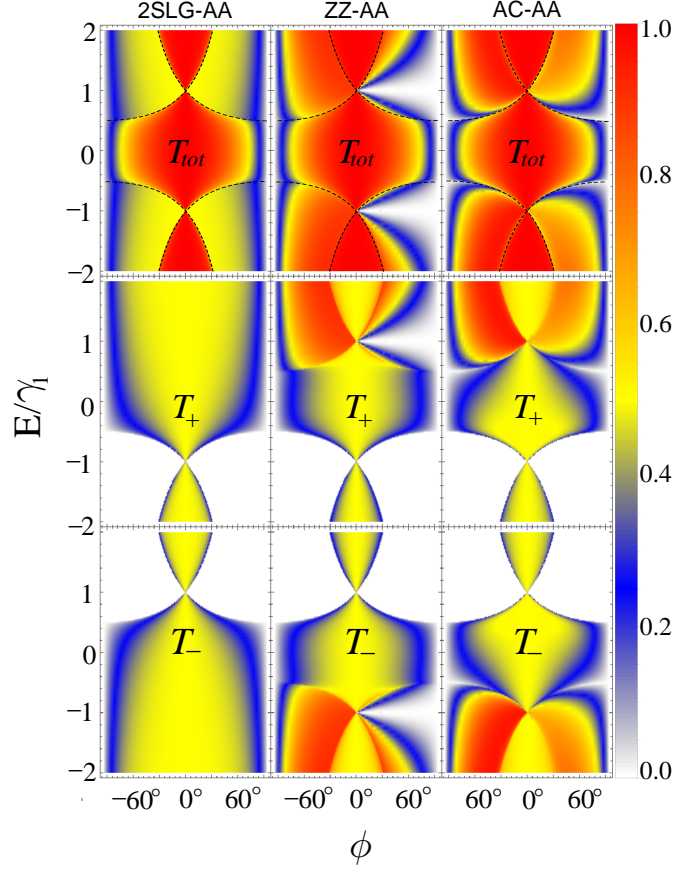


Figure 6.6: Comparison between the transmission probabilities obtained from SC approach for 2SLG-AA and SLG-AA with zigzag- and armchair-edges with $v_0 = 0$. T_+ and T_- are the intra-cone transmission probabilities where carriers scatter into the lower and upper cones, respectively.

domain wall located at the origin ($y = 0$), afterward they scatter to either lower (solid) or upper (dashed) cones with different transmission angles. Both approaches show a strong agreement for carriers trajectories. For example, according to SC the transmission angles associated with $\phi = 50^\circ$ and $E = 4$ meV are $0.17^\circ(-0.18^\circ)$ which coincide with lower (upper) cones, while the WD calculations give the transmitted angles as $4.60^\circ(0.17^\circ)$. The plus and minus signs of the transmission angle reveal that the respective charge carriers will diverge and converge, respectively, at large distance. The transmission probabilities obtained from the two approaches agreed qualitatively as will be explained later. Experimentally, it is often found that some islands in the sample have single layer graphene

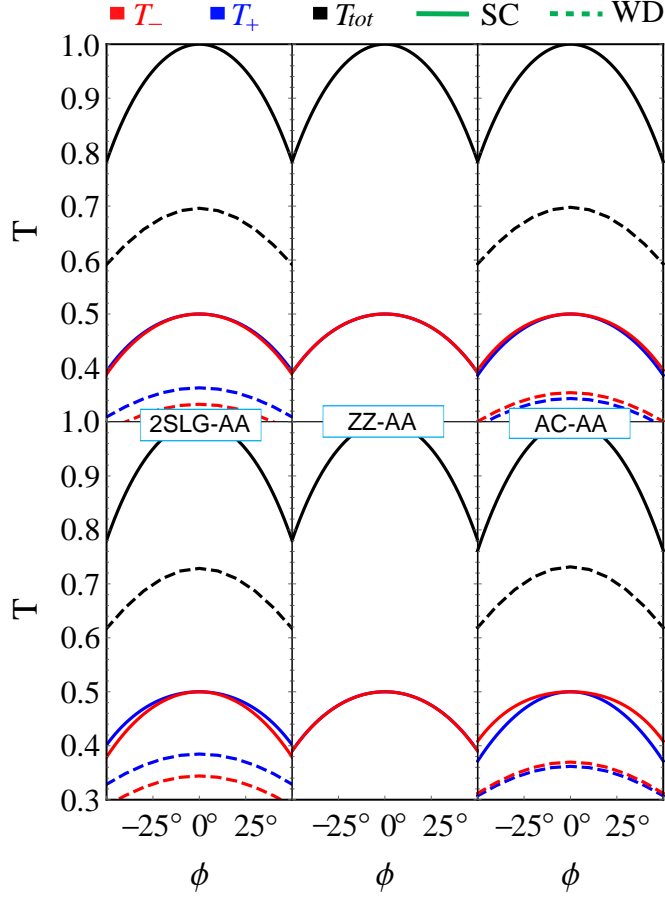


Figure 6.7: Comparison between the transmission probabilities obtained from the wave packet dynamics (WD) and semi-classical approach (SC). Note that for SLG-AA the WD results are only for AC-Edge. The incident energies are (4, 16 meV for top and bottom rows, respectively, while the electrostatic potential $v_0 = 0$.

connected to bilayer graphene flakes. In Fig. 6.5, we show the carriers trajectories through such structure. We notice that even though the transmission probabilities are slightly altered, the system still attains the collimation. We can say that the results are almost identical for 2SLG-AA and AC-AA as depicted in Figs. (6.4, 6.5), respectively.

To validate this understanding and quantitatively determine the degree of agreement, we next carry out a transmission comparison between different systems and approaches. Using the SC dynamics, we show in Fig. 6.6 the intra-cone as well as the total transmission probabilities in 2SLG-AA, ZZ-AA, and AC-AA systems. In the intra-cone channels T_+

and T_- the charge carriers scatter from SLG region into the lower and upper cones, respectively. In 2SLG-AA system the transmission is symmetric with respect to normal incidence, while it becomes asymmetric in ZZ-AA and AC-AA systems at high energy. Such an asymmetry is a manifestation of inversion symmetry breaking of the system. Notice that the transmission remains symmetric in the regions where both modes k^+ and k^- are propagating and the asymmetry feature only appears when one of them becomes evanescent. The critical energy that separates these two domains are given by $E_c^\pm(\phi) = \pm\gamma_1/(1 + \sin\phi)$ and superimposed as dashed-black curves on T_{tot} in Fig. 6.6. The critical energy decreases with increasing the incident angle which reaches $E_c^\pm = \pm\gamma_1/2$ for $\phi = \pi/2$. Therefore, within this energy range, the electron beam is symmetrically collimated. Moreover, within the same energy range the intensity of the collimated beam is almost the same for all systems. Note that in the other valley K' the total transmission probability in ZZ-AA and AC-AA attains the following symmetry $T_K(\phi) = T_{K'}(-\phi)$. There is a trait in Fig. 6.6 that is of particular importance, we see that around the normal incidence both cones contribute equally, i.e. $T_+ = T_- = 1/2$. This suggests that the device can also be used as a 50/50 electronic beam splitter [98].

For comparison with the WD calculations, we show in Fig. 6.7 the transmission probabilities as a function of the incident angle at two different energies. The fundamental characteristics of the system are qualitatively captured by both approaches. Of particular importance is the deviation in the intra-cone transmission at higher incident angles in 2SLG-AA and AC-AA. At normal incidence and in the SC picture, the intra-cone channels are equal, such that $T_+ = T_- = 1/2$, while for oblique angles they start deviating from each other. For 2SLG-AA junction, we notice that $T_+ > T_-$ while it is revers for AC-AA

as can be inferred from the solid blue and red curves in Fig. 6.7. This behaviour is also captured by the WD as can be seen from the dashed blue and red curves. For ZZ-AA, the results are only shown for SC while they are not applicable in WD calculations due to the *Zitterbewegung* effect, as we mentioned earlier. Furthermore, it is clear that transmission amplitudes from SC and WD do not match precisely. For example, at normal incidence T_{tot} is always unity for all systems according to SC, while it is significantly attenuated in WD. In fact, this is expected since the first one consider a plane wave with single value of the energy and momentum. While the latter one uses a wave packet that defines a burst of particles with a momenta distribution $\hbar\Delta k_x$. Thus a perfect transmission is not expected since only part of the wave packet coincides with normal incidence which will be completely transmitted. While the part the associates with $k_x \neq 0$ will be partially transmitted and reflected [216].

6.4 Effect of a magnetic field

So far, we have shown the electron collimation through different configurations in the absence of a magnetic field. Gaining the control over the electron beams direction can be accessed through a magnetic field without losing collimation. To thoroughly examine the effect of the magnetic field on the collimated beams, we assume that the magnetic field is applied only in AA-BLG region, i.e. for $y > 0$. This can be justified by considering the electron point source is located near the domain wall such that the distance is much smaller than r_{SL} . Note that even a global magnetic field is subject to the system, the directional collimation will be maintained as long as $r_{SL} \gg y_0$. To assess the effect of the

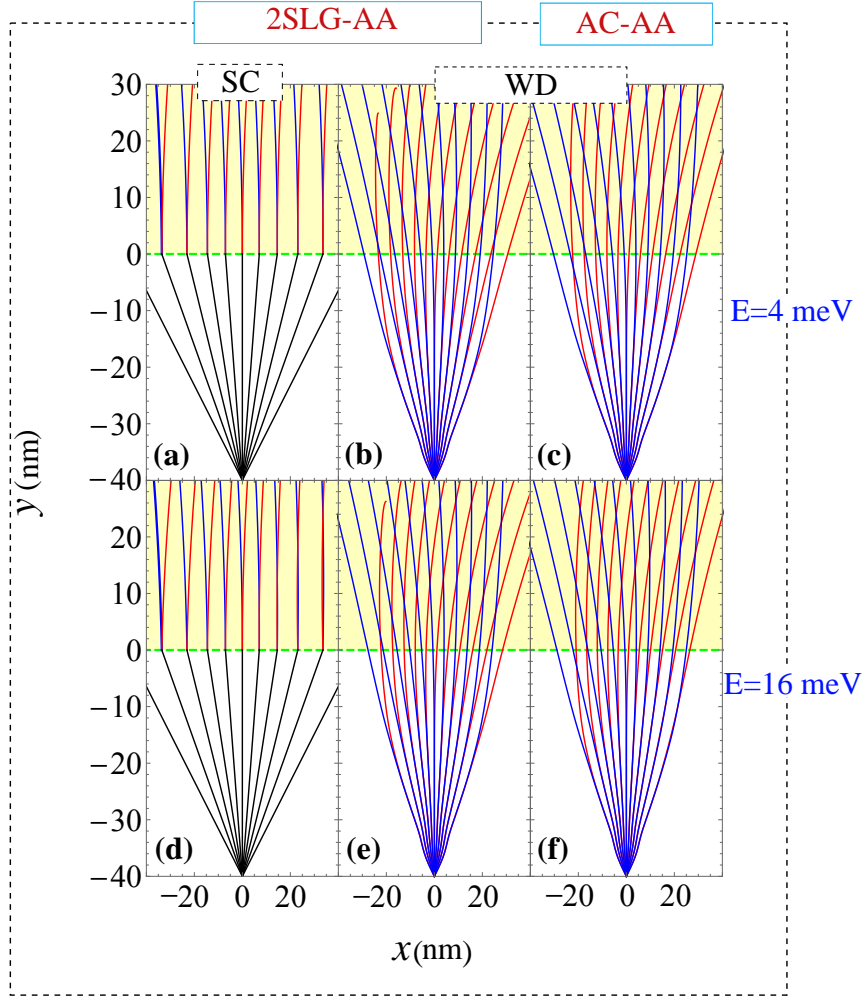


Figure 6.8: Trajectories of the charge carriers scattering from 2SLG into AA-BLG in the presence of a perpendicular magnetic field $B = 1\text{T}$ (only in the yellow region $y > 40\text{ nm}$) in the $x - y$ plane for 2SLG-AA junction with $v_0 = 0$. Red and blue trajectories correspond to the upper k^- and lower k^+ cones as indicated in the top of Fig. 6.1(b).

magnetic field, we calculate the classical trajectories in 2SLG-AA and AC-AA using SC and WD as shown in Fig. 6.8. We consider an electron beams with maximum incidence angles $\phi = \pm 50^\circ$. The essence of SC approach lies in expressing the relative refraction index n in terms of the wave vectors on both sides of the domain wall. Consequently, the classical trajectories for all considered configurations in the current paper are the same; thus, we show in Fig. 6.8. the trajectories for only 2SLG-AA. This is also confirmed by the WD calculation where it shows that the trajectories for 2SLG-AA and AC-AA

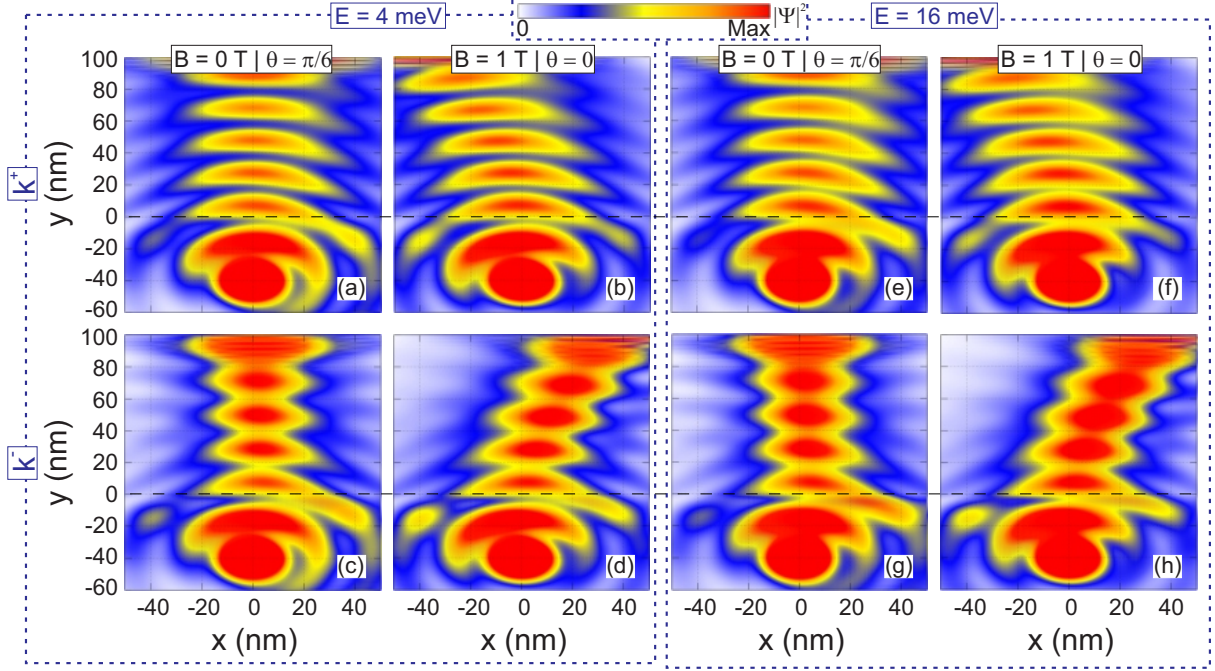


Figure 6.9: Contour plots of the time average for the squared modulus of the Gaussian wave function scattering from 2SLG into AA-stacked BLG with an initial energy (a-b) $E = 4$ meV and (e-h) $E = 16$ meV, for an incident angle $\phi = \pi/6$. The amplitude of the magnetic field was assumed to be (a, c, e, g) $B = 0$ and (b, d, f, h) $B = 1$ T. The Solid-dashed black line indicates the interface of the junction. Top (bottom) panels correspond to the lower k^+ (upper k^-) cones in the AA-BLG spectrum.

are almost the same, see Fig. 6.8(b,c) & (e, f). Both SC and WD show contributions from two types of trajectories which is a direct consequence of the electron- and hole-like nature of the carriers associated with the lower and upper cones, respectively. The two trajectories are steered by the magnetic field in diametrically opposite directions.

Finally, to clearly visualize the effect of the magnetic field on the whole wave packet, we show in Fig. 6.9 the contour plots of the time average for the squared modulus of the Gaussian wave for 2SLG-AA. We set the incidence angle in all panels to be $\phi = 30^\circ$ and show the scattering to each cone separately in the presence and absence of the magnetic field. For $B = 0$, once the wave packet reaches the domain wall it starts moving nearly along the $y-$ direction, see Figs. 6.9(a, c) & (e, g). In the presence of finite magnetic

field, the wave packets corresponding to lower and upper cones are steered in different directions without losing the collimation. Note that the wave packet feels the magnetic field even before reaching the interface and this can be clearly also seen in Fig. 6.8. Such behaviour is a manifestation of the quantum non-locality nature of the charge carriers in graphene.

CHAPTER 7

CONCLUSIONS

In the current thesis, we theoretically investigated the electronic and transport properties of locally delaminated bilayer graphene. Electron tunneling, confined states, and collimation in this system are of particular importance. During this study, we solved the Dirac-Weyl equation to explore the different properties in the proposed system.

In **chapter 2**, we briefly reviewed the electronic properties of graphene and its bilayered systems. In particular, we focused on those properties that are relevant to our research such as band structure, chirality, and Klein tunneling in single layer graphene and its bilayer with AA- and AB-stackings.

In **chapter 3**, we used the four-band model we obtained the conductance, transmission and reflection probabilities through single and double domain walls separating delaminated and AA/AB-stacked bilayer graphene. We discussed in detail the scattering mechanism from detached layers to bilayer graphene and presented compact analytical formulae for the transmission probabilities across single domain walls. These results showed that one can find the inter-layer coupling strength solely through measuring the conductance.

We found that an electrostatic potential applied to AB-BL, in an 2SL-AB junction, breaks the layer symmetry in the single-valley transmission probability channels. Such asymmetry originates from the asymmetric coupling in AB-BL and arises as a consequence of the mismatch in energy between the 2SL and AB-BL Dirac cones caused by the electrostatic potentials applied to the AB-BL region. Layer asymmetry exists when only one propagating mode is present and hence is not seen in configurations consisting of AA-BL where the entire energy range is associated with two transport channels.

We have also evaluated the robustness of chirality-induced properties, such as Klein tunnelling and anti-Klein tunnelling, to scattering on domains without inter-layer coupling. We found that in domain walls separating 2SL and AA-BL, Klein tunnelling is still preserved. On the other hand, for domain walls separating 2SL and AB-BL, the well known anti-Klein tunnelling in AB-BL is not preserved any more, but neither is Klein tunnelling itself. Moreover, in two domain walls separating three regions whose inter-layer coupling is all different, i.e. the AA-2SL-AB case, we find that although perfect Klein tunnelling does not hold, the tunnelling does not depend on the thickness of the 2SL region either. This remarkable effect is attributed to a conservation of parity of the modes. Finally, we showed that for a given sample with unknown sizes of local stacking domains, the average inter-layer coupling can be estimated through quantum transport measurements.

In **chapter 4**, we have investigated a system consisting of two locally coupled graphene sheets and have shown that it is a promising candidate for application as a layer switch. We showed that independently of the BLG stacking configuration, the layer selectivity can be controlled by an applied gate potential. The different peculiarities associated to the

two stacking configurations for achieving maximal switching behaviour were discussed. While our final results are calculated for abrupt interfaces, we showed that a smooth interface does not affect our findings.

In **chapter 5**, we used the continuum model to analytically calculate the wave functions and thus the discrete energy levels of bound states trapped in a locally delaminated bilayer graphene system that is called GQB. We have investigated the energy spectrum and eigenstates of such system under the application of an electrostatic potential difference between the graphene layers. GQBs are unique electrostatic tunable graphene-based quantum dots. They support bound states with diverging lifetime that can be elegantly realized by means of only electrostatic gating and are robust against changes in the GQBs morphology. A big advantage of GQBs is the tunability through gate variations. Also, we pointed out that by changing the contents of the blisters, one could access another degree of freedom to establish quantum dot systems with specific energy levels as required for different applications. Therefore, we expect that the GQBs can form the basis of a new subfield in graphene physics where the graphene sheet structure is used together with electric fields to achieve tunable quantum systems.

In **chapter 6**, we have shown that electrons can be highly collimated through locally delaminated AA-BLG systems. We considered two domain walls that separate AA-BLG and either 2SLG or SLG with zigzag and armchair edges. We have presented SC model that combines quantum mechanical calculations of the transmission probabilities with classical trajectories to explain the electron scattering. The SC model takes advantage of representing the refraction index in terms of the wave vectors on both sides of the domain wall. This results in identical trajectories for the two considered domain walls whose

transmission probabilities are different. We found that charge carriers associated with lower and upper cones are distinctly collimated in two beams. In particular, both beams can be bent in opposite directions using a magnetic field. To validate the SC approach, we carried out WD calculations that showed a strong quantitative and qualitative agreement with SC model. Furthermore, the reported collimation is robust against the types of edges and domain walls.

Our study reveals that the presence of the local domain wall in bilayer graphene samples changes the electronic and transport properties significantly. Finally, we hope that the results presented in this study may shed light on the design of electronic devices based on bilayer graphene.

APPENDICES

A Transmission across single domain wall

The transmission probabilities are calculated by applying appropriate boundary conditions at the 2SL-BL interfaces together with the transfer matrix. After some cumbersome algebra, we obtain for 2SL-AB

$$T_j^\pm = 4\text{Re}(k^\pm) \frac{\eta \left[\eta^2 + (\text{Im}(k^\mp) + \kappa_j v_0 \sin \phi)^2 \right]}{C_0 + \sum_{m=1}^4 C_m \cos(m\phi)}, \quad (\text{A1})$$

where

$$C_0 = 2 (\text{Im}(k^\mp) \text{Re}(k^\pm))^2 + \epsilon^2 (\text{Im}^2(k^\mp) + \text{Re}^2(k^\pm)) + \Gamma_1,$$

$$\Gamma_1 = 2v_0^4 - 4v_0^3 E + 5v_0^2 E^2 - 3v_0 E^3 + \frac{3}{4} E^4,$$

$$C_1 = -\epsilon \text{Re}(k^\pm) \left[4(v_0^2 + \text{Im}^2(k^\mp)) - 6v_0 E + 3E^2 \right],$$

$$C_2 = \epsilon^2 (\text{Im}^2(k^\mp) + \text{Re}^2(k^\pm)) + \Gamma_2,$$

$$\Gamma_2 = E(-4v_0^3 + 6v_0^2E - 4v_0E^2 + E^3),$$

$$C_3 = \text{Re}(k^\pm)E(2v_0^2 - 3v_0E + E^2),$$

$$C_4 = \frac{1}{4}E^2(E - 2v_0)^2.$$

Similarly, the transmission probabilities for the AB-2SL system are obtained as

$$T_\pm^j = 4\text{Re}(k_j)k^\pm \frac{\lambda[\mu^\pm + \kappa_j v_0 \sin \phi \text{Im}(k^\mp)]}{|Q^\pm|^2}, \quad (\text{A2})$$

$$\mu^\pm = \frac{\epsilon \left(\text{Im}^2(k^\mp) + E^2 \right) - E(\pm 1 + E)(E + v_0) \sin^2 \phi}{2\sqrt{E(\pm 1 + E)}},$$

$$\lambda = E\sqrt{E(\pm 1 + E)},$$

$$Q^\pm = \frac{1}{2}[z_0 - z_1(k^\pm + i\text{Im}(k^\mp)) + z_2k^\pm \text{Im}(k^\mp)],$$

with

$$z_0 = 2i[v_0\alpha - ik_jE][\alpha(-ik_j + \alpha) + \epsilon E],$$

$$z_1 = E[(ik_j + \alpha)^2 - \epsilon^2],$$

and finally

$$z_2 = 2\epsilon[ik_j + \alpha],$$

where $\alpha = \sqrt{E^2 \pm E} \sin \phi$.

REFERENCES

- [1] A. C. Neto, F. Guinea, and N. M. Peres, *Drawing conclusions from graphene*, Phys. World **19**, 33 (2006).
- [2] N. Savage, *Materials science: Super carbon*, Nature **483**, S30 (2012).
- [3] M. Barbier, *Transport properties of nanostructures and superlattices on single-layer and bilayer graphene*, Ph.D. thesis, University of Antwerp, 2012.
- [4] A. Bostwick, T. Ohta, T. Seyller, K. Horn, and E. Rotenberg, *Quasiparticle dynamics in graphene*, Nat. Phys. **3**, 36 (2007).
- [5] M. R. Masir, *Electronic properties of graphene in inhomogeneous magnetic fields*, Ph.D. thesis, University of Antwerp, 2012.
- [6] A. K. Geim, *Graphene prehistory*, Phys. Scr. **T146**, 014003 (2012).
- [7] H. Boehm, R. Setton, and E. Stumpp, *Nomenclature and terminology of graphite intercalation compounds*, Carbon **24**, 241 (1986).
- [8] B. C. Brodie, *On the Atomic Weight of Graphite*, Philos. Trans. Roy. Soc. London **149**, 249 (1859).

- [9] D. R. Dreyer, S. Park, C. W. Bielawski, and R. S. Ruoff, *The chemistry of graphene oxide*, Chem. Soc. Rev. **39**, 228 (2010).
- [10] P. R. Wallace, *The Band Theory of Graphite*, Phys. Rev. **71**, 622 (1947).
- [11] H. P. Boehm, A. Clauss, G. O. Fischer, and U. Hofmann, *Das Adsorptionsverhalten sehr dünner Kohlenstoff-Folien*, Z. Anorg. Allg. Chem. **316**, 119 (1962).
- [12] K. S. Novoselov, A. K. Geim, S. V. Morozov, D. Jiang, Y. Zhang, S. V. Dubonos, I. V. Grigorieva, and A. A. Firsov, *Electric Field Effect in Atomically Thin Carbon Films*, Science **306**, 666 (2004).
- [13] M. L. Sadowski, G. Martinez, M. Potemski, C. Berger, and W. A. de Heer, *Landau Level Spectroscopy of Ultrathin Graphite Layers*, Phys. Rev. Lett. **97**, 266405 (2006).
- [14] O. Klein, *Die Reflexion von Elektronen an einem Potentialsprung nach der relativistischen Dynamik von Dirac*, Zeitschrift für Physik **53**, 157 (1929).
- [15] K. S. Novoselov, A. K. Geim, S. V. Morozov, D. Jiang, M. I. Katsnelson, I. V. Grigorieva, S. V. Dubonos, and A. A. Firsov, *Two-dimensional gas of massless Dirac fermions in graphene*, Nature (London) **438**, 197 (2005).
- [16] Y. Zhang, Y.-W. Tan, H. L. Stormer, and P. Kim, *Experimental observation of the quantum Hall effect and Berry's phase in graphene*, Nature (London) **438**, 201 (2005).
- [17] K. S. Novoselov, E. McCann, S. V. Morozov, V. I. Fal'ko, M. I. Katsnelson, U. Zeitler, D. Jiang, F. Schedin, and A. K. Geim, *Unconventional quantum Hall effect and Berry's phase of 2 in bilayer graphene*, Nat. Phys. **2**, 177 (2006).

- [18] K. S. Novoselov, Z. Jiang, Y. Zhang, S. V. Morozov, H. L. Stormer, U. Zeitler, J. C. Maan, G. S. Boebinger, P. Kim, and A. K. Geim, *Room-Temperature Quantum Hall Effect in Graphene*, *Science* **315**, 1379 (2007).
- [19] A. H. C. Neto, F. Guinea, N. M. R. Peres, K. S. Novoselov, and A. K. Geim, *The electronic properties of graphene*, *Rev. Mod. Phys.* **81**, 109 (2009).
- [20] F. Zhang, J. Jung, G. A. Fiete, Q. Niu, and A. H. MacDonald, *Spontaneous Quantum Hall States in Chirally Stacked Few-Layer Graphene Systems*, *Phys. Rev. Lett.* **106**, 156801 (2011).
- [21] D. Jariwala, V. K. Sangwan, L. J. Lauhon, T. J. Marks, and M. C. Hersam, *Carbon nanomaterials for electronics, optoelectronics, photovoltaics, and sensing*, *Chem. Soc. Rev.* **42**, 2824 (2013).
- [22] E. McCann and M. Koshino, *The electronic properties of bilayer graphene*, *Rep. Prog. Phys.* **76**, 056503 (2013).
- [23] C. Bena and G. Montambaux, *Remarks on the tight-binding model of graphene*, *New J. Phys.* **11**, 095003 (2009).
- [24] S. Reich, J. Maultzsch, C. Thomsen, and P. Ordejón, *Tight-binding description of graphene*, *Phys. Rev. B* **66**, 035412 (2002).
- [25] H. R. (Ed.), in *Graphene Nanoelectronics: Metrology, Synthesis, Properties and Applications* (Berlin: Springer-Verlag, 2012), pp. 237–275.
- [26] M. O. Goerbig, *Electronic properties of graphene in a strong magnetic field*, *Rev. Mod. Phys.* **83**, 1193 (2011).

- [27] D. L. Miller, K. D. Kubista, G. M. Rutter, M. Ruan, W. A. de Heer, P. N. First, and J. A. Stroscio, *Observing the Quantization of Zero Mass Carriers in Graphene*, *Science* **324**, 924 (2009).
- [28] G. Li, A. Luican, and E. Y. Andrei, *Scanning Tunneling Spectroscopy of Graphene on Graphite*, *Phys. Rev. Lett.* **102**, 176804 (2009).
- [29] Y. J. Song, A. F. Otte, Y. Kuk, Y. Hu, D. B. Torrance, P. N. First, W. A. de Heer, H. Min, S. Adam, M. D. Stiles, A. H. MacDonald, and J. A. Stroscio, *High-resolution tunnelling spectroscopy of a graphene quartet*, *Nature* **467**, 185 (2010).
- [30] L.-J. Yin, K.-K. Bai, W.-X. Wang, S.-Y. Li, Y. Zhang, and L. He, *Landau quantization of Dirac fermions in graphene and its multilayers*, *Frontiers of Physics* **12**, (2017).
- [31] E. Y. Andrei, G. Li, and X. Du, *Electronic properties of graphene: a perspective from scanning tunneling microscopy and magnetotransport*, *Rep. Prog. Phys.* **75**, 056501 (2012).
- [32] Y. Zhang, V. W. Brar, C. Girit, A. Zettl, and M. F. Crommie, *Origin of spatial charge inhomogeneity in graphene*, *Nat. Phys.* **5**, 722 (2009).
- [33] Y. Zhang, V. W. Brar, F. Wang, C. Girit, Y. Yayon, M. Panlasigui, A. Zettl, and M. F. Crommie, *Giant phonon-induced conductance in scanning tunnelling spectroscopy of gate-tunable graphene*, *Nat. Phys.* **4**, 627 (2008).

- [34] H. W. Kim, W. Ko, J. Ku, I. Jeon, D. Kim, H. Kwon, Y. Oh, S. Ryu, Y. Kuk, S. W. Hwang, and H. Suh, *Nanoscale control of phonon excitations in graphene*, Nat. Commun. **6**, (2015).
- [35] F. D. Natterer, Y. Zhao, J. Wyrick, Y.-H. Chan, W.-Y. Ruan, M.-Y. Chou, K. Watanabe, T. Taniguchi, N. B. Zhitenev, and J. A. Stroscio, *Strong Asymmetric Charge Carrier Dependence in Inelastic Electron Tunneling Spectroscopy of Graphene Phonons*, Phys. Rev. Lett. **114**, 245502 (2015).
- [36] N. Levy, S. A. Burke, K. L. Meaker, M. Panlasigui, A. Zettl, F. Guinea, A. H. C. Neto, and M. F. Crommie, *Strain-Induced Pseudo-Magnetic Fields Greater Than 300 Tesla in Graphene Nanobubbles*, Science **329**, 544 (2010).
- [37] Y. Wang, D. Wong, A. V. Shytov, V. W. Brar, S. Choi, Q. Wu, H.-Z. Tsai, W. Regan, A. Zettl, R. K. Kawakami, S. G. Louie, L. S. Levitov, and M. F. Crommie, *Observing Atomic Collapse Resonances in Artificial Nuclei on Graphene*, Science **340**, 734 (2013).
- [38] S.-Y. Li, K.-K. Bai, W.-J. Zuo, Y.-W. Liu, Z.-Q. Fu, W.-X. Wang, Y. Zhang, L.-J. Yin, J.-B. Qiao, and L. He, *Tunneling Spectra of a Quasifreestanding Graphene Monolayer*, Phys. Rev. Appl **9**, 054031 (2018).
- [39] C. W. J. Beenakker, *Colloquium: Andreev reflection and Klein tunneling in graphene*, Rev. Mod. Phys. **80**, 1337 (2008).
- [40] P. A. M. Dirac, *The Quantum Theory of the Electron*, Proceedings of the Royal Society A: Mathematical, Physical and Engineering Sciences **117**, 610 (1928).

- [41] A. Rycerz, J. Tworzydło, and C. W. J. Beenakker, *Valley filter and valley valve in graphene*, Nat. Phys. **3**, 172 (2007).
- [42] J. Tworzydło, I. Snyman, A. R. Akhmerov, and C. W. J. Beenakker, *Valley-isospin dependence of the quantum Hall effect in a graphene-p-n-junction*, Phys. Rev. B **76**, 035411 (2007).
- [43] D. Gunlycke and C. T. White, *Graphene Valley Filter Using a Line Defect*, Phys. Rev. Lett. **106**, (2011).
- [44] J. D. Bernal, *The Structure of Graphite*, Proc. R. Soc. A **106**, 749 (1924).
- [45] E. McCann, D. S. Abergel, and V. I. Fal'ko, *Electrons in bilayer graphene*, Solid State Commun. **143**, 110 (2007).
- [46] J. Cserti, A. Csordás, and G. Dávid, *Role of the Trigonal Warping on the Minimal Conductivity of Bilayer Graphene*, Phys. Rev. Lett. **99**, 066802 (2007).
- [47] B. Van Duppen and F. M. Peeters, *Four-band tunneling in bilayer graphene*, Phys. Rev. B **87**, 205427 (2013).
- [48] T. Ohta, A. Bostwick, T. Seyller, K. Horn, and E. Rotenberg, *Controlling the Electronic Structure of Bilayer Graphene*, Science **313**, 951 (2006).
- [49] E. V. Castro, K. S. Novoselov, S. V. Morozov, N. M. R. Peres, J. M. B. L. dos Santos, J. Nilsson, F. Guinea, A. K. Geim, and A. H. C. Neto, *Electronic properties of a biased graphene bilayer*, J. Phys.: Condens. Matter **22**, 175503 (2010).

- [50] Y. Zhang, T.-T. Tang, C. Girit, Z. Hao, M. C. Martin, A. Zettl, M. F. Crommie, Y. R. Shen, and F. Wang, *Direct observation of a widely tunable bandgap in bilayer graphene*, Nature **459**, 820 (2009).
- [51] D. R. da Costa, A. Chaves, S. H. R. Sena, G. A. Farias, and F. M. Peeters, *Valley filtering using electrostatic potentials in bilayer graphene*, Phys. Rev. B **92**, 045417 (2015).
- [52] J. W. González, H. Santos, M. Pacheco, L. Chico, and L. Brey, *Electronic transport through bilayer graphene flakes*, Phys. Rev. B **81**, 195406 (2010).
- [53] M. Zarenia, A. Chaves, G. A. Farias, and F. M. Peeters, *Energy levels of triangular and hexagonal graphene quantum dots: A comparative study between the tight-binding and Dirac equation approach*, Phys. Rev. B **84**, 245403 (2011).
- [54] A. N. Pal and A. Ghosh, *Resistance Noise in Electrically Biased Bilayer Graphene*, Phys. Rev. Lett. **102**, 126805 (2009).
- [55] A. Varlet, M.-H. Liu, V. Krueckl, D. Bischoff, P. Simonet, K. Watanabe, T. Taniguchi, K. Richter, K. Ensslin, and T. Ihn, *Fabry-Pérot Interference in Gapped Bilayer Graphene with Broken Anti-Klein Tunneling*, Phys. Rev. Lett. **113**, 116601 (2014).
- [56] J. L. Mañes, F. Guinea, and M. A. H. Vozmediano, *Existence and topological stability of Fermi points in multilayered graphene*, Phys. Rev. B **75**, 155424 (2007).
- [57] E. McCann and V. I. Fal'ko, *Landau-Level Degeneracy and Quantum Hall Effect in a Graphite Bilayer*, Phys. Rev. Lett. **96**, 086805 (2006).

- [58] I. Lobato and B. Partoens, *Multiple Dirac particles in AA-stacked graphite and multilayers of graphene*, Phys. Rev. B **83**, 165429 (2011).
- [59] M. Sanderson, Y. S. Ang, and C. Zhang, *Klein tunneling and cone transport in AA-stacked bilayer graphene*, Phys. Rev. B **88**, 245404 (2013).
- [60] Z. Q. Li, E. A. Henriksen, Z. Jiang, Z. Hao, M. C. Martin, P. Kim, H. L. Stormer, and D. N. Basov, *Band Structure Asymmetry of Bilayer Graphene Revealed by Infrared Spectroscopy*, Phys. Rev. Lett. **102**, 037403 (2009).
- [61] Y. Xu, X. Li, and J. Dong, *Infrared and Raman spectra of AA-stacking bilayer graphene*, Nanotechnology **21**, 065711 (2010).
- [62] H. M. Abdullah, B. Van Duppen, M. Zarenia, H. Bahlouli, and F. M. Peeters, *Quantum transport across van der Waals domain walls in bilayer graphene*, J. Phys.: Condens. Matter **29**, 425303 (2017).
- [63] M. I. Katsnelson, K. S. Novoselov, and A. K. Geim, *Chiral tunnelling and the Klein paradox in graphene*, Nat. Phys. **2**, 620 (2006).
- [64] P. E. Allain and J. N. Fuchs, *Klein tunneling in graphene: optics with massless electrons*, Eur. Phys. J. B **83**, 301 (2011).
- [65] B. Van Duppen and F. M. Peeters, *Klein paradox for a pn junction in multilayer graphene*, Europhys. Lett. **102**, 27001 (2013).
- [66] N. Stander, B. Huard, and D. Goldhaber-Gordon, *Evidence for Klein Tunneling in Graphene-p-n Junctions*, Phys. Rev. Lett. **102**, 026807 (2009).

- [67] A. F. Young and P. Kim, *Quantum interference and Klein tunnelling in graphene heterojunctions*, Nat. Phys. **5**, 222 (2009).
- [68] A. Rahman, J. W. Guikema, N. M. Hassan, and N. Marković, *Angle-dependent transmission in graphene heterojunctions*, Appl. Phys. Lett. **106**, 013112 (2015).
- [69] J. M. B. L. dos Santos, N. M. R. Peres, and A. H. C. Neto, *Graphene Bilayer with a Twist: Electronic Structure*, Phys. Rev. Lett. **99**, 256802 (2007).
- [70] E. J. Mele, *Commensuration and interlayer coherence in twisted bilayer graphene*, Phys. Rev. B **81**, 161405(R) (2010).
- [71] J. M. B. L. dos Santos, N. M. R. Peres, and A. H. C. Neto, *Continuum model of the twisted graphene bilayer*, Phys. Rev. B **86**, 155449 (2012).
- [72] A. O. Sboychakov, A. L. Rakhmanov, A. V. Rozhkov, and F. Nori, *Electronic spectrum of twisted bilayer graphene*, Phys. Rev. B **92**, 075402 (2015).
- [73] M. Van der Donck, C. D. Beule, B. Partoens, F. M. Peeters, and B. Van Duppen, *Piezoelectricity in asymmetrically strained bilayer graphene*, 2D Mater. **3**, 035015 (2016).
- [74] M. Van der Donck, F. M. Peeters, and B. Van Duppen, *Comment on “Creating in-plane pseudomagnetic fields in excess of 1000 T by misoriented stacking in a graphene bilayer”*, Phys. Rev. B **93**, 247401 (2016).
- [75] Long-Jing, S.-Y. Li, J.-B. Qiao, W.-J. Zuo, and L. He, *Spatial variation of energy gap and Landau levels around gapped bilayer graphene domain walls*, arXiv:1509.04405 (2015).

- [76] W. Yan, S.-Y. Li, L.-J. Yin, J.-B. Qiao, J.-C. Nie, and L. He, *Spatially resolving unconventional interface Landau quantization in a graphene monolayer-bilayer planar junction*, Phys. Rev. B **93**, 195408 (2016).
- [77] K. W. Clark, X.-G. Zhang, G. Gu, J. Park, G. He, R. Feenstra, and A.-P. Li, *Energy Gap Induced by Friedel Oscillations Manifested as Transport Asymmetry at Monolayer-Bilayer Graphene Boundaries*, Phys. Rev. X **4**, 011021 (2014).
- [78] L. Ju, Z. Shi, N. Nair, Y. Lv, C. Jin, J. Velasco, C. Ojeda-Aristizabal, H. A. Bechtel, M. C. Martin, A. Zettl, J. Analytis, and F. Wang, *Topological valley transport at bilayer graphene domain walls*, Nature (London) **520**, 650 (2015).
- [79] M. Pelc, W. Jaskólski, A. Ayuela, and L. Chico, *Topologically confined states at corrugations of gated bilayer graphene*, Phys. Rev. B **92**, 085433 (2015).
- [80] F. Giannazzo, I. Deretzis, A. L. Magna, F. Roccaforte, and R. Yakimova, *Electronic transport at monolayer-bilayer junctions in epitaxial graphene on SiC*, Phys. Rev. B **86**, 235422 (2012).
- [81] A. Nourbakhsh, M. Cantoro, A. V. Klekachev, G. Pourtois, T. Vosch, J. Hofkens, M. H. van der Veen, M. M. Heyns, S. D. Gendt, and B. F. Sels, *Single Layer vs Bilayer Graphene: A Comparative Study of the Effects of Oxygen Plasma Treatment on Their Electronic and Optical Properties*, J. Phys. Chem. C **115**, 16619 (2011).
- [82] B. Z. Rameshti, M. Zareyan, and A. G. Moghaddam, *Supercurrent reversal in Josephson junctions based on bilayer graphene flakes*, Phys. Rev. B **92**, 085403 (2015).

- [83] B. Wang, M. Huang, N. Y. Kim, B. V. Cunning, Y. Huang, D. Qu, X. Chen, S. Jin, M. Biswal, X. Zhang, S. H. Lee, H. Lim, W. J. Yoo, Z. Lee, and R. S. Ruoff, *Controlled Folding of Single Crystal Graphene*, *Nano Lett.* **17**, 1467 (2017).
- [84] J. C. Rode, C. Belke, H. Schmidt, and R. J. Haug, *Interlayer Configurations in Twisted Bilayers of Folded Graphene*, arXiv: 1608.08133 (2016).
- [85] M. Schmitz, S. Engels, L. Banszerus, K. Watanabe, T. Taniguchi, C. Stampfer, and B. Beschoten, *High-quality dry transferred CVD bilayer graphene*, arXiv:1704.04352 (2017).
- [86] Y. Hao *et al.*, *Oxygen-activated growth and bandgap tunability of large single-crystal bilayer graphene*, *Nat. Nanotechnol.* **11**, 426 (2016).
- [87] L.-J. Yin, W.-X. Wang, Y. Zhang, Y.-Y. Ou, H.-T. Zhang, C.-Y. Shen, and L. He, *Observation of chirality transition of quasiparticles at stacking solitons in trilayer graphene*, *Phys. Rev. B* **95**, 081402(R) (2017).
- [88] L.-J. Yin, H. Jiang, J.-B. Qiao, and L. He, *Direct imaging of topological edge states at a bilayer graphene domain wall*, *Nat. Commun.* **7**, 11760 (2016).
- [89] B. Huard, J. A. Sulpizio, N. Stander, K. Todd, B. Yang, and D. Goldhaber-Gordon, *Transport Measurements Across a Tunable Potential Barrier in Graphene*, *Phys. Rev. Lett.* **98**, 236803 (2007).
- [90] M. Barbier, P. Vasilopoulos, and F. M. Peeters, *Kronig-Penney model on bilayer graphene: Spectrum and transmission periodic in the strength of the barriers*, *Phys. Rev. B* **82**, 235408 (2010).

- [91] B. Van Duppen, S. H. R. Sena, and F. M. Peeters, *Multiband tunneling in trilayer graphene*, Phys. Rev. B **87**, 195439 (2013).
- [92] Y. Blanter and M. Büttiker, *Shot noise in mesoscopic conductors*, Phys. Rep. **336**, 1 (2000).
- [93] B. Van Duppen and F. M. Peeters, *Comment on “Chiral tunneling in trilayer graphene” [Appl. Phys. Lett. 100, 163102 (2012)]*, Appl. Phys. Lett. **101**, 226101 (2012).
- [94] S. B. Kumar and J. Guo, *Chiral tunneling in trilayer graphene*, Appl. Phys. Lett. **100**, 163102 (2012).
- [95] I. Snyman and C. W. J. Beenakker, *Ballistic transmission through a graphene bilayer*, Phys. Rev. B **75**, 045322 (2007).
- [96] J. W. González, H. Santos, E. Prada, L. Brey, and L. Chico, *Gate-controlled conductance through bilayer graphene ribbons*, Phys. Rev. B **83**, 205402 (2011).
- [97] T. Nakanishi, M. Koshino, and T. Ando, *Transmission through a boundary between monolayer and bilayer graphene*, Phys. Rev. B **82**, 125428 (2010).
- [98] L. R. F. Lima, A. R. Hernández, F. A. Pinheiro, and C. Lewenkopf, *A 50/50 electronic beam splitter in graphene nanoribbons as a building block for electron optics*, J. Phys.: Condens. Matter **28**, 505303 (2016).
- [99] P. Brandimarte, M. Englund, N. Papior, A. Garcia-Lekue, T. Frederiksen, and D. Sánchez-Portal, *A tunable electronic beam splitter realized with crossed graphene nanoribbons*, J. Chem. Phys. **146**, 092318 (2017).

- [100] M. R. Masir, P. Vasilopoulos, and F. M. Peeters, *Fabry-Pérot resonances in graphene microstructures: Influence of a magnetic field*, Phys. Rev. B **82**, 115417 (2010).
- [101] J. Güttinger, F. Molitor, C. Stampfer, S. Schnez, A. Jacobsen, S. Dröscher, T. Ihn, and K. Ensslin, *Transport through graphene quantum dots*, Rep. Prog. Phys. **75**, 126502 (2012).
- [102] P. G. Silvestrov and K. B. Efetov, *Quantum Dots in Graphene*, Phys. Rev. Lett. **98**, 016802 (2007).
- [103] A. D. Güçlü, P. Potasz, M. Korkusinski, and P. Hawrylak, *Graphene Quantum Dots* (Springer Berlin Heidelberg, 2014).
- [104] A. D. Güçlü, P. Potasz, and P. Hawrylak, in *Future Trends in Microelectronics* (John Wiley & Sons, Inc., 2013), pp. 308–318.
- [105] M. Bacon, S. J. Bradley, and T. Nann, *Graphene Quantum Dots*, Particle & Particle Systems Characterization **31**, 415 (2014).
- [106] B. Trauzettel, D. V. Bulaev, D. Loss, and G. Burkard, *Spin qubits in graphene quantum dots*, Nat. Phys. **3**, 192 (2007).
- [107] H. Sun, L. Wu, W. Wei, and X. Qu, *Recent advances in graphene quantum dots for sensing*, Mater. Today **16**, 433 (2013).
- [108] A. D. Martino, L. Dell’Anna, and R. Egger, *Magnetic Confinement of Massless Dirac Fermions in Graphene*, Phys. Rev. Lett. **98**, 066802 (2007).
- [109] N. M. R. Peres, A. H. C. Neto, and F. Guinea, *Dirac fermion confinement in graphene*, Phys. Rev. B **73**, 241403(R) (2006).

- [110] A. Rozhkov, G. Giavaras, Y. P. Bliokh, V. Freilikher, and F. Nori, *Electronic properties of mesoscopic graphene structures: Charge confinement and control of spin and charge transport*, Phys. Rep. **503**, 77 (2011).
- [111] P. Recher, J. Nilsson, G. Burkard, and B. Trauzettel, *Bound states and magnetic field induced valley splitting in gate-tunable graphene quantum dots*, Phys. Rev. B **79**, 085407 (2009).
- [112] H. Fehske, G. Hager, and A. Pieper, *Electron confinement in graphene with gate-defined quantum dots*, Phys. Stat. Solidi B **252**, 1868 (2015).
- [113] H.-Y. Chen, V. Apalkov, and T. Chakraborty, *Fock-Darwin States of Dirac Electrons in Graphene-Based Artificial Atoms*, Phys. Rev. Lett. **98**, 186803 (2007).
- [114] G. Giavaras and F. Nori, *Dirac gap-induced graphene quantum dot in an electrostatic potential*, Phys. Rev. B **83**, 165427 (2011).
- [115] G. Giorgos and F. Nori, *Graphene quantum dots formed by a spatial modulation of the Dirac gap*, Appl. Phys. Lett. **97**, 243106 (2010).
- [116] G. Giavaras, P. A. Maksym, and M. Roy, *Magnetic field induced confinement–deconfinement transition in graphene quantum dots*, J. Phys.: Condens. Matter **21**, 102201 (2009).
- [117] T. Espinosa-Ortega, I. A. Luk'yanchuk, and Y. G. Rubo, *Magnetic properties of graphene quantum dots*, Phys. Rev. B **87**, 205434 (2013).
- [118] P. Hewagegana and V. Apalkov, *Electron localization in graphene quantum dots*, Phys. Rev. B **77**, 245426 (2008).

- [119] D. da Costa, M. Zarenia, A. Chaves, G. Farias, and F. Peeters, *Analytical study of the energy levels in bilayer graphene quantum dots*, Carbon **78**, 392 (2014).
- [120] M. Mirzakhani, M. Zarenia, S. A. Ketabi, D. R. da Costa, and F. M. Peeters, *Energy levels of hybrid monolayer-bilayer graphene quantum dots*, Phys. Rev. B **93**, 165410 (2016).
- [121] M. Zarenia, J. M. Pereira, A. Chaves, F. M. Peeters, and G. A. Farias, *Simplified model for the energy levels of quantum rings in single layer and bilayer graphene*, Phys. Rev. B **81**, 045431 (2010).
- [122] D. P. Żebrowski, E. Wach, and B. Szafran, *Confined states in quantum dots defined within finite flakes of bilayer graphene: Coupling to the edge, ionization threshold, and valley degeneracy*, Phys. Rev. B **88**, 165405 (2013).
- [123] A. Gutiérrez-Rubio and T. Stauber, *Mass-profile quantum dots in graphene and artificial periodic structures*, Phys. Rev. B **91**, 165415 (2015).
- [124] Y. Liu, X. Liu, Y. Zhang, Q. Xia, and J. He, *Effect of magnetic field on electronic transport in a bilayer graphene nanomesh*, Nanotechnology **28**, 235303 (2017).
- [125] Y. Li, Q. Wan, Y. Peng, G. Wang, Z. Qian, G. Zhou, and M. B. A. Jalil, *The effect of magnetic field on chiral transmission in p-n-p graphene junctions*, Sci. Rep. **5**, 18458 (2015).
- [126] K. Todd, H.-T. Chou, S. Amasha, and D. Goldhaber-Gordon, *Quantum Dot Behavior in Graphene Nanoconstrictions*, Nano Lett. **9**, 416 (2009).

- [127] C. R. Woods *et al.*, *Commensurate–incommensurate transition in graphene on hexagonal boron nitride*, Nat. Phys. **10**, 451 (2014).
- [128] C. R. Dean, A. F. Young, I. Meric, C. Lee, L. Wang, S. Sorgenfrei, K. Watanabe, T. Taniguchi, P. Kim, K. L. Shepard, and J. Hone, *Boron nitride substrates for high-quality graphene electronics*, Nat. Nanotechnol. **5**, 722 (2010).
- [129] J. Xue, J. Sanchez-Yamagishi, D. Bulmash, P. Jacquod, A. Deshpande, K. Watanabe, T. Taniguchi, P. Jarillo-Herrero, and B. J. LeRoy, *Scanning tunnelling microscopy and spectroscopy of ultra-flat graphene on hexagonal boron nitride*, Nat. Mater. **10**, 282 (2011).
- [130] R. Decker, Y. Wang, V. W. Brar, W. Regan, H.-Z. Tsai, Q. Wu, W. Gannett, A. Zettl, and M. F. Crommie, *Local Electronic Properties of Graphene on a BN Substrate via Scanning Tunneling Microscopy*, Nano Lett. **11**, 2291 (2011).
- [131] E. Rotenberg, A. Bostwick, T. Ohta, J. L. McChesney, T. Seyller, and K. Horn, *Origin of the energy bandgap in epitaxial graphene*, Nat. Mater. **7**, 258 (2008).
- [132] S. Zhou, D. Siegel, A. Fedorov, F. Gabaly, A. Schmid, A. C. Neto, D.-H. Lee, and A. Lanzara, *Origin of the energy bandgap in epitaxial graphene*, Nat. Mater. **7**, 259 (2008).
- [133] K. A. Guerrero-Becerra and M. Rontani, *Wigner localization in a graphene quantum dot with a mass gap*, Phys. Rev. B **90**, 125446 (2014).
- [134] S. Jung, G. M. Rutter, N. N. Klimov, D. B. Newell, I. Calizo, A. R. Hight-Walker, N. B. Zhitenev, and J. A. Stroscio, *Evolution of microscopic localization in graphene*

- in a magnetic field from scattering resonances to quantum dots*, Nat. Phys. **7**, 245 (2011).
- [135] J. Mao, Y. Jiang, D. Moldovan, G. Li, K. Watanabe, T. Taniguchi, M. R. Masir, F. M. Peeters, and E. Y. Andrei, *Realization of a tunable artificial atom at a supercritically charged vacancy in graphene*, Nat. Phys. **12**, 545 (2016).
- [136] A. Matulis and F. M. Peeters, *Quasibound states of quantum dots in single and bilayer graphene*, Phys. Rev. B **77**, 115423 (2008).
- [137] Y. Zhao, J. Wyrick, F. D. Natterer, J. F. Rodriguez-Nieva, C. Lewandowski, K. Watanabe, T. Taniguchi, L. S. Levitov, N. B. Zhitenev, and J. A. Stroscio, *Creating and probing electron whispering-gallery modes in graphene*, Science **348**, 672 (2015).
- [138] F. Ghahari, D. Walkup, C. Gutiérrez, J. F. Rodriguez-Nieva, Y. Zhao, J. Wyrick, F. D. Natterer, W. G. Cullen, K. Watanabe, T. Taniguchi, L. S. Levitov, N. B. Zhitenev, and J. A. Stroscio, *An on/off Berry phase switch in circular graphene resonators*, Science **356**, 845 (2017).
- [139] C. Gutiérrez, L. Brown, C.-J. Kim, J. Park, and A. N. Pasupathy, *Klein tunnelling and electron trapping in nanometre-scale graphene quantum dots*, Nat. Phys. **12**, 1069 (2016).
- [140] J. Lee, D. Wong, J. V. Jr, J. F. Rodriguez-Nieva, S. Kahn, H.-Z. Tsai, T. Taniguchi, K. Watanabe, A. Zettl, F. Wang, L. S. Levitov, and M. F. Crommie, *Imaging electrostatically confined Dirac fermions in graphene quantum dots*, Nat. Phys. **12**, 1032 (2016).

- [141] K.-K. Bai, J.-B. Qiao, H. Jiang, H. Liu, and L. He, *Massless Dirac fermions trapping in a quasi-one-dimensional npn junction of a continuous graphene monolayer*, Phys. Rev. B **95**, 201406(R) (2017).
- [142] N. M. Freitag, L. A. Chizhova, P. Nemes-Incze, C. R. Woods, R. V. Gorbachev, Y. Cao, A. K. Geim, K. S. Novoselov, J. Burgdörfer, F. Libisch, and M. Morgenstern, *Electrostatically Confined Monolayer Graphene Quantum Dots with Orbital and Valley Splittings*, Nano Lett. **16**, 5798 (2016).
- [143] J.-B. Qiao, H. Jiang, H. Liu, H. Yang, N. Yang, K.-Y. Qiao, and L. He, *Bound states in nanoscale graphene quantum dots in a continuous graphene sheet*, Phys. Rev. B **95**, 081409(R) (2017).
- [144] A. Müller, B. Kaestner, F. Hohls, T. Weimann, K. Pierz, and H. W. Schumacher, *Bilayer graphene quantum dot defined by topgates*, J. Appl. Phys. **115**, 233710 (2014).
- [145] J. M. Pereira, P. Vasilopoulos, and F. M. Peeters, *Tunable Quantum Dots in Bilayer Graphene*, Nano Lett. **7**, 946 (2007).
- [146] M. Zarenia, J. M. Pereira, F. M. Peeters, and G. A. Farias, *Electrostatically Confined Quantum Rings in Bilayer Graphene*, Nano Lett. **9**, 4088 (2009).
- [147] W. Jaskólski, M. Pelc, G. W. Bryant, L. Chico, and A. Ayuela, *Controlling the layer localization of gapless states in bilayer graphene with a gate voltage*, 2D Mater. **5**, 025006 (2018).

- [148] H. M. Abdullah, M. Zarenia, H. Bahlouli, F. M. Peeters, and B. Van Duppen, *Gate tunable layer selectivity of transport in bilayer graphene nanostructures*, Europhys. Lett. **113**, 17006 (2016).
- [149] T. L. M. Lane, M. Anđelković, J. R. Wallbank, L. Covaci, F. M. Peeters, and V. I. Fal'ko, *Ballistic electron channels including weakly protected topological states in delaminated bilayer graphene*, Phys. Rev. B **97**, 045301 (2018).
- [150] B. E. Feldman, J. Martin, and A. Yacoby, *Broken-symmetry states and divergent resistance in suspended bilayer graphene*, Nat. Phys. **5**, 889 (2009).
- [151] M. Morgenstern, N. Freitag, A. Nent, P. Nemes-Incze, and M. Liebmann, *Graphene Quantum Dots Probed by Scanning Tunneling Microscopy*, Ann. d. Phys. **529**, 1700018 (2017).
- [152] M. Schmitz, S. Engels, L. Banszerus, K. Watanabe, T. Taniguchi, C. Stampfer, and B. Beschoten, *High mobility dry-transferred CVD bilayer graphene*, Appl. Phys. Lett. **110**, 263110 (2017).
- [153] N. Kim, K. S. Kim, N. Jung, L. Brus, and P. Kim, *Synthesis and Electrical Characterization of Magnetic Bilayer Graphene Intercalate*, Nano Lett. **11**, 860 (2011).
- [154] P. Ge and M. Foulletier, *Electrochemical intercalation of sodium in graphite*, Solid State Ionics **28-30**, 1172 (1988).
- [155] K. Kanetani, K. Sugawara, T. Sato, R. Shimizu, K. Iwaya, T. Hitosugi, and T. Takahashi, *Ca intercalated bilayer graphene as a thinnest limit of superconducting C6Ca*, PNAS **109**, 19610 (2012).

- [156] S. Ichinokura, K. Sugawara, A. Takayama, T. Takahashi, and S. Hasegawa, *Superconducting Calcium-Intercalated Bilayer Graphene*, ACS Nano **10**, 2761 (2016).
- [157] D. Guo, T. Kondo, T. Machida, K. Iwatake, S. Okada, and J. Nakamura, *Observation of Landau levels in potassium-intercalated graphite under a zero magnetic field*, Nat. Commun. **3**, (2012).
- [158] J. Wang, D. C. Sorescu, S. Jeon, A. Belianinov, S. V. Kalinin, A. P. Baddorf, and P. Maksymovych, *Atomic intercalation to measure adhesion of graphene on graphite*, Nat. Commun. **7**, 13263 (2016).
- [159] R. Shimizu, K. Sugawara, K. Kanetani, K. Iwaya, T. Sato, T. Takahashi, and T. Hitosugi, *Charge-Density Wave in Ca-Intercalated Bilayer Graphene Induced by Commensurate Lattice Matching*, Phys. Rev. Lett. **114**, 146103 (2015).
- [160] W.-X. Wang, Y.-W. Wei, S.-Y. Li, X. Li, X. Wu, J. Feng, and L. He, *Imaging the dynamics of an individual hydrogen atom intercalated between two graphene sheets*, Phys. Rev. B **97**, 085407 (2018).
- [161] J. E. Scheerder, T. Picot, N. Reckinger, T. Sneyder, V. S. Zharinov, J.-F. Colomer, E. Janssens, and J. V. de Vondel, *Decorating graphene with size-selected few-atom clusters: a novel approach to investigate graphene–adparticle interactions*, Nanoscale **9**, 10494 (2017).
- [162] H. Rezania and M. Yarmohammadi, *Controlling dynamical thermal transport of biased bilayer graphene by impurity atoms*, AIP Advances **6**, 075121 (2016).

- [163] J. M. Pereira, F. M. Peeters, P. Vasilopoulos, R. N. C. Filho, and G. A. Farias, *Landau levels in graphene bilayer quantum dots*, Phys. Rev. B **79**, 195403 (2009).
- [164] M. R. Masir, P. Vasilopoulos, and F. M. Peeters, *Tunneling, conductance, and wavevector filtering through magnetic barriers in bilayer graphene*, Phys. Rev. B **79**, 035409 (2009).
- [165] H. M. Abdullah, A. E. Mouhafid, H. Bahlouli, and A. Jellal, *Band tunneling through double barrier in biased graphene bilayer*, Mater. Res. Express **4**, 025009 (2017).
- [166] L. J. P. Xavier, J. M. Pereira, A. Chaves, G. A. Farias, and F. M. Peeters, *Topological confinement in graphene bilayer quantum rings*, Appl. Phys. Lett. **96**, 212108 (2010).
- [167] M. Abramowitz and I. A. Stegun, *Handbook of mathematical functions: with formulas, graphs, and mathematical tables* (National Bureau of Standards, Washington, 1970).
- [168] L. Cohnitz, A. D. Martino, W. Häusler, and R. Egger, *Chiral interface states in graphene p-n junctions*, Phys. Rev. B **94**, 165443 (2016).
- [169] L. Lain, A. Toree, and J. M. Alvarino, *Radial probability density and normalization in hydrogenic atoms*, J. Chem. Educ. **58**, 617 (1981).
- [170] J. von Neumann and E. P. Wigner, Phys. Z. **30**, 467 (1929).
- [171] W. Greiner, B. Muller, and J. Rafelski, *Quantum Electrodynamics of Strong Fields* (Springer-Verlag, Berlin, 1985).

- [172] M. Neek-Amal, L. Covaci, K. Shakouri, and F. M. Peeters, *Electronic structure of a hexagonal graphene flake subjected to triaxial stress*, Phys. Rev. B **88**, 115428 (2013).
- [173] V. V. Cheianov, V. Fal'ko, and B. L. Altshuler, *The Focusing of Electron Flow and a Veselago Lens in Graphene p-n Junctions*, Science **315**, 1252 (2007).
- [174] V. G. Veselago, *The Electrodynamics of Substances with Simultaneously Negative Values of ϵ and μ* , Sov. Phys. Usp. **10**, 509 (1968).
- [175] P. V. Parimi, W. T. Lu, P. Vodo, J. Sokoloff, J. S. Derov, and S. Sridhar, *Negative Refraction and Left-Handed Electromagnetism in Microwave Photonic Crystals*, Phys. Rev. Lett. **92**, 127401 (2004).
- [176] E. Cubukcu, K. Aydin, E. Ozbay, S. Foteinopoulou, and C. M. Soukoulis, *Subwavelength Resolution in a Two-Dimensional Photonic-Crystal-Based Superlens*, Phys. Rev. Lett. **91**, 207401 (2003).
- [177] A. A. Houck, J. B. Brock, and I. L. Chuang, *Experimental Observations of a Left-Handed Material That Obeys Snell's Law*, Phys. Rev. Lett. **90**, 137401 (2003).
- [178] A. Grbic and G. V. Eleftheriades, *Overcoming the Diffraction Limit with a Planar Left-Handed Transmission-Line Lens*, Phys. Rev. Lett. **92**, 117403 (2004).
- [179] K. E. Aidala, R. E. Parrott, T. Kramer, E. J. Heller, R. M. Westervelt, M. P. Hanson, and A. C. Gossard, *Imaging magnetic focusing of coherent electron waves*, Nat. Phys. **3**, 464 (2007).

- [180] S. W. LaGasse and J. U. Lee, *Understanding magnetic focusing in graphene p-n junctions through quantum modeling*, Phys. Rev. B **95**, 155433 (2017).
- [181] S.-H. Zhang, W. Yang, and F. M. Peeters, *Veselago focusing of anisotropic massless Dirac fermions*, Phys. Rev. B **97**, 205437 (2018).
- [182] C. G. Péterfalvi, L. Oroszlány, C. J. Lambert, and J. Cserti, *Intraband electron focusing in bilayer graphene*, New J. Phys. **14**, 063028 (2012).
- [183] G.-H. Lee, G.-H. Park, and H.-J. Lee, *Observation of negative refraction of Dirac fermions in graphene*, Nat. Phys. **11**, 925 (2015).
- [184] S. Chen, Z. Han, M. M. Elahi, K. M. M. Habib, L. Wang, B. Wen, Y. Gao, T. Taniguchi, K. Watanabe, J. Hone, A. W. Ghosh, and C. R. Dean, *Electron optics with p-n junctions in ballistic graphene*, Science **353**, 1522 (2016).
- [185] C.-H. Park, Y.-W. Son, L. Yang, M. L. Cohen, and S. G. Louie, *Electron Beam Supercollimation in Graphene Superlattices*, Nano Lett. **8**, 2920 (2008).
- [186] S. Choi, C.-H. Park, and S. G. Louie, *Electron Supercollimation in Graphene and Dirac Fermion Materials Using One-Dimensional Disorder Potentials*, Phys. Rev. Lett. **113**, 026802 (2014).
- [187] M.-H. Liu, C. Gorini, and K. Richter, *Creating and Steering Highly Directional Electron Beams in Graphene*, Phys. Rev. Lett. **118**, 066801 (2017).
- [188] A. W. Barnard, A. Hughes, A. L. Sharpe, K. Watanabe, T. Taniguchi, and D. Goldhaber-Gordon, *Absorptive pinhole collimators for ballistic Dirac fermions in graphene*, Nat. Commun. **8**, 15418 (2017).

- [189] S. Bhandari, G. H. Lee, K. Watanabe, T. Taniguchi, P. Kim, and R. M. Westervelt, *Imaging electron flow from collimating contacts in graphene*, 2D Mater. **5**, 021003 (2018).
- [190] C. Handschin, B. Fülöp, P. Makk, S. Blanter, M. Weiss, K. Watanabe, T. Taniguchi, S. Csonka, and C. Schönenberger, *Point contacts in encapsulated graphene*, Appl. Phys. Lett. **107**, 183108 (2015).
- [191] A. Kinikar, T. P. Sai, S. Bhattacharyya, A. Agarwala, T. Biswas, S. K. Sarker, H. R. Krishnamurthy, M. Jain, V. B. Shenoy, and A. Ghosh, *Quantized edge modes in atomic-scale point contacts in graphene*, Nat. Nanotechnol. **12**, 564 (2017).
- [192] H. Overweg, H. Eggimann, X. Chen, S. Slizovskiy, M. Eich, R. Pisoni, Y. Lee, P. Rickhaus, K. Watanabe, T. Taniguchi, V. Fal'ko, T. Ihn, and K. Ensslin, *Electrostatically Induced Quantum Point Contacts in Bilayer Graphene*, Nano Lett. **18**, 553 (2017).
- [193] H. M. Abdullah, M. Van der Donck, H. Bahlouli, F. M. Peeters, and B. Van Duppen, *Graphene quantum blisters: A tunable system to confine charge carriers*, Appl. Phys. Lett. **112**, 213101 (2018).
- [194] H. M. Abdullah, H. Bahlouli, F. M. Peeters, and B. Van Duppen, *Confined states in graphene quantum blisters*, J. Phys.: Condens. Matter **30**, 385301 (2018).
- [195] K. Reijnders, T. Tudorovskiy, and M. Katsnelson, *Semiclassical theory of potential scattering for massless Dirac fermions*, Ann. Phys. **333**, 155 (2013).

- [196] S. P. Milovanović, D. Moldovan, and F. M. Peeters, *Veselago lensing in graphene with a p-n junction: Classical versus quantum effects*, J. Appl. Phys. **118**, 154308 (2015).
- [197] K. J. A. Reijnders and M. I. Katsnelson, *Symmetry breaking and (pseudo)spin polarization in Veselago lenses for massless Dirac fermions*, Phys. Rev. B **95**, 115310 (2017).
- [198] S. P. Milovanović, M. R. Masir, and F. M. Peeters, *Magnetic electron focusing and tuning of the electron current with a pn-junction*, J. Appl. Phys. **115**, 043719 (2014).
- [199] G. M. Maksimova, V. Y. Demikhovskii, and E. V. Frolova, *Wave packet dynamics in a monolayer graphene*, Phys. Rev. B **78**, (2008).
- [200] A. Chaves, L. Covaci, K. Y. Rakhimov, G. A. Farias, and F. M. Peeters, *Wave-packet dynamics and valley filter in strained graphene*, Phys. Rev. B **82**, 205430 (2010).
- [201] V. Krueckl and T. Kramer, *Revivals of quantum wave packets in graphene*, New J. Phys. **11**, 093010 (2009).
- [202] M. Mirzakhani, M. Zarenia, and F. M. Peeters, *Edge states in gated bilayer-monolayer graphene ribbons and bilayer domain walls*, J. Appl. Phys. **123**, 204301 (2018).
- [203] J. M. Pereira, F. M. Peeters, A. Chaves, and G. A. Farias, *Klein tunneling in single and multiple barriers in graphene*, Semicond. Sci. Technol. **25**, 033002 (2010).

- [204] M. Barbier, P. Vasilopoulos, and F. M. Peeters, *Single-layer and bilayer graphene superlattices: collimation, additional Dirac points and Dirac lines*, Phil. Trans. R. Soc. A **368**, 5499 (2010).
- [205] S. Park and H.-S. Sim, *Berry phase and Veselago lens in a bilayer graphene np junction*, Phys. Rev. B **84**, 235432 (2011).
- [206] V. T. Phong and J. F. Kong, *Fermionic Lensing in Smooth Graphene P-N Junctions*, arXiv: 1610.00201v1 (2016).
- [207] K. Zou, X. Hong, and J. Zhu, *Effective mass of electrons and holes in bilayer graphene: Electron-hole asymmetry and electron-electron interaction*, Phys. Rev. B **84**, 085408 (2011).
- [208] F. Batista, A. Chaves, D. da Costa, and G. Farias, *Curvature effects on the electronic and transport properties of semiconductor films*, Physica E **99**, 304 (2018).
- [209] D. R. da Costa, A. Chaves, G. A. Farias, and F. M. Peeters, *Valley filtering in graphene due to substrate-induced mass potential*, J. Phys.: Condens. Matter **29**, 215502 (2017).
- [210] A. Chaves, D. R. da Costa, G. O. de Sousa, J. M. Pereira, and G. A. Farias, *Energy shift and conduction-to-valence band transition mediated by a time-dependent potential barrier in graphene*, Phys. Rev. B **92**, 125441 (2015).
- [211] L. S. Cavalcante, A. Chaves, D. R. da Costa, G. A. Farias, and F. M. Peeters, *All-strain based valley filter in graphene nanoribbons using snake states*, Phys. Rev. B **94**, 075432 (2016).

- [212] D. R. da Costa, A. Chaves, G. A. Farias, L. Covaci, and F. M. Peeters, *Wave-packet scattering on graphene edges in the presence of a pseudomagnetic field*, Phys. Rev. B **86**, 115434 (2012).
- [213] A. Chaves, G. A. Farias, F. M. Peeters, and B. Szafran, *Wave packet dynamics in semiconductor quantum rings of finite width*, Phys. Rev. B **80**, 125331 (2009).
- [214] M. H. Degani and M. Z. Maialle, *Numerical Calculations of the Quantum States in Semiconductor Nanostructures*, J. Comput. Theor. Nanosci. **7**, 454 (2010).
- [215] A. Chaves, G. A. Farias, F. M. Peeters, and R. Ferreira, *The Split-Operator Technique for the Study of Spinorial Wavepacket Dynamics*, Comm. Comput. Phys. **17**, 850 (2015).
- [216] K. Y. Rakhimov, A. Chaves, G. A. Farias, and F. M. Peeters, *Wavepacket scattering of Dirac and Schrödinger particles on potential and magnetic barriers*, J. Phys.: Condens. Matter **23**, 275801 (2011).
- [217] T. Kramer, *Time-dependent approach to transport and scattering in atomic and mesoscopic physics*, AIP Conf. Proc. **1334**, 142 (2011).



Phys. Dept., KFUPM, Dhahran 31261 – Saudi Arabia
☎ (+966)13-89443348 • ✉ alshehab211@gmail.com
Born: May 6, 1984, Taiz, Yemen

Hasan M. Abdullah

Curriculum Vitae

"Life is a conservative field" - Hasan Abdullah

Education

- 2014–2018 **PhD in Physics**, KFUPM, Saudi Arabia, GPA – 3.53/4.
Title of thesis: Electronic and transport properties of locally delaminated bilayer graphene
- 2010–2014 **Master in physics** KFUPM, Saudi Arabia, GPA – 3.75/4
Title of thesis: Transport properties in bilayer graphene
- 2003–2007 **Bachelor of science in physics** Taiz University, Yemen, GPA – 3.50/4

Computer skills

- Oper. system Windows, Linux.
Office Word, PowerPoint, Excel
Programming Mathematica, \LaTeX , basic knowledge in C, MATLAB, and ATK

Languages

- Arabic **native**
English **very good**

Publications

1. **Hasan. M. Abdullah**, D. R. da Costa, H. Bahlouli, F. M. Peeters and B. Van Duppen, "Electron collimation at van der Waals domain walls in bilayer graphene", In progress.
2. **Hasan. M. Abdullah**, Mohammed Al Ezzi and H. Bahlouli, "Band gap engineering in AStacked bilayer graphene ", Accepted in Journal of Applied Physics.
3. **Hasan. M. Abdullah**, H. Bahlouli, F. M. Peeters, and B. Van Duppen, "Confined states in graphene quantum blisters", Journal of Physics: Condensed Matter **30**, 385301(2018).

4. **Hasan. M. Abdullah**, M. Van der Donck, H. Bahlouli, F. M. Peeters, and B. Van Duppen, "Graphene quantum blisters: a tunable system to confine charge carriers". Applied Physics Letters **112** (2018). **Editor's Pick**
5. **Hasan. M. Abdullah** and Hocine Bahlouli, "Substrate effects on transport properties of a biased AA-stacked bilayer graphene", Journal of Computational Science **26**, 135 (2018).
6. **Hasan. M. Abdullah**, B. Van Duppen, M. Zarenia, H. Bahlouli, and F. M. Peeters, "Quantum transport across van der Waals domain walls in bilayer graphene", Journal of Physics: Condensed Matter **29**, 425303 (2017). **Annual Journal Highlights (2017)**
7. **Hasan. M. Abdullah**, Hocine Bahlouli, Abderrahim El Mouhafid and Ahmed Jellal, "Band tunneling through double barrier in biased graphene bilayer", Material Research Express **4**, 025009 (2017).
8. Nacir Tit, Mohammed M. Ezzi, **Hasan. M. Abdullah**, Maksudbek Yusupov, Summayya Kouser, H. Bahlouli, Zain H. Yamani, "Detection of CO₂ using CNT-based sensors: Role of Fe catalyst on sensitivity and selectivity", Materials Chemistry and Physics **186**, 353 (2017).
9. **Hasan. M. Abdullah**, M. Zarenia, H. Bahlouli, F. M. Peeters and B. Van Duppen, "Gate tunable layer selectivity of transport in bilayer graphene nanostructures", Europhysics Letters **113**, 17006 (2016).
10. G. R. Berdiyrov, **Hasan. M. Abdullah**, M. Al Ezzi, G. V. Rakhmatullaeva, H. Bahlouli and N. Tit, "CO₂ adsorption on Fe-doped graphene nanoribbons: First principles electronic transport calculations", AIP advances **6**, 125102 (2016).

Conferences and Workshops

1. **Hasan. M. Abdullah** and Hocine Bahlouli, *Substrate effects on transport properties of a biased AA-stacked bilayer graphene*, Physics Day at KFUPM, April 30th, 2018.
2. **Hasan. M. Abdullah** and Hocine Bahlouli, "Electrostatic tunable confined states in graphene quantum blisters", KFUPM 9th Internal Conference, May 1-2, 2018.
3. **Hasan. M. Abdullah**, and Hocine Bahlouli, "Substrate effects on transport properties of a biased AA-stacked bilayer graphene", ICSEC-2017 conference, October 23-24, 2017, Qatar.
4. **Hasan. M. Abdullah**, and H. Bahlouli, "Layer Filtering in Hybrid Monolayer-Bilayer Graphene Systems", the 4-th Saudi International Nanotechnology Conference, KFUPM, Dhahran, Saudi Arabia, October 25-27, 2016.
5. G. R. Berdiyrov, **Hasan. M. Abdullah**, M. Al-Azzi, H. Bahlouli, N. Tit, and M. El Amine, "CO₂ Adsorption on Fe-Doped Graphene Nanoribbons: First Principle Electronic Transport Calculations", the 4-th Saudi International Nanotechnology Conference, KFUPM, Dhahran, Saudi Arabia, October 25-27, 2016.
6. Nacir Tit, Mohammed Elezzi, **Hasan. M. Abdullah**, Hocine Bahlouli, Zain Yamani, *Absorption of CO₂ on Carbon-based Sensors: First-Principle Analysis*, American Physical Society Meeting, March 2016.
7. **Hasan. M. Abdullah** and H. Bahlouli, "Gate Tunable Nanostructure Graphene Based Layer Switch", Fifth Saudi International Meeting on Frontiers of Physics, 16-18 of February, 2016, Jazan University, Saudi-Arabia.

Google Scholar

<https://scholar.google.be/citations?user=GeecOggAAAAJ&hl=en>

Awards and Honors

- My paper in Appl. Phys. Lett. 112, (2018) has been selected as Editor's Pick.
- My poster in Physics Day at KFUPM, April 30th, (2018) won the second prize.
- My paper in J. of Phys.: Cond. Matt. 29, 425303 (2017) has been selected for Annual Journal Highlights (2017).

References

- Prof. Hocine Bahlouli (Advisor), Professor of Physics Department, KFUPM, Saudi Arabia.
Email: bahlouli@kfupm.edu.sa
- Prof. Dr. Francois. M. Peeters (Co-Advisor), Professor of Physics Department (Head of CMT research group), University of Antwerp, Belgium.
Email: francois.peeters@uantwerpen.be
- Dr. Ben Van Duppen, Assistant Prof. in Physics Department, University of Antwerp, Belgium.
Email: ben.vanduppen@uantwerpen.be

Updated: October 29, 2018